

12-14-2015

Guided Wave Based Integrated Structural Health Monitoring and Nondestructive Evaluation

Zhenhua Tian
University of South Carolina - Columbia

Follow this and additional works at: <https://scholarcommons.sc.edu/etd>



Part of the [Mechanical Engineering Commons](#)

Recommended Citation

Tian, Z. (2015). *Guided Wave Based Integrated Structural Health Monitoring and Nondestructive Evaluation*. (Doctoral dissertation). Retrieved from <https://scholarcommons.sc.edu/etd/3269>

This Open Access Dissertation is brought to you by Scholar Commons. It has been accepted for inclusion in Theses and Dissertations by an authorized administrator of Scholar Commons. For more information, please contact digres@mailbox.sc.edu.

GUIDED WAVE BASED INTEGRATED STRUCTURAL HEALTH MONITORING
AND NONDESTRUCTIVE EVALUATION

by

Zhenhua Tian

Bachelor of Science
North China Electric Power University, 2008

Submitted in Partial Fulfillment of the Requirements

For the Degree of Doctor of Philosophy in

Mechanical Engineering

College of Engineering and Computing

University of South Carolina

2015

Accepted by:

Lingyu Yu, Major Professor

Victor Giurgiutiu, Committee Member

Yuh J. Chao, Committee Member

Paul Ziehl, Committee Member

Cara A.C. Leckey, Committee Member

Lacy Ford, Senior Vice Provost and Dean of Graduate Studies

© Copyright by Zhenhua Tian, 2015
All Rights Reserved

ACKNOWLEDGEMENTS

I would like to express my deepest gratitude to my advisor, Dr. Lingyu Yu, for her dedicated guidance, thoughtful advice, tremendous support and willingness to allow me to explore research areas I am truly passionate about. It is an honor to be her first Ph.D. student and follow her as a role model of successful professor and independent thinker. Her enthusiasm in research has motivated me throughout my Ph.D. journey and will continuously encourage me in my future career.

I would like to give special thanks to my committee members. I am lucky to have Dr. Victor Giurgiutiu as an excellent example to follow, to learn from his outstanding work and insightful suggestions in Friday meetings. I also gained valuable guidance from Dr. Cara A.C. Leckey, Dr. Yuh J. Chao and Dr. Paul Ziehl, who have enriched my knowledge and broadened my horizon.

My gratitude is also extended to my dear colleagues in VSHM and LAMSS, who have contributed immensely to my professional and personal life in the past four years. The collaboration and friendship among us enlightened me to explore and achieve more. The great conversations with Dr. Jingjing Bao, Dr. Bin Lin, Dr. Yanfeng Shen and Banibrata Poddar, always inspired spark in me.

Lastly, I want to thank my parents for their unconditional love and support, and Dr. Hong Xu from NCEPU for his unending encouragement. My friends in Columbia are also appreciated for giving me the unforgettable memories. I would like to thank my girlfriend Xue Bai, for her understanding, quiet patience and belief in me.

ABSTRACT

Damage detection and health monitoring are critical for ensuring the structural safety in various fields, such as aerospace, civil and nuclear engineering. Structural health monitoring (SHM) performs online nondestructive evaluation (NDE) and can predict the structural remaining life through appropriate diagnosis and prognosis technologies. Among various SHM/NDE technologies, guided ultrasonic waves have shown great potential for fast and large area SHM/NDE, due to their sensitivity to small defects and capability to propagate long distances. Recent advances in guided wave based SHM/NDE technologies have demonstrated the feasibility of detecting damage in simple structures such as metallic plates and pipes. However, there remain many challenging tasks for quantifying damage, especially for damage quantification in complex structures such as laminated composites and honeycomb sandwich structures. Moreover, guided wave propagations in complex structures, and wave interactions with various types of defects such as crack, delamination and debonding damage, need to be investigated.

The objective of this dissertation research is to develop guided wave based integrated SHM and NDE methodologies for damage detection and quantification in complex structures. This objective is achieved through guided wave modeling, optimized sensor and sensing system development, and quantitative and visualized damage diagnoses. Moreover, the developed SHM/NDE methodologies are used for various damage detection and health monitoring applications.

This dissertation is organized in two major parts. Part I focuses on the development of integrated SHM/NDE damage diagnosis methodologies. A non-contact laser vibrometry sensing system is optimized to acquire high spatial resolution wavefields of guided waves. The guided wavefields in terms of time and space dimensions contain a wealth of information regarding guided wave propagations in structures and wave interactions with structural discontinuities. To extract informative wave signatures from the time-space wavefields and characterize the complex wave propagation and interaction phenomenon, guided wavefield analysis methods, including frequency-wavenumber analysis, wavefield decomposition and space-frequency-wavenumber analysis, are investigated. Using these analysis methods, the multi-modal and dispersive guided waves can be resolved, and the complex wave propagation and interaction can be interpreted and analyzed in time, space, frequency, and wavenumber multi-domains.

In Part I, a hierarchical damage diagnosis methodology is also developed for quantitative and visualized damage detection. The hierarchical methodology systematically combines phased array imaging and wavefield based imaging to achieve efficient and precise damage detection and quantification. The generic phased array imaging is developed based on classic delay-and-sum principle and works for both isotropic and anisotropic materials. Using the phased array imaging, an intensity scanning image of the structure is generated to efficiently visualize and locate the damage zone. Then the wavefield based imaging methods such as filter reconstruction imaging and spatial wavenumber imaging are performed to precisely quantify the damage size, shape and depth.

In Part II, the developed methodologies are applied to five different SHM/NDE applications: (1) gas accumulation detection and quantification in water loaded structures, (2) crack damage detection and quantification in isotropic plates, (3) thickness loss evaluation in isotropic plates, (4) delamination damage detection and quantification in composite laminates, (5) debonding detection and quantification in honeycomb sandwich structures.

This dissertation research will initiate sensing and diagnosis methodologies that provide rapid noncontact inspection of damage and diagnosis of structural health. In the long run, it contributes to the development of advanced sensor and sensing technologies based on guided waves, and to providing on-demand health information at component or subsystem level for the safety and reliability of the structure.

TABLE OF CONTENTS

ACKNOWLEDGEMENTS.....	iii
ABSTRACT	iv
LIST OF TABLES	x
LIST OF FIGURES	xi
CHAPTER 1 INTRODUCTION	1
1.1. BACKGROUND.....	1
1.2. MOTIVATION.....	3
1.3. OBJECTIVES	8
CHAPTER 2 STATE OF THE ART.....	10
2.1. GUIDED WAVE PROPAGATION STUDY	10
2.2. GUIDED WAVE EXCITATION AND SENSING.....	18
2.3. GUIDED WAVEFIELD DATA ANALYSIS AND DAMAGE DIAGNOSIS METHODOLOGIES	26
PART I: INTEGRATED SHM/NDE DIAGNOSIS METHODOLOGIES	38
CHAPTER 3 ANALYTICAL AND NUMERICAL STUDIES OF GUIDED WAVES	38
3.1. DISPERSION AND MODE SHAPE DERIVATIONS	38
3.2. WAVE PROPAGATION AND INTERACTION SIMULATIONS	44
CHAPTER 4 WAVEFIELD ACQUISITION AND INTRINSIC CHARACTERIZATION	53
4.1. HYBRID PZT-SLDV SENSING SYSTEM FOR WAVEFIELD ACQUISITION	53
4.2. FREQUENCY-WAVENUMBER ANALYSIS	57

4.3. GUIDED WAVEFIELD DECOMPOSITION	59
4.4. SPACE-FREQUENCY-WAVENUMBER ANALYSIS	61
CHAPTER 5 QUANTITATIVE AND VISUALIZED DAMAGE DIAGNOSIS	64
5.1. GUIDED WAVE PHASED ARRAYS IMAGING	64
5.2. FILTER RECONSTRUCTION IMAGING	85
5.3. SPATIAL WAVENUMBER IMAGING	87
PART II: SHM/NDE APPLICATIONS	89
CHAPTER 6 GUIDED WAVES IN WATER LOADED STRUCTURES AND WATER LEVEL DETECTION.....	89
6.1. GUIDED WAVE WATER LEVEL DETECTION	89
6.2. GAS ACCUMULATION DETECTION IN NUCLEAR COOLANT PIPES.....	96
CHAPTER 7 CRACK DETECTION AND QUANTIFICATION IN ISOTROPIC PLATES.....	103
7.1. MOTIVATION AND INTRODUCTION	103
7.2. WAVE INTERACTION WITH CRACK DAMAGE.....	104
7.3. CRACK DETECTION AND QUANTIFICATION	106
CHAPTER 8 THICKNESS LOSS EVALUATION IN ISOTROPIC PLATES	112
8.1. MOTIVATION AND INTRODUCTION	112
8.2. WAVE INTERACTION WITH MATERIAL LOSS DAMAGE.....	112
8.3. DISPERSION CURVE REGRESSION FOR MATERIAL THICKNESS QUANTIFICATION	116
8.4. EVALUATION OF SIMULATED PITTING CORROSION DAMAGE.....	119
CHAPTER 9 DELAMINATION DETECTION AND QUANTIFICATION IN COMPOSITE LAMINATES	121
9.1. MOTIVATION AND INTRODUCTION	121
9.2. WAVE INTERACTION WITH DELAMINATION DAMAGE	123
9.3. DETECTION AND QUANTIFICATION OF SIMULATED DELAMINATION DAMAGE ..	128

9.4. DETECTION AND QUANTIFICATION OF IMPACT-INDUCED DELAMINATION DAMAGE.....	133
CHAPTER 10 DEBONDING DETECTION AND QUANTIFICATION IN HONEYCOMB SANDWICH STRUCTURES	144
10.1. MOTIVATION AND INTRODUCTION	144
10.2. GUIDED WAVES IN HONEYCOMB SANDWICH STRUCTURES.....	145
10.3. WAVE INTERACTION WITH DEBONDING DAMAGE.....	150
10.4. DEBONDING DETECTION AND QUANTIFICATION	157
CHAPTER 11 CONCLUDING REMARKS AND FUTURE WORK	158
11.1. RESEARCH CONCLUSIONS	160
11.2. MAJOR CONTRIBUTIONS.....	168
11.3. RECOMMENDATION FOR FUTURE WORK.....	172
REFERENCES	175

LIST OF TABLES

Table 3.1	Wave modes in EFIT results when incident waves are A_0 mode	48
Table 3.2	Wave modes in EFIT results when incident waves are S_0 mode	49
Table 3.3	Geometry parameters of the finite element model. (Units: mm)	50
Table 5.1	Material properties of a single ply.	71
Table 5.2	Configurations of three rectangular arrays for beamforming study.....	71
Table 5.3	$BF(\mathbf{k})$ characteristics of the three rectangular arrays	74
Table 5.4	Full width of the mainlobe at one-half peak value.....	77
Table 9.1	Material properties of the IM7/8552 lamina.	125
Table 10.1	Geometry parameters of the honeycomb sandwich structure (units: mm).	147

LIST OF FIGURES

Figure 1.1	The comparison between human nervous system and SHM system.	2
Figure 1.2	Guided waves in different waveguides	3
Figure 1.3	Dispersion curves of a 1 mm thickness aluminum plate (2024-T3).	4
Figure 1.4	Complex structure examples	5
Figure 1.5	Examples of various defects	5
Figure 1.6	An illustration of an 8×8 piezoelectric transducers phased array	6
Figure 1.7	Guided wave waveforms	6
Figure 2.1	Sketches of multilayered structures	11
Figure 2.2	Illustration of structures with complex cross sections.	13
Figure 2.3	Examples of the SAFE method for solving the dispersion problems of periodical structures	13
Figure 2.4	An example of the analytical simulation of guided waves generated by a piezo-disc	14
Figure 2.5	An example of FEM simulation of guided waves in a honeycomb sandwich	17
Figure 2.6	Examples of EFIT simulations	18
Figure 2.7	Examples of various transducers	19
Figure 2.8	PWAS interaction with a structure	21
Figure 2.9	PWAS tuning curves of a round PWAS (7mm diameter, 0.2mm thickness) bonded on an aluminum 2024-T3 plate (1mm thick)	22
Figure 2.10	Schematics of PWAS applications	22
Figure 2.11	A schematic of SLDV principle (BS: beam splitter).	23

Figure 2.12	Visualization of wave interaction with a fatigue crack by using laser vibrometry.....	25
Figure 2.13	The experimental wavefields in a structure (fabricated from two 0.8 mm thick aluminum plates that were epoxy-bonded together).....	26
Figure 2.14	Amplitude profile of a guided wavefield for delamination detection.....	28
Figure 2.15	Source removal for delamination detection	28
Figure 2.16	Standing wave filtering for delamination detection.....	28
Figure 2.17	Sparse array imaging results for the detection of a through hole with a diameter of 3.2 mm.....	31
Figure 2.18	Sparse array imaging results for the detection of a 6 mm diameter through hole	32
Figure 2.19	Baseline-free imaging.....	32
Figure 2.20	Sparse array imaging for crack detection.....	32
Figure 2.21	Comparisons between omnidirectional guided waves and focused guided waves.....	33
Figure 2.22	EUSR detection results	34
Figure 2.23	2-D planar arrays.....	35
Figure 3.1	Sketches for: (a) free plate and (b) plate with one side in water.....	39
Figure 3.2	Wavenumber dispersion curves of a free steel plate with 1.2 mm thickness.....	39
Figure 3.3	Wavenumber dispersion curves of a 1.2 mm thick steel plate with one side in water	41
Figure 3.4	Theoretical wave mode shapes of the quasi-Scholte mode	41
Figure 3.5	SAFE model of a CFRP composite plate with $[0_2/90_2]_s$ layup	42
Figure 3.6	Dispersion curves of guided waves propagating in 90° direction in the $[0_2/90_2]_s$ CFRP composite plate	43
Figure 3.7	Wavenumber and group velocity curves at 300 kHz for guided waves in the $[0_2/90_2]_s$ CFRP composite plate	43

Figure 3.8	Mode shapes of guided waves at 300 kHz propagating in 90° direction in the $[0_2/90_2]_s$ CFRP composite plate	43
Figure 3.9	Configuration of EFIT simulation for the study of guided waves in a water loaded plate	45
Figure 3.10	v_z velocity results of EFIT simulation at 100 kHz excitation	45
Figure 3.11	v_z velocity results of EFIT simulation at 600 kHz excitation	46
Figure 3.12	The EFIT simulation configuration for the study of wave interaction with delamination damage in a CFRP plate with $[0_2/90_2]_s$ layup.	46
Figure 3.13	EFIT results at 300 kHz for A_0 mode interaction with delamination damage	48
Figure 3.14	EFIT results at 300 kHz for S_0 mode interaction with delamination damage	49
Figure 3.15	The finite element model of the honeycomb sandwich structure with a surface-bonded PZT.....	50
Figure 3.16	Simulation results of displacements in the z direction u_z	50
Figure 4.1	A schematic of the PZT-SLDV sensing.....	55
Figure 4.2	Crack detection by using the PZT-SLDV sensing.....	55
Figure 4.3	Delamination detection by using the PZT-SLDV sensing.....	57
Figure 4.4	Frequency-wavenumber analysis on guided waves in a 6.35 mm thick T304 steel plate.....	58
Figure 4.5	Guided wave decomposition by using frequency-wavenumber filtering ..	60
Figure 4.6	An example of the window function.....	63
Figure 4.7	An example of the space-frequency-wavenumber analysis.....	63
Figure 5.1	Schematics of geometric relations of guided waves in composite plates ..	66
Figure 5.2	Schematic of a $P \times Q$ rectangular array	70
Figure 5.3	Wavenumber curve $k(\gamma)$ of the 90 kHz A_0 mode in the $[0/45/90/-45]_s$ CFRP composite laminate.....	71
Figure 5.4	$BF(\mathbf{k})$ images for the array (1).....	74

Figure 5.5	$BF(\mathbf{k})$ images when the phase delays $(-0.02, 0.68) \cdot \mathbf{p}_{p,q}$ is applied.....	74
Figure 5.6	$BF(\theta)$ plots for array (1).....	77
Figure 5.7	$BF(\theta)$ plots when the beamsteering directions are $\theta_s = 0^\circ, 45^\circ, 90^\circ$ and 135°	77
Figure 5.8	Experimental setup for multi-defects detection on a CFRP composite laminate.....	80
Figure 5.9	SLDV measurements.....	82
Figure 5.10	Beamforming and imaging of array (2)	84
Figure 5.11	Array imaging results.....	84
Figure 5.12	Filter reconstruction imaging for delamination detection in a CFRP composite plate.	86
Figure 5.13	Spatial wavenumber imaging for delamination detection in a CFRP plate.....	88
Figure 6.1	The PZT-SLDV experiment on a water tank.....	91
Figure 6.2	Experimental results.....	92
Figure 6.3	Frequency-wavenumber analysis results	92
Figure 6.4	An illustration of the pitch-catch configuration.....	95
Figure 6.5	Water influence on wave propagation at 100 kHz.....	95
Figure 6.6	The experimental setup.....	97
Figure 6.7	Experimental results.....	97
Figure 6.8	Frequency-wavenumber analysis.....	98
Figure 6.9	An illustration of the pitch-catch sensing on a small scale pipe.	100
Figure 6.10	Experimental results for the small scale pipe	100
Figure 6.11	Test on a tilted large scale pipe.....	102
Figure 6.12	Experimental results for the tilted large scale pipe.....	102

Figure 7.1	Experimental setup for crack detection in a 1 mm thick aluminum plate.....	104
Figure 7.2	Wavefield images measured by the SLDV at 360 kHz excitation on a 1 mm thick aluminum plate with a TT crack.....	105
Figure 7.3	Filter reconstruction imaging with experimental data in an aluminum plate with a TT crack	107
Figure 7.4	Spatial Wavenumber imaging with experimental data in an aluminum plate with a TT crack.	107
Figure 7.5	The filter reconstruction imaging results at 360 kHz.....	110
Figure 7.6	Amplitudes along the cracks extracted from the filter reconstruction imaging results. Broken, solid and dotted lines are for TT, 3X and hTT cracks, respectively	110
Figure 7.7	Spatial wavenumber imaging results at 360kHz.....	111
Figure 7.8	Wavenumber distributions along the crack. Broken, solid and dotted lines are for TT, 3X and hTT cracks, respectively.	111
Figure 8.1.	Experimental setup.....	113
Figure 8.2.	Chirp excitation.....	114
Figure 8.3	Spectral fields (real parts) for the plate with 0.75 mm depth material loss damage.....	115
Figure 8.4	Spatial wavenumber images for the plate with 0.75 mm depth material loss damage.....	115
Figure 8.5	A_0 mode wavenumber versus plate thickness and wave frequency.....	116
Figure 8.6	Dispersion curve regression result at the location (0, 60) mm, when the damage depth is 0.75 mm.	118
Figure 8.7	The thickness loss quantification results.....	118
Figure 8.8.	Experimental setup.....	119
Figure 8.9	Spectral fields (real parts) for the plate with simulated pitting corrosion damage	119
Figure 8.10.	Imaging result of the plate with simulated pitting corrosion damage.....	120

Figure 9.1	The scanning laser vibrometry test	126
Figure 9.2	Time-space wavefields of waves propagating along the y axis	126
Figure 9.3	SLDV wavefield snapshots at $15 \mu\text{s}$	127
Figure 9.4	Wavenumber spectra at 300 kHz excitation frequency	128
Figure 9.5	The filtering process in wavenumber domain.....	130
Figure 9.6	The filter reconstruction imaging results	130
Figure 9.7	Spatial wavenumber image of the Teflon delaminated plate.....	132
Figure 9.8	Dispersion curves of A_0 modes propagating towards the 90° direction ..	133
Figure 9.9	Quasi-static indentation for delamination damage growth.....	135
Figure 9.10	The 26 ply laminate after the quasi-static indentation test	135
Figure 9.11	The SLDV phased array sensing layout for detecting and imaging the impact-induced delamination damage.	136
Figure 9.12.	SLDV measurements	137
Figure 9.13	Phased array imaging results for detecting and imaging the impact-induced delamination damage.....	138
Figure 9.14	Experimental setup for quantifying the impact-induced delamination. ...	139
Figure 9.15	SLDV wavefield images at $45 \mu\text{s}$ for 100 kHz excitation.	140
Figure 9.16	SLDV wavefield images at $40 \mu\text{s}$ for 500 kHz excitation	140
Figure 9.17	Filter reconstruction imaging at the low frequency 100 kHz	141
Figure 9.18	Filter reconstruction imaging at the high frequency 500 kHz	142
Figure 9.19	Spatial wavenumber imaging result in the frequency band 480~520 kHz.....	143
Figure 10.1	A schematic of the PZT-SLDV sensing setup.	146
Figure 10.2	Wavefields measured from the experiment	147
Figure 10.3	Wavenumber spectra.....	149

Figure 10.4	The sensing layout of the PZT-SLDV experiment on a honeycomb sandwich with debonding damage in the center of the sandwich.	150
Figure 10.5	Experimental results at the high frequency 100 kHz for the pristine (left column) and damaged (right column) sandwich structures	151
Figure 10.6	Wavenumber spectra at 100 kHz: (a) for the pristine sandwich and (b) for the sandwich with debonding damage.	151
Figure 10.7	Wave decomposition for the pristine sandwich	153
Figure 10.8	Wave decomposition of the waves in the sandwich with debonding damage	154
Figure 10.9	Experimental results at the low frequency 40 kHz for the pristine (left column) and damaged (right column) sandwich structures	155
Figure 10.10	Wavenumber analysis results at 40 kHz	156
Figure 10.11	Debonding detection and quantification	157

CHAPTER 1

INTRODUCTION

1.1. BACKGROUND

Structural health monitoring (SHM) assesses the state of structural health, and through appropriate data processing and interpretation, may predict the remaining life the structure [1]. Over the past two decades, SHM has been experiencing spectacular progress in various areas such as aerospace, marine, civil, and nuclear engineering [1-3]. An SHM system behaves like the nervous system (as shown in Figure 1.1) with the particular purpose of monitoring structural behavior in quasi-real time, indicating the health state of structure, and “triggering” safety and remedial actions [4]. In the SHM system, there are four important elements: data collection, data processing, information processing to define the current state, and the decision making and dissemination [4]. The SHM system can perform in two main ways: passive and active [1, 4]. The passive SHM is concerned with measuring various operational parameters (such as acoustic emissions, vibration levels, stresses in critical locations, etc.) by using receivers and then inferring the health state of structure [1]. In contrast, the active SHM is concerned with directly assessing the health state of structure by using both actuators and receivers [1].

The health state of the structure is indicated by the presence and extent of structural damage. The damage can be changes to material properties, geometric parameters, and boundary conditions, which adversely affect the present and future safety of structures [2]. Generally, the identification of the damage state involves the following

five aspects: (1) the existence of damage, (2) the locations of damage, (3) the types of damage, (4) the severity of the damage, and (5) the remaining service life of the structure [5].

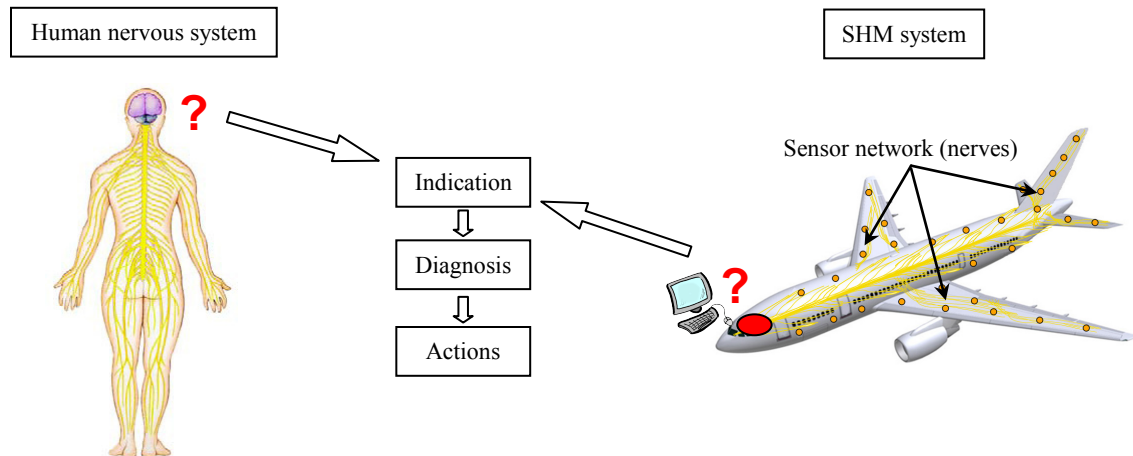


Figure 1.1 The comparison between a human nervous system and an SHM system [4].

Various means, such as ultrasonic waves, structure vibration, electromechanical impedance, eddy current, micro waves, etc., can be used for NDE and SHM [1, 4, 6]. Particularly, this dissertation study focuses on the guided ultrasonic waves, which are elastic waves propagating along waveguides [7]. Different structural components, such as plate-like structures and pipes can serve as waveguides [7-11]. In these waveguides, the guided waves travel in different forms. For example, Rayleigh waves travel along a free surface (Figure 1.2a), symmetric Lamb waves travel along a plate (Figure 1.2b), torsional guided waves travel in a cylinder (Figure 1.2c), etc. Other cases, like a solid-water interface, a solid-solid interface, etc., can also serve as the waveguides [7-11].

Compared to bulk waves, guided waves have the advantage of long propagation distance with less energy loss. Moreover, guided waves have high sensitivity to small defects, such as crack, corrosion, delamination, etc. [6, 8]. These merits enable the guided wave SHM of large areas from small sensing areas. In the past two decades, various

guided wave SHM technologies have been developed for the purpose of health monitoring, such as phased arrays [12-21], sparse arrays [22, 23], time-reversal method [24-26], guided wave tomography [27, 28] and full-wavefield imaging [29-32]. These advances in guided SHM technologies have demonstrated the feasibility of health monitoring by using guided waves.

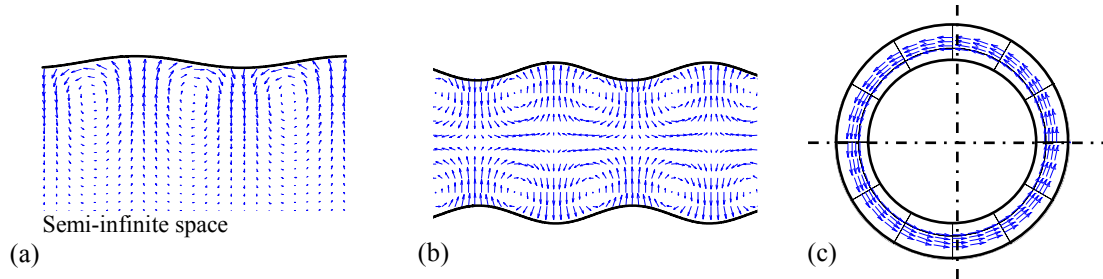


Figure 1.2 Guided waves in different waveguides: (a) Rayleigh waves along a free surface of a semi-infinite space solid medium; (b) symmetric Lamb waves in a plate; (c) torsional guided wave in a cylinder.

1.2. MOTIVATION

Although the advances in guided wave technologies have demonstrated the feasibility of guided wave SHM, there remain many challenges for applications of guided wave SHM, especially for structures with complex geometries and subjected to multiple damage when serving in harsh environment conditions.

The followings summarize the challenges:

- (1) Guided wave propagation and interaction mechanisms
 - Guided waves have multimodal and dispersive features [8]. For example, in the dispersion curves of a 1 mm thickness aluminum plate (Figure 1.3), there are at least two wave modes, A_0 and S_0 , existing simultaneously even at low frequencies. When the product of frequency and plate half-thickness goes higher, more wave

modes (such as A_1 and S_1) appear. Moreover, the dispersive nature shows the guided wave speed changes with respect to frequency.

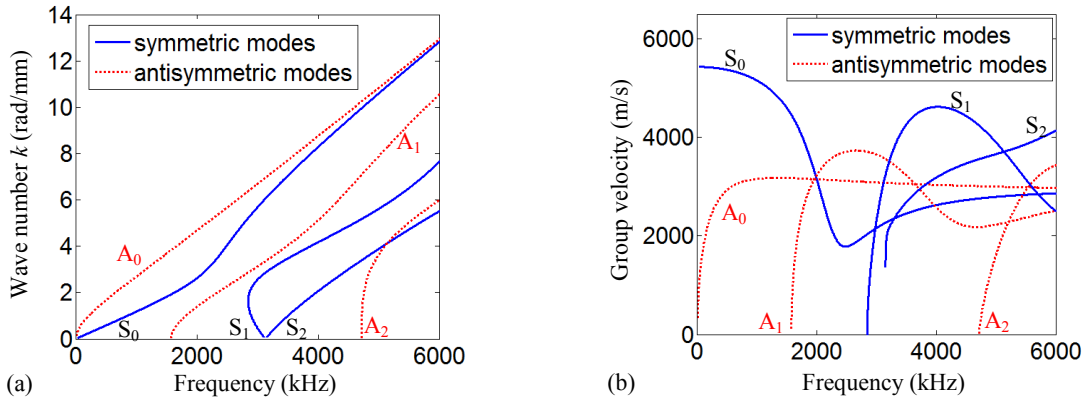


Figure 1.3 Dispersion curves of a 1 mm thickness aluminum plate (2024-T3): (a) frequency-wavenumber dispersion curves, and (b) group velocity dispersion curves.

- The dispersion curves are important features of guided waves and play an important role for guided wave SHM. The dispersion curves can be used to determine the wave propagation speed, identify the guided wave mode, and develop appropriate data analysis algorithms for damage detection [1]. For simple structures, such as isotropic plates and pipes, the dispersion curves can be easily obtained by solving the guide wave characteristic equations which have been fully developed in many textbooks and articles [1, 8-11, 33]. However, for complex structures, such as multilayer structures, arbitrary cross section structures, periodical structures, etc., it is more challenge to derive their dispersion curves and understand how the guided waves propagate in these complex structures.
- Structures can have various types of defects, such as cracks, delaminations and corrosions (Figure 1.5). In order to develop effective methods to detect defects, it is necessary to understand the mechanism of how defects affect the guided wave propagation.

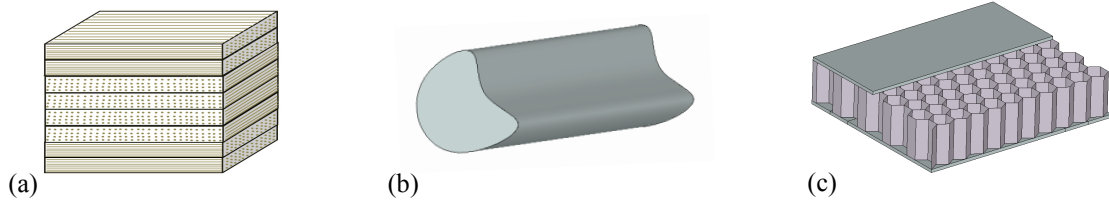


Figure 1.4 Complex structure examples: (a) multilayer structure; (b) arbitrary cross section structure; (c) periodical structure.

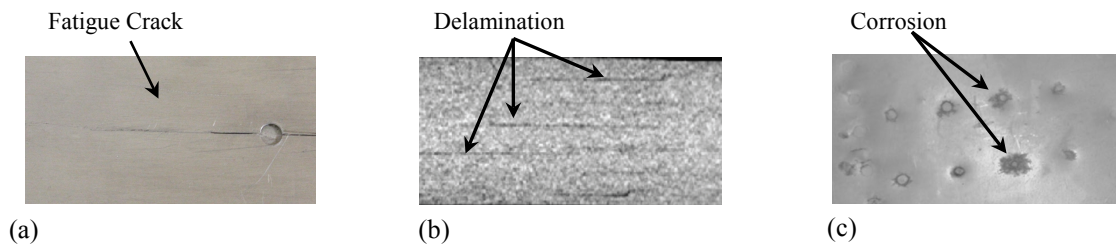


Figure 1.5 Examples of various defects: (a) fatigue crack; (b) X-Ray CT image of delamination damage [34]; (c) corrosion damage near the rivets [35].

(2) Guided wave excitation and sensing.

- The traditional guided wave sensing system may require a large amount of sensors, such as the 8×8 phased array in Figure 1.6, resulting in great sensor installation, wiring and weight penalties.
- Traditional guided wave transducers, such as piezoelectric transducers in Figure 1.6, may have large sensor profiles, which limit the spatial sampling resolution of the sensing.
- Guided wave sensors may work in harsh environment, such as high temperature and radiation, which may affect the sensor properties. For example, in nuclear applications, the sensors may work in the high temperature and radiation environment.
- The accessible area for inspection may be limited, and the surface bounded sensor may not be allowed in real applications.



Figure 1.6 An illustration of an 8×8 piezoelectric transducers phased array [17].

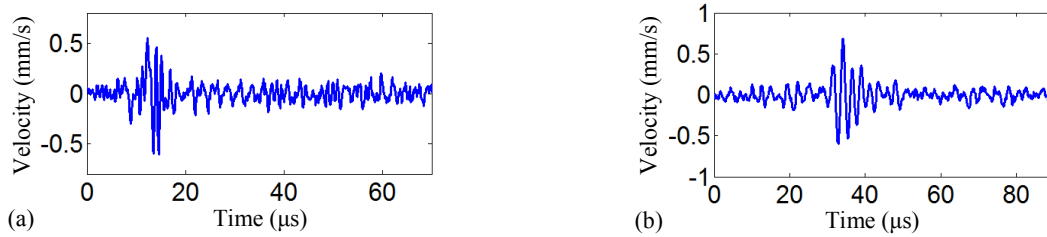


Figure 1.7 Guided wave waveforms: (a) a waveform which contains 7 wave modes (A_0 , A_1 , A_2 , A_3 , S_0 , S_1 and S_2); (b) a waveform which contains both incident and reflection waves (incident A_0 and S_0 modes, and reflection A_0 and S_0 modes)

(3) Data interpretation and damage diagnosis methodologies

- Due to the dispersive and multimodal natures of guided waves, the data interpretation of guided wave signal becomes very challenging. For example, in Figure 1.7a, a guided waveform, there are seven different wave modes (A_0 , A_1 , A_2 , A_3 , S_0 , S_1 and S_2). When multiple dispersive wave modes coexist and interact with each other, the wave interpretation and analysis become very difficult. It is desired that different modes can be separated for individual analysis and the dispersion effect can be mitigated.
- Structures can have various types of defects, such as cracks, delaminations and corrosions. When guided waves interact with these defects, reflection, scattering and mode conversion waves may present. These damage induced waves make the interpretation of guided wave signal very difficult. For example, the guided waveform in Figure 1.7b, contains incident A_0 and S_0 modes generated from the

actuator, and reflection A_0 and S_0 modes induced by the damage. Since these different components coexist and interact with each other, the interoperation of wave signal becomes very difficult. To analyze the damage affections, such as the damage reflection and scattering coefficients, the damage induced waves are needed. Moreover, for damage detection, the damage induced waves which contain the damage information are needed. Therefore, it is desired that the damage induced waves can be extracted for wave analysis and damage detection.

- Various damage detection algorithms have been developed, such as phased arrays [12-21], sparse arrays [22, 23], time-reversal method [24-26], guided wave tomography [27, 28] and full-wavefield imaging [29-32]. Although recent advances in SHM technology have demonstrated the feasibility of detecting damage, quantifying the damage based on sensory data still remains a challenging task. It is challenging to quantify the location, size and shape of the damage. Moreover, the challenges will be accentuated when the damage diagnosis methods are applied on complex structures.

These challenges involve researches and studies in multidisciplinary areas. Hence, this dissertation research aims to address the above challenges and move guided wave based SHM and NDE toward field applications. This dissertation focuses on the excitation and sensing technologies, data interpretation and damage diagnosis methodologies. Wave propagation and interaction are also studied for the purpose of optimization of damage detection and quantification.

1.3. OBJECTIVES

Considering the challenges summarized in section 1.2, the following detailed research objectives are targeted:

- (1) Both the analytical modeling and numerical modeling of guided waves will be investigated, in order to acquire preliminary understanding of the guided waves in the complex structures, to obtain theoretical data for comparison to experimental results, as well as to provide abundant data for parametric study;
- (2) Guided wave excitation and sensing systems will be investigated and optimized in order to reduce the sensor installation, generate high energy guided waves, and acquire the high resolution guided wavefield;
- (3) Advanced data analysis approaches will be developed to characterize the multimodal and dispersive guided waves in complex structures, analyze the wave interaction with damage, and extract wave characteristic parameters (such as dispersion, frequency, and wavenumber contents);
- (4) Quantitative structural integrity assessment methodologies will be developed for SHM\NDE in complex structures, in order to quantify the damage location, size, and detailed geometry features;
- (5) The methodology for wave propagation and interaction analysis in complex structures will be developed. The framework of how to use the fundamental knowledge of guided wave modeling, excitation and sensing, and data analysis methods for the analysis wave propagation and interaction problems will be established. Case studies on various representative complex structures will be performed: (i) guided waves in water loaded structures and water level detection; (ii)

crack detection and quantification in isotropic plates; (iii) damage thickness mapping in isotropic plates; (iv) delamination detection and quantification in composite laminates; (v) debonding detection and quantification in honeycomb sandwich structures.

CHAPTER 2

STATE OF THE ART

Guided waves have been widely used for NDE/SHM in the past couple of decades [1, 8, 36, 37]. Significant works have been done in guided wave modeling, guided wave generation and sensing, and damage detection. This section presents the state of the art in these research areas with particular emphasis on guided waves in complex structures.

2.1. GUIDED WAVE PROPAGATION STUDY

Modeling can serve as an efficient and cost effective way to assist the guided wave study and the development of diagnostic algorithms before conducting labor and/or time consuming experiments [1, 8, 36, 37]. Modeling is also helpful in investigating scenarios that are difficult to set up experimentally. With modeling, important guided wave features such as dispersions and wave mode shapes can be acquired. Moreover, wave propagations in complex structures and wave interactions with structural discontinuities can be easily simulated [1, 8, 36, 37].

2.1.1. Dispersion curve and mode shape derivations

Dispersion curves and mode shapes are important features of guided waves. They can be used to determine the wave propagation speed, identify the guided wave mode, and assist the development of appropriate data analysis algorithms for damage detection [1]. In order to obtain the dispersion relations and mode shapes, analytical and numerical methods have been developed [1, 8-10, 38-42].

2.1.1.1. Analytical methods

The analytical methods are based on closed-form solutions of guided wave characteristic equations [1, 8-10, 33]. They are very convenient to solve the dispersion relations for simple geometry structures, such as single layer plates and pipes. The characteristic equations and solutions for these simple structures have been fully developed as given in many textbooks and articles [1, 8-11, 33].

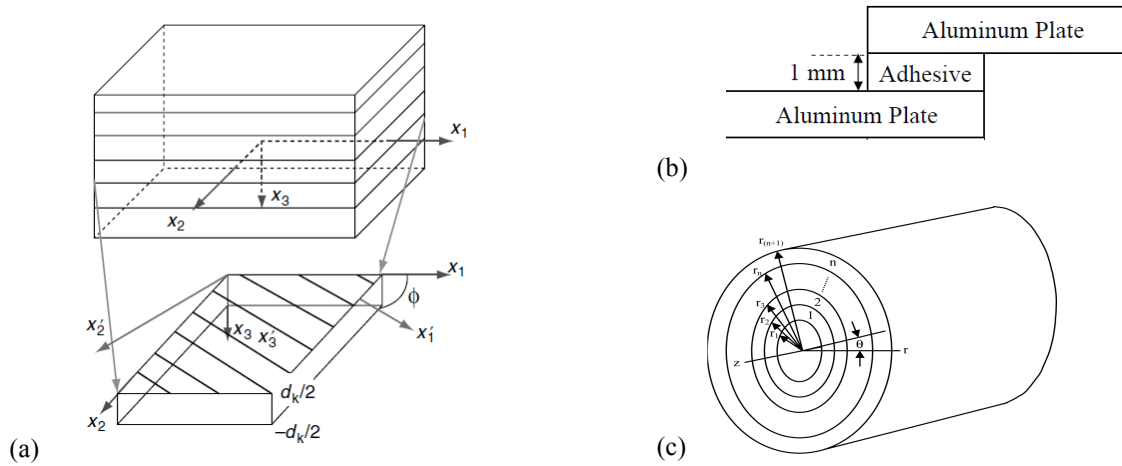


Figure 2.1 Sketches of multilayered structures: (a) a laminated composite [1]; (b) an adhesive joint[43]; (c) a multilayered pipe [44].

For multilayered structures such as laminated composites (Figure 2.1a), adhesive joints (Figure 2.1b), and pipes with coating layers (Figure 2.1c), their dispersion curves are usually obtained analytically using matrix methods [33]. The matrix methods are developed in matrix formulations by combining the dynamic behaviors of the continuum within each layer [33]. Two matrix methods are widely used, the transfer matrix method (TMM) and the global matrix method (GMM) [33]. The TMM works by condensing the multilayered system into a single layer system relating the boundary conditions at the first interface to the boundary conditions at the last interface [33]. In this process, the equations for the intermediate interfaces are eliminated so that all the layers of the plate

are described solely in terms of the external boundary conditions. The advantage of the TMM is that the condensed matrix is small and therefore it needs less computation time [33]. A drawback of the transfer matrix method is the dispersion solution becomes unstable for large frequency-thickness product [33].

The idea of GMM is to directly assemble a single matrix which represents the complete system [33]. The GMM is based on satisfying the boundary conditions at each interface [33]. The solution is carried out on the full matrix, addressing all of the equations concurrently. The advantage of GMM is that it is robust and stable for any frequency-thickness product. The disadvantage is that the global matrix might be large and therefore the method needs more computational effort.

2.1.1.2. Numerical methods

For arbitrary cross section structures, such as the structures in Figure 2.2, it is difficult to use analytical methods to solve the guided wave dispersion problems [40]. For these cases, numerical methods emerge and show their advantages [38-41]. One promising numerical method is the semi-analytical finite element (SAFE) method that has also been referred to as spectral or waveguide finite element method [38-41].

For the structure with a uniform arbitrary cross section (Figure 2.2a), the SAFE method simply requires the finite element discretization of the cross-section, and assumes harmonic motion along the wave propagation direction [38]. By this means, the guided wave dispersion problem can be casted into an eigenvalue problem which can be easily solved. For example, Fan and Lowe used SAFE to solve the guided wave dispersion problem of a welded joint which was considered as an uniform arbitrary cross section

structure [45]. Bartoli et al. used SAFE method to solve the dispersion problem of a rail [38].

Besides the structure with a uniform arbitrary cross section, the SAFE method has also been used to solve the dispersion problem for the periodic structure that has changing cross sections [39, 42]. Figure 2.3 gives two examples of using the SAFE method to solve the dispersion problems for 1-D and 2-D periodical structures [39, 42]. The SAFE method simply requires the finite element discretization of a unit cell, and assumes periodic boundary conditions on the unit cell [39, 42].

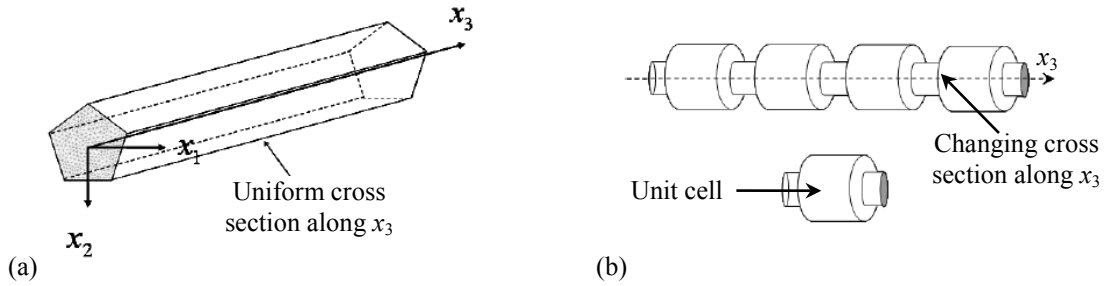


Figure 2.2 Illustration of structures with complex cross sections : (a) with a uniform arbitrary cross-section, and (b) with periodically changing cross-sections [40].

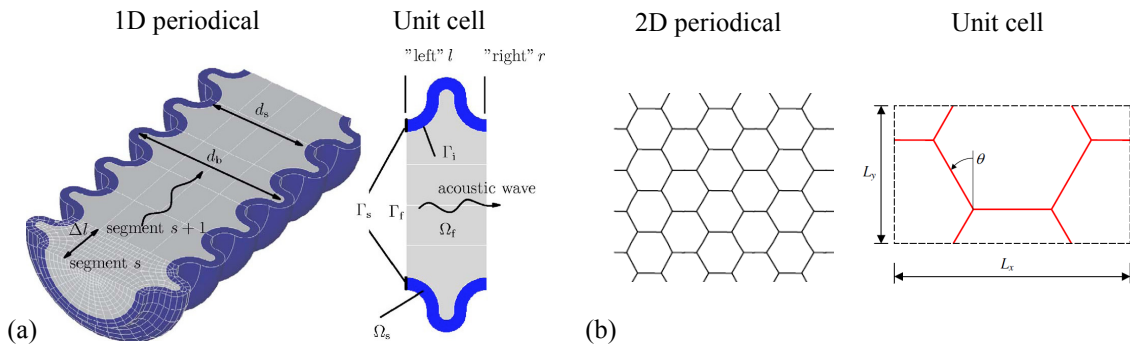


Figure 2.3 Examples of the SAFE method for solving the dispersion problems of periodical structures: (a) 1-D periodical structure [39]; (b) 2-D periodical structure[42].

2.1.2. Wave propagation simulations

Guided wave simulations can provide guided wave propagation and interaction details, such as how guided waves propagate in the structure and how guided waves interact with defects [1, 37, 46]. To simulate guided waves, there are various methods, such as analytical method [47, 48], finite element method (FEM) [49-51], elastodynamic finite integration technique (EFIT) [52-54], finite difference method (FDM) [55-58], spectral element method (SEM) [59, 60], local interaction simulation approach (LISA) [61, 62], distributed point source method (DPSM) [63], hybrid global-local method (HGL) [64-66], boundary element method (BEM) [67-69], etc. The analytical method, FEM and EFIT will be reviewed as followed.

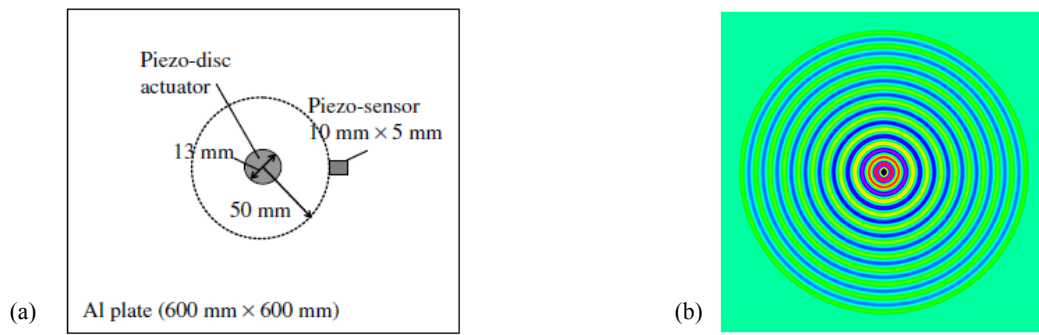


Figure 2.4 An example of the analytical simulation of guided waves generated by a piezo-disc: (a) simulation configuration; (b) simulated guided waves [47].

2.1.2.1. Analytical method

The analytical method is based on closed-form solutions of guided wave transfer functions. To get the closed-form solutions, guided wave equations are usually solved by using Fourier transform [1, 47, 48]. Once the closed-form solutions of the guided wave transfer functions are obtained, the guided wave propagation can be simulated efficiently.

Figure 2.4 shows a simulation example of guided waves actuated by a piezo-disc [47]. Although the analytical method is computational efficient, this method is restricted to structures with simple geometries. When the structure geometry is complex, it is difficult to get the closed-form solutions of structure transfer functions.

2.1.2.2. Numerical methods

Numerical methods begin with the mathematical models represented by Partial Differential Equations (PDEs) which govern the wave mechanics [49-51]. To solve the PDEs, there are various numerical methods, such as FDM, EFIT, FEM, etc. [49-58]. These methods have the advantage of handling complicated guided wave propagation and interaction problems, such as wave propagations in complex geometry structures, wave interactions with various defects, nonlinear guided wave propagation, etc. [48, 70-72]. However, the numerical methods have inherent errors induced by the time and space discretization (or approximation). The success of numerical methods strongly depends on the minimization of approximation errors, which requires sufficient time and space discretization. In addition, the numerical methods require large computational resources, such as computation time and computer memory.

2.1.2.2.1. *Finite element method (FEM)*

FEM, which is a powerful numerical technique to solve problems governed by PDEs over complex domains, has served as a primary numerical tool to simulate the elastic wave propagation [49-51]. In the FEM, the governing PDEs are transformed to weak formulations, which are integral representations of the governing PDEs. The analysis domain is discretized into a collection of finite elements. The FEM then approximates the

solutions to PDEs over finite elements in the analysis domain. The details of FEM are available in many text books for example [49-51].

Nowadays, with off the shelf commercial FEM software products such as ABAQUS, ANSYS, and COMSOL, it is very convenient to use the FEM for the guided wave simulation [70-72]. These commercial software products have many advantages, such as user friendly model construction tools, various element types in the element library, robust meshing tools, efficient FEM solvers, strong post processing and analysis tools, etc. With these merits, many researchers used the commercial FEM products to study various guided wave problems [70-73]. For example, Song et al. studied guided wave propagations in honeycomb sandwiches by using ANSYS [72]. Figure 2.5a shows their finite element model of the honeycomb sandwich. In their model, they took the advantage of ANSYS element library to model the piezoelectric transducers using SOLID5 element, hexagonal honeycomb core using SHELL63 element, and skin panels using SOLID45 element. With efficient solvers and strong post processing tools, they were able to solve the wave propagation problem, obtain detailed waveforms, and visualize guided waves (Figure 2.5a) for further analyses and studies. Pistone et al. simulated guided waves in an immersed plate by using ANSYS [71]. In their finite element model, they used the PLANE42 and FLUID29 elements of the ANSYS element library to model the isotropic plate and surrounding water, respectively. By using the ANSYS post processing tools, they can easily visualize the wave interactions among the leaky waves, bulk waves and quasi-Scholte waves.

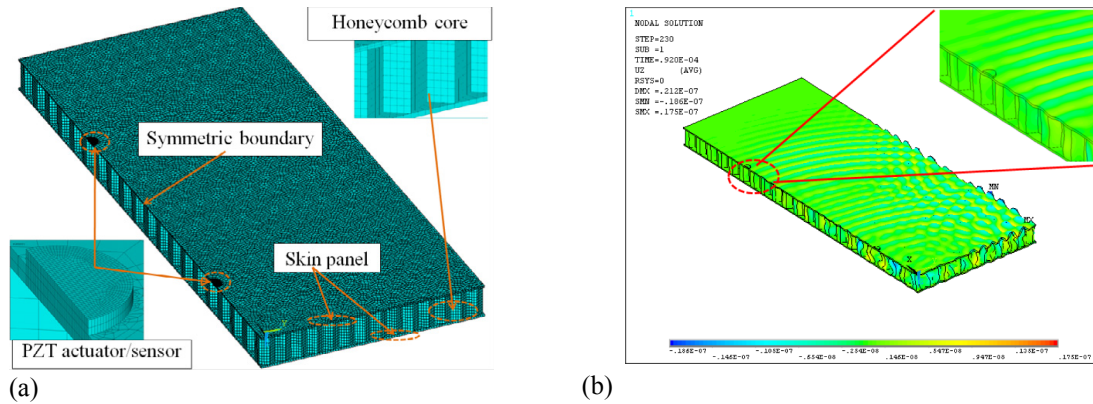


Figure 2.5 An example of FEM simulation of guided waves in a honeycomb sandwich: (a) the FEM model and (b) the simulated guided waves [72].

2.1.2.2.2. Elastodynamic finite integration technique (EFIT)

EFIT is another prominent numerical method to simulate guided waves. The EFIT is based on the finite integration technique (FIT) which integrates PDEs over a control volume and then approximates the integrals [52]. For guided wave simulations, the EFIT have following advantages: (1) the EFIT naturally requires staggered spatial and temporal grids which lead to stability, (2) the boundary conditions are easily incorporated in the EFIT model, and (3) the mathematical analysis is straight-forward and leads to equations that can be easily implemented in any programming language [53].

In the past two decades, many researchers used EFIT to study various guided waves related problems, such as guided waves in structures with complex geometries, and guided wave interaction with damage [53, 54, 74-79]. Leckey et al. studied guided wave interactions with defects, such as the material loss defect and microcracks using the EFIT [53, 54]. With the EFIT simulation, they can directly visualize how the guided waves interact with defects (Figure 2.6). Rudd et al. simulated the guided waves in pipe bends [77]. With the EFIT simulation, they directly showed energy concentrations at pipe bends. Schubert simulated wave propagation and scattering in a concrete structure by

using the EFIT [79]. The structure details such as sand aggregates and structural porosity were successfully modeled with the EFIT.

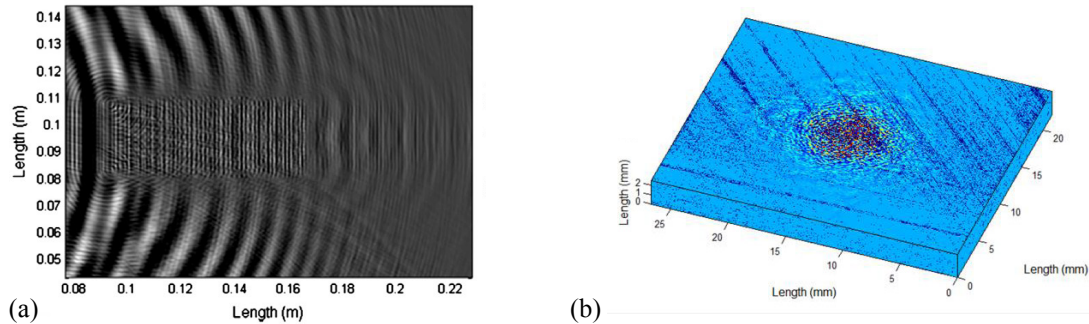


Figure 2.6 Examples of EFIT simulations: (a) guided wave interaction with a material loss damage in an isotropic plate [53]; (b) guided wave interactions with microcracks in a composite plate [54]

2.2. GUIDED WAVE EXCITATION AND SENSING

For guided wave excitation and sensing, various transducers have been used, such as piezoelectric wafer active sensors (PWAS) (Figure 2.7a), comb transducer (Figure 2.7b), macro fiber composites (MFC) (Figure 2.7c), wedge transducers (Figure 2.7d), fiber optics (Figure 2.7e), electromagnetic acoustic transducers (EMAT) (Figure 2.7f), air-coupled transducers (Figure 2.7g) and laser devices (Figure 2.7h) [80-94]. Among these transducers, the low profile PWAS are widely used for guided wave excitation and sensing [1]. PWAS are small and light, and suitable for integration into host structures (surface-mounting or embedding in composites) without significant intrusion, serving as good candidates for built-in transducers. Moreover, PWAS can serve several purposes, such as high-bandwidth strain sensors and exciters, resonators, and embedded modal sensors [1]. Recently, the laser devices, such as the high power pulse laser and the laser Doppler vibrometer, have emerged for non-contact guided wave applications [94]. The pulse laser can excite high energy wide band guided waves based on either the thermal elastic effect or structure surface ablation. The laser Doppler vibrometer can measure the

velocity or displacement at the sensing point on structural surface in the direction of the laser beam based on the Doppler effect. Their non-contact and remote sensing natures have attracted a lot of attention.

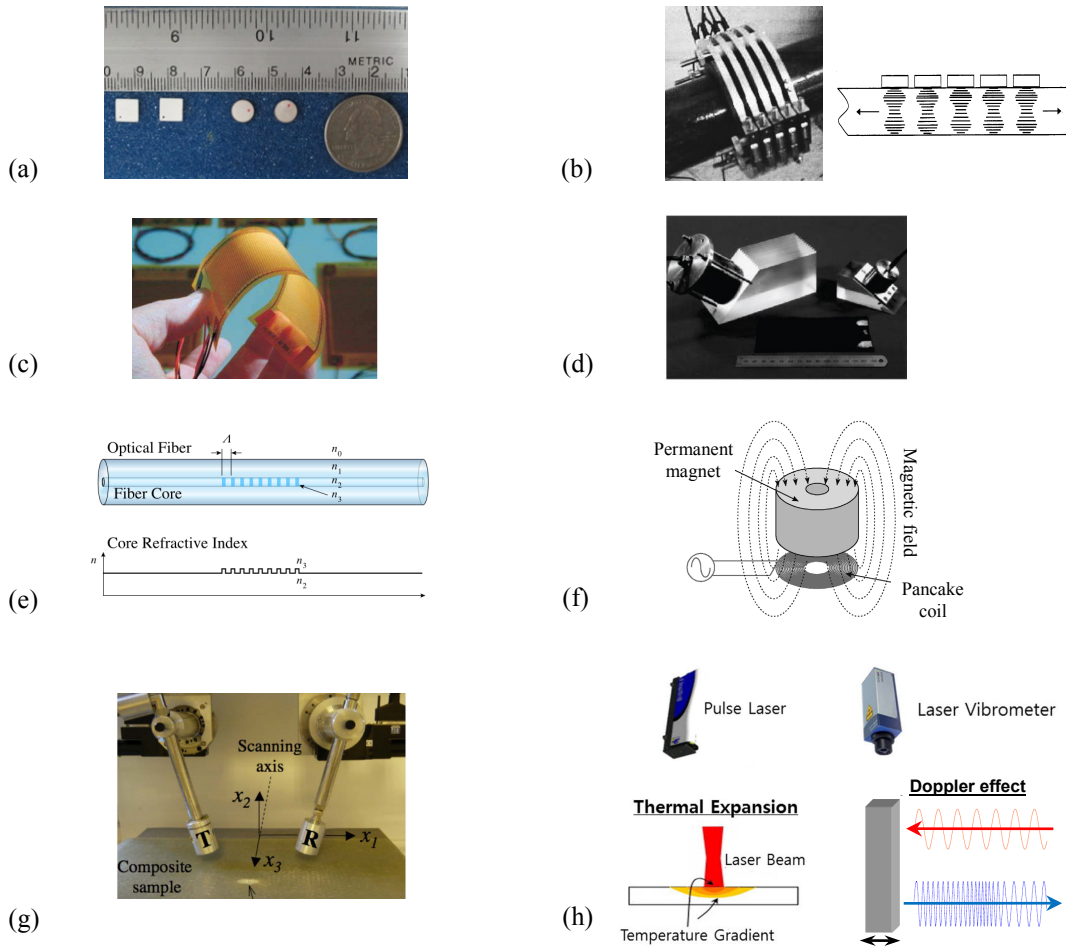


Figure 2.7 Examples of various transducers: (a) PWAS [1]; (b) comb transducer [84, 92]; (c) MFC [90]; (d) wedge transducers [93]; (e) FBG [95]; (f) EMAT transducer [80]; (g) air-coupled transducer [96]; (h) laser transducers [97].

2.2.1. PWAS guided wave transducers

PWAS work on the piezoelectric principle and couple the electrical and mechanical effects (mechanical strain S_{ij} , mechanical stress T_{kl} , electrical field E_k , and electrical displacement D_j), as described in the piezoelectric constitutive equations [1]

$$\begin{aligned}
S_{ij} &= s_{ijkl}^E T_{kl} + d_{kij} E_k \\
D_j &= d_{jkl} T_{kl} + \varepsilon_{jk}^T E_k
\end{aligned}
\tag{2.1}$$

where s_{ijkl}^E is the mechanical compliance of the material measured at zero electric field ($E=0$), ε_{jk}^T is the dielectric permittivity measured at zero mechanical stress ($T=0$), and d_{kij} represents the piezoelectric coupling effect. PWAS can excite and receive guided waves through in-plane motion coupling through the d_{31} piezoelectric coupling effect [1]. Compared to conventional ultrasonic probes, PWAS transducers have the following fundamental differences [1]: (1) PWAS achieve Lamb wave excitation and sensing through surface “pinching” (in-plane strains), while conventional ultrasonic probes work through surface “tapping” (normal stress); (2) PWAS are strongly coupled with the structure and follow the structural dynamics, while conventional ultrasonic probes are relatively free from the structure and follow their own dynamics; (3) PWAS are non-resonant wideband devices, while conventional ultrasonic probes are narrow-band resonators.

Many researchers have contributed to the development, modeling, and applications of PWAS to NDE/SHM [1, 88, 98-101]. Giurgiutiu studied the coupling effect between PWAS and the host structure, and proposed a pin force model [101]. The surface bonded PWAS (Figure 2.8 a) can couple their in-plane motion with the surface of the host structure through the bonding layer. When the bonding layer is very thin ($1\mu\text{m}$), the shear stress transmitted to the structure is only at the ends of PWAS (Figure 2.8 b). With the ideal bonding assumption, the transmitted shear stress can be considered using a pin force model which has all loads confined to an infinitesimal region at the PWAS edge [101].

An important characteristic of PWAS, which distinguishes them from conventional ultrasonic transducers, is their capability of tuning into various guided wave modes. The tuning effect of PWAS will benefit the selective actuation and sensing of guided wave modes. Giurgiutiu and Santoni et al. did comprehensive studies of the PWAS tuning effect through theoretical analyses and experimental tests [100, 101]. Figure 2.9 shows theoretical and experimental tuning curves of a round PWAS (7 mm diameter, 0.2 mm thickness) bonded on an aluminum 2024-T3 plate (1 mm thickness). The theoretical tuning curves agree well with the experimental tuning curves, and show mode amplitudes vary with excitation frequencies. At 300 kHz, the amplitude of the S_0 mode is dominated, while the A_0 mode hits zero. Therefore, the 300 kHz is a “sweet spot” for single S_0 mode excitation. With the embedded guided wave excitation and sensing abilities, PWAS have been used for various SHM applications [1, 17, 88, 98-101], such as (1) active sensing of far-field damage using pitch-catch (Figure 2.10 a), pulse-echo (Figure 2.10 b) and phased array (Figure 2.10 e) methods, (2) active sensing of near field damage using E/M impedance method (Figure 2.10 f) and thickness sensing mode (Figure 2.10 c), and (3) passive sensing of acoustic emission (AE) events (Figure 2.10 d).

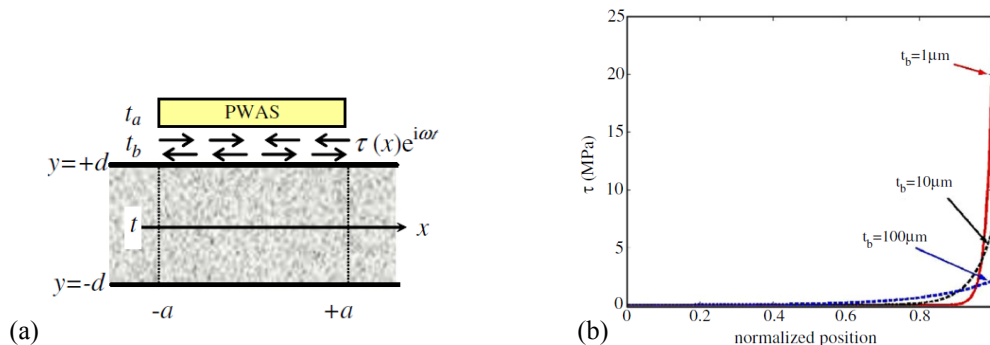


Figure 2.8 PWAS interaction with a structure: (a) a model of layer interaction between PWAS and structure; (b) variation of shear-lag transfer mechanism with bond thickness for a APC-850 PWAS attached to a thin-wall aluminum through a bond layer [17].

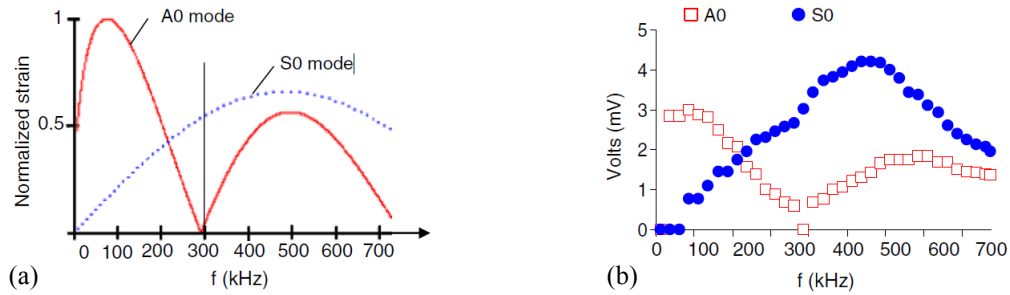


Figure 2.9 PWAS tuning curves of a round PWAS (7mm diameter, 0.2mm thickness) bonded on an aluminum 2024-T3 plate (1mm thick): (a) theoretical results, and (b) experimental results [17].

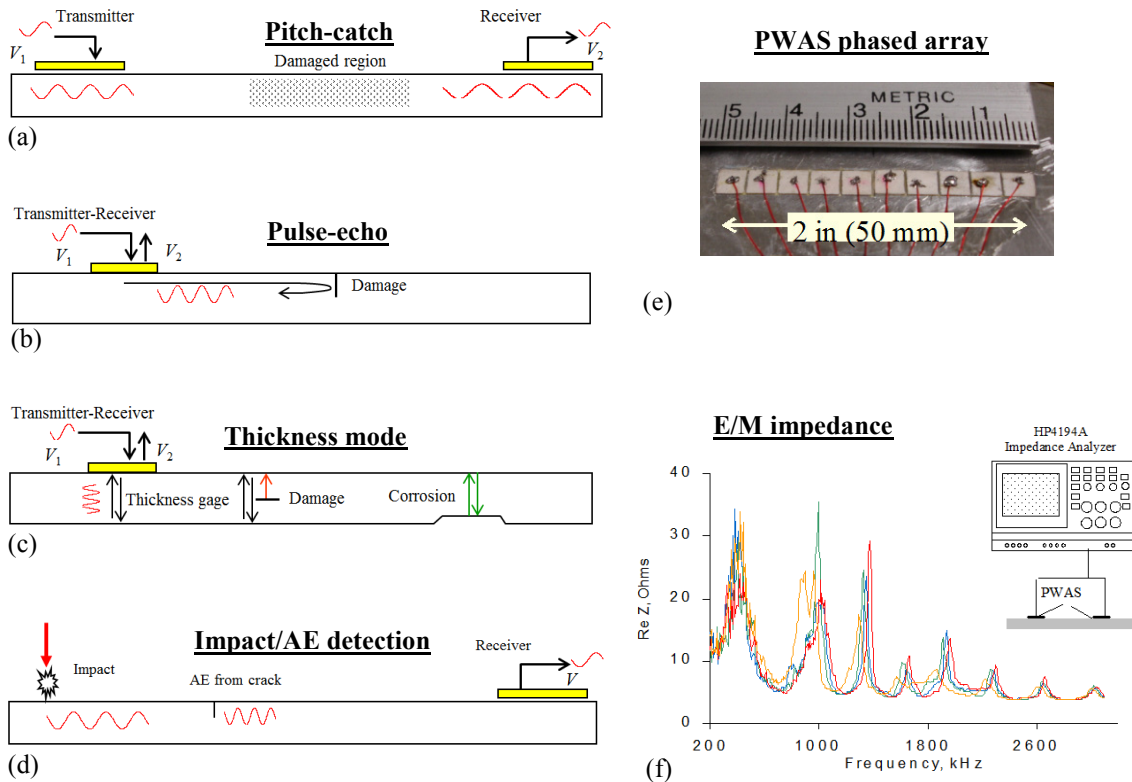


Figure 2.10 Schematics of PWAS applications: (a) pitch-catch sensing; (b) pulse-echo sensing; (c) thickness sensing mode; (d) impact/AE detection; (e) PWAS phased array; (f) E/M impedance method[1, 17, 88, 98-101].

2.2.2. SLDV high spatial resolution guided wave sensor

The scanning laser Doppler vibrometer (SLDV) can make accurate surface velocity/displacement measurements of an object based on Doppler effect on light waves. Figure 2.11 shows a schematic of the laser vibrometry principle [102]. The laser beam is split by a beam splitter (BS1) into a reference beam and a measurement beam. After focusing, the measurement beam is directed to the surface of the vibrating object through vertical and horizontal scanning mirrors. The reflection light from the vibrating object exhibits a frequency shift due to Doppler effect in response to the motion at the scanning point on the vibrating object. The SLDV receives the reflection light and compares its frequency against the reference beam and generates a voltage corresponding to the frequency shift. This voltage signal is correlated to the surface velocity.

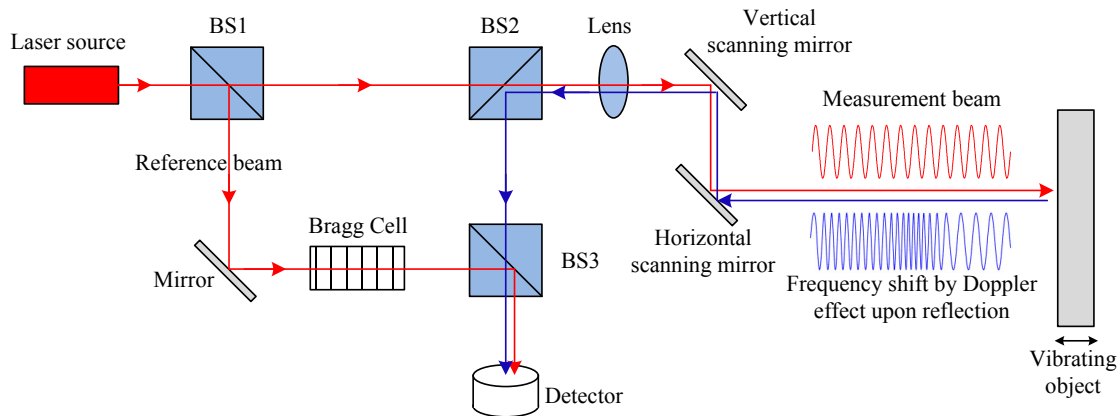


Figure 2.11 A schematic of SLDV principle (BS: beam splitter).

In recent years, the SLDV have been used as a non-contact means for guided wave sensing and wavefield visualization. The visualization can provide deeper understanding of guided waves in various structures and their interactions with structural

discontinuities. Many researchers have used laser vibrometry for wave propagation visualization, damage detection, model validation, etc. [29, 30, 103-110]. Staszewski et al. studied laser vibrometry for guided wave measurements and visualized wave interactions with fatigue cracks by using a 3-D SLDV for the purpose of fatigue crack detection [104]. As shown in their laser vibrometry results in Figure 2.12, the 3-D laser vibrometry sensing provides a series of images which visualize the wave propagation and interaction. In addition, 3-D SLDV provides 3-D wave components (X, Y and Z components), which contain a wealth of information to assist the analysis of such complicated wave propagation and interaction. Ostachowicz et al. used a 3-D laser scanning vibrometer to measure wavefields of Lamb waves and to understand the interactions between the waves and structural discontinuities such as notch and holes [108]. Swenson et al. compared the 1-D and 3-D SLDV measurements of Lamb waves that were excited by a piezoelectric transducer [106]. They showed the 3-D SLDV can provide both in- and out-of-plane wave components, which are especially important for the study of both symmetric and anti-symmetric wave modes. However, the 1-D SLDV can only measure the motion along the laser beam. When the test specimens are placed normal to the laser beam, the 1-D SLDV can measure the out-of-plane wave components which are well-suited for studying anti-symmetric Lamb wave modes. Due to the large cost of the 3-D SLDV, most researchers use the 1-D SLDV instead. Sohn et al. used a 1-D SLDV to visualize the wave interaction with delamination damage in a CFRP composite plate, and observed the “standing waves” trapped at the delamination damage [103]. Ruzzene [30] and Michaels et al. [29, 105] measured full wavefield with a 1-D SLDV to detect delamination and crack damage. They also compared the wavefield measured by the 1-D SLDV with the

wavefield measured by the traditional scanning air-coupled ultrasonic transducer (SAUT) [29], as shown in Figure 2.13. The comparison shows the SAUT measurement has a better signal-to-noise ratio (SNR), while the SLDV result exhibits less ringing and is more broadband. The laser vibrometry also provides a means to validate guided wave simulation. Olson et al. verified the FEM simulations of guided waves in aluminum plates by using laser vibrometry [107]. Yu et al. verified out-of-plane EFIT simulation results of guided waves in aluminum plates by using 1-D SLDV measurements [111]. Various wave features of EFIT simulations such as wavefield, group velocity and wave amplitude, were verified by the SLDV measurements.

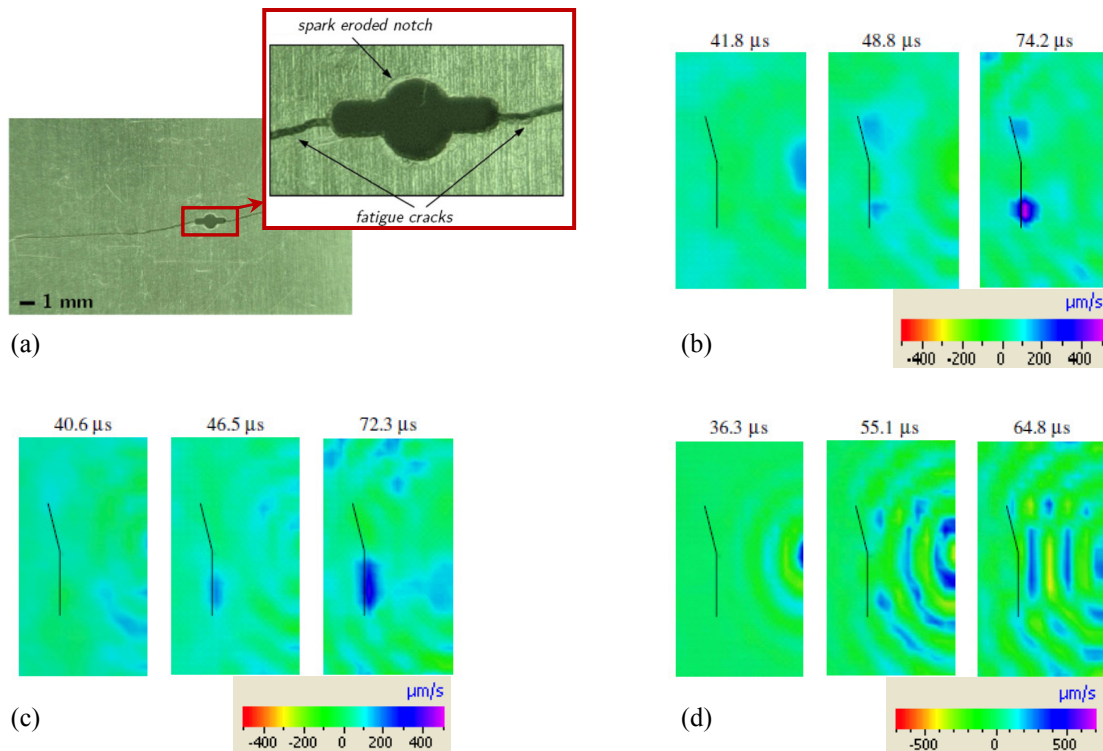


Figure 2.12 Visualization of wave interaction with a fatigue crack by using laser vibrometry: (a) photos of the fatigue crack, (b) in-plane X-components, (c) in-plane Y-components, and (d) out-of-plane Z-components [104].

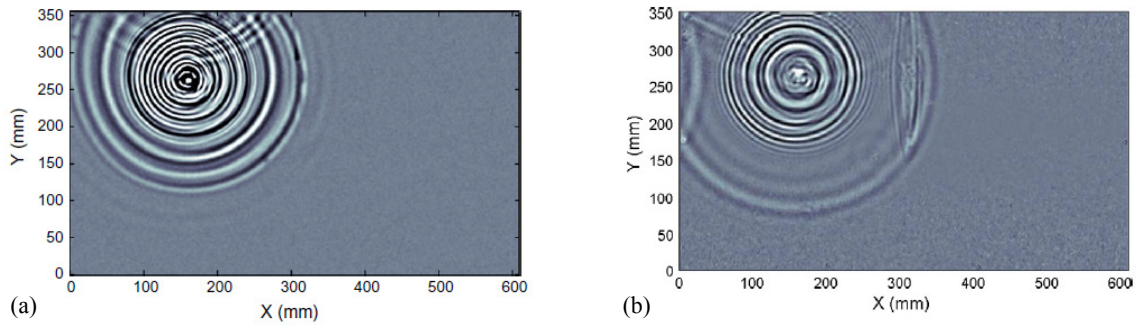


Figure 2.13 The experimental wavefields in a structure (fabricated from two 0.8 mm thick aluminum plates that were epoxy-bonded together): (a) the wavefield at $45\mu\text{s}$ measured by SAUT, and (b) the wavefield at $45\mu\text{s}$ measured by SLDV [29]. The excitation was a wideband pulse with 40Hz repetition rate.

2.3. GUIDED WAVEFIELD DATA ANALYSIS AND DAMAGE DIAGNOSIS METHODOLOGIES

2.3.1. Guided wavefield analysis

Guided wavefields are multi-dimensional wave signals of guided waves in terms of time (t) and space (x, y) dimensions. The SLDV can provide rapid and precise measurements of guided wavefields with very high spatial resolutions to allow for multi-dimensional analyses of guided waves. In contrast, guided wavefields acquired with densely distributed sensors, such as wedge transducers and wafer type piezoelectric sensors, have low spatial resolutions limited by sensor sizes.

Compared to the traditional 1-D waveform data with only the time argument, the guided wavefields acquired from the SLDV extend to the time-space domain and include additional spatial information to allow for obtaining more details of guided waves. Depending on the number of spatial argument, the guided wavefields can be 2-D time-space wavefields $v(t, x)$ representing 1-D wave propagation or 3-D time-space wavefields $v(t, x, y)$ representing 2-D wave propagation. Hence, the guided wavefields include a wealth of information regarding the wave propagation and interaction in both time and space dimensions. Various methods have been used to analyze the guided wavefield, such

as wavefield amplitude profile, multi-dimensional Fourier transform, frequency-wavenumber filtering, standing wave filtering, local wavenumber analysis, etc. [29-32, 103, 112-114]. Among them, the frequency-wavenumber analysis through multi-dimensional Fourier transform provides information in terms of frequency-wavenumber components, enabling wave mode identification, isolation, and damage detection, etc.

Staszewski et al. used amplitude profiles of guided wavefields to detect delamination damage [112]. As illustrated in Figure 2.14, an amplitude profile directly shows both the location and size of the delamination damage. Alleyne and Cawley used 2D FT to transform a guide wavefield into frequency-wavenumber domain where they obtained detailed dispersion information of multi-modal Lamb waves [113]. Hayashi and Kawashima used a filtering technique in frequency-wavenumber domain and successfully separated A_0 and S_0 modes [114]. Ruzzene presented a damage visualization technique by filtering the damage reflection waves in frequency-wavenumber domain and demonstrated an application on crack damage visualization [30]. Michaels et al. presented source removal and wave mode separation techniques by using frequency-wavenumber filtering and demonstrated applications on delamination and crack detection [29]. As illustrated in Figure 2.15, after source removal, delamination induced scattering waves were highlighted. Sohn et al. proposed a “standing wave filter” which can isolate standing wave components in a given wavefield for delamination detection in composites [103]. As shown in Figure 2.16, after filtering, the standing waves at the delamination were isolated indicating the location of the delamination. Rogge and Leckey presented a local wavenumber analysis to process guided wavefields and demonstrated their method can be used to quantify the depth and size of delamination damage [32]. Flynn et al.

presented a structural imaging method, which used frequency-wavenumber filtering and local wavenumber estimation, and showed their method was able to detect wall-thinning damage in an aluminum plate and a steel pipe, and delamination damage in a composite structure [31].

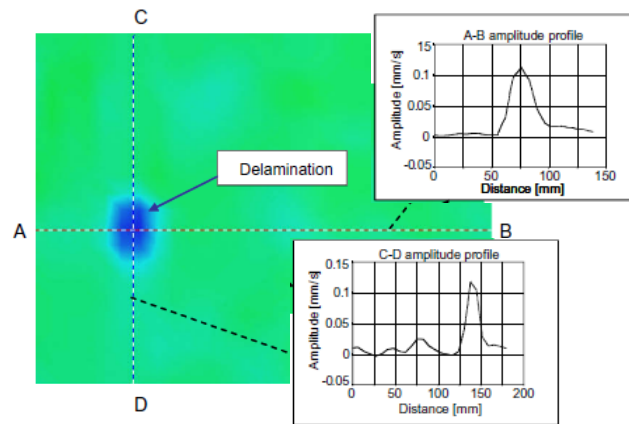


Figure 2.14 Amplitude profile of a guided wavefield for delamination detection [112].

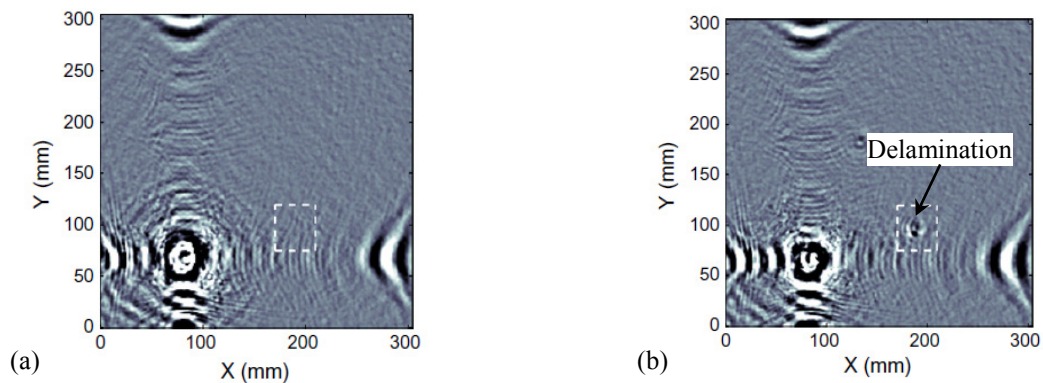


Figure 2.15 Source removal for delamination detection: (a) for a composite plate without damage, and (b) for a composite plate with delamination damage [29].



Figure 2.16 Standing wave filtering for delamination detection: (a) the wavefield before filtering; (b) the wavefield after filtering [103].

2.3.2. Guided wave array imaging

In NDE/SHM applications, various guided wave array imaging methods have been developed. In general, they can be categorized into two groups, the sparse array imaging where sensors are distributed over the structure being inspected [23-26, 115], and the phased array imaging where sensors are physically placed close to each other [12-21]. Both methods can visually show the damage location [12-21, 23, 115].

2.3.2.1. Guided wave sparse arrays

Guided wave sparse arrays employ sparsely distributed sensors over the region of interest to inspect and monitor the structure [115]. The idea of the sparse array approach is to minimize the number of required sensors and optimize the array configuration for practical applications. The sparse array sensors work in the round-robin pattern, in which each sensor can act in turn as the wave actuator to send interrogation waves and the rest as the receivers to record diagnostic wave signals [115]. By using sparse array imaging methods, such as delay-and-sum imaging, minimum variance ultrasonic imaging, and time-reversal imaging, scanning images of the structure being inspected can be constructed from the diagnostic wave signals. The scanning images can visually show the damage location and may indicate the size [115-117].

In recent years, guided wave sparse arrays have been studied by many researchers from various perspectives, such as array optimization, array imaging algorithm, and sparse array applications. The guided wave sparse arrays for SHM were initially proposed by Wang et al. [117]. In their approach, a synthetic time-reversal imaging algorithm was used to process sparse array data to obtain an intensity image for locating and sizing damage. Later, Michaels and Michaels presented an image fusion method to

process sparse array data for damage localization [118]. Their method used time shift averaging to process the differential signals filtered at multiple frequencies, resulting in multiple images of the component being inspected. Then, images generated at different frequencies were fused to improve the damage localization accuracy and reduce the background noise (Figure 2.17). Later, Michaels presented an in-situ sparse array for damage detection, localization and characterization in plates (Figure 2.18a) [115]. This approach used differential signals between diagnostic signals and baselines, and the delay-and-sum algorithm to construct intensity images. Hall and Michaels proposed a minimum variance distortionless response (MVDR) imaging whereby weighting coefficients were adaptively computed at each pixel location, and showed the MVDR can significantly improve the image quality compared to the delay-and-sum imaging (Figure 2.18b) [116]. The time-reversal, delay-and-sum, and MVDR methods all rely upon baseline subtraction to separate scattered signals from direct arrivals and geometrical reflections. However, in real applications, baseline data may not be available, or the baseline data may have been recorded under mismatched environmental or operational conditions. For such situations, Lee et al. developed a baseline-free imaging method which was based upon estimating the source waveform and then adaptively removing the direct arrival from each received signal [21]. As shown in Figure 2.19a, the imaging result with raw received signals showed only the source. After adaptive source removal, the imaging result (Figure 2.19b) with residual signals clearly showed the scatterer.

The sparse arrays have been used for various applications. Clarke et al. studied the damage detection capability of a sparse array on a complex structure under varying thermal conditions [23]. By using the signals after temperature compensation, they could

get good localization of holes with a 5-mm diameter or above in a complex structure. Yu and Leckey explored the sparse array approach for crack detection in aluminum plates [119]. With the sparse array, the crack tips could be clearly detected (Figure 2.20a). Su et al. used sparse arrays to detect delamination damage in composite laminates [120]. Cho and Lissenden used a sparse array on a multi-fastener joint for fatigue crack growth monitoring [121]. Compared to phased arrays which use backscattering waves for damage detection, the sparse arrays can also take advantage of the so-called shadowing effect or forward scattering waves, which are partially blocked by the damage [122].

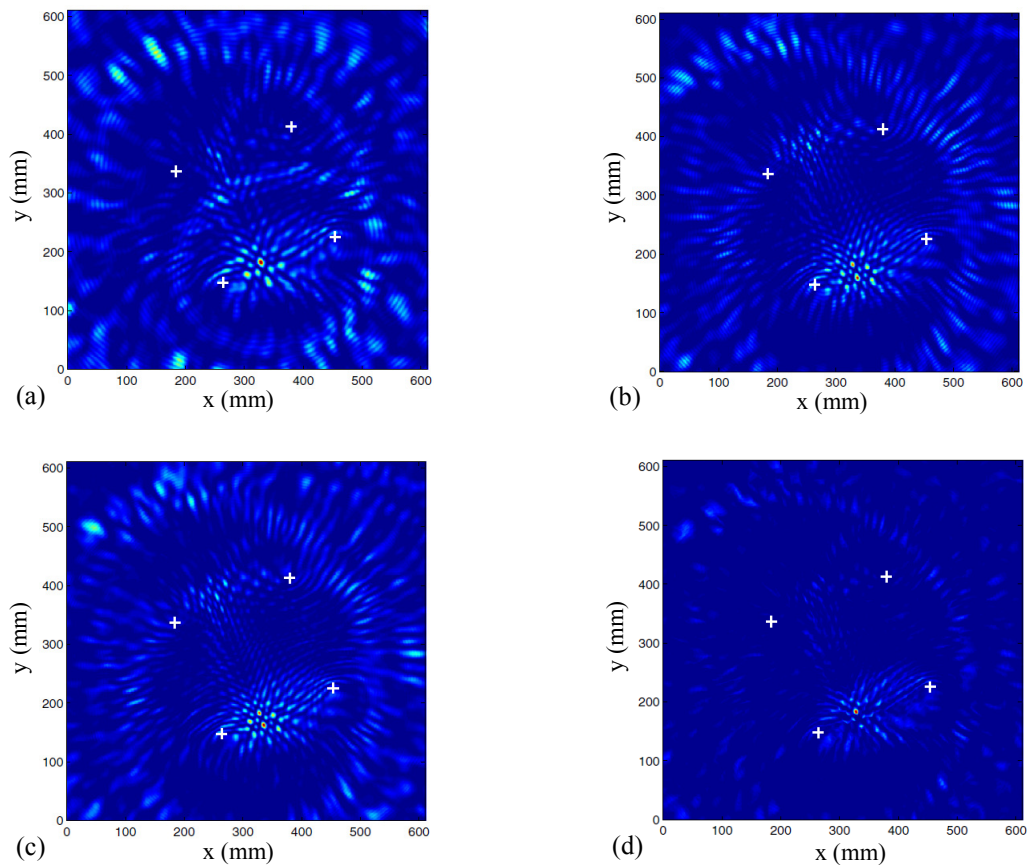


Figure 2.17 Sparse array imaging results for the detection of a through hole with a diameter of 3.2 mm: (a) result at 140 kHz, (b) result at 230 kHz, (c) result at 320 kHz, and (d) the fused result. The “+” represents the location of the through hole[118].

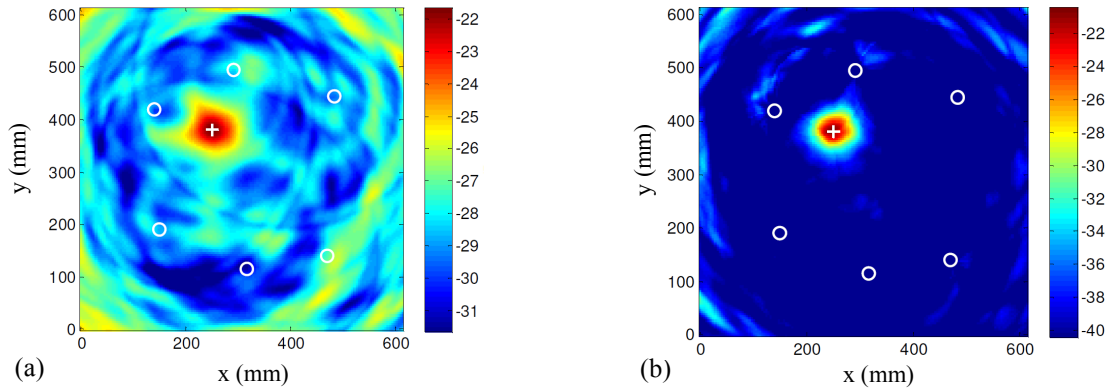


Figure 2.18 Sparse array imaging results for the detection of a 6 mm diameter through hole: (a) the result of delay-and-sum imaging (10 dB color scale) [115], and (b) the result of MVDR imaging (20 dB color scale) [116]. The open circles represent the transducers, and the “+” represents the through hole.

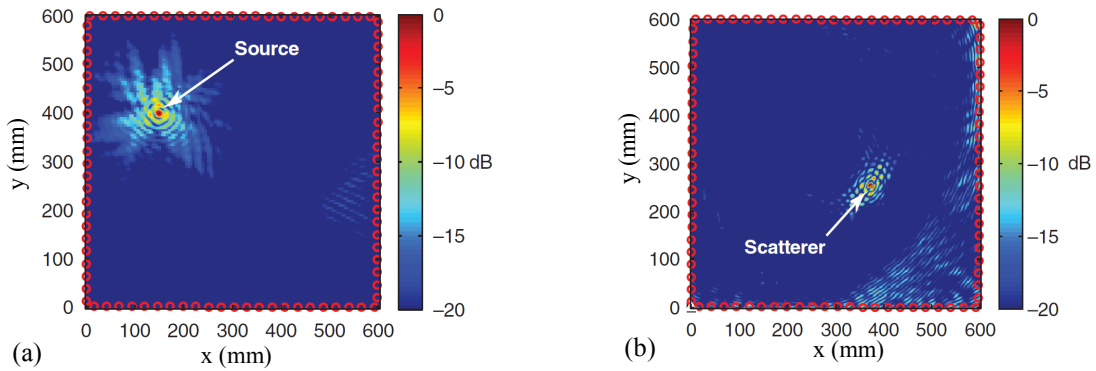


Figure 2.19 Baseline-free imaging: (a) delay-and-sum imaging of the source constructed from the raw data, and (b) delay-and-sum imaging of the scatter constructed from signals with direct arrivals removed via adaptive source removal. The open circles represent the receivers [21].

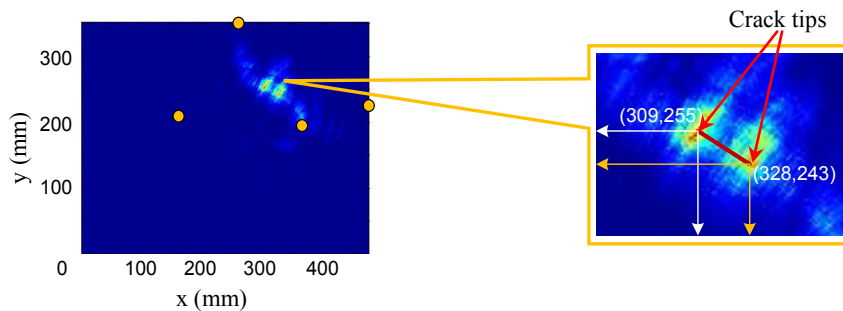


Figure 2.20 Sparse array imaging for crack detection [119].

2.3.2.2. Guided wave phased arrays

The guided wave phased array employs sensors physically placed in a compact format in which the relative phases of sensor signals are controlled in such a way that guided waves (Figure 2.16 a) are focused into a wave beam in a desired direction (Figure 2.16 b) [1, 17, 123]. By steering the wave beam to all directions, the phased arrays can inspect and monitor a large area of a structure. In NDE/SHM applications, the guided wave phased arrays show multiple advantages such as reinforced wave energy in the beam, efficient and flexible control of the beam direction, improved signal-to-noise-ratio, large area inspection through a small sensing area, and promising damage detection results [12, 17, 124].

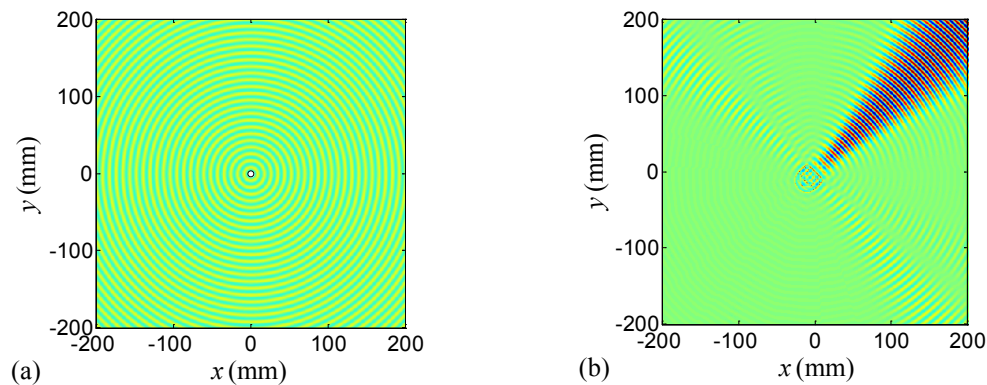


Figure 2.21 Comparisons between omnidirectional guided waves and focused guided waves: (a) omnidirectional guided waves, (b) the focused guided waves in 45° direction.

Guided wave phased arrays have been studied intensively [12-19, 125-130]. Giurgiutiu and Bao developed an embedded-ultrasonic structural radar (EUSR) with 1-D linear phased arrays for in-situ NDE/SHM of thin-wall metallic structures [12]. They showed the capability of 1-D linear phased array in detecting both broadside and offside cracks in metallic plates (Figure 2.22). The 1-D linear arrays have shown that they can successfully detect damage by performing large area scanning and diagnosis. However,

the 1-D linear arrays encounter some major shortcomings, such as (a) the degradations of beamforming properties at angles close to 0° and 180° directions, and (b) the half-plane mirror effect, which does not allow discriminating between a target placed above the array and a target placed below the array (Figure 2.22c) [1].

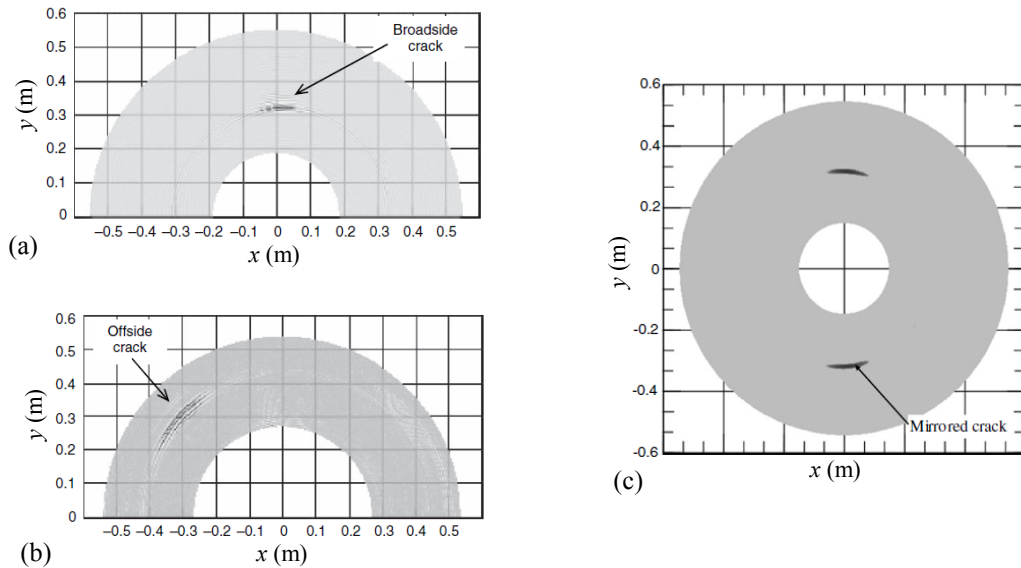


Figure 2.22 EUSR detection results: (a) detection of a broadside crack, (b) detection of an offside crack, (c) detection result showing the half-plane mirror effect [12, 17].

To overcome the shortcomings of 1-D linear arrays, 2-D planar arrays have been adopted, which not only provide more control and optimization parameters for improving the array performance, but also are able to perform full-range 360° beam steering and reduce the mirror effect [1, 16, 17]. Wilcox studied omni-directional guided wave phased arrays with 2-D circular configurations (Figure 2.23 (d) and (e)) for the rapid inspection of large areas of aluminum plates [16]. In his work, phased arrays were constructed by electromagnetic acoustic transducers. The measured time domain wave signals were converted to wavenumber domain where the dispersion effect was compensated. After the dispersion compensation, the phased addition algorithm in wavenumber domain was used to achieve beam steering in different steering directions and to construct an omni-

direction, B-scan image. Yu and Giurgiutiu studied the 2-D phased arrays design and implementation for damage detection in aluminum plates [17]. Various 2-D phased array configurations were studied and compared, such as cross-shaped array, rectangular grid array, rectangular ring array, circular ring array, and concentric circular array in Figure 2.23 (a)-(e), respectively. Yoo et al. developed a 2-D spiral phased array (Figure 2.23 (f)) by using piezoelectric-paint for SHM of thin isotropic panels [19]. Ambrozinski et al. developed an efficient tool for the designing of 2-D phased arrays for isotropic plates [131]. Koduru et al. proposed a 2-D phased annular array transducer (Figure 2.23 (f)) that can generate mode controlled omnidirectional guided waves in isotropic plate-like structures by independently controlling the amplitude and phase of each array element [132]. Senesi et al. designed a 2-D periodic frequency-steerable array (Figure 2.23 (g)) for SHM of aluminum plates. The array was composed of PZT discs in a quadrilateral periodic topology. The beamsteering direction of the array can be controlled by the excitation frequency [20].

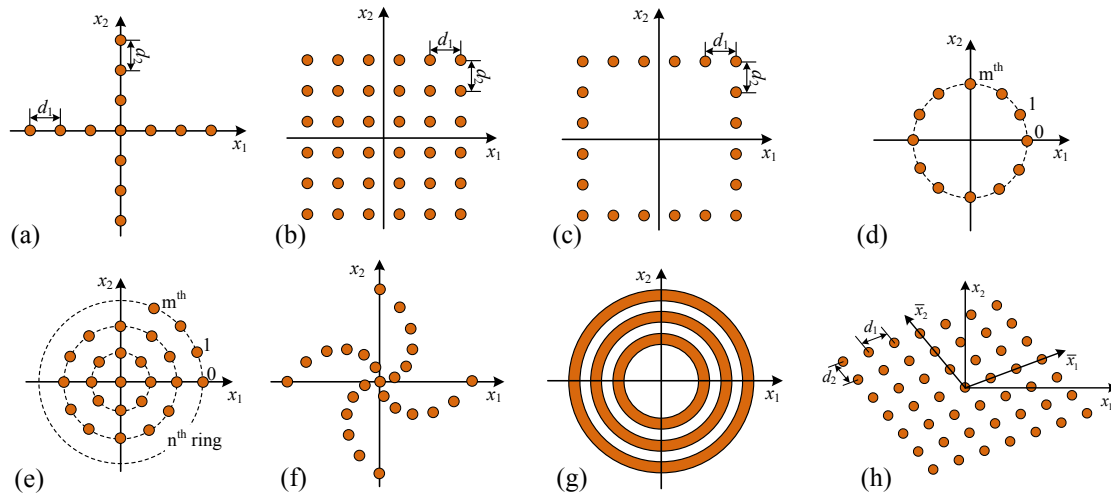


Figure 2.23 2-D planar arrays: (a) cross-shaped array [17], (b) rectangular grid array [17], (c) rectangular ring array [17], (d) circular ring array [16], (e) concentric circular array [16], (f) spiral array [19], (g) annular array [132], and (h) quadrilateral periodic array [20].

Although most research works focus on phased arrays for isotropic materials, some researchers have investigated the phased arrays for composite materials [14]. Yan and Rose studied beamsteering of linear arrays in composite plates [133]. They found the traditional beamsteering technique for isotropic materials might fail in composite materials due to the anisotropic behavior of the composite plates. Hence, they chose a quasi-isotropic wave mode for beamsteering, which can suppress the influence of the anisotropic behavior. Rajagopalan et al. adopted an array of a single transmitter and multiple receivers (STMR) to locate a defect (hole) in a composite plate [134]. In their array imaging method, they used a weakly anisotropic wave mode and assumed that the phase and group velocity directions coincide locally. Later, Vishnuvardhan et al. used the STMR array to detect impact induced delamination damage in a quasi-isotropic composite plate. Leleux et al. used ultrasonic phased array probes for long range detection of defects in composite plates [129]. Their method was limited to wave modes having phase and group velocities oriented in the same direction, where the skew angle was zero. Purekar and Pines investigated the capability of 1-D linear phased arrays in detecting delamination damage in a cross-ply composite plate [14]. They showed the array can detect damage at 0° direction, where the phase and group velocities had the same orientation. Osterc et al. investigated the beamsteering of 1-D linear arrays in composite laminates [135]. In their study, the exact phase velocity curve was used to develop a beamforming algorithm that accounted for non-omnidirectional guided waves in anisotropic materials.

Compared to the array beamforming in isotropic plates, the array beamforming in anisotropic composite plates are more challenge. In anisotropic composite plates, guided

wave parameters such as wavenumber, phase velocity and group velocity are directionally dependent, due to the directionally dependent physical properties of composite materials [11, 136, 137]. Moreover, the guided waves have energy skewness that the group velocity direction is not always parallel to the phase velocity direction. Last but not least, the wave fronts of guided waves are no longer circular shapes. These properties of guided waves in composite plates have significant influences on the phased array beamforming. The traditional beamforming technique for isotropic materials might fail in composite materials.

PART I: INTEGRATED SHM/NDE DIAGNOSIS METHODOLOGIES

CHAPTER 3

ANALYTICAL AND NUMERICAL STUDIES OF GUIDED WAVES

Analytical and numerical studies can provide a preliminary understanding of wave propagations in complex structures and wave interactions with structural discontinuities, theoretical data for assisting experimental work, and abundant information for parametric studies. This chapter presents both analytical and numerical studies of guided waves in complex structures. The GMM and the SAFE methods are used to obtain wave dispersion curves and mode shapes, while the EFIT and the FEM methods are adopted to simulate wave propagation and interaction.

3.1. DISPERSION AND MODE SHAPE DERIVATIONS

3.1.1. Water loaded plates

The classic problem of guided wave propagation in a traction-free homogeneous and isotropic plate has been thoroughly studied and can be found in many references such as [1, 8, 33, 138]. In a plate with traction-free boundary conditions (Figure 3.1 a), the characteristic equation can be derived and expressed as [1, 8, 33]:

$$\begin{vmatrix} k_s^2 - \xi^2 & k_s^2 - \xi^2 & -2k_s\xi & 2k_s\xi \\ 2k_L\xi & -2k_L\xi & k_s^2 - \xi^2 & k_s^2 - \xi^2 \\ (k_s^2 - \xi^2)g_L & \frac{k_s^2 - \xi^2}{g_L} & -2k_s\xi g_s & \frac{2k_s\xi}{g_s} \\ 2k_L\xi g_L & \frac{-2k_L\xi}{g_L} & (k_s^2 - \xi^2)g_s & \frac{k_s^2 - \xi^2}{g_s} \end{vmatrix} = 0 \quad (3.2)$$

where,

$$k_L^2 = \frac{\omega^2}{c_L^2} - \xi^2, \quad k_S^2 = \frac{\omega^2}{c_S^2} - \xi^2, \quad \xi = \frac{2\pi}{\lambda},$$

$$c_L = \sqrt{\frac{2\mu(1-\nu)}{\rho(1-2\nu)}}, \quad c_S = \sqrt{\frac{\mu}{\rho}}, \quad g_L = e^{ik_L d}, \quad g_S = e^{ik_S d}, \quad d = 2h$$

h , ω , ξ and λ are half plate thickness, circular frequency, wavenumber and wavelength, respectively. c_L and c_S are longitudinal and transverse bulk wave velocities, respectively. ρ , μ and ν are density, shear modulus and Poisson's ratio, respectively. Solutions of Eq.(3.2) can be found in many classic references such as [1, 8, 33, 138]. Figure 3.2 plots frequency-wavenumber dispersion curves of a steel plate with 1.2 mm thickness. At frequencies lower than 1000 kHz, there are fundamental anti-symmetric A_0 and symmetric S_0 modes.

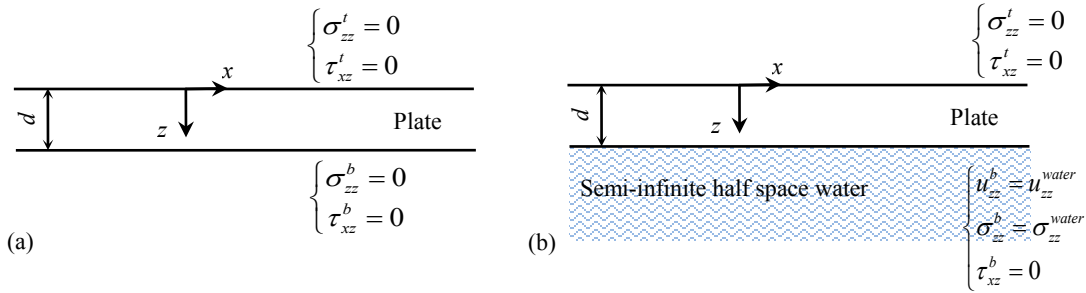


Figure 3.1 Sketches for: (a) free plate and (b) plate with one side in water.

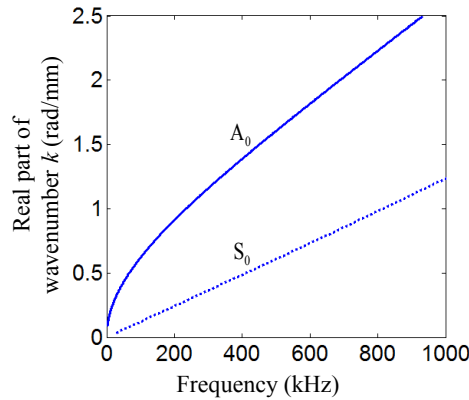


Figure 3.2 Wavenumber dispersion curves of a free steel plate with 1.2 mm thickness. (Note only the real parts are given. The imaginary parts are zero.)

When one side of a plate is immersed in water (*plate-half space water* waveguide, as shown in Figure 3.1 b), the top surface of the plate maintains traction-free boundary conditions. On the bottom surface of the plate, wave energy can transmit into water since the normal displacement u_{zz} and stress σ_{zz} are continuous at the plate-water interface. The shear stress τ_{xz} remains zero at the interface, since water does not support the shear stress. The characteristic equation for the immersed plate can be assembled and expressed as,

$$\begin{vmatrix} k_S^2 - \xi^2 & k_S^2 - \xi^2 & -2k_S\xi & 2k_S\xi & 0 \\ 2k_L\xi & -2k_L\xi & k_S^2 - \xi^2 & k_S^2 - \xi^2 & 0 \\ (k_S^2 - \xi^2)g_L & \frac{k_S^2 - \xi^2}{g_L} & -2k_S\xi g_S & \frac{2k_S\xi}{g_S} & \frac{\omega^2 \rho_w}{\mu} \\ 2k_L\xi g_L & \frac{-2k_L\xi}{g_L} & (k_S^2 - \xi^2)g_S & \frac{k_S^2 - \xi^2}{g_S} & 0 \\ k_L g_L & \frac{-k_L}{g_L} & -\xi g_S & \frac{-\xi}{g_S} & \gamma \end{vmatrix} = 0 \quad (3.3)$$

where, $\gamma^2 = \frac{\omega^2}{c_{Lw}^2} - \xi^2$ and $c_{Lw} = \sqrt{\frac{\lambda_w}{\rho_w}}$. ρ_w , λ_w and c_{Lw} are density, bulk stiffness, and bulk wave velocity of water, respectively. By solving Eq. (3.3), the dispersion curves for the 1.2 mm thick steel plate with one side in water can be obtained. Due to the energy leakage, the wavenumber roots of Eq. (3.3) have complex values with the real parts indicating wave components and the imaginary parts giving the extent of energy attenuation.

Figure 3.3 a plots the real parts of wavenumber roots for the immersed plate. The fundamental symmetric and antisymmetric guided wave modes are present and are notated as A_0^{WP} and S_0^{WP} to distinguish them from the A_0 and S_0 modes in the free plate. Furthermore, there is an additional mode that exhibits the same dispersive behavior as the quasi-Scholte mode discovered in a two-side immersed plate [139], which is dispersive at

low frequencies and asymptotes to the non-dispersive Scholte mode at high frequencies [139]. The one-side immersed steel plate in this study shows its capability to support the quasi-Scholte mode as well.

Figure 3.4 gives mode shapes of the quasi-Scholte mode at various frequencies. At 150 kHz, the mode shape in Figure 3.4 a shows large in-plane and out-of-plane displacements in the plate. When frequency increases, both in-plane and out-of-plane displacements in the plate decrease, as shown in Figure 3.4 b and c at 300 kHz and 600 kHz. At the high frequency of 600 kHz, the displacement is dominated by the in-plane displacement in the water, and the displacement in the plate is almost zero.

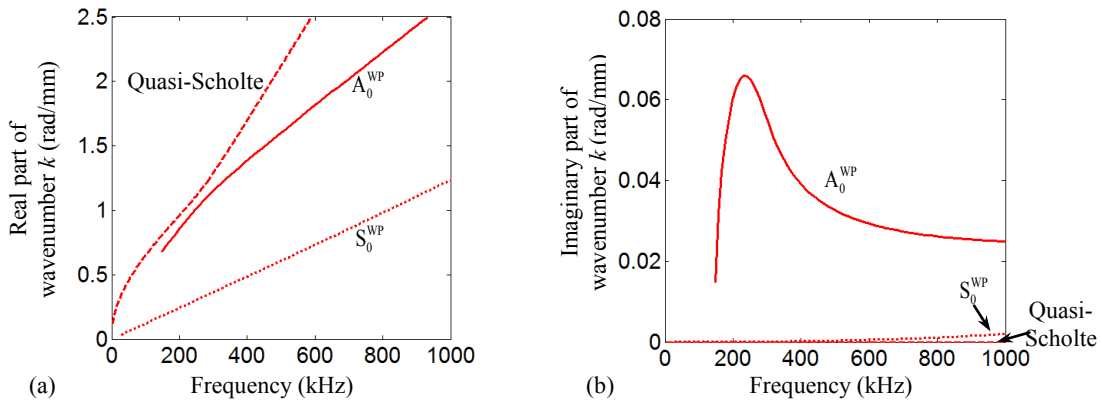


Figure 3.3 Wavenumber dispersion curves of a 1.2 mm thick steel plate with one side in water: (a) real parts, (b) imaginary parts.

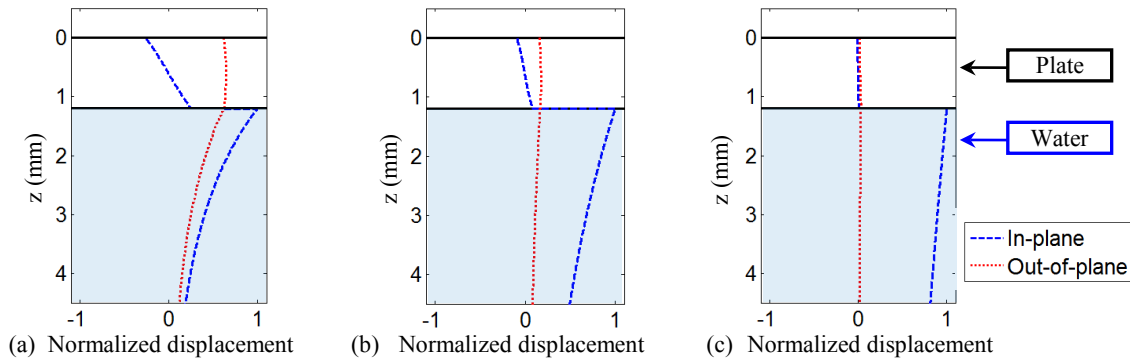


Figure 3.4 Theoretical wave mode shapes of the quasi-Scholte mode: (a) at 150 kHz, (b) at 300 kHz, and (c) at 600 kHz.

3.1.2. Composite laminates

Composite laminates are multilayer structures. Knowing their dispersion curves is important for selecting the appropriate wave mode for NDE/SHM in composites. The SAFE method has shown its effectiveness and efficiency for deriving dispersion curves and mode shapes [38]. For the development of NDE/SHM in composites, the SAFE method is used to obtain dispersion curves and mode shapes of guided waves in CFRP composite laminates. Figure 3.5 a gives a schematic of an 8-ply CFRP composite plate with $[0_2/90_2]_s$ layup. In the SAFE model, the cross section of the composite plate is discretized using 3 node quadratic elements, as illustrated in Figure 3.5 b. In each ply, two elements are used for finite element approximation. By solving the discretized model with the SAFE method, dispersion curves and mode shapes can be derived.

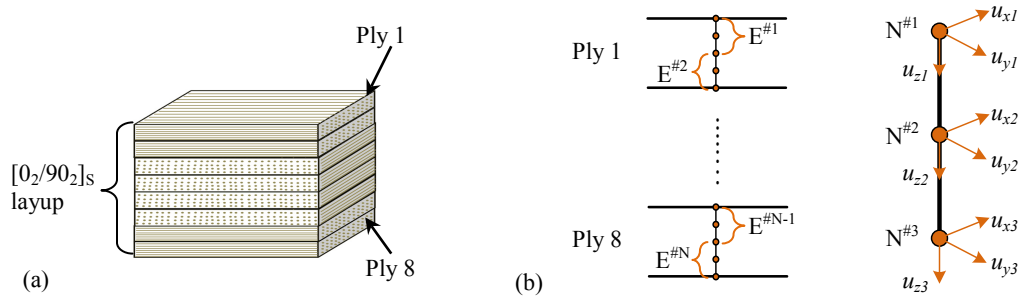


Figure 3.5 SAFE model of a CFRP composite plate with $[0_2/90_2]_s$ layup: (a) an illustration of the composite plate, (b) an illustration of the finite element discretization.

Figure 3.6 plots the dispersion curves of guided waves propagating in 90° direction in the composite plate. Figure 3.7 plots wavenumbers and group velocities in all directions at 300 kHz. It is seen that both wavenumber and group velocity depend on wave propagation direction in the composite plate.

Figure 3.8 gives the mode shapes for A_0 , S_0 and SH_0 modes at 300 kHz propagating in 90° direction in the composite plate. For the A_0 mode, the out-of-plane

displacement u_z is dominated. For the S_0 mode, the in-plane displacement u_y is dominated.

For the SH_0 mode, the in-plane displacement u_x is dominated.

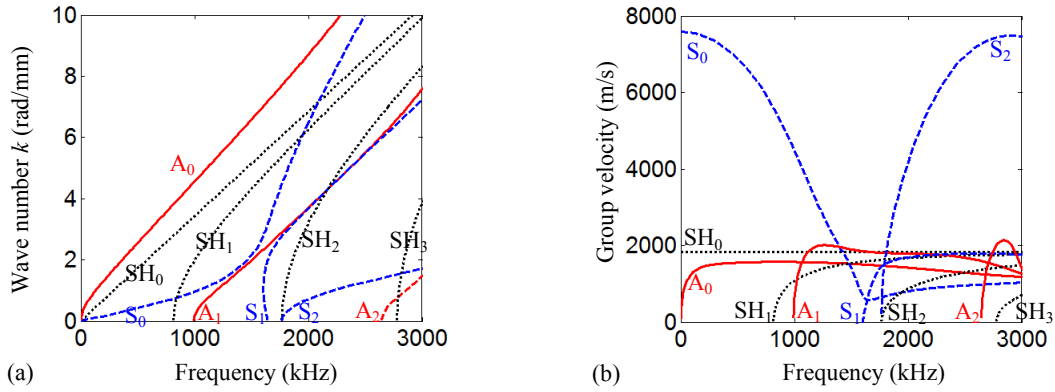


Figure 3.6 Dispersion curves of guided waves propagating in 90° direction in the $[0_2/90_2]_s$ CFRP composite plate: (a) frequency-wavenumber dispersion curves; (b) group velocity dispersion curves.

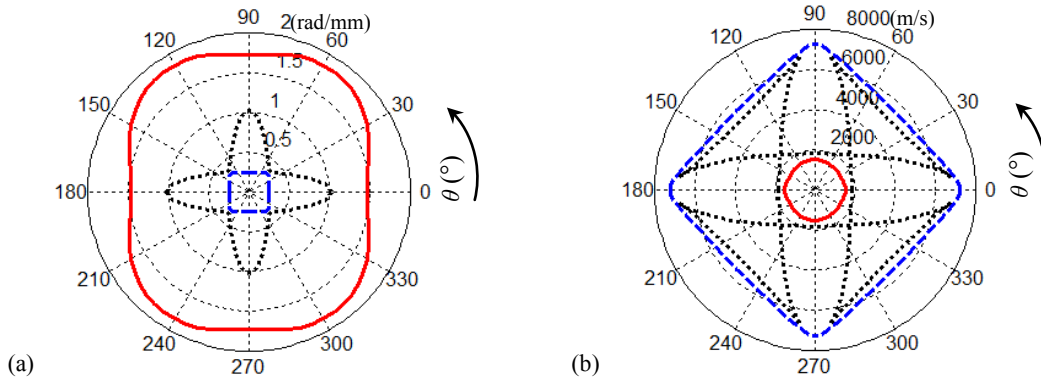


Figure 3.7 Wavenumber and group velocity curves at 300 kHz for guided waves in the $[0_2/90_2]_s$ CFRP composite plate: (a) wavenumber curves; (b) group velocity curves. The solid, broken and dotted lines are for the A_0 , S_0 and SH_0 modes.

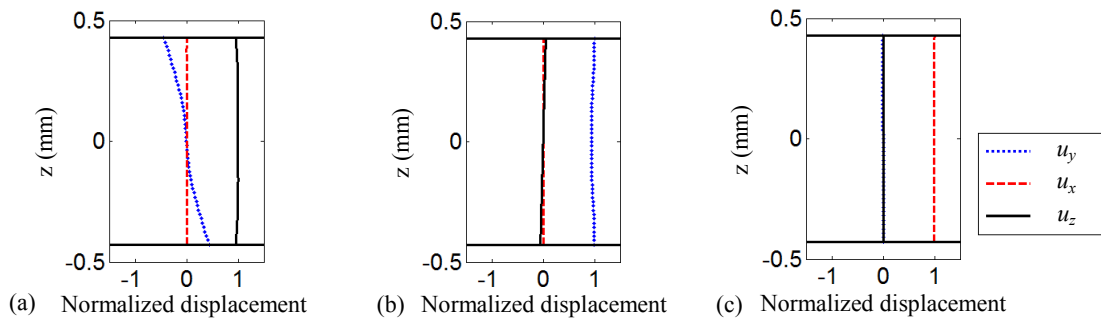


Figure 3.8 Mode shapes of guided waves at 300 kHz propagating in 90° direction in the $[0_2/90_2]_s$ CFRP composite plate: (a) A_0 mode, (b) S_0 mode and (c) SH_0 mode.

3.2. WAVE PROPAGATION AND INTERACTION SIMULATIONS

To simulate guided wave propagation and interaction, both the EFIT and the FEM methods are used. With straightforward equations, EFIT computational codes are developed using Matlab programming language. The EFIT method is used to simulate guided waves in a water loaded plate and guided wave interaction with delamination damage in a laminated composite plate. In addition, the commercial FEM software ANSYS is adopted to simulate guided waves in a honeycomb sandwich structure.

3.2.1. EFIT for water loaded plates

Figure 3.9 plots the configuration of EFIT simulation for the study of guided waves in a water loaded plate. A T304 steel plate with 1.2 mm thickness has one surface in water. A PZT is installed on the top surface of the plate for guided wave generation. In the EFIT model, the PZT excitation is simulated as pin forces at the edges of the PZT. By using the EFIT method, guided waves in the water loaded plate are simulated.

Figure 3.10 plots EFIT simulation results (out-of-plane velocity v_z) at 100 kHz excitation. The simulation results show three wave components: quasi-Scholte waves, leaky S_0 waves and pressure waves (P-waves). The quasi-Scholte waves are present at the plate-water interface and propagate along the interface. The leaky S_0 waves in water are induced by the energy leakage of plate S_0 waves. In addition, the leaky S_0 waves have plane wave fronts and propagate faster compared to the P-waves which have circular wave fronts.

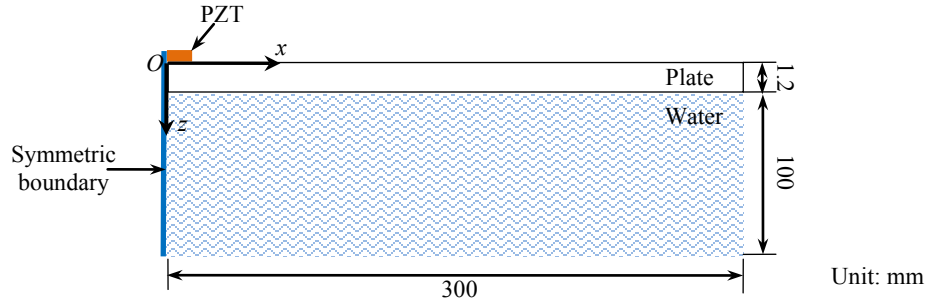


Figure 3.9 Configuration of EFIT simulation for the study of guided waves in a water loaded plate.

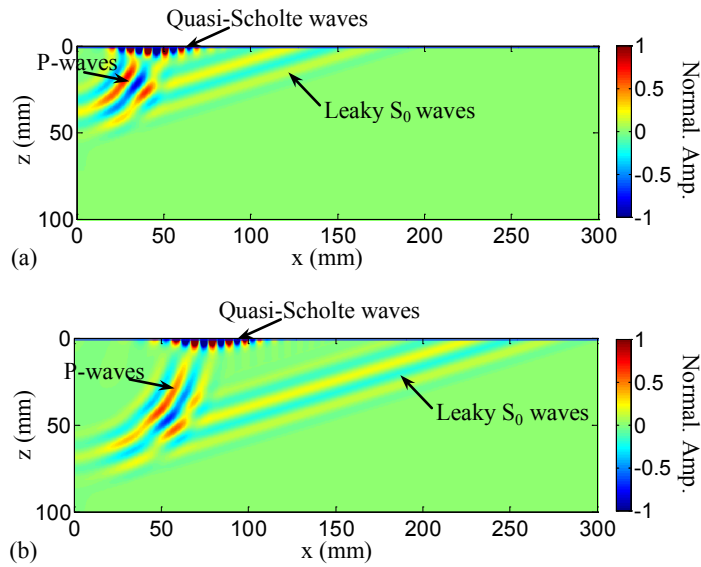


Figure 3.10 v_z velocity results of EFIT simulation at 100 kHz excitation: (a) at 40 μ s and (b) at 60 μ s.

Figure 3.11 plots EFIT simulation results (out-of-plane velocity v_z) at 600 kHz excitation. The simulation results show three wave components: leaky A_0 waves, leaky S_0 waves, and P-waves. Compared to the results at the lower frequency 100 kHz, at the higher frequency 600 kHz, quasi-Scholte waves at the plate-water interface disappear, while leaky A_0 waves present, which are induced by the energy leakage of plate A_0 waves.

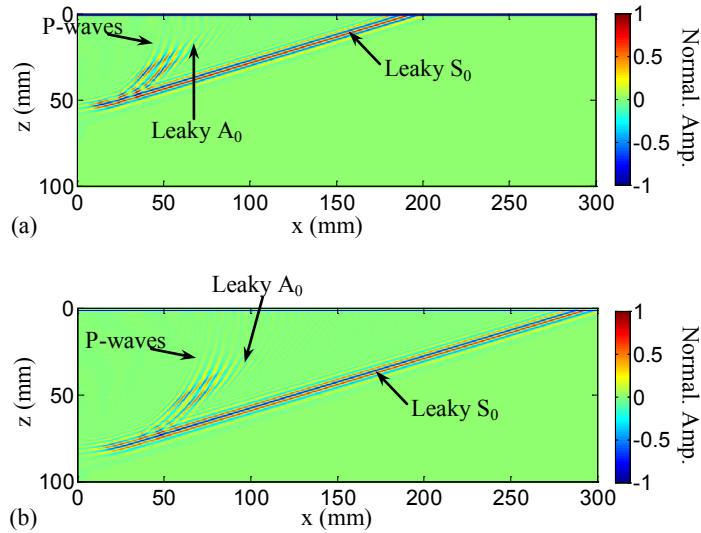


Figure 3.11 v_z velocity results of EFIT simulation at 600 kHz excitation: (a) at 40 μ s and (b) at 60 μ s.

3.2.2. EFIT for composite laminates

EFIT simulations are implemented to investigate guided wave interaction with delamination damage. Figure 3.12 gives the simulation configuration of a CFRP plate with $[0_2/90_2]_s$ layup. Under the second ply there is a 40 mm length delamination defect with its center at $x=100$ mm. In the EFIT simulation, the delamination is modeled by using stress free boundary conditions. Two PZT elements on the top and bottom surfaces of the plate are used for wave generation and mode control. When the two PZT elements are excited in-phase, symmetric modes will be generated. When the two PZT elements are excited out-of-phase, anti-symmetric modes will be generated.

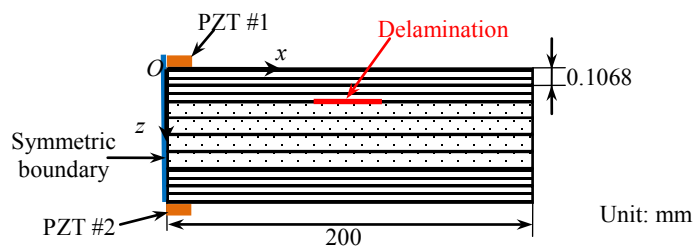


Figure 3.12 The EFIT simulation configuration for the study of wave interaction with delamination damage in a CFRP plate with $[0_2/90_2]_s$ layup.

Figure 3.13 plots in-plane v_x and out-of-plane v_z velocity components of the EFIT simulation results when two PZT elements are excited out-of-phase and only an incident A_0 mode is actuated. Table 3.1 lists all the wave modes, including the incident A_0 mode and other modes induced by delamination damage observed from the simulation results. These wave modes have been verified by comparing their wavelengths and group velocities with their theoretical values.

At 40 μs , both the v_x and v_z components show only an incident A_0 mode (incident #1 in Figure 3.13 a and c). Since delamination damage separates the full $[0_2/90_2]_s$ laminate to two laminates with different layups, one above the delamination with $[0]_2$ layup and the other below the delamination with $[(90)_4/0_2]$ layup, it is expected that guided waves are different in these two laminates.

As expected, simulation results at 70 μs show that the incident A_0 mode separates to different waves above and below the delamination damage. The in-plane v_x plot shows weak A_0 (#3 in Figure 3.13 b) and strong S_0 (#4 in Figure 3.13 b) modes supported by the $[0]_2$ laminate above the delamination. Below the delamination, an A_0 mode (#5 in Figure 3.13 b) supported by the $[(90)_4/0_2]$ laminate is observed.

The out-of-plane v_z plot at 70 μs shows an A_0 mode (#3 in Figure 3.13 d) in the $[0]_2$ laminate above the delamination. Compared to the in-plane v_x plot, the S_0 mode in the $[0]_2$ laminate is not observed in the out-of-plane v_z plot. The reason is that the out-of-plane motion of the S_0 mode is too weak to be observed from the image in Figure 3.13 d. Below the delamination, an A_0 mode (#5 in Figure 3.13 d) supported by the $[(90)_4/0_2]$ laminate is observed, which agrees well with the A_0 mode (#5 in Figure 3.13 b) observed in the in-plane v_x plot.

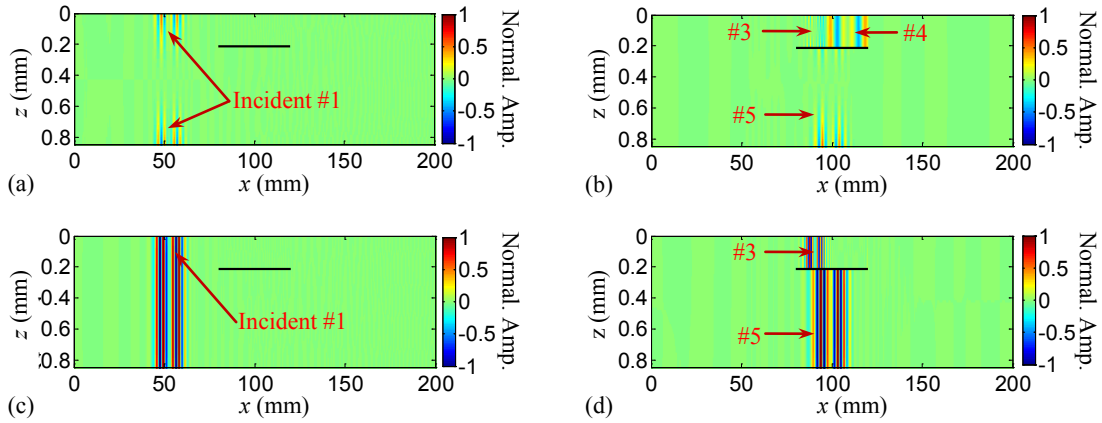


Figure 3.13 EFIT results at 300 kHz for A_0 mode interaction with delamination damage: (a) and (b) are in-plane v_x velocity plots at 40 μ s and 70 μ s; (c) and (d) are out-of-plane v_z velocity plots at 40 μ s and 70 μ s.

Table 3.1 Wave modes in EFIT results when incident waves are A_0 mode

Number	Wave Components
#1	A_0 in the $[0_2/90_2]_s$ laminate
#3	A_0 mode in the $[0]_2$ laminate above the delamination
#4	S_0 mode in the $[0]_2$ laminate above the delamination
#5	A_0 mode in the $[(90)_4/0_2]$ laminate below the delamination

Figure 3.14 plots in-plane v_x and out-of-plane v_z velocity components of EFIT simulation results, when two PZT elements are excited in-phase and only an incident S_0 mode is actuated. Table 3.3.2 lists all the wave modes, including the incident S_0 mode and other modes induced by delamination damage observed from the simulation results. At 10 μ s, an incident S_0 mode (incident #2) is observed from the in-plane v_x simulation result in Figure 3.14 a, while the out-of-plane v_z motion of the S_0 mode is too weak to be observed from the out-of-plane v_z simulation result in Figure 3.14 c.

At delamination damage, the incident S_0 mode interacts with the damage and is separated to different waves above and below the damage, as shown in Figure 3.14 b. The in-plane v_x plot at 20 μ s shows three strong components: an S_0 mode (#4 in Figure 3.14 b) mode supported by the $[0]_2$ laminate above the delamination, an S_0 mode (#6 in Figure

3.14 b) supported by the $[(90)_4/0_2]$ laminate below the delamination, and a transmitted S_0 mode (transmitted #2 in Figure 3.14 b) in the full $[0_2/90_2]_s$ laminate. Note that there is no A_0 mode induced by the delamination observed in the in-plane v_x plot (Figure 3.14 b), since its in-plane motion is too weak.

The out-of-plane v_z plot at $20 \mu s$ shows an A_0 mode (#3 in Figure 3.14 d) in the $[0]_2$ laminate above the delamination and an A_0 mode (#5 in Figure 3.14 d) in the $[(90)_4/0_2]$ laminate below the delamination. Note that there is no S_0 mode induced by the delamination observed in the out-of-plane v_z plot (Figure 3.14 d), since its out-of-plane motion is too weak.

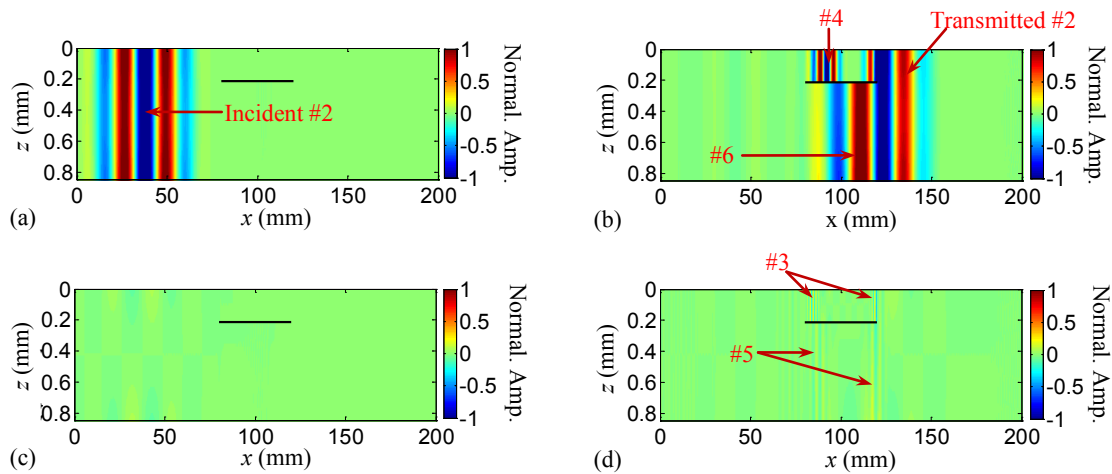


Figure 3.14 EFIT results at 300 kHz for S_0 mode interaction with delamination damage: (a) and (b) are in-plane v_x velocity plots at $10 \mu s$ and $20 \mu s$; (c) and (d) are out-of-plane v_z velocity plots at $10 \mu s$ and $20 \mu s$.

Table 3.2 Wave modes in EFIT results when incident waves are S_0 mode

Number	Wave modes
#2	S_0 in the $[0_2/90_2]_s$ laminate
#3	A_0 mode in the $[0]_2$ laminate above the delamination
#4	S_0 mode in the $[0]_2$ laminate above the delamination
#5	A_0 mode in the $[(90)_4/0_2]$ laminate below the delamination
#6	S_0 mode in the $[(90)_4/0_2]$ laminate below the delamination

3.2.3. FEM for honeycomb sandwich structures

To simulate guided waves in honeycomb sandwich structures, the commercial FEM software, ANSYS/Multiphysics 11.0 is used. The honeycomb sandwich investigated in this study is composed of two aluminum skin plates and one aluminum honeycomb core. The skin plates and honeycomb core have the same material properties, Young's modulus 70 GPa, Poisson's ratio 0.33, and density 2700 kg/m³.

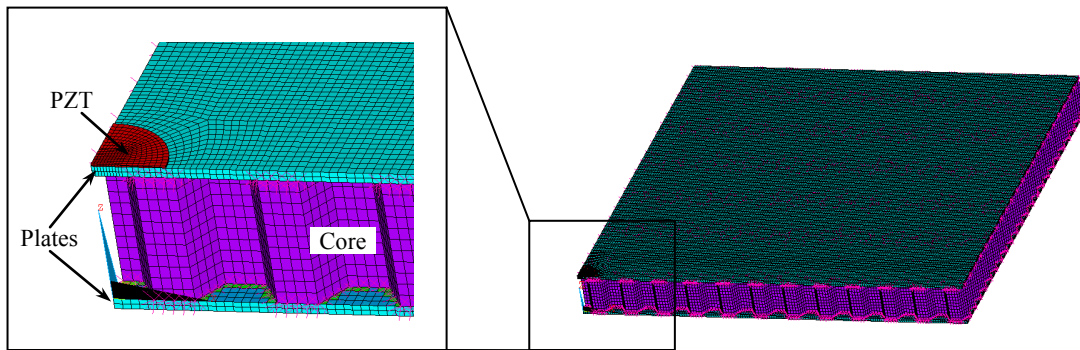


Figure 3.15 The finite element model of the honeycomb sandwich structure with a surface-bonded PZT.

Table 3.3 Geometry parameters of the finite element model. (Units: mm)

Skin panels			Honeycomb core			PZT actuator	
Length	Width	Thickness	Cell size	Wall thickness	Height	Diameter	Thickness
135	135	1	6.35	0.055	12.7	7	0.2

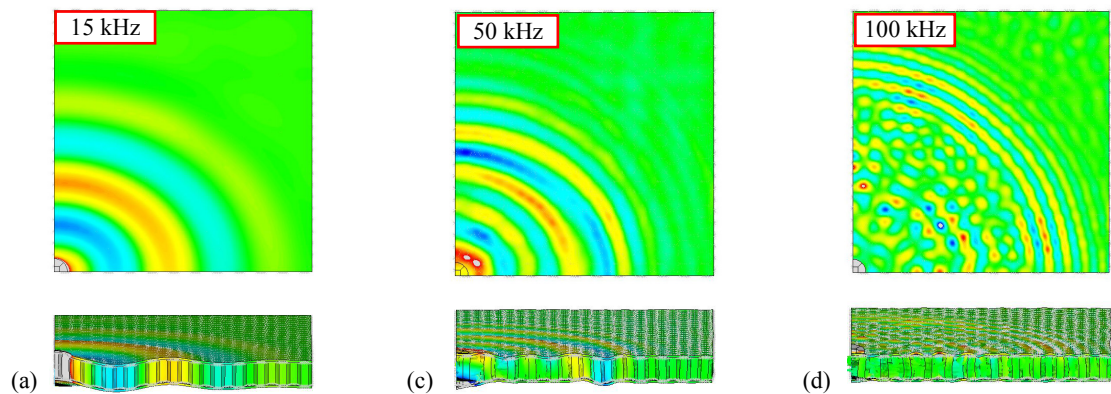


Figure 3.16 Simulation results of displacements in the z direction u_z : (a) top and front views at 15 kHz excitation, (b) top and front views at 50 kHz excitation, (c) top and front views at 100 kHz excitation.

Figure 3.15 plots the finite element model of the honeycomb sandwich with a surface bonded PZT. The geometry parameters of the model are listed in Table 3.3.3. The SOLID45 elements are used to build the two skin plates. The SHELL63 elements are used to build the honeycomb core that has hexagonal cells. The coupled field SOLID5 elements are selected to construct the finite element model of the PZT. Due to symmetry of the problem, only a quarter-volume of the honeycomb sandwich is modeled. Symmetric boundary conditions are applied on all the nodes on the two symmetric planes (O-X-Z plane and O-Y-Z plane). The PZT excitations are 3 count tone burst signals with center frequencies selected at 15kHz, 50kHz and 100kHz.

Transient analysis is used to simulate guided waves in the honeycomb sandwich. In order to accurately simulate the guided waves that propagate in the honeycomb sandwich, sizes of elements need to be small enough such that at least ten elements per wavelength along the wave propagation direction [72]. In this study, the sizes of elements are in the range 0.5 mm ~ 1.0 mm. Moreover, the integration time step should be small enough for the stability of the transient analysis [72]. In this study, the time step is 0.2 μ s.

Figure 3.16 gives the simulation results of displacements in the z direction u_z at 15 kHz, 50 kHz and 100 kHz excitation frequencies. At the low frequency 15 kHz, the simulation result in Figure 3.16 a shows that global guided waves propagate in the entire sandwich. These global guided waves have large wavelengths and elliptical wave fronts. In this case, the entire sandwich can be considered as a solid plate-like waveguide which supports the global guided waves. At 50 kHz, although the global guided waves can still be observed, their wave fronts become closer to circular shapes other than elliptical shapes. At the high frequency 100 kHz, the global guided waves disappear. There are

guided waves propagating in skin plates with circular wave fronts. Moreover, the 100 kHz simulation result shows complex wave interactions, which could be induced by the wave interaction with the honeycomb core.

CHAPTER 4

WAVEFIELD ACQUISITION AND INTRINSIC CHARACTERIZATION

Wavefields of guided waves in terms of time and space dimensions contain a wealth of information regarding guided wave propagations in structures and interactions with structural discontinuities. In this chapter, a wavefield sensing system is developed and optimized to acquire high spatial resolution guided wavefields. To extract informative wave signatures from the wavefields for wave characterization, wavefield analysis methods, including frequency-wavenumber analysis, wavefield decomposition and space-frequency-wavenumber analysis are presented.

4.1. HYBRID PZT-SLDV SENSING SYSTEM FOR WAVEFIELD ACQUISITION

The hybrid PZT-SLDV sensing system takes the advantages of PZT guided wave generation and the SLDV non-contact high spatial resolution wavefield sensing. On one hand, the low profile PZT is a commonly used guided wave actuator, which works on piezoelectric principles and converts electric energy into mechanical energy and vice versa [1]. When a PZT is bonded on a structure surface, it can couple its in-plane motion with the structure through the bonding layer and generate guided waves [1]. The PZT guided wave actuation and tuning mechanisms have been well established and proved already [1, 88, 98-101]. In this dissertation study, PZT actuators (low profile: 5~10 mm

dimension and 0.2~0.5mm thickness) made of the piezo material APC 850 or 851¹ are used.

On the other hand, the SLDV is a rapid, high spatial resolution and non-contact means for guided wave sensing and visualization [29, 30, 140]. In this study, the Polytec PSV-400-M2² scanning laser Doppler vibrometer is used. The particle displacement/velocity in the direction of the laser beam is measured based on the Doppler effect. The SLDV can direct the laser beam to various locations for measurements, by employing two moving scanning mirrors driven by galvanometric actuators. For the Polytec PSV-400-M2 used in this study, angular resolutions of the two scanning mirrors are less than 0.002°.

Figure 4.1 gives a schematic of the PZT-SLDV sensing system. The PZT actuator is surface bonded on the structure to generate guided waves. The excitation signal, such as a signal of Hanning window modulated 3-cycle sine waves, is generated by an arbitrary waveform generator and then amplified through a voltage amplifier. The SLDV is used to measure velocities or displacements of guided waves at user-defined scanning points. The SLDV acquires a waveform of guided waves (velocity or displacement as a function of time) at a scanning point and then moves to the next point to acquire the next waveform. The scan can be performed over user-defined scanning points in various configurations, such as linear distribution for 1-D scanning and rectangular grid distribution for 2-D scanning.

¹ APC851 <http://www.americanpiezo.com/apc-materials/choosing.html>

² Polytec PSV-400-M2 <http://www.polytec.com/us/products/vibration-sensors/scanning-vibrometers/>

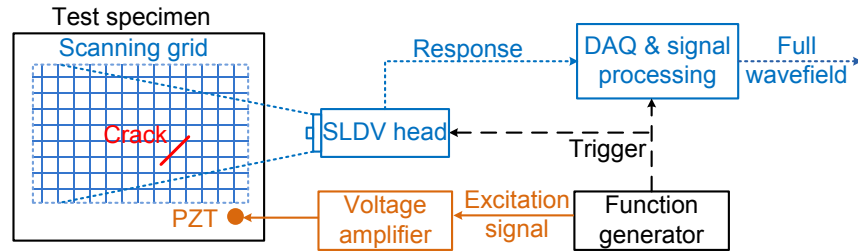


Figure 4.1 A schematic of the PZT-SLDV sensing.

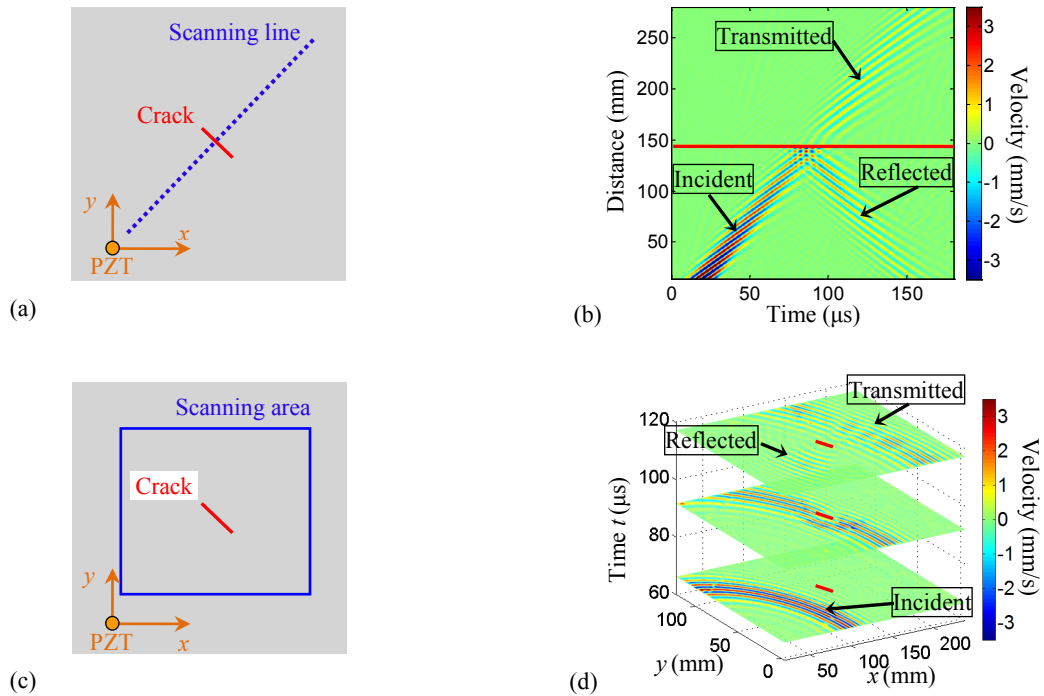


Figure 4.2 Crack detection by using the PZT-SLDV sensing: (a) and (b) are the scanning configuration and the measured time-space wavefield for the 1-D scanning; (c) and (d) are the scanning configuration and the measured time-space wavefield for the 2-D scanning.

The hybrid PZT-SLDV sensing system can be used to visualize guided wave interactions with structural discontinuities. Moreover, the sensing system provides an immediate means of damage detection. Figure 4.2 gives an example of using the hybrid PZT-SLDV sensing system for crack detection in a 1 mm thick aluminum plate. Figure 4.2 a and c gives the configurations of 1-D scanning with points along a line and 2-D scanning with points in a scanning area. The guided waves are generated from a PZT

(APC 850: 0.2 mm thickness and 7 mm diameter) bonded on the plate surface. The excitation signal is a 3-cycle tone burst with the frequency of 120 kHz and amplitude of 40 V. Figure 4.2 b and Figure 4.2 d plot the time-space wavefields measured from the 1-D scanning and the 2-D scanning. Both wavefields show three wave components: incident, reflected and transmitted waves. When incident waves arrive at the crack damage, reflected and transmitted waves occur. From the guided wavefields, the complex wave propagation and interaction are visualized. Moreover, the crack location can be qualitatively indicated from the observed wave behaviors.

Figure 4.3 gives another example of applying the hybrid PZT-SLDV sensing system for delamination detection. The test specimen is an 8-ply IM7/8552 composite plate with $[0_2/90_2]_s$ layup. Under the second ply, there is a 20 mm \times 20 mm Teflon film embedded during the manufacturing process to create delamination damage. Figure 4.3 a and c give 1-D and 2-D scanning configurations. Guided waves are generated from a PZT patch (APC 850: 0.2 mm thickness and 7 mm diameter) bonded on the plate surface. The excitation signal is a 3-cycle tone burst with the frequency of 300 kHz and amplitude of 40 V. Figure 4.3 b plots the time-space wavefield measured from the 1-D scanning, showing that guided waves interact with the delamination. Guided waves propagating back and forth between the top ($y=20$ mm) and bottom ($y=40$ mm) boundaries of the delamination, can be distinctively seen, exhibiting the “trapped wave” phenomenon [103, 141-143]. Meanwhile, the wavefield image at 15 μ s (in Figure 4.3 d) acquired by the 2-D scanning, shows wave interaction at the delamination region, as waves are propagating between delamination boundaries (denoted by the dotted box). Therefore, with the PZT-SLDV sensing, the complex wave interaction with delamination damage is visualized.

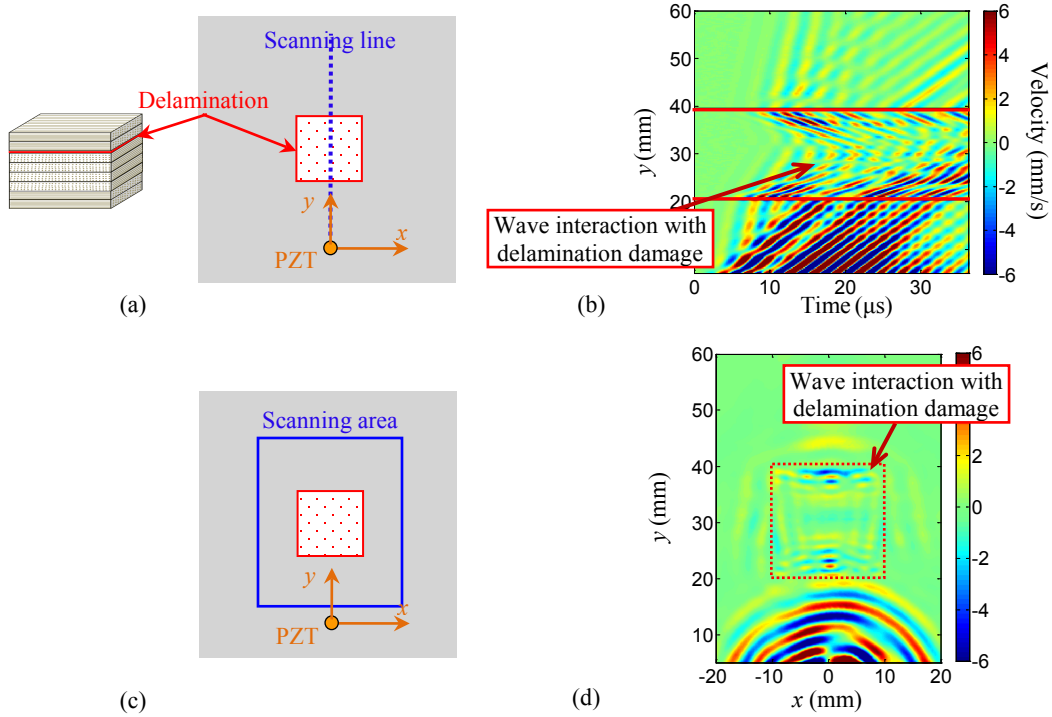


Figure 4.3 Delamination detection by using the PZT-SLDV sensing: (a) and (b) are the scanning configuration and the measured time-space wavefield for the 1-D scanning; (c) and (d) are the scanning configuration and the measured time-space wavefield for the 2-D scanning.

4.2. FREQUENCY-WAVENUMBER ANALYSIS

Although guided wavefields in time-space domain can visually show guided wave propagation and interaction, the detailed wave signatures such as wave modes, frequencies and wavenumbers are not available. To achieve these detailed wave signatures for further analysis, the guided wavefields in time-space domain can be converted to the representation in frequency-wavenumber domain by using the three dimensional (3-D) Fourier Transform (FT), given as [29, 30, 113, 140, 142, 144]

$$V(f, \mathbf{k}) = \mathcal{F}[v(t, \mathbf{x})] = \int_{-\infty}^{\infty} \int_{-\infty}^{\infty} v(t, \mathbf{x}) e^{-i(2\pi ft - \mathbf{k} \cdot \mathbf{x})} dt d\mathbf{x} \quad (4.4)$$

where the space vector \mathbf{x} and the wavenumber vector \mathbf{k} are defined as (x, y) and (k_x, k_y) . $v(t, \mathbf{x})$ is the time-space wavefield in terms of time t and space vector \mathbf{x} . $V(f, \mathbf{k})$ is the

resulting frequency-wavenumber representation or “spectrum” in terms of frequency f and wavenumber vector \mathbf{k} . As the frequency is the counter part of time, the wavenumber is the counter part of space.

With the spectrum in frequency-wavenumber domain, the frequency, wavenumber, wave mode and wave dispersion can be readily achieved and analyzed. Figure 4.4 gives an example of frequency-wavenumber analysis on guided waves generated by a PZT actuator on a 6.35 mm thick T304 steel plate. The excitation signal is a broadband pulse with 0.8 μs duration and 10 V amplitude. The measured time-space wavefield is plotted in Figure 4.4 a, which shows complex wave propagation and interaction. From the wavefield in time-space domain, it is hard to identify the wave mode, frequency, and wavenumber. However, these components can be easily achieved in frequency wavenumber domain. As plotted in Figure 4.4 b, the frequency-wavenumber spectrum reveals the frequency, wavenumber and wave mode. Within 0 to 800 kHz, in the frequency-wavenumber spectrum, six wave modes including A_0 , A_1 , A_2 , S_0 , S_1 and S_2 are discernible and identifiable. This information is otherwise unavailable in the time-space wavefield.

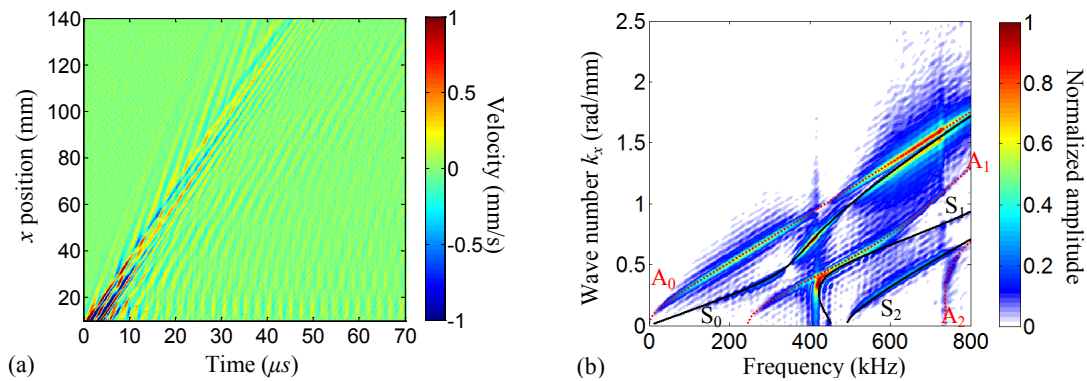


Figure 4.4 Frequency-wavenumber analysis on guided waves in a 6.35 mm thick T304 steel plate: (a) time-space wavefield, and (b) frequency-wavenumber spectrum.

4.3. GUIDED WAVEFIELD DECOMPOSITION

By using FT, time-space wavefields are transformed to frequency-wavenumber spectra, where different wave modes and wave components can be easily identified. Therefore, any wave component of interest can be extracted for further analysis, through a filtering process in the frequency-wavenumber domain. Similar to the digital filtering [145], the filtering process in frequency-wavenumber domain is mathematically expressed as the product between the original frequency-wavenumber spectrum $V(f, \mathbf{k})$ and the filter function $F(f, \mathbf{k})$ as:

$$V_F(f, \mathbf{k}) = V(f, \mathbf{k})F(f, \mathbf{k}) \quad (4.5)$$

where $V_F(f, \mathbf{k})$ is the filtered spectrum, which keeps the desired frequency-wavenumber component. By transforming the filtered spectrum $V_F(f, \mathbf{k})$ back into time-space domain through inverse 3-D FT, the filtered wavefield $v_F(t, \mathbf{x})$ can be obtained as

$$v_F(t, \mathbf{x}) = \mathcal{F}^{-1}[V_F(f, \mathbf{k})] = \frac{1}{(2\pi)^2} \int_{-\infty}^{\infty} \int_{-\infty}^{\infty} V_F(f, \mathbf{k}) e^{j(2\pi ft - \mathbf{k} \cdot \mathbf{x})} df d\mathbf{k} \quad (4.6)$$

With the frequency-wavenumber filtering, guided waves which have multiple wave modes that propagate in various directions can be decomposed into individual modes. To obtain a desired wave mode, the band pass filter is designed to keep the frequency-wavenumber component of the wave mode,

$$F(f, \mathbf{k}) = w_f(f)w_k(f, \mathbf{k}) \quad (4.7)$$

where $w_f(f)$ is a raised-cosine filter in frequency domain to extract the frequency component of the desired wave mode. $w_k(f, \mathbf{k})$ is a 3-D filter centered at the theoretical wavenumber value $k(f)$ of the desired wave mode to be extracted, as:

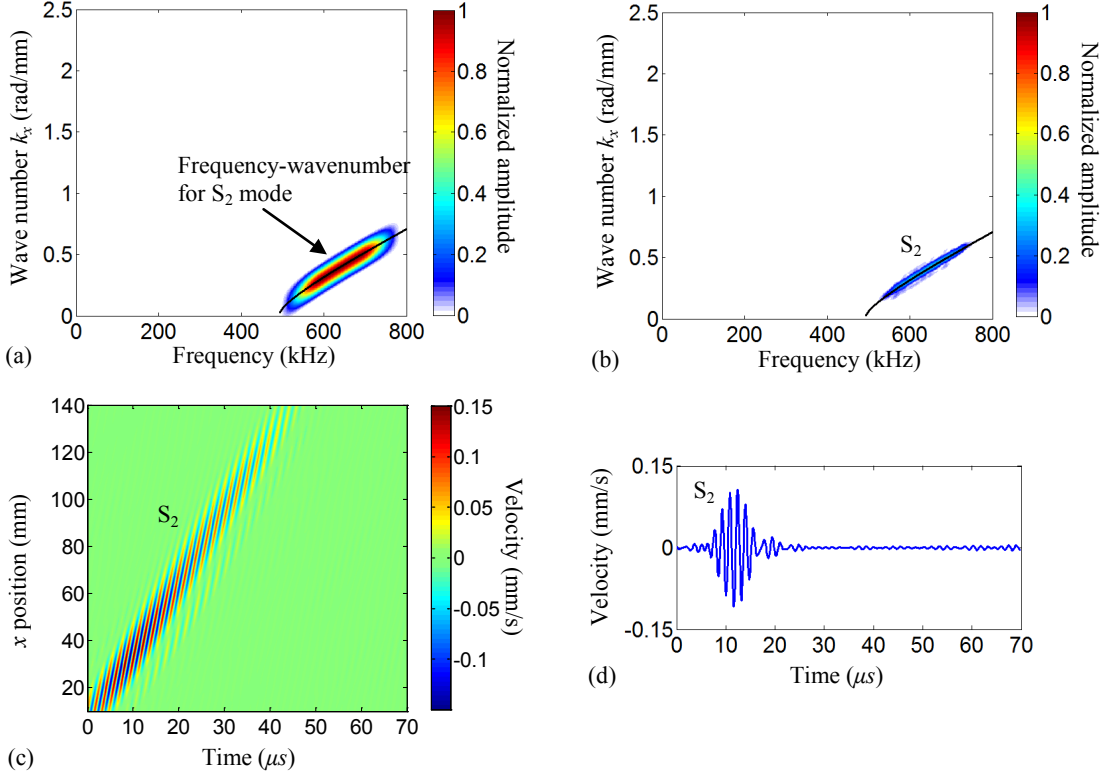


Figure 4.5 Guided wave decomposition by using frequency-wavenumber filtering: (a) frequency-wavenumber filter for the S_2 mode; (b) filtered frequency-wavenumber spectrum; (c) reconstructed time-space wavefield of the S_2 mode; (d) reconstructed waveform of the S_2 mode at $x=40$ mm.

$$w_k(f, \mathbf{k}) = \begin{cases} 0.5 \left[1 + \cos \left(2\pi \frac{D_k(f, \mathbf{k})}{D_{wk}} \right) \right] & \text{if } D_k(f, \mathbf{k}) \leq D_{wk} / 2 \\ 0 & \text{otherwise} \end{cases} \quad (4.8)$$

with

$$D_k(f, \mathbf{k}) = \left| \|\mathbf{k}\| - k(f) \right| \quad (4.9)$$

where D_{wk} is the wavenumber bandwidth.

Figure 4.5 shows an example of guided wave decomposition. The original time-space wavefield in Figure 4.4 a, contains six wave modes including A_0 , A_1 , A_2 , S_0 , S_1 and S_2 . To extract the S_2 mode, a band pass filter (Figure 4.5a) is designed, which only keeps the frequency-wavenumber component of S_2 mode and rejects everything else. Through

the filtering process in frequency-wavenumber domain, the S_2 mode within the frequency range 500~750 kHz and the wavenumber range 0~1 rad/mm is extracted (Figure 4.5b). Then the extracted frequency-wavenumber spectrum of the S_2 mode is reconstructed back into time-space domain. Figure 4.5 c and d plot the reconstructed wavefield and the waveform at $x = 40$ mm, which only contain the S_2 mode.

4.4. SPACE-FREQUENCY-WAVENUMBER ANALYSIS

The wavefield analysis in frequency-wavenumber domain can reveal wave propagation characteristics that cannot be explicitly seen in time-space domain. However, after the FT, spatial information of guided wavefields is lost. It will be beneficial if the spatial information can be retained. To retain the spatial information, the space-frequency-wavenumber analysis is used.

The space-frequency-wavenumber analysis is a straightforward extension of the short time FT [146] to multi-dimensional problems. It breaks down a time-space wavefield into small segments over the spatial dimension before the Fourier transformation. Hence, it is also called *short space* FT. The small segment is acquired by multiplying the wavefield with a window function which is non-zero for only a short period in space while constant over the entire time dimension. When the window slides along the space dimension, a set of windowed wavefield segments is generated. The FT is applied to these segments, resulting in a set of frequency-wavenumber spectra that are indexed by window locations such that the spatial information is retained. Mathematically, the *short space* FT is given as

$$S(\bar{\mathbf{x}}, f, \mathbf{k}) = \int_{-\infty}^{\infty} \int_{-\infty}^{\infty} u(t, \mathbf{x}) W^*(t, \mathbf{x} - \bar{\mathbf{x}}) e^{-j(2\pi ft - \mathbf{k} \cdot \mathbf{x})} dt d\mathbf{x} \quad (4.10)$$

where $\bar{\mathbf{x}}$ is the retained spatial vector (\bar{x}, \bar{y}) of the windowed segments. $W(t, \mathbf{x})$ is the window function that keeps constant in time and varies in space. For example, a Hanning function can be used to construct the window $W(t, \mathbf{x})$, given as:

$$W(t, \mathbf{x}) = \begin{cases} 0.5 \left[1 + \cos \left(2\pi \frac{|\mathbf{x}|}{D_x} \right) \right] & \text{if } |\mathbf{x}| \leq D_x/2 \\ 0 & \text{otherwise} \end{cases} \quad (4.11)$$

where D_x is the window length in space domain. Figure 4.6 gives an example of the window function $W(t, \mathbf{x})$. Note that in this example, only the dimensions of time t and space x are included for plotting. As shown in Figure 4.6, the window function keeps constant in the time dimension and varies in the space dimension.

Since the *short space* FT retains the spatial information, the relation between space and wavenumber can be investigated. Figure 4.7 gives an example of using the *short space* FT to analyze a guided wavefield and show how wavenumber components vary in space. The time-space wavefield in Figure 4.7 a shows a forward propagating A_0 mode. By applying a window function located at $x = 25$ mm, a small segment of the wavefield is isolated, as plotted in Figure 4.7 b with its frequency-wavenumber spectrum in Figure 4.7 c. In the short space FT process, the window slides through the wavefield from 0 to 270 mm with a step size of 0.5 mm resulting in a set of windowed wavefield segments. All the segments are then transformed to frequency-wavenumber domain and stacked up, generating a space-frequency-wavenumber representation. Figure 4.7 d presents the space-wavenumber spectrum at a selected frequency 120 kHz. The spectrum is centered about the wavenumber 0.73 rad/mm and long the entire spatial extent. When the wave propagates away from the source (increasing of x) the amplitude in the space-wavenumber spectrum drops gradually.

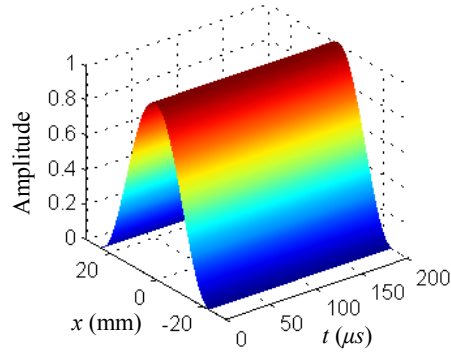


Figure 4.6 An example of the window function.

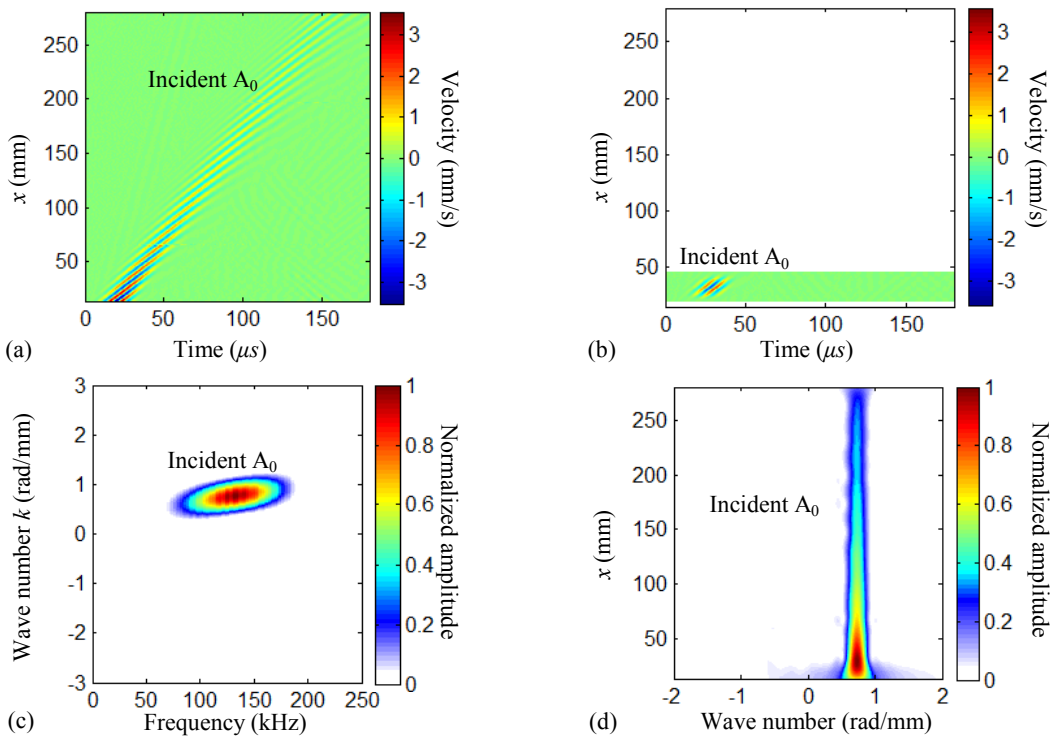


Figure 4.7 An example of the space-frequency-wavenumber analysis: (a) the original time-space wavefield; (b) windowed wavefield; (c) frequency-wavenumber spectrum of the windowed wavefield; (d) space-wavenumber spectrum at a selected frequency 120 kHz.

CHAPTER 5

QUANTITATIVE AND VISUALIZED DAMAGE DIAGNOSIS

This chapter presents quantitative and visualized damage diagnosis methods for NDE/SHM. The generic formation of phased array imaging for anisotropic composite laminates is developed, based on classic delay-and-sum principle. The phased array imaging can generate an intensity image of the composite been inspected to visualize and locate the damage in the composite. To further quantify the damage size, wavefield based imaging methods such as filter reconstruction imaging and spatial wavenumber imaging are used. The systemic combination of the phased array imaging and wavefield based imaging provides a hierarchical damage diagnosis, which can efficiently and effectively locate the damage and quantify the damage size.

5.1. GUIDED WAVE PHASED ARRAYS IMAGING

Guided wave phased arrays employs sensors physically placed in a compact format in which the relative phases of sensor signals are controlled such that guided waves are focused into a beam in a desired direction [1]. By steering the focused beam to all directions, the phased array can inspect a large area of a structure to detect damage. In NDE/SHM applications, the guided wave phased array has advantages, such as reinforced wave energy in the beam, efficient and flexible control of the beam direction, improved signal-to-noise-ratio, large area inspection through a small sensing area, and promising damage detection results [12, 17, 124].

Compared to the array beamforming in isotropic plates, the array beamforming in anisotropic composite plates are more challenging. In anisotropic composite plates, guided wave parameters such as wavenumber, phase velocity and group velocity are directionally dependent due to the directionally dependent physical properties of composite materials [11, 136, 137]. Moreover, the guided waves have energy skewness and the group velocity direction is not always parallel to the phase velocity direction. Last but not least, the wave fronts of guided waves are no longer circular shapes. These properties of guided waves in composite plates have significant influences on the phased array beamforming. The traditional beamforming technique for isotropic materials might fail in composite materials.

In this section, the guided wave beamforming in anisotropic composite plates is investigated. Based on the classic delay-and-sum principle, the formation of beamforming in anisotropic composite plates is developed, in which the directional dependent guided wave parameters are considered. This formulation is valid not only for the case that phase and group velocities have the same orientation, but also for the general case that the two velocities are in different directions. Moreover, the array characterization and optimization for beamforming in composite plates are investigated with demonstrations of 2-D rectangular grid arrays. For the proof of concept, experimental tests are performed by using rectangular grid arrays made of scanning points of a non-contact SLDV. The experimental results show that multiple defects in various directions can be successfully detected.

5.1.1. Beamforming in composite laminates

5.1.1.1. Guided waves in composite laminates

In anisotropic composite laminates, guided wave parameters such as wavenumber, phase velocity and group velocity are directionally dependent, due to the directionally dependent physical properties of composite materials [11, 136, 137]. Figure 5.1 a plots the wavenumber curve $k(\gamma)$, and shows the geometry relation between the wavenumber vector \mathbf{k} which is perpendicular to the wave front and the group velocity vector \mathbf{c}_g which is orthogonal to the wavenumber curve [11, 136, 137]. The angle of wavenumber vector \mathbf{k} is γ , referred to as wavenumber angle. The angle of group velocity vector \mathbf{c}_g is θ , referred to as group velocity angle (or energy propagation angle). The angle β between \mathbf{k} and \mathbf{c}_g is referred to as skew angle with $\beta = \gamma - \theta$. When the skew angle β is not zero, \mathbf{c}_g is not parallel to \mathbf{k} , and hence the wave energy propagation direction is not perpendicular to the wave front.

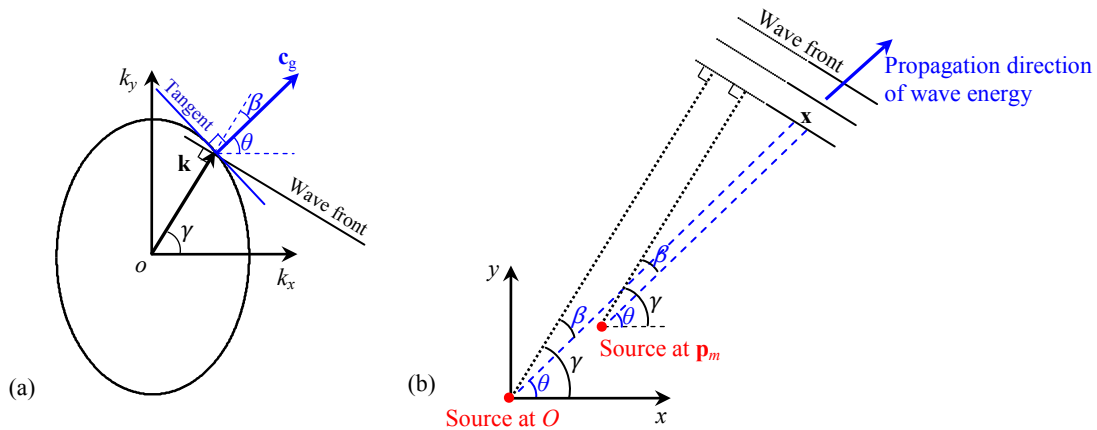


Figure 5.1 Schematics of geometric relations of guided waves in composite plates: (a) the geometric relation between the wavenumber vector \mathbf{k} and the group velocity vector \mathbf{c}_g , and (b) the geometric relation of guided waves (in the far field) generated by sources at different locations.

When a source located at the coordinate origin O generates a guided wave with frequency ω and wavenumber \mathbf{k} , the wave arriving at a location \mathbf{x} that is far away from the source (Figure 5.1 b) can be expressed as [1, 8, 11]

$$u(t, \mathbf{x}) = Ae^{j(\omega t - \mathbf{k} \cdot \mathbf{x})} \quad (5.12)$$

where A is the amplitude. With the geometric relation illustrated in Figure 5.1 b, we have

$$\mathbf{k} \cdot \mathbf{x} = |\mathbf{k}||\mathbf{x}|\cos\beta = k(\gamma)|\mathbf{x}|\cos\beta \quad (5.13)$$

And hence,

$$u(t, \mathbf{x}) = Ae^{j[\omega t - k(\gamma)|\mathbf{x}|\cos\beta]} \quad (5.14)$$

For a source located at \mathbf{p}_m , the generated wave at the location \mathbf{x} is

$$u_m(t, \mathbf{x}) = Ae^{j[\omega t - \mathbf{k} \cdot (\mathbf{x} - \mathbf{p}_m)]} = Ae^{j[\omega t - k(\gamma)|\mathbf{x} - \mathbf{p}_m|\cos\beta]} \quad (5.15)$$

5.1.1.2. Delay-and-sum beamforming

Consider an array with M identical elements located at $\{\mathbf{p}_m\}$ ($m=0, 2, 3, \dots, M-1$) which are physically close to each other. The phase center is set as the origin O of the Cartesian coordinate system, i.e., $\frac{1}{M} \sum_{m=0}^{M-1} \mathbf{p}_m = \mathbf{0}$. Each element serves as a guided wave source.

When all elements generate a guided wave with frequency ω and wavenumber vector \mathbf{k} at the same time, the total output of the array at the location \mathbf{x} can be derived as

$$z(t, \mathbf{x}) = \sum_{m=0}^{M-1} Ae^{j[\omega t - \mathbf{k} \cdot (\mathbf{x} - \mathbf{p}_m)]} = u(t, \mathbf{x}) \sum_{m=0}^{M-1} e^{j\mathbf{k} \cdot \mathbf{p}_m} \quad (5.16)$$

It is seen from Eq. (5.16) the synthetic wave is an amplification of the wave emitting from a source at the Origin and the amplification is controlled by the exponential components in Eq. (5.16), which can be maximized when the exponent become zero. The exponent becomes zero when a delay Δ_m is applied to result in:

$$e^{j(\mathbf{k} \cdot \mathbf{p}_m - \Delta_m)} = e^{j0} \quad (5.17)$$

The delay Δ_m relates to the m^{th} element position and the wavenumber vector \mathbf{k} . By judiciously selecting Δ_m , the total output $Z(t, \mathbf{x})$ of the array can be maximized at a desired direction, i.e., generating a directional “beam”. In principle, the delay Δ_m can be implemented through time delay in the time domain or phase shift in the frequency domain [1, 16, 17, 144]. In our study, the latter is adopted. In addition to delay, weighting factors w_m can also be applied to the output of individual delayed wave to improve the output. In a summary, the beamforming can be represented as

$$z(t, \mathbf{x}) = u(t, \mathbf{x}) \sum_{m=0}^{M-1} w_m e^{j(\mathbf{k} \cdot \mathbf{p}_m - \Delta_m)} \quad (5.18)$$

Assume the array output is directed toward a desired direction θ_S and the corresponding delay is denoted as $\Delta_m(\theta_S)$. We introduce the beamforming factor [1, 17], BF , which is given as

$$BF = \frac{1}{M} \sum_{m=0}^{M-1} w_m e^{j[\mathbf{k} \cdot \mathbf{p}_m - \Delta_m(\theta_S)]} \quad (5.19)$$

And Eq. (5.18) can be re-written as

$$z(t, \mathbf{x}) = M \cdot u(t, \mathbf{x}) \cdot BF \quad (5.20)$$

To maximize the BF in the desired direction θ_S , the delay $\Delta_m(\theta_S)$ should be selected to result in zero exponent i.e.,

$$\Delta_m(\theta_S) = \mathbf{k} \cdot \mathbf{p}_m \quad (5.21)$$

The wavenumber vector \mathbf{k} here depends on the wave frequency ω and wavenumber angle γ_S that corresponds to the wave energy steering angle θ_S , i.e., \mathbf{k} can be expressed as $\mathbf{k}(\omega, \gamma_S)$. Based on the geometry relation that $\gamma_S = \theta_S + \beta_S$, Eq. (5.21) can be written as

$$\Delta_m(\theta_S) = \mathbf{k}(\omega, \theta_S + \beta_S) \cdot \mathbf{p}_m \quad (5.22)$$

where β_S is referred to as the skew angle between the wavenumber angle γ_S and the wave energy steering angle θ_S . With the phase delay, it can be seen that the total output $z(t, \mathbf{x})$ is $\sum_{m=0}^{M-1} w_m$ times reinforcement of the individual wavefield $u(t, \mathbf{x})$ in the θ_S direction. The weighting factor w_m can be used to further enhance the synthetic beam shape and reduce sidelobe levels [1, 144].

By substituting Eq. (5.22) into Eq.(5.19), the beamforming factor becomes,

$$BF(\mathbf{k} | w_m, \mathbf{p}_m, M, \theta_S) = \frac{1}{M} \sum_{m=0}^{M-1} w_m e^{j[\mathbf{k}-\mathbf{k}(\omega, \theta_S + \beta_S)] \cdot \mathbf{p}_m} \quad (5.23)$$

The beamforming factor as given in Eq. (5.23) can be interpreted as a function of wavenumber vector \mathbf{k} , denoted as, $BF(\mathbf{k})$ in the wavenumber domain. w_m, \mathbf{p}_m, M and θ_S are the parameters of the wavenumber function $BF(\mathbf{k})$. For 2D wave propagation, $BF(\mathbf{k})$ evaluates the beamforming result at any wavenumber vector \mathbf{k} in the k_x - k_y wavenumber plane.

The beamforming can also be represented as a function of the wave energy propagation angle θ as,

$$BF(\theta | w_m, \mathbf{p}_m, M, \theta_S) = \frac{1}{M} \sum_{m=0}^{M-1} w_m e^{j[\mathbf{k}(\omega, \theta + \beta) - \mathbf{k}(\omega, \theta_S + \beta_S)] \cdot \mathbf{p}_m} \quad (5.24)$$

where $\mathbf{k}(\omega, \theta + \beta)$ is the wavenumber dispersion relation of guided waves in composite laminates. The $BF(\theta)$ evaluates the beamforming output *w.r.t.* the wave energy propagation angle θ for the guided waves with the wavenumber dispersion relation $\mathbf{k}(\omega, \theta + \beta)$. Hence it can directly indicate the phased array's directional beamforming pattern.

5.1.2. Implementation and characterization of rectangular arrays

Phased arrays can be configured with various arrangements, such as linear arrays[12], rectangular arrays[17], and spiral arrays[19]. In this work, rectangular arrays with array elements being uniformly arranged on rectangular grids are investigated. Figure 5.2 illustrates a $P \times Q$ rectangular array (total of $M = P \times Q$ elements) with its phase center coinciding with the coordinate origin O . The coordinates of the $(p, q)^{\text{th}}$ ($p = 0, 1, 2, \dots, P-1$ and $q = 0, 1, 2, \dots, Q-1$) element of the array are

$$\mathbf{p}_{p,q} = \left(\left(p - \frac{P-1}{2} \right) d_x, \left(q - \frac{Q-1}{2} \right) d_y \right) \quad (5.25)$$

where d_x and d_y are array spacings in x and y directions. The array spans in x and y directions are

$$D_x = (P-1)d_x \text{ and } D_y = (Q-1)d_y \quad (5.26)$$

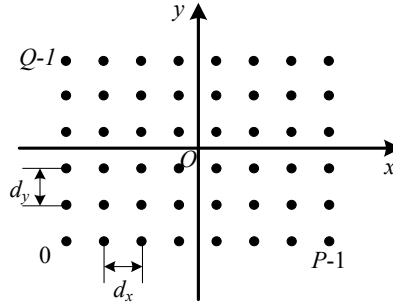


Figure 5.2 Schematic of a $P \times Q$ rectangular array

For the beamforming study in composite material, an 8-ply $[0/45/90/-45]_s$ layup CFRP composite plate with 2.54 mm thickness (material properties in Table 5.5.1) is used. The A_0 Lamb mode at 120 kHz (wavenumber curve $k(\gamma)$ is plotted in Figure 5.3) is used for the beamforming, with the maximum wavenumber components in k_x and k_y directions being $k_{x,\max} = 0.55$ rad/mm and $k_{y,\max} = 0.68$ rad/mm, resulting in the minimum wavelengths $\lambda_{x,\min} = 2\pi/k_{x,\max} = 11.4$ mm and $\lambda_{y,\min} = 2\pi/k_{y,\max} = 9.2$ mm. To study the

beamforming, three array configurations listed in Table 5.5.2 are considered. Note (a) arrays (1) and (2) have the same spacings, while the spans in array (2) are twice of those in array (1); (b) Arrays (2) and (3) have the same spans, while the spacings in array (3) are twice of those in array (2). In the following subsections, both beamforming factor $BF(\mathbf{k})$ in Eq. (5.23) and beam pattern $BF(\theta)$ in Eq. (5.24) will be used to evaluate the beamforming of each array.

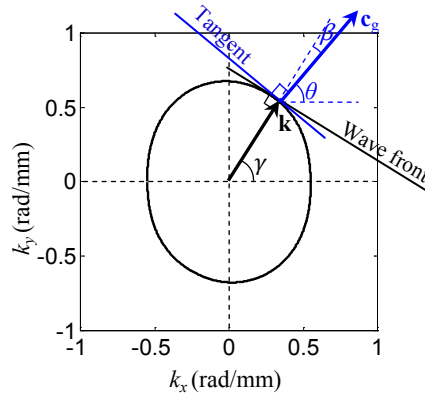


Figure 5.3 Wavenumber curve $k(\gamma)$ of the 90 kHz A_0 mode in the $[0/45/90/-45]_s$ CFRP composite laminate.

Table 5.1 Material properties of a single ply.

ρ (kg/m ³)	E_1 (GPa)	E_2 (GPa)	E_3 (GPa)	G_{12} (GPa)	G_{13} (GPa)	G_{23} (GPa)	ν_{12}	ν_{13}	ν_{23}	Thickness (mm)
1577.8	129.6	8.7	8.7	4.8	4.8	2.9	0.30	0.30	0.34	0.3175

Table 5.2 Configurations of three rectangular arrays for beamforming study

	Number of elements $P \times Q$	Spacing d (mm)	Span D (mm)
Array (1)	11×11	$d_{x,1} = d_{y,1} = \lambda_{y,\min}/4 = 2.3$	$D_{x,1} = D_{y,1} = 23$
Array (2)	21×21	$d_{x,2} = d_{y,2} = \lambda_{y,\min}/4 = 2.3$	$D_{x,2} = D_{y,2} = 46$
Array (3)	11×11	$d_{x,3} = d_{y,3} = \lambda_{y,\min}/2 = 4.6$	$D_{x,3} = D_{y,3} = 46a$

5.1.2.1. $BF(\mathbf{k})$ characterization

The array performance is studied by the beamforming factor $BF(\mathbf{k})$ in Eq.(5.23). By substituting the array coordinates in Eq. (5.25) into Eq. (5.23), we can derive the $BF(\mathbf{k})$ equation for rectangular arrays,

$$BF(\mathbf{k} | w_{p,q}, d_x, d_y, P, Q, \theta_S) = \frac{1}{PQ} \sum_{p=0}^{P-1} \sum_{q=0}^{Q-1} w_{p,q} e^{j[\mathbf{k}-\mathbf{k}(\omega, \theta_S + \beta_S)] \left[\left(p - \frac{P-1}{2} \right) d_x, \left(q - \frac{Q-1}{2} \right) d_y \right]} \quad (5.27)$$

By substituting the array spans in Eq.(5.26) into Eq.(5.27), the $BF(\mathbf{k})$ becomes

$$BF(\mathbf{k} | w_{p,q}, d_x, d_y, D_x, D_y, \theta_S) = \frac{1}{\left(\frac{D_x}{d_x} + 1 \right) \left(\frac{D_y}{d_y} + 1 \right)} \sum_{p=0}^{\frac{D_x}{d_x}} \sum_{q=0}^{\frac{D_y}{d_y}} w_{p,q} e^{j[\mathbf{k}-\mathbf{k}(\omega, \theta_S + \beta_S)] \left[p d_x - \frac{D_x}{2}, q d_y - \frac{D_y}{2} \right]} \quad (5.28)$$

This equation shows the beamforming factor $BF(\mathbf{k})$ is a function of \mathbf{k} defined up to the parameters $w_{p,q}, d_x, d_y, D_x, D_y$ and θ_S .

Figure 5.4 a graphically plots the $BF(\mathbf{k})$ of array (1) as an intensity image in the k_x - k_y wavenumber plane, when phase delays are not applied. Four intensified spots at $(0, 0)$, $(0, 4k_{y,\max})$, $(4k_{y,\max}, 0)$ and $(4k_{y,\max}, 4k_{y,\max})$ are present in the given region. The sizes of intensified spots are evaluated by using the full widths of the intensified spots at one-half peak value (denoted as $FWHM_x$ and $FWHM_y$ for k_x and k_y directions) [144], which are listed in Table 5.5.3. The intensified spots represent local maxima of $BF(\mathbf{k})$. When the array generates guided waves of wavenumbers at these local maxima, the array's output will be optimized. Note that Figure 5.4a only plots the $BF(\mathbf{k})$ in the wavenumber range - $1.0 \text{ rad/mm} \leq k_x \leq 3.7 \text{ rad/mm}$ and $-1.0 \text{ rad/mm} \leq k_y \leq 3.7 \text{ rad/mm}$. Indeed the intensified spots present in a periodical pattern within the entire wavenumber domain. The periodical pattern can be perceived from the expression of the beamforming factor $BF(\mathbf{k})$ in

Eq.(5.28). The periods K_x and K_y of the periodical pattern in k_x and k_y directions are listed in Table 5.5.3.

The wavenumber curve $k(\gamma)$ of the 120 kHz A_0 mode in the subject composite plate is also plotted in Figure 5.4a. It can be seen that no maximum of $BF(\mathbf{k})$ falls on the wavenumber curve. This signifies that if the array generates the 120 kHz A_0 mode without delaying, the array will not have maximized output. Hence, array's output can be maximized by applying phase delays given in Eq. (5.22), i.e., applying phase delays that relocate a maximum of $BF(\mathbf{k})$ on the wavenumber curve. Figure 5.4b plots the $BF(\mathbf{k})$ of the array (1) with the phase delays $(-0.02, 0.68) \cdot \mathbf{p}_{p,q}$. The delay is selected such that the local maxima located at $(0, 0)$ before the delay is now moved to $(-0.02, 0.68)$ rad/mm on the wavenumber curve.

Figure 5.5 a and b plot the $BF(\mathbf{k})$ images of arrays (2) and (3), when the phase delays $(-0.02, 0.68) \cdot \mathbf{p}_{p,q}$ are applied. Their $FWHM$ values are listed in Table 5.5.3, in addition to those of array (1). $FWHM$ values of arrays (2) and (3) (with the same spans $D_{x,2} = D_{y,2} = D_{x,3} = D_{y,3} = 46$ mm) are the same and smaller than those of array (1) (with smaller spans $D_{x,1} = D_{y,1} = 23$ mm). This means larger array spans give smaller size intensified spots and better wavenumber resolutions.

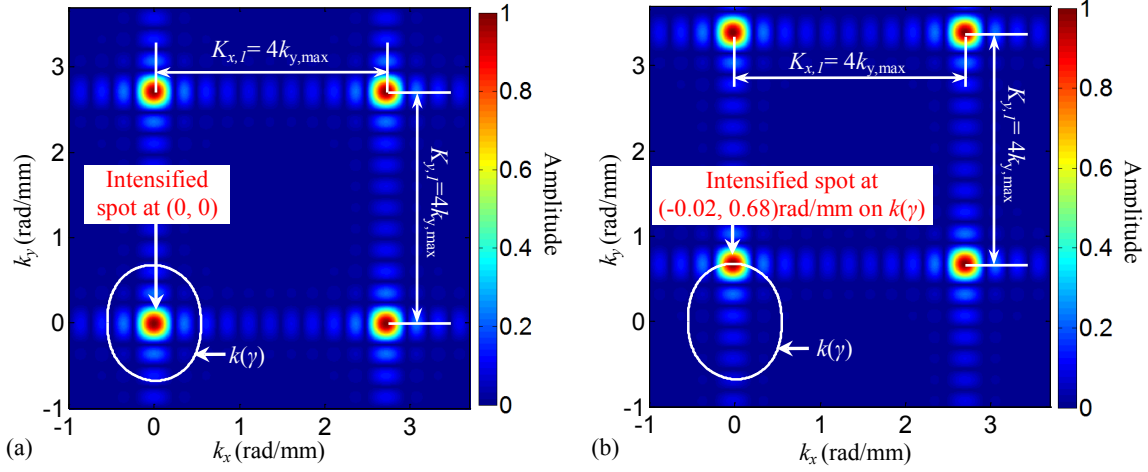


Figure 5.4 $BF(\mathbf{k})$ images for the array (1): (a) without phase delay, and (b) with the phase delay $(0, k_{y,\max}) \cdot \mathbf{p}_{p,q}$. The solid white curve is the wavenumber curve $k(\gamma)$ of the 120 kHz A_0 mode in the $[0/45/90/-45]_s$ CFRP composite plate.

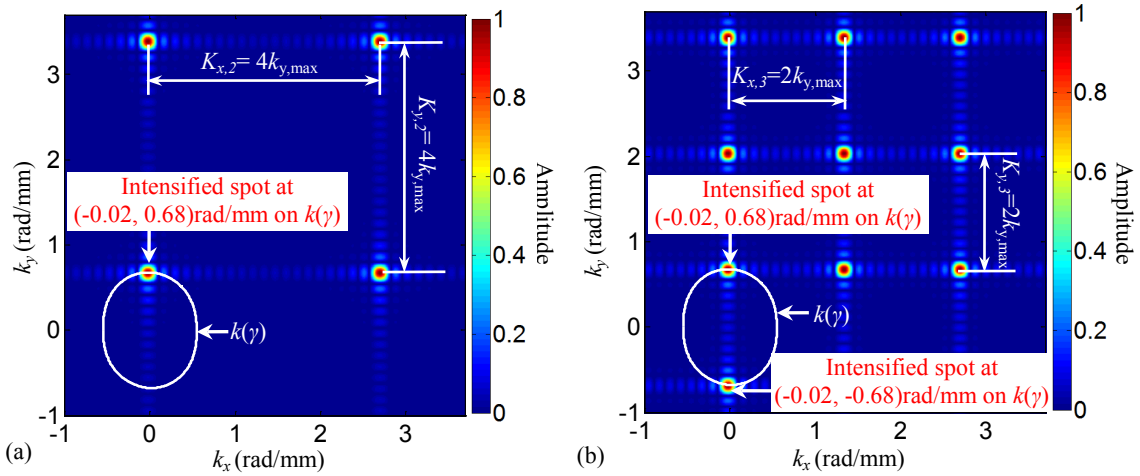


Figure 5.5 $BF(\mathbf{k})$ images when the phase delays $(-0.02, 0.68) \cdot \mathbf{p}_{p,q}$ is applied: (a) for array (2), and (b) for array (3). The solid white curve is the wavenumber curve $k(\gamma)$ of the 120 kHz A_0 mode in the $[0/45/90/-45]_s$ CFRP composite plate.

Table 5.3 $BF(\mathbf{k})$ characteristics of the three rectangular arrays

	Wavenumber periods, K (rad/mm)	Full widths of intensified spots at the one-half peak value, $FWHM$ (rad/mm)
Array (1)	$K_{x,l} = K_{y,l} = 2\pi/d_{x,l} = 2\pi/d_{y,l} = 4k_{y,\min} = 2.72$	$FWHM_{x,l} = FWHM_{y,l} = 0.30$
Array (2)	$K_{x,2} = K_{y,2} = 2\pi/d_{x,2} = 2\pi/d_{y,2} = 4k_{y,\min} = 2.72$	$FWHM_{x,2} = FWHM_{y,2} = 0.15$
Array (3)	$K_{x,3} = K_{y,3} = 2\pi/d_{x,3} = 2\pi/d_{y,3} = 2k_{y,\min} = 1.36$	$FWHM_{x,3} = FWHM_{y,3} = 0.15$

The wavenumber periods of arrays (1), (2) and (3) are also compared in Table 5.5.3. Wavenumber periods of arrays (1) and (2) (with the same array spacings $d_{x,1} = d_{y,1} = d_{x,2} = d_{y,2} = 2.3$ mm) are the same and larger than those of array (3) (with larger array spacings $d_{x,3} = d_{y,3} = 4.6$ mm). This means smaller array spacings generate larger wavenumber periods. The wavenumber periods can affect the beamforming performance. For illustration, for the array (3) which has the array spacings $d_{x,3} = d_{y,3} = 4.6$ mm, the $BF(\mathbf{k})$ image in Figure 5.5b shows there are two intensified spots at $(-0.02, 0.68)$ rad/mm and $(-0.02, -0.68)$ rad/mm on the wavenumber curve $k(\gamma)$ of the 120 kHz A_0 mode. This means if the array (3) generates the 120 kHz A_0 mode with the phase delays $(-0.02, 0.68) \cdot \mathbf{p}_{p,q}$, the synthetic waves generated from the array will have two intensified components: (i) waves with the wavenumber $(-0.02, 0.68)$ rad/mm, and (ii) waves with the wavenumber $(-0.02, -0.68)$ rad/mm. The component (ii) is not desired and should be avoided, since it gives misleading beamforming result. In order to avoid the undesired component, the wavenumber periods should satisfy $K_x > 2k_{x,\max}$ and $K_y > 2k_{y,\max}$, i.e., the array spacings should satisfy $d_x < \lambda_{x,\min}/2$ and $d_y < \lambda_{y,\min}/2$.

5.1.2.2. $BF(\theta)$ characterization

The beamforming can also be studied by the directional beam pattern $BF(\theta)$ given in Eq.(5.24). By substituting the array coordinates in Eq.(5.25) into Eq. (5.24), we can derive the $BF(\theta)$ equation for rectangular arrays,

$$BF(\theta | w_{p,q}, d_x, d_y, P, Q, \theta_s) = \frac{1}{PQ} \sum_{p=0}^{P-1} \sum_{q=0}^{Q-1} w_{p,q} e^{j[\mathbf{k}(\omega, \theta + \beta) - \mathbf{k}(\omega, \theta_s + \beta_s)] \left[\left(p - \frac{P-1}{2} \right) d_x, \left(q - \frac{Q-1}{2} \right) d_y \right]} \quad (5.29)$$

By substituting the array spans in Eq.(5.26) into Eq.(5.29), the $BF(\theta)$ becomes,

$$BF(\theta | w_{p,q}, d_x, d_y, D_x, D_y, \theta_s) = \frac{1}{\left(\frac{D_x}{d_x} + 1\right)\left(\frac{D_y}{d_y} + 1\right)} \sum_{p=0}^{\frac{D_x}{d_x}} \sum_{q=0}^{\frac{D_y}{d_y}} w_{p,q} e^{j[\mathbf{k}(\omega, \theta + \beta) - \mathbf{k}(\omega, \theta_s + \beta_s)] \cdot \left(p d_x - \frac{D_x}{2}, q d_y - \frac{D_y}{2}\right)} \quad (5.30)$$

This equation shows the beam pattern $BF(\theta)$ is a function of θ defined up to the parameters $w_{p,q}, d_x, d_y, D_x, D_y$ and θ_s .

Figure 5.6a plots the directional beam pattern $BF(\theta)$ of array (1) using the 120 kHz A_0 mode without phase delays. The amplitude is seen low at all directions. In order to steer and maximize $BF(\theta)$ to a desired direction θ_s , phase delays determined from Eq. (5.22) are applied. Figure 5.6 b plots beamsteering results toward $0^\circ, 45^\circ, 90^\circ$ and 135° directions, by applying delays at $(0.55, -0.02) \cdot \mathbf{p}_{p,q}$, $(0.37, 0.51) \cdot \mathbf{p}_{p,q}$, $(-0.02, 0.68) \cdot \mathbf{p}_{p,q}$ and $(-0.37, 0.54) \cdot \mathbf{p}_{p,q}$, respectively.

To evaluate the beamforming quality, the full width of the mainlobe at one-half peak value ($FWHM$) (as illustrated in Figure 5.6 b) is used [144]. The smaller $FWHM$ will give better directional resolution of beamforming. The $FWHM$ results of array (1) are listed in Table 5.5.4. By comparing the $FWHM$ results of the four steering angles, it is found that the $FWHM$ of 0° has the smallest value. Hence, the beamforming toward 0° has the best resolution.

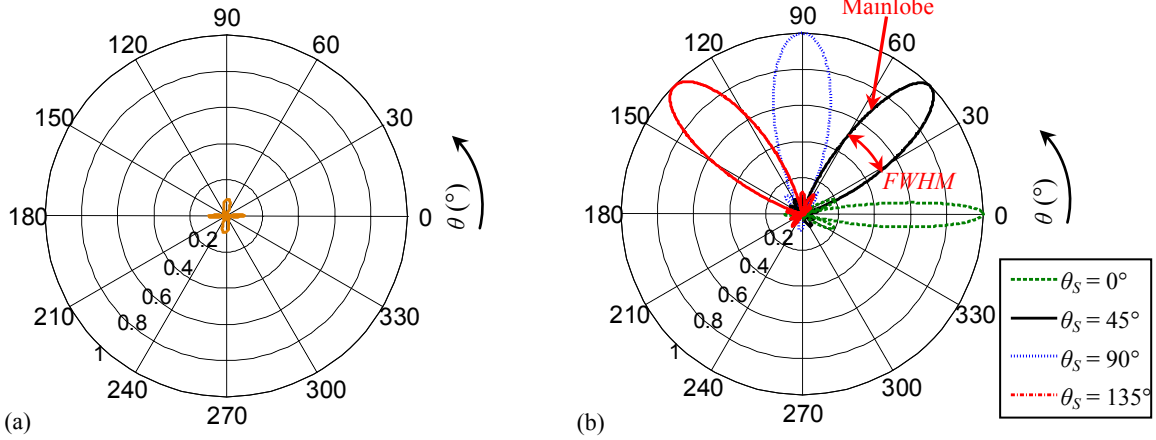


Figure 5.6 $BF(\theta)$ plots for array (1): (a) without beamsteering, and (b) with beamsteering in $\theta_s = 0^\circ, 45^\circ, 90^\circ$ and 135° .

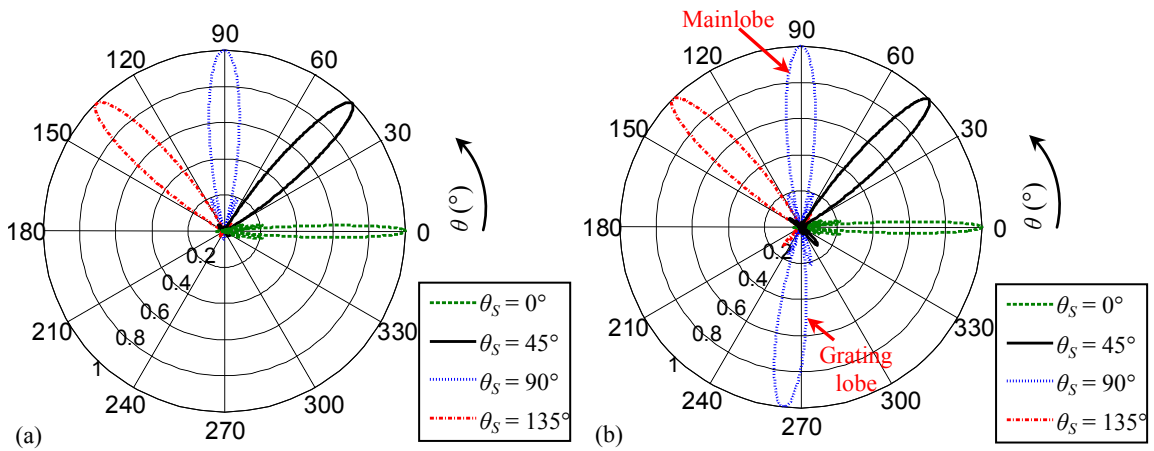


Figure 5.7 $BF(\theta)$ plots when the beamsteering directions are $\theta_s = 0^\circ, 45^\circ, 90^\circ$ and 135° : (a) for array (2), and (b) for array (3).

Table 5.4 Full width of the mainlobe at one-half peak value

	$\theta_s = 0^\circ$	$\theta_s = 45^\circ$	$\theta_s = 90^\circ$	$\theta_s = 135^\circ$
Array (1)	14°	31°	35°	35°
Array (2)	7°	16°	18°	18°
Array (3)	7°	16°	18°	18°

Figure 5.7 a and Figure 5.7 b plot the directional beam patterns of arrays (2) and (3), when the beamsteering directions are 0° , 45° , 90° and 135° . For 0° , 45° and 135° beamsteering directions, the beam patterns of array (2) are nearly the same as those of array (3). However, for the 90° beamsteering direction, the beam pattern of array (3) in Figure 5.7 b (dotted line) shows an additional lobe at 265° with nearly the same amplitude as the mainlobe. This additional lobe in 265° is called grating lobe caused by spatial aliasing [1, 144]. The grating lobe is not desired and should be avoided, since it gives misleading beamforming result. In addition, the presence of grating lobe can also be seen from the $BF(\mathbf{k})$ image in Figure 5.5 b, which shows two intensified spots on the wavenumber curve $k(\gamma)$, one at $(-0.02, 0.68)$ rad/mm and the other at $(-0.02, -0.68)$ rad/mm.

The *FWHM* results of arrays (1), (2) and (3) are compared in Table 5.5.4. *FWHM* values of arrays (2) and (3) are the same and both smaller than those of array (1). This means array (2) and (3) gives better angular resolution than array (1). The better angular resolution found here is inconsistent with the better wavenumber resolution, which is found in the comparison among $BF(\mathbf{k})$ images of arrays (1), (2) and (3).

5.1.3. SLDV guided wave phased array

In this subsection, beamforming algorithms are implemented using rectangular grid arrays made of scanning points of a non-contact SLDV. For the proof of concept, experimental tests are performed on a CFRP composite laminate with four surface bonded quartz rods as defects. By using the SLDV phased array, the four defects are successfully detected.

5.1.3.1. SLDV phased array setup

Figure 5.8 a and c show a photo and a schematic of the experimental setup for the SLDV phased array sensing. The test specimen is an 8-ply $[0/45/90/-45]_s$ layup CFRP composite plate with 2.54 mm thickness (material properties in Table 5.5.1). Four defects are simulated by four quartz rods (Q_1, Q_2, Q_3 and Q_4) bonded on the front side of the plate, which are the same distance 100 mm away from the plate center and in different angles $0^\circ, 45^\circ, 90^\circ$ and 135° , as shown in Figure 5.8 b. A PZT wafer (APC 851: 7 mm diameter, 0.2 mm thickness) is bonded on the plate to generate guided waves. The center of the PZT is set as the coordinate origin. A 3-cycle toneburst with the frequency 90 kHz is generated from the function generator (model: Agilent 33522B), amplified to 30V by a voltage amplifier (model: Krohn-Hite 1506), and applied to the PZT wafer for excitation. A SLDV (model: Polytec PSV-400-M2) is used to acquire the velocity wavefield of guided waves over the scanning area on the back side of the plate, a 45 mm \times 45 mm square with the center at the coordinate origin. The horizontal and vertical spatial resolutions of the scanning are 0.1 mm. Based on Doppler Effect, the SLDV can measure the velocity wavefield $v(t, \mathbf{x})$ (as a function of both time t and space \mathbf{x}) of guided waves over the scanning area. The laser beam is set perpendicular to the plate such that the out-of-plane motion of guided waves is measured. The phased array is then constructed using selected SLDV scanning points at $\{\mathbf{p}_m\}$ ($m=0, 1, 2, \dots, M-1$), whose phase center satisfies

$$\frac{1}{M} \sum_{m=0}^{M-1} \mathbf{p}_m = \mathbf{0}.$$

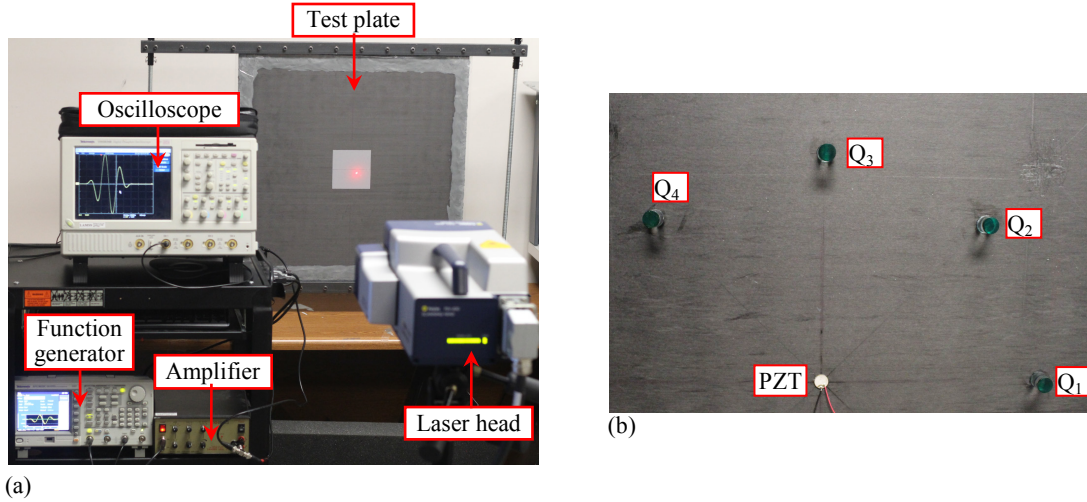


Figure 5.8 Experimental setup for multi-defects detection on a CFRP composite laminate: (a) photo of test setup, (b) front side of the test specimen, and (c) schematic of the sensing layout.

5.1.3.2. Array beamsteering and imaging

From the time-space wavefield $v(t, \mathbf{x})$ acquired by the SLDV, the time signal of the m^{th} array point at location \mathbf{p}_m can be found as $v_m(t) = v(t, \mathbf{p}_m)$. Its frequency spectrum can be derived through the Fourier transform, as

$$V_m(\omega) = \mathcal{F}[v_m(t)] = \int_{-\infty}^{\infty} v_m(t) e^{-j\omega t} dt \quad (5.31)$$

By using the frequency spectrum $V_m(\omega)$, we can derive a synthetic frequency-space representation $Z(\omega, \mathbf{x})$,

$$Z(\omega, \mathbf{x}) = \sum_{m=0}^{M-1} w_m V_m(\omega) e^{j[-\varphi(\omega, \mathbf{x}) - \Delta_m(\omega, \mathbf{x})]} \quad (5.32)$$

where

$$\Delta_m(\omega, \mathbf{x}) = \mathbf{k}(\omega, \gamma) \cdot \mathbf{p}_m, \text{ and } \varphi(\omega, \mathbf{x}) = -2\mathbf{k}(\omega, \gamma) \cdot \mathbf{x} \quad (5.33)$$

$\Delta_m(\omega, \mathbf{x})$ is the phase delay applied to the m^{th} array point for beamsteering. $\varphi(\omega, \mathbf{x})$ represents the spatial phase shift. Since the guided waves received from the array undergone spatial phase shift $\varphi(\omega, \mathbf{x})$ as the guided waves travelled from the PZT to the damage and then back to the array, $-\varphi(\omega, \mathbf{x})$ is apply to Eq. (5.32) in order to compensate the spatial phase shift $\varphi(\omega, \mathbf{x})$. In Eq. (5.33), $\mathbf{k}(\omega, \gamma)$ is the wavenumber vector at the frequency ω and wavenumber angle γ , which is obtained from wavenumber dispersion curve. The wavenumber angle γ is determined from the geometry relation $\gamma = \theta + \beta$, where θ is the energy propagation angle and equals to the angle of vector \mathbf{x} , i.e., $\theta = \angle \mathbf{x}$, and β is the skew angle corresponding to the energy propagation angle θ .

Using inverse Fourier transform, the synthetic frequency-space representation $Z(\omega, \mathbf{x})$ can be transformed to the time-space domain, as

$$z(t, \mathbf{x}) = \mathcal{F}^{-1}[Z(\omega, \mathbf{x})] = \frac{1}{2\pi} \int_{-\infty}^{\infty} Z(\omega, \mathbf{x}) e^{j\omega t} d\omega \quad (5.34)$$

where $z(t, \mathbf{x})$ represents the synthetic time-space wavefield with beamsteering. In order to generate an image of the plate being inspected by the phased array, using the synthetic time-space wavefield $z(t, \mathbf{x})$, the pixel value at location \mathbf{x} is defined as:

$$I(\mathbf{x}) = |z(t = 0, \mathbf{x})| \quad (5.35)$$

5.1.3.3. Experimental results

5.1.3.3.1. SLDV measurements

Figure 5.9 gives the SLDV measurements, when the four quartz rods have the same diameter 8 mm and height 10 mm, i.e., four defects with the same size 8 mm. At 30 μs , the wavefield in Figure 5.9 a shows incident waves with non-circular wavefronts generated from the PZT wafer. At 145 μs , the wavefield in Figure 5.9 b shows guided waves reflected by the four defects. Figure 5.9 c and d plot wavenumber spectra achieved by frequency-wavenumber analysis on wavefields of incident and reflected waves[29, 140, 142]. Both spectra show components on the wavenumber curve of A_0 mode, indicating that the incident and reflected waves are A_0 mode.

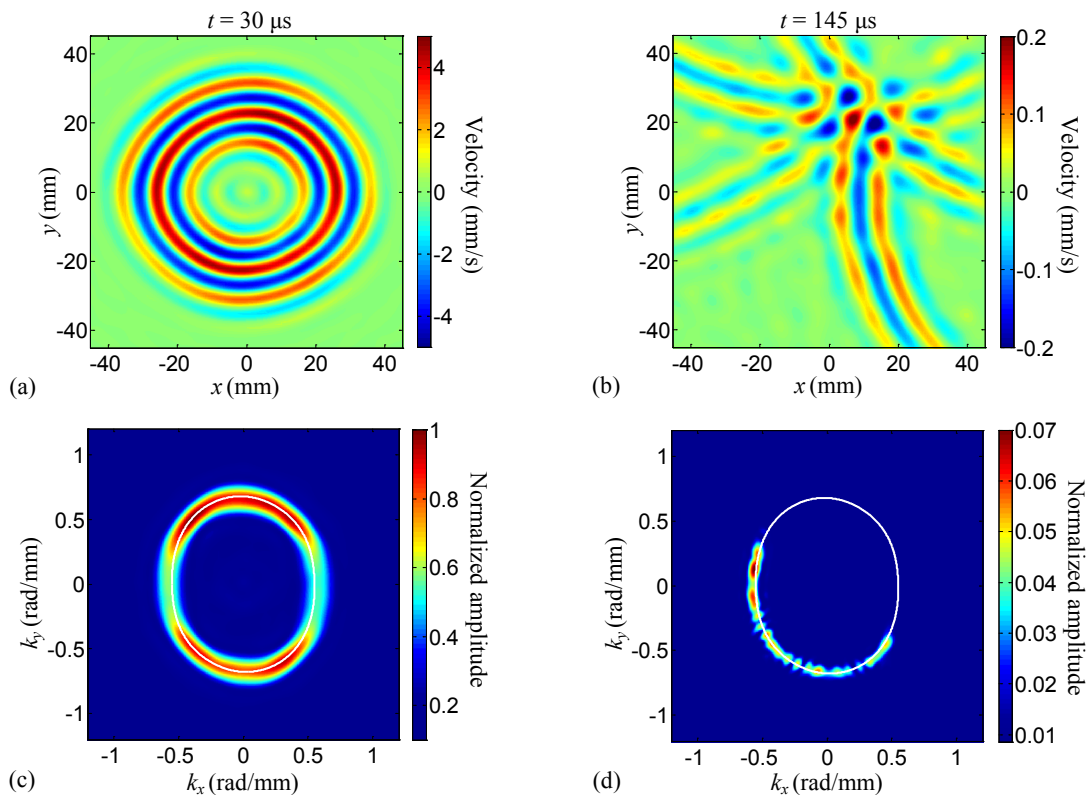


Figure 5.9 SLDV measurements: (a) and (b) are wavefields at 30 μs and 145 μs , showing the incident and reflected waves; (c) and (d) are wavenumber spectra of incident and reflected waves at 120 kHz. The solid white line is the wavenumber curve of the A_0 mode at 120 kHz.

5.1.3.3.2. Array imaging results

21×21 SLDV scanning points are chosen to construct the array (2) whose configuration is listed in Table 5.5.2. By using the beamsteering method, a synthetic time-space wavefield $z(t, \mathbf{x})$ is constructed. The wavefield images at $t = 80 \mu\text{s}$, $40 \mu\text{s}$ and $0 \mu\text{s}$ (Figure 5.10 a, b and c) show four beamformed waves in 0° , 45° , 90° and 135° directions. With the decrease of time, the beamformed waves are gradually getting closer to the four defects. At $0 \mu\text{s}$, the waves are at the four defects. An intensity image of the plate is constructed using the synthetic wavefield $z(t=0, \mathbf{x})$ and Eq. (5.35). Figure 5.10 d plots the array imaging result, clearly showing four intensified areas which indicate the four defects.

Figure 5.11 a and b give the imaging results of arrays (1) and (3) whose array configurations are listed in Table 5.5.2. By comparing the imaging results of arrays (1), (2) and (3) in Figure 5.11 a, 10 d and 11 b, it can be found that arrays (2) and (3) give four intensified areas (indicating the four defects) with smaller sizes than array (1). It means the imaging results of arrays (2) and (3) have better resolution than array (1). This is in consistent with the $BF(\theta)$ comparison in Figure 5.7, which shows that $BF(\theta)$ plots of arrays (2) and (3) have smaller $FWHM$ and better angular resolution than the array (1).

Although arrays (2) and (3) nearly give the same imaging results at the four defects, the imaging result of array (3) shows an additional intensified area around the location $(-10, -100)$ mm. This additional area is induced by the spatial aliasing, and in consistent with the $BF(\theta)$ plot of the array (3) (in Figure 5.7 b) which shows a grating lobe at 265° direction.

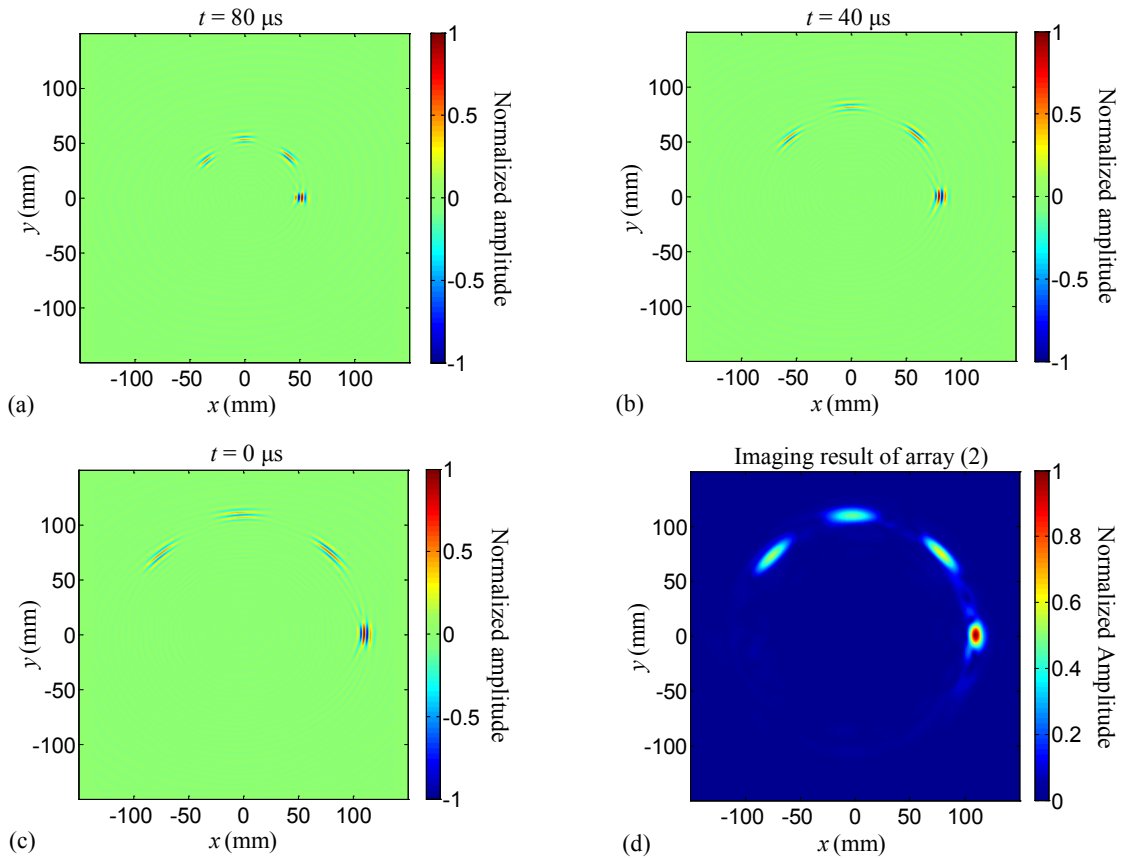


Figure 5.10 Beamforming and imaging of array (2): (a), (b) and (c) are synthetic wavefields $z(t, \mathbf{x})$ at $80 \mu\text{s}$, $40 \mu\text{s}$ and $0 \mu\text{s}$, (d) is the imaging result.

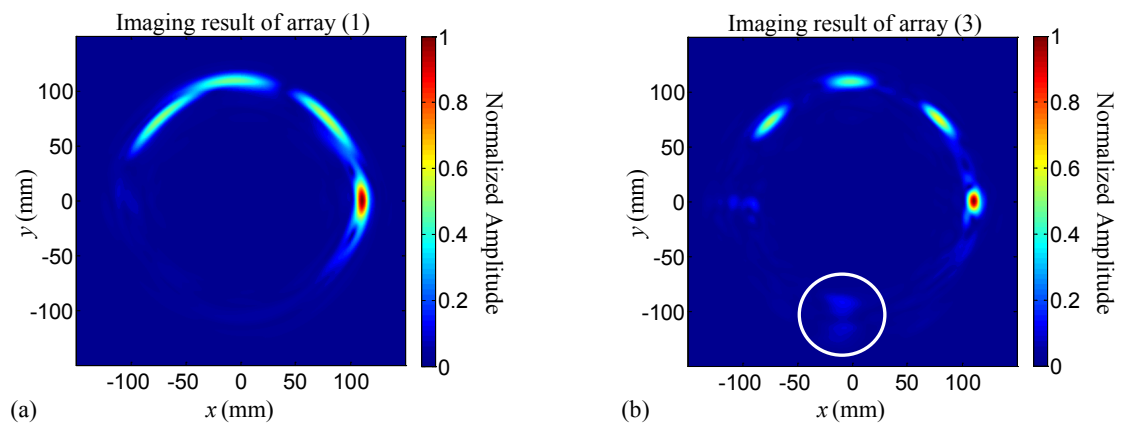


Figure 5.11 Array imaging results: (a) for array (1), and (b) for array (3).

5.2. FILTER RECONSTRUCTION IMAGING

The filter reconstruction imaging is based on the frequency-wavenumber filtering process (presented in Chapter 4) by extracting damage induced frequency-wavenumber components and reconstructing them to the time-space wavefield $v_F(t, \mathbf{x})$ which only contains damage induced waves. Then, the cumulative wave energy of the damage induced waves can be derived [103, 147] for the purpose of damage detection and imaging, as:

$$E_F(\mathbf{x}, t) = \int_0^t \frac{1}{2} v_F^2(\tau, \mathbf{x}) d\tau \quad (5.36)$$

where $E_F(\mathbf{x}, t)$ represents the cumulative wave energy of the damage induced waves.

Figure 5.12 gives an example of filter reconstruction imaging for the detection of delamination damage in a CFRP composite. The details of this example can be found in [148]. As shown in the wavefield (Figure 5.12a) measured by a SLDV, there are damage induced waves in the delamination area. Accordingly, the wavenumber spectrum (Figure 5.12b) shows additional wavenumber components. A “band-pass” wavenumber filter (Figure 5.12c) is designed to retain only the additional wavenumber components and remove the rest. The filtering is then implemented by multiplying the band-pass filter with the spectrum. The filtered spectrum in Figure 5.12d only contains the delamination induced additional wavenumber values. Meanwhile, the reconstructed wavefield in Figure 5.12e only has the delamination induced waves which are confined in the delamination area. The resulting cumulative energy map in Figure 5.12f shows a high energy concentration area which indicates the delamination location and size.

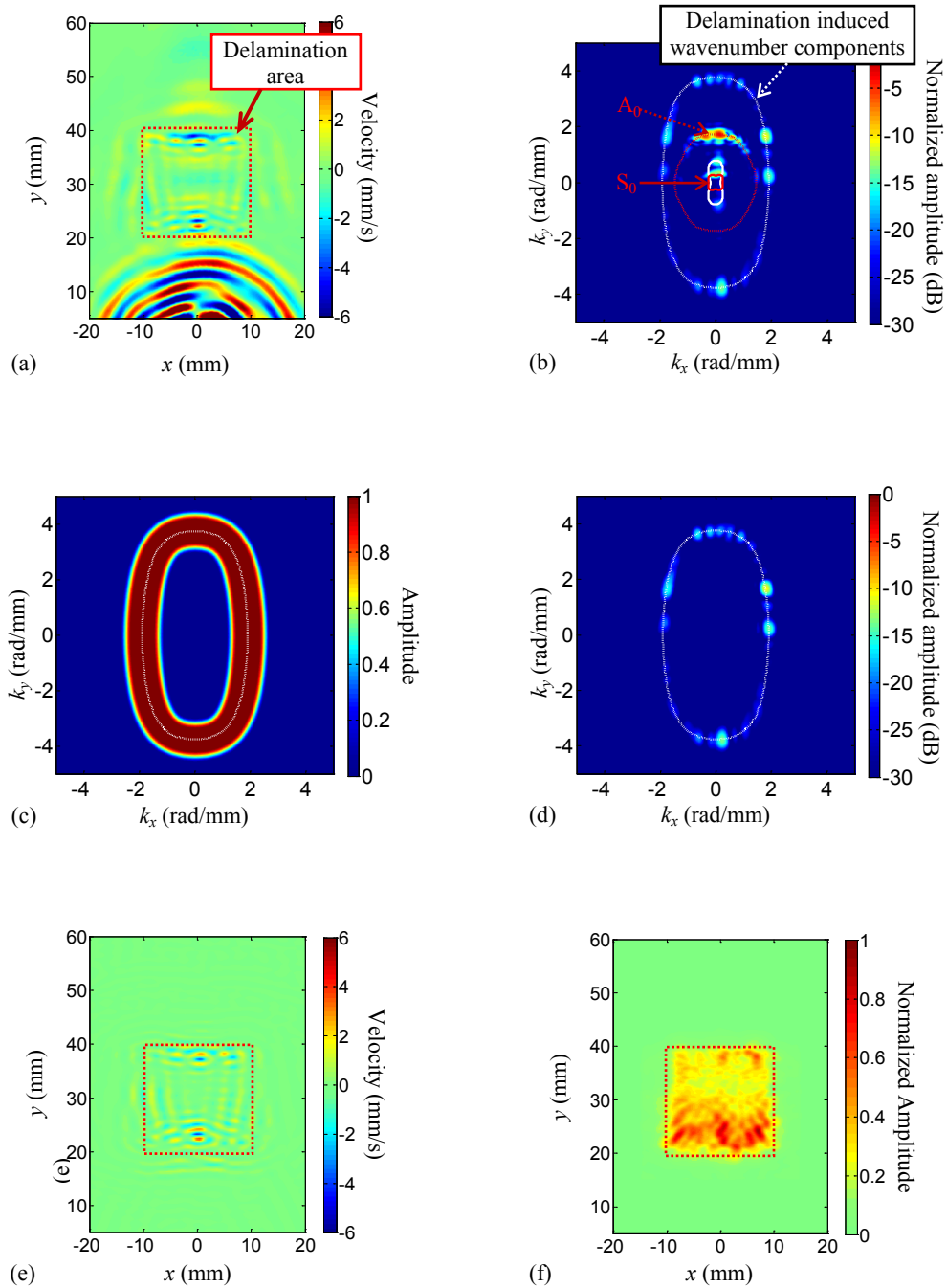


Figure 5.12 Filter reconstruction imaging for delamination detection in a CFRP composite plate: (a) the wavefield at $15 \mu\text{s}$ on a CFRP plate with delamination damage, (b) the wavenumber spectrum of the wavefield showing delamination induced wavenumber components, (c) a band pass filter in wavenumber domain, (d) the filtered wavenumber spectrum, (e) the reconstructed wavefield at $15 \mu\text{s}$, (f) the accumulated energy map in the time range 0 to $50 \mu\text{s}$. The red dotted box indicates the actual delamination region.

5.3. SPATIAL WAVENUMBER IMAGING

The space-frequency-wavenumber analysis (presented in Chapter 4) can generate the space-frequency-wavenumber representation $S(\bar{\mathbf{x}}, f, \mathbf{k})$. From this representation, spatial wavenumber functions can be derived for damage detection and imaging. In the following, two different methods to derive spatial wavenumber functions are provided.

In the first method (weighted sum method), the spatial wavenumber function at the frequency f_0 is defined through a weighted sum of $|\mathbf{k}|$ [32], i.e.,

$$k_{sw}(\bar{\mathbf{x}}, f_0) = \frac{\sum_{\mathbf{k}} [|S(\bar{\mathbf{x}}, f_0, \mathbf{k})| |\mathbf{k}|]}{\sum_{\mathbf{k}} |S(\bar{\mathbf{x}}, f_0, \mathbf{k})|} \quad (5.37)$$

This method considers the contribution of each wavenumber $|\mathbf{k}|$ weighted by its amplitude, and generates a spatial function of effective wavenumber $k_{sw}(\bar{\mathbf{x}}, f_0)$. In practice, when two or more wave modes exist, the function $k_{sw}(\bar{\mathbf{x}}, f_0)$ is influenced by the contribution of all the present wave modes.

In the second method (local maximum method), the spatial wavenumber function is defined by finding the wavenumber where the representation $|S(\bar{\mathbf{x}}, f_0, \mathbf{k})|$ has the largest amplitude [149], i.e.,

$$k_{sw}(\bar{\mathbf{x}}, f_0) = |\mathbf{k}_{sw}(\bar{\mathbf{x}}, f_0)| \quad (5.38)$$

$$\mathbf{k}_{sw}(\bar{\mathbf{x}}, f_0) = \arg \max_{\mathbf{k}} |S(\bar{\mathbf{x}}, f_0, \mathbf{k})| \quad (5.39)$$

This method only considers the wavenumber where the largest $|S(\bar{\mathbf{x}}, f_0, \mathbf{k})|$ appears. In practice, when two or more wave modes exist, the function $k_{sw}(\bar{\mathbf{x}}, f_0)$ is only influenced by the wave mode with the largest amplitude.

The two methods above generate wavenumber functions at a selected frequency f_0 . Considering that no real signal has a singular frequency component but will have some finite bandwidth Δf , the spatial wavenumber function is defined as:

$$k_{sw}(\bar{\mathbf{x}}) = \frac{1}{N} \sum_{i=1}^N k_{sw}(\bar{\mathbf{x}}, f_i) \quad (5.40)$$

where f_i ($i=1,2,3,\dots,N$) is a series of frequency samples over the frequency bandwidth Δf .

The spatial wavenumber function contains the local wavenumber information, and can be used damage detection. Figure 5.13 gives an example of the spatial wavenumber method for delamination detection in a CFRP plate. The wavefield in Figure 5.13 a shows complex wave interactions in the delamination area. By using the spatial wavenumber method, the wavenumber information of the wavefield is unveiled. As shown in in Figure 5.13 b, the spatial wavenumber image indicates an area of approximately 20 mm \times 20 mm which has larger wavenumber values than the rest of the plate. This area matches well with the delamination damage (indicated by the red dotted box in Figure 5.13 b). Obviously, the delamination affects wavenumbers of waves that propagate in the delamination region. The spatial wavenumber method shows its potential for detecting and quantifying delamination damage. The details of this example can be found in [148].

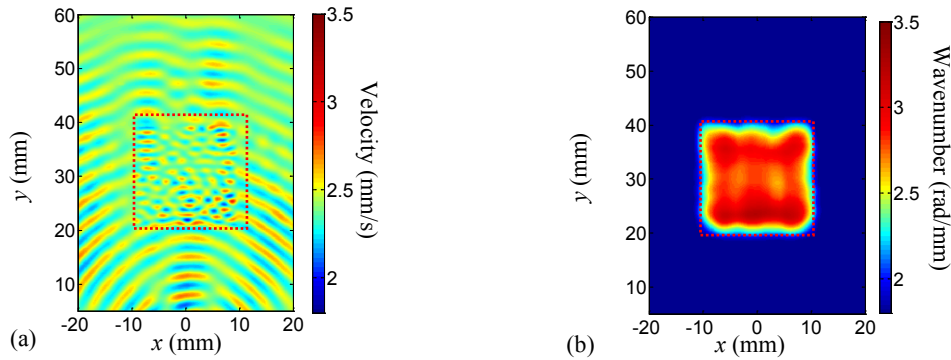


Figure 5.13 Spatial wavenumber imaging for delamination detection in a CFRP plate: (a) a wavefield at 45 μ s showing wave interactions with delamination damage, and (b) the spatial wavenumber image indicating the delamination damage.

PART II: SHM/NDE APPLICATIONS

CHAPTER 6

GUIDED WAVES IN WATER LOADED STRUCTURES AND WATER LEVEL DETECTION

6.1. GUIDED WAVE WATER LEVEL DETECTION

6.1.1. Motivation and introduction

Guided waves have been used for damage detection in water loaded structures, such as ship hulls and submarines [150-155]. Nevertheless, using guided waves for evaluating structural surface condition change due to the presence of water is much less discussed. When a free plate is immersed in water, guided waves in the plate will be affected. The out-of-plane motions of the guided waves in the plate will transmit into water through the plate-water interface [8]. The surrounding water provides a way for guided wave energy to leak outwards from the plate known as leaky guided waves [8]. Compared to guided waves in a free plate, the guided waves in a water loaded plate have different behaviors, such as mode shapes, wave speeds and attenuations [11, 63, 139, 156-159]. Moreover, there is another wave mode reported by Cegla et al. known as quasi-Scholte mode present in the water loaded plate [139, 159]. They studied the quasi-Scholte mode in a plate with both sides immersed in infinite water, where the plate is considered as a symmetrically loaded waveguide [139]. It was found that the quasi-Scholte mode is dispersive at low frequencies and asymptotes to the non-dispersive Scholte mode behavior at high frequencies [139]. Also at low frequencies energy of the quasi-Scholte mode

predominantly flows in the plate, while at high frequencies most of the energy is in the water [139].

In this study, both simulations and experiments are performed to further investigate guided waves in one-side water loaded plates. The numerical simulations are performed with the EFIT method. The experimental investigations are enabled by the PZT-SLDV sensing. Both results confirm the existence of quasi-Scholte waves in one-side water loaded plates. In addition, the influence of water amount on guided waves is investigated. It is seen that the water amount affects the wave propagation time, which can be potentially used for the estimation of water level in a container.

6.1.2. Modeling of guided waves in one-side water loaded plates

To investigate the characteristics of guided waves in one-side water loaded plates, the modeling techniques presented in Chapter 3 are used. Using the GMM method, guided wave dispersion curves and mode shapes in a one-side water loaded plate are derived, and using the EFIT numerical method, the wave propagation is simulated. The related model setups and results are presented in Chapter 3.

6.1.3. Experimental characterizations

A test tank (Figure 6.1 a) has been designed with the front wall as the test plate (a 1.2 mm thick T304 steel plate). When the tank is empty, the front wall is considered as a free plate; with water in the tank, it is then considered as a water loaded plate. A PZT wafer (APC 850: 7 mm×7 mm dimensions, 0.2 mm thickness) is bonded close to the bottom of the front wall as the wave actuator. A coordinate x is defined with the origin O being set at the center of the PZT and aligned vertically upward. Figure 6.1b gives the overall

experimental setup using the hybrid PZT-SLDV sensing. In the test, the laser beam is normal to the plate such that only the out-of-plane wave motion is measured.

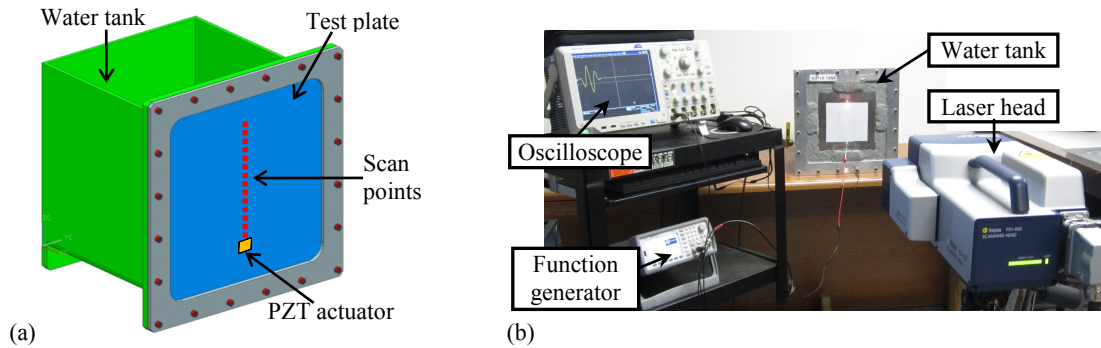


Figure 6.1 The PZT-SLDV experiment on a water tank: (a) an illustration of the water tank, and (b) the overall test setup.

A pulse signal with $0.5 \mu\text{s}$ duration and 10V amplitude is sent to the PZT from an arbitrary function generator (model: Agilent 33500B) to excite guided waves. Waves at multiple scanning points along a vertical line started from the PZT actuator, as indicated in Figure 6.1a, are measured by the SLDV. The spatial resolution of the scanning is 0.3 mm . Two situations, a free plate (from an empty tank) and a fully loaded plate (from a full tank), are investigated. Figure 6.2 a and b plot waveforms measured at 40 mm away from the PZT, and Figure 6.2 c and d plot time-space wavefields in the free and fully loaded plates, respectively. Discernible differences can be observed from both the waveforms and the wavefields of the two cases. However, it is difficult to identify the guided wave modes. It is also hard to qualitatively and quantitatively analyze the differences between the two cases.

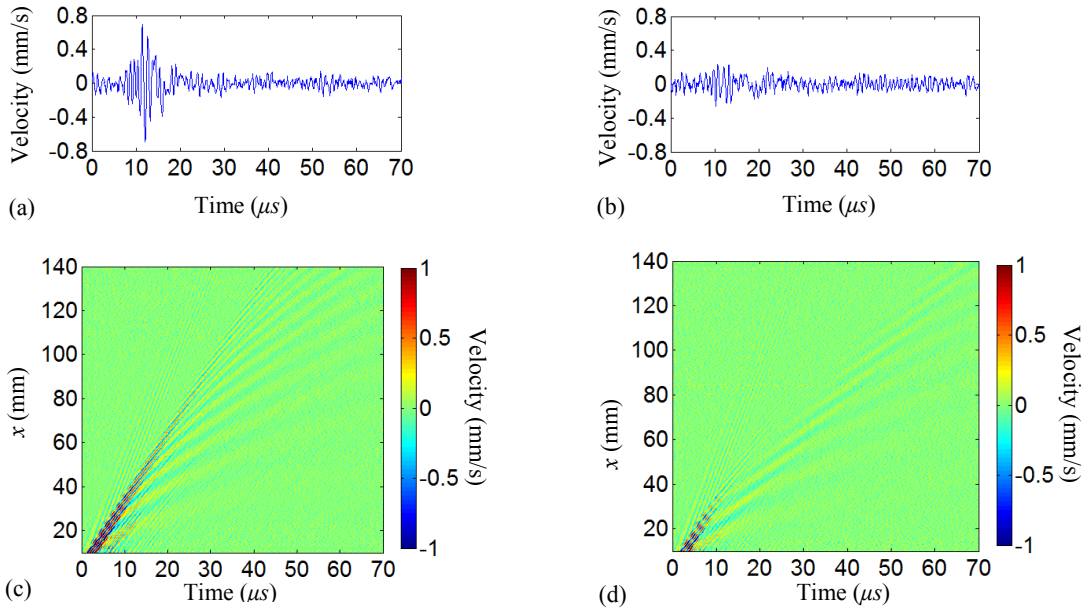


Figure 6.2 Experimental results: (a) and (b) are received waveforms at 40 mm away from the PZT in free and water loaded plates; (c) and (d) are time-space wavefields measured in free and water loaded plates.

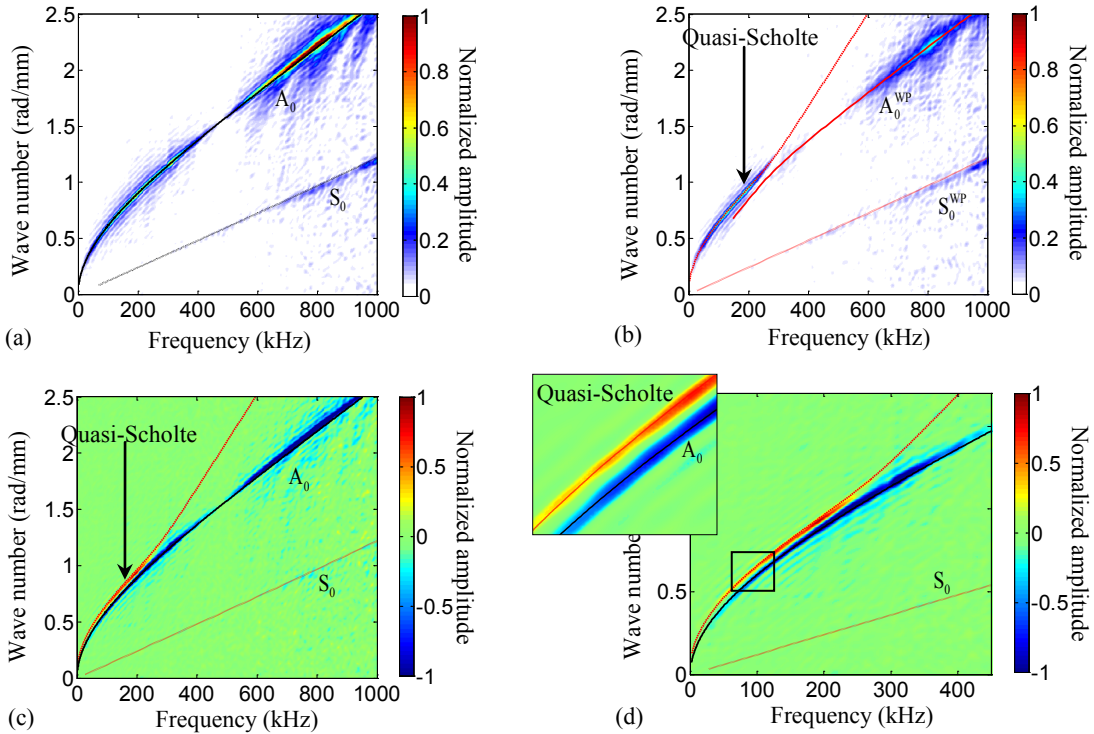


Figure 6.3 Frequency-wavenumber analysis results: (a) for the free plate, (b) for the water loaded plate, (c) spectrum difference obtained by subtracting the spectrum of the free plate from the spectrum of the water loaded plate, and (d) zoom-in plot of figure (c).

Using frequency-wavenumber analysis, time-space wavefields for free and fully loaded plates are transformed into frequency-wavenumber spectra, as presented in Figure 6.3 a and b. The wavenumber dispersion curves solved from the GMM are also plotted in Figure 6.3, in order to identify the wave modes in the spectra. By comparing the spectra with the wavenumber curves, each wave mode can be identified. In the free plate spectrum in Figure 6.3 a, A_0 and S_0 modes are discernibly identified. Note that since the out-of-plane motion of A_0 mode is much stronger than that of S_0 mode and the SLDV only measures the out-of-plane motion, the amplitude of A_0 mode in the spectrum is larger than that of S_0 mode since [140]. Particularly, at frequencies below 500 kHz, the S_0 mode is barely seen due to the small out-of-plane motion in the low frequency range.

In the spectrum of the water loaded plate (Figure 6.3b), three wave modes including A_0^{WP} , S_0^{WP} and quasi-Scholte modes are identified. Compared to the spectrum of the free plate, the spectrum of the water loaded plate shows that the amplitude of S_0^{WP} mode remains nearly the same as S_0 mode, while the amplitude of A_0^{WP} mode significantly decreases due to the energy leakage. Particularly, at frequencies below 500 kHz, the A_0^{WP} mode nearly disappears. Meanwhile, the quasi-Scholte mode shows up in the frequency range up to 300 kHz, which is consistent with what has been reported in [139]. Moreover, it is seen that the quasi-Scholte mode has different wavenumbers compared to the A_0 mode.

To clearly show the difference, the free plate spectrum (Figure 6.3 a) is subtracted from the immersed plate spectrum (Figure 6.3 b). The subtraction result and a zoomed-in plot are given in Figure 6.3c and d. It is noticed in Figure 6.3c that S_0 and S_0^{WP} modes

have almost been canceled out after the subtraction since S_0 and S_0^{WP} modes are nearly the same in both the free and immersed plates. At low frequencies, both quasi-Scholte and A_0 modes are remained. The difference plot confirms that the quasi-Scholte mode in the immersed plate has different wavenumbers compared to the A_0 mode in the free plate.

6.1.4. Wave signature and water level correlation

Figure 6.4 plots the pitch-catch sensing setup on the same water tank given in Figure 6.1, to investigate the influence of water level on guided waves. The guided waves are generated from a PZT with a 3 count tone burst signal at 100 kHz. The waves at 140 mm away from the PZT are measured by an SLDV receiver. Wave signals are acquired at different water levels d_W from 5 to 135 mm with a 10 mm step.

As shown in the setup, the wave propagation path d_{T-R} consists of the water path d_W in the immersed plate portion, and the dry path $d_{T-R}-d_W$ in the free plate portion. The guided waves leave the actuator as the quasi-Scholte mode in the immersed portion d_W , then convert to the A_0 mode in the free portion $d_{T-R}-d_W$. Therefore, the total wave traveling time t_{T-R} can be expressed as,

$$t_{T-R} = \frac{d_W}{c_{QS}} + \frac{d_{T-R} - d_W}{c_{A0}} \quad (6.41)$$

where c_{QS} and c_{A0} are group velocities of quasi-Scholte and A_0 modes (at 100 kHz, $c_{QS}=1811$ m/s and $c_{A0}=1895$ m/s). Using the case $d_W=0$ as the baseline, the change of traveling time at any water level d_W *w.r.t.* the baseline can be derived as,

$$\Delta t_{T-R} = d_W \left(\frac{1}{c_{QS}} - \frac{1}{c_{A0}} \right) \quad (6.42)$$

Eq.(6.42) shows a linear relation between the change of traveling time Δt_{T-R} and the water level d_W . This linear relation is plotted in Figure 6.5 a (the solid line). Thus, once the time difference Δt_{T-R} is known, the water level can be determined based on the linear relation.

Figure 6.5 b presents the baseline signal at $d_W=0$ (solid line) and the signal at $d_W=95$ mm (broken line) measured by the SLDV. The change of traveling time Δt_{T-R} can be estimated by calculating the time difference between the signal at $d_W=95$ mm and the baseline. For all the water levels from 5 to 135 mm, their Δt_{T-R} are plotted in Figure 6.5 a (triangle markers), in comparison to the theoretical prediction (the solid line). It is seen that the experimental data agrees very well with theoretical prediction, which validates the linear relationship between the change of traveling time and the water level. Hence, this sensing methodology can be potentially used for water level detection in a container.

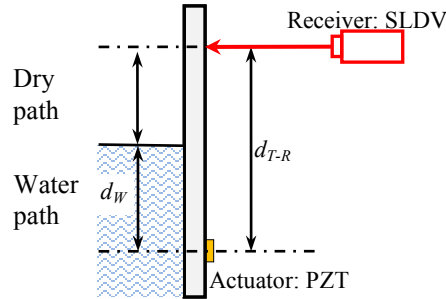


Figure 6.4 An illustration of the pitch-catch configuration.

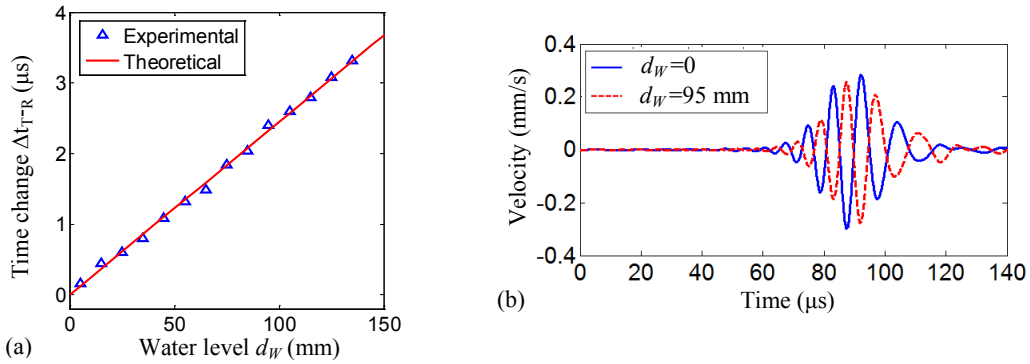


Figure 6.5 Water influence on wave propagation at 100 kHz: (a) the relation between the water level and the change of traveling time Δt_{T-R} , and (b) received waveforms when water level $d_W=0$ (solid line) and $d_W=95$ mm (broken line).

6.2. GAS ACCUMULATION DETECTION IN NUCLEAR COOLANT PIPES

6.2.1. Motivation and introduction

The U.S. Nuclear Regulatory Commission (NRC) issued Generic Letter 2008-01 due to the safety concern associated with gas accumulation events in emergency core cooling pipes of nuclear power plants [160]. Since the gas accumulation may critically damage pipes, pumps, and valves and affect the safety operation of nuclear power plants, the gas accumulation needs to be detected as well as quantified. In a pipe with water inside, when a large amount of gas presents and accumulates, there will be a gas-water boundary between the gas and the water. Therefore, the location of the gas-water boundary can be used as an indication of gas accumulation.

Based on the study of guided wave water level detection in the last section, the gas accumulation detection using guided waves for nuclear coolant pipes are investigated in this section. Guided waves in an empty pipe and a water loaded pipe are acquired through experiments, and analyzed using the frequency wavenumber analysis. Analysis results show that guided wave characteristics such as wavenumbers and wave speeds are different between empty and water loaded pipes. A gas accumulation detection method is developed and verified through laboratory proof-of-concept tests.

6.2.2. Guided waves in water loaded pipes

When water presents in a pipe, guided waves in the pipe will be affected. In order to understand how the water affects the guided waves, experiments using PZT-SLDV sensing are performed. Figure 6.6 a plots a schematic of the experimental setup. A small scale test pipe with 1.56 mm wall thickness and 114.4 mm outer diameter made of stainless steel (T304) is used. A PZT actuator (APC 850: 5 mm × 5 mm dimensions and

0.2 mm thickness) is surface mounted on the pipe to generate guided waves. The excitation signal is a pulse with 2.5 μs duration and 60 V amplitude. An SLDV is used to measure the guided waves at various scanning points along a vertical line with a spatial resolution of 0.3 mm.

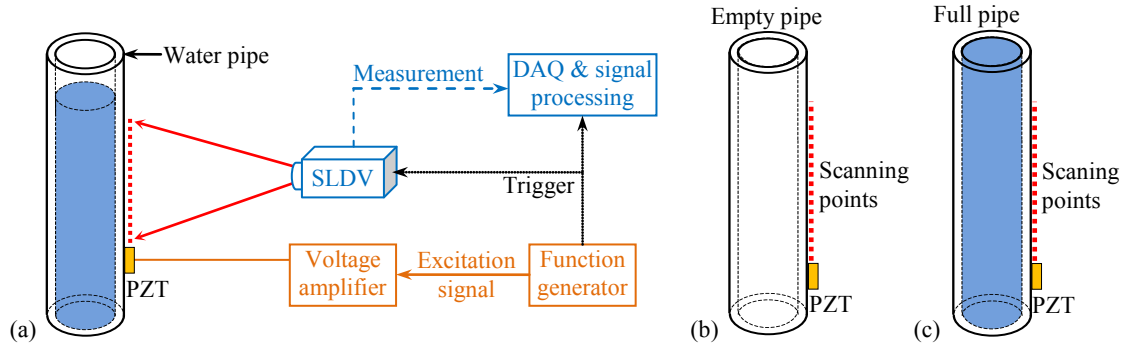


Figure 6.6 The experimental setup: (a) a schematic of the setup, (b) illustration of an empty pipe, (c) illustration of a full pipe.

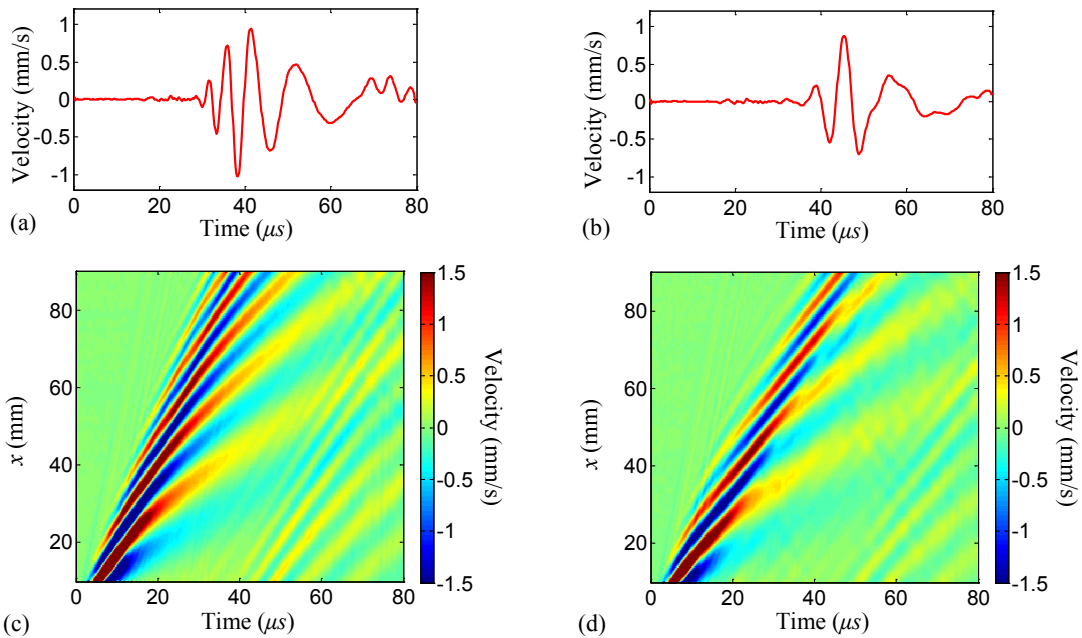


Figure 6.7 Experimental results: (a) and (b) are received waveforms at 90 mm away from the PZT in the empty and full pipes; (c) and (d) are time-space wavefields measured in the empty and full pipes.

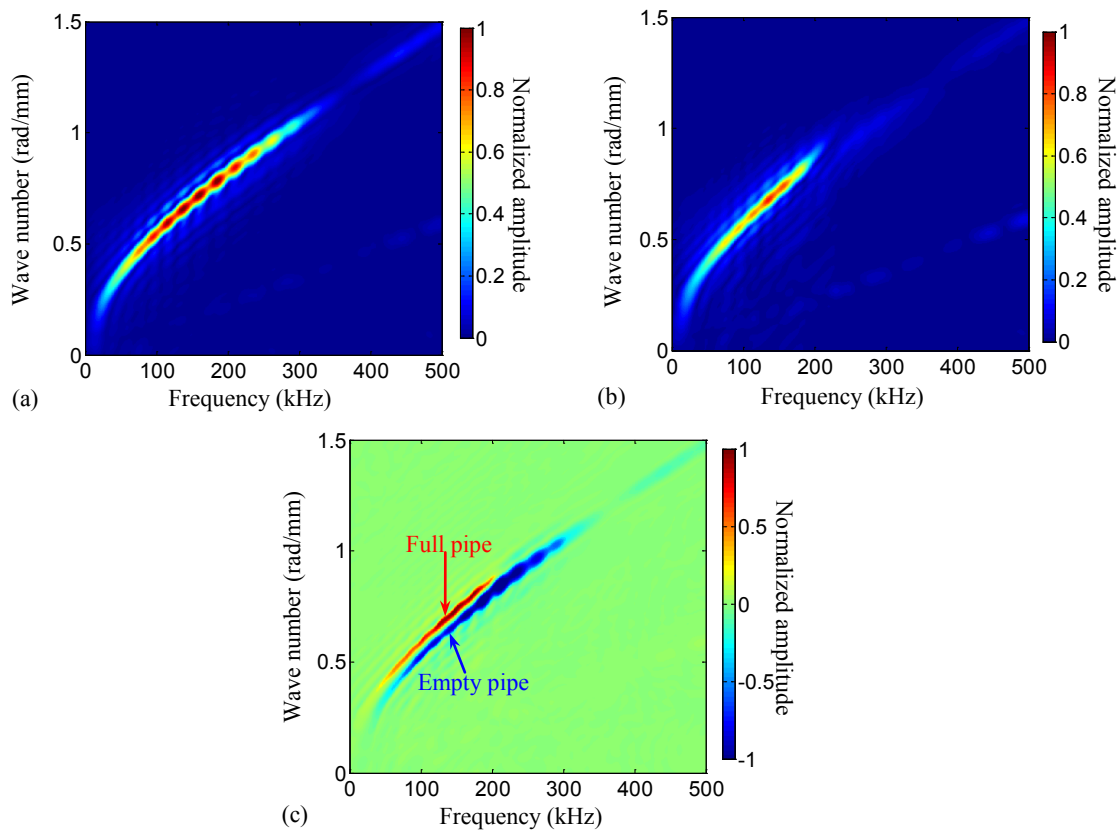


Figure 6.8 Frequency-wavenumber analysis: (a) and (b) are frequency-wavenumber spectra for empty and full pipes; (c) the spectrum difference obtained by subtracting the spectrum of the empty pipe from the spectrum of the full pipe.

Figure 6.7 a and b plot waveforms at 90 mm away from the actuator for empty and full pipes. Figure 6.7 c and d plot time-space wavefields for both cases. Compared to guided waves in the empty pipe, guided waves in the full pipe travel slower with smaller amplitudes. The time-space wavefields are further processed using frequency-wavenumber analysis. The frequency-wavenumber spectra for both cases are given in Figure 6.8 a and b. The two spectra show components with large amplitudes at frequencies lower than 250 kHz. To show the difference between the two spectra, the empty pipe spectrum in Figure 6.8 a is subtracted from the full pipe spectrum in Figure

6.8 b. The subtraction result is plotted in Figure 6.8 c, in which the red and the blue component are for guided waves in full and empty pipes, respectively. Figure 6.8 c shows guided waves in the full pipe have larger wavenumbers than those in the empty pipe.

6.2.3. Gas accumulation detection

6.2.3.1. Test on a small scale pipe

Figure 6.9 plots the pitch-catch sensing setup on the small scale pipe, to investigate the influence of water level on guided waves. Guided waves are generated from a PZT. The excitation is a three-cycle toneburst with 30 V amplitude and 100 kHz frequency. The guided waves at 90 mm away from the PZT are measured by an SLDV receiver. In order to investigate how water levels affect guided waves, the guided waves are measured at different water levels d_W from 0 to 90 mm with a step of 10 mm.

As shown in the pitch-catch sensing configuration in Figure 6.9, the wave propagation path (d_{T-R}) from the actuator to the receiver consists of water path d_W and dry path $d_{T-R}-d_W$. That's to say, the total wave traveling time t_{T-R} can be expressed as

$$t_{T-R} = \frac{d_W}{c_{waterpipe}} + \frac{d_{T-R} - d_W}{c_{emptypipe}} \quad (6.43)$$

where $c_{waterpipe}$ and $c_{emptypipe}$ are group velocities of guided waves in the full pipe and the empty pipe, respectively. Thus, using the empty pipe when $d_W = 0$ as the baseline, the change of traveling time at any water level of d_W *w.r.t.* the baseline can be derived as

$$\Delta t_{T-R} = d_W \left(\frac{1}{c_{waterpipe}} - \frac{1}{c_{emptypipe}} \right) \quad (6.44)$$

Eq. (6.44) shows a linear relation between the change of traveling time Δt_{T-R} and the water level d_W . This linear relation is plotted in Figure 6.10 a (solid line).

Figure 6.10 b plots guided wave signals measured at water levels $d_w=0, 50$ and 90 mm. From these waveforms, it is found that the wave traveling time increases and the wave amplitude decreases with the increase of water level. The time differences Δt_{T-R} for different water levels are plotted in Figure 6.10 a (triangle markers). The experimental results show a linear relation between the change of traveling time and the water level, and agree well with the theoretical prediction. Thus, by measuring the traveling time of guided waves, the water amount (or gas amount) in the pipe can be estimated.

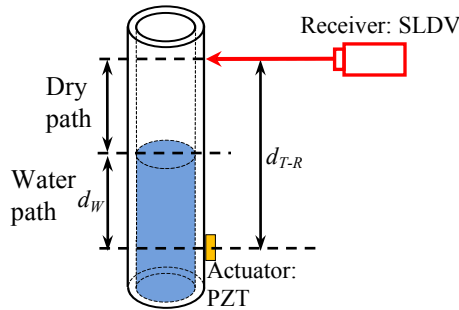


Figure 6.9 An illustration of the pitch-catch sensing on a small scale pipe.

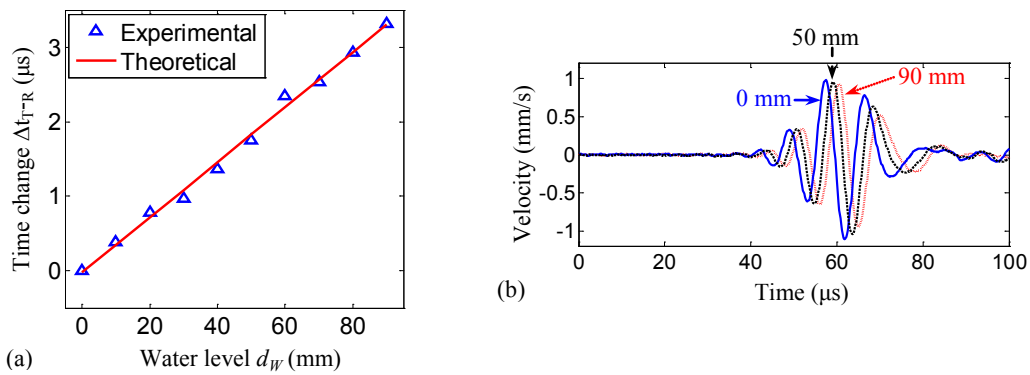


Figure 6.10 Experimental results for the small scale pipe: (a) the relation between the water level and change of traveling time Δt_{T-R} , (b) received waveforms when water levels are 0 mm, 50 mm and 90 mm.

6.2.3.2. Test on a tilted full scale pipe

Beside the test on the small scale pipe, an experimental test is performed on a tilted full scale pipe. Figure 6.11 a gives the overall test setup. The test pipe (material: T304 steel, wall thickness: 7.1 mm, outer diameter: 168.3 mm) is tilted and supported by a wood frame. Figure 6.11 b plots the pitch-catch sensing configuration. Two PZT sensors (APC 850: 7 mm×7 mm dimension and 0.2 mm thickness) are mounted on the pipe outer surface with 300 mm apart along the axial direction of the pipe. The lower PZT is used the actuator and the upper PZT is used as the receiver. The excitation signal is a 3 count toneburst with 30 kHz frequency and amplitude 25 V amplitude. The guided waves are measured at different water levels d_w from 0 to 300 mm with a step of 30 mm.

Figure 6.12 b plots guided wave signals measured at water levels $d_w=0$, 150 and 300 mm. These signals show that the wave traveling time increases and the wave amplitude decreases with the increase of water level. This trend is the same as what is observed in the small scale pipe. The time differences Δt_{T-R} for different water levels are plotted in Figure 6.12 b (triangle markers), in comparison with the theoretical prediction (solid line). The experimental results show a linear relation between the change of traveling time and the water level, and agree well with the theoretical prediction. Thus, by measuring the traveling time of guided waves, the location of the gas-water boundary can be detected. Hence, the water amount (or gas amount) in the pipe can be estimated. This confirms the presented guided wave sensing method is able to detect and quantify the gas accumulation.

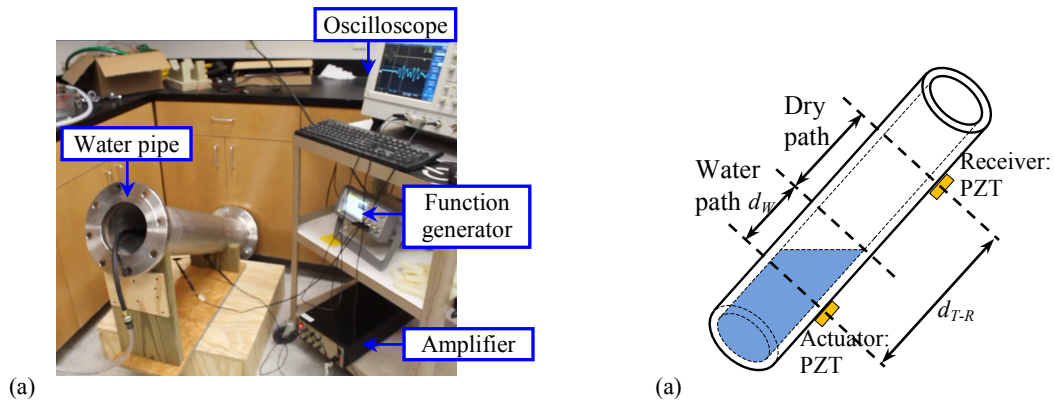


Figure 6.11 Test on a tilted large scale pipe: (a) photo of the test setup, (b) schematic of the pitch-catch sensing configuration with PZT transducers.

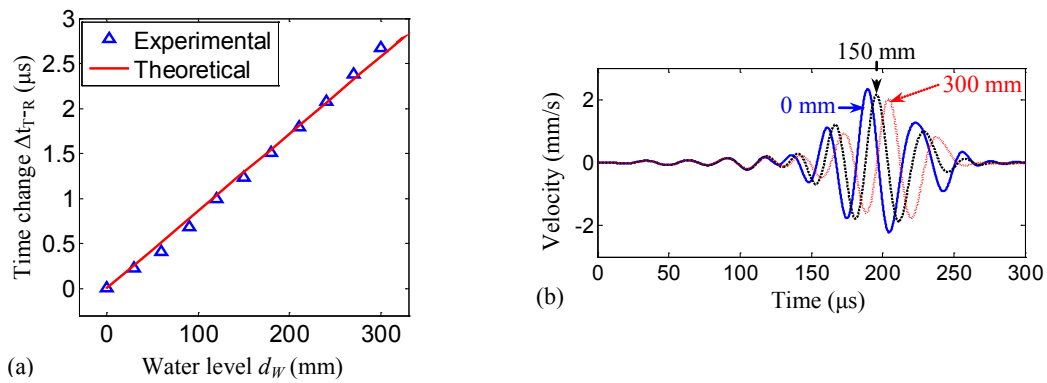


Figure 6.12 Experimental results for the tilted large scale pipe: (a) the relation between the water level and change of traveling time Δt_{T-R} , (b) received waveforms when water levels are 0 mm, 150 mm and 300 mm.

CHAPTER 7

CRACK DETECTION AND QUANTIFICATION IN ISOTROPIC PLATES

7.1. MOTIVATION AND INTRODUCTION

Among various crack detection methods, Lamb wave based NDE/SHM has shown great potential for crack detection in plate-like structures, due to the sensitivity of Lamb waves to a variety of defects and their capability of traveling long distances in the plate-like structures [29, 161]. Intensive studies of Lamb wave based NDE/SHM have been presented in literature about using Lamb waves to detect crack damage in isotropic plates, as well as to quantify the crack size [12, 19-24, 80, 117, 121, 122, 124, 131, 162-178]. Ihn and Chang used a built-in piezoelectric sensor/actuator network to detect and monitor crack growth [179]. Tua et al. used PZT transducers on a square grid to detect through, half-through, and concealed cracks in aluminum plates [167]. Lu et al. used Lamb wave scattering to quantitatively assess the through-thickness crack size [180]. Yu and Leckey used Lamb wave based sparse arrays to detect crack damage [165]. Chen et al. developed a load-differential imaging method to process Lamb wave signals received from a sparse array, for the purpose of crack detection and localization [122].

In literature, many Lamb wave based damage detection approaches use measurements from distributive sensors, and damage estimation is performed by processing data acquired from the point-wise locations of the sensors. Methods based on such point-wise measurements have several limitations due to the sparsity of data, such as the limitation in accurate determination of damage size, and the variation in detectability

of damage which relates to relative locations of sensors *w.r.t.* the damage [165]. These limitations have led to recent advancements in the acquisition and analysis of full wavefields [104, 109, 110, 161, 181, 182].

The work presented in this chapter focuses on crack detection and quantitative evaluation using PZT-SLDV sensing and wavefield analysis. The intention of this work is to demonstrate contactless wavefield measurement and wavefield processing methods for detection and quantification of crack damage. In particular, this work presents two robust damage imaging methods, filter reconstruction and spatial wavenumber imaging, in order to detect crack damage and quantify the crack length, depth and width.

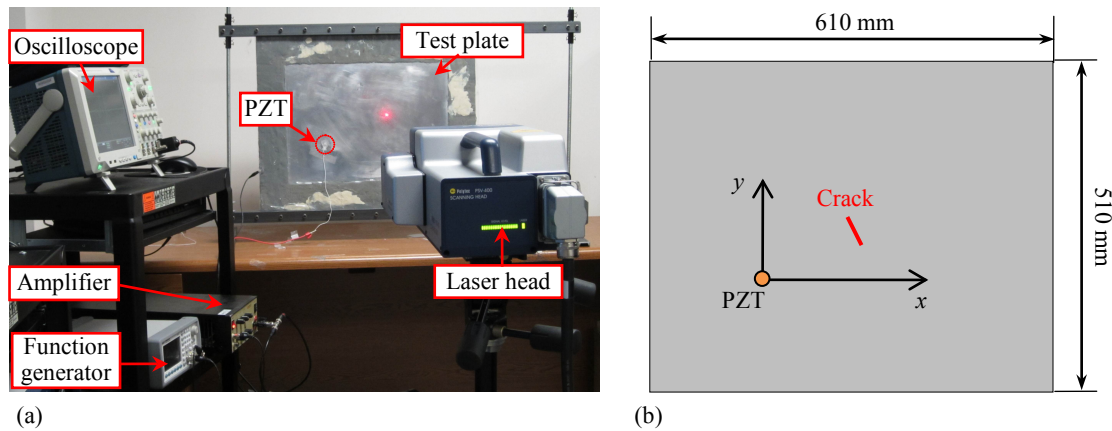


Figure 7.1 Experimental setup for crack detection in a 1 mm thick aluminum plate: (a) overall test setup, and (b) schematic of the test plate.

7.2. WAVE INTERACTION WITH CRACK DAMAGE

Figure 7.1 gives the overall experimental setup. The test specimen is a 2024-T3 aluminum plate (dimensions: 610 mm \times 510 mm \times 1 mm) with a through-thickness (TT) crack. The crack is made by electric discharge machining (EDM) and has a length of 31 mm. A round shaped PZT (APC 850: 7 mm diameter and 0.2 mm thickness) is used to

generate Lamb waves and the center of the PZT is set as the origin of the x - y coordinate system. The excitation signal is a 3 count toneburst with 360 kHz frequency and 40 V amplitude. An SLDV (Polytec PSV-400-M2) is used to measure Lamb waves. Note that the laser beam is set normal to the plate, in order to acquire the out-of-plane velocity (v_z) component. Lamb waves in a 190 mm \times 110 mm scanning area are measured, with a spatial sampling interval Δd of 0.5 mm. Note the sampling interval Δd is selected by meeting the sampling theorem requirement, i.e., $\Delta d \leq \lambda/2$, where λ is the wavelength of the interrogating wave mode [145]. Additionally, experience has shown that a smaller Δd will result in a better spatial resolution. In our test, the wavelength of the interrogating A_0 mode is 4.6 mm. Hence, the 0.5 mm sampling interval satisfies the sampling theorem while providing a good spatial resolution.

Figure 7.2 a and b plot wavefield images acquired by the SLDV at 36 μ s and 65 μ s, respectively. The wavefield images clearly capture incident A_0 and incident S_0 modes as well as their interactions with the crack. At 36 μ s, the incident S_0 mode has passed the crack, and the incident A_0 has not yet arrived. The wavefield shows a reflection S_0 mode and a scattering A_0 mode generated from S_0 to A_0 mode conversion. At 65 μ s, the A_0 mode has passed the crack and a reflection A_0 mode is generated.

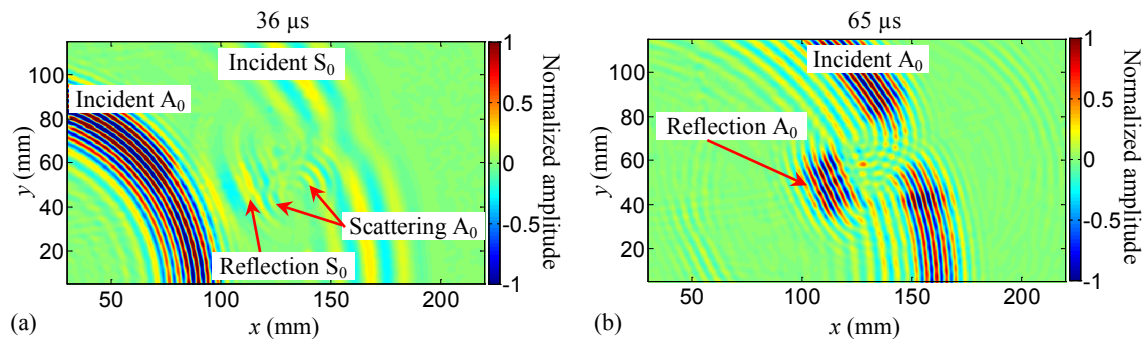


Figure 7.2 Wavefield images measured by the SLDV at 360 kHz excitation on a 1 mm thick aluminum plate with a TT crack: (a) at 36 μ s, and (b) at 65 μ s.

7.3. CRACK DETECTION AND QUANTIFICATION

7.3.1. Crack detection and quantification with experimental data

For the purpose of crack detection and quantification, the filter reconstruction imaging is applied to the time-space wavefield measured by the SLDV. Figure 7.3 c plots the wavenumber spectrum at 360 kHz with theoretical wavenumber curves of A_0 and S_0 modes. The wavenumber spectrum shows strong components on the curves of A_0 and S_0 modes, representing the wavenumber components A_0 and S_0 modes. Besides the A_0 and S_0 modes, there are other wavenumber components (diagonally distributed components) in the spectrum. The wavenumber filtering is then applied to keep only the diagonal wavenumbers by using a wavenumber filter as plotted in Figure 7.3 a and b. Figure 7.3 d plots the reconstructed image after wavenumber filtering, showing a high amplitude area representing the detected crack damage. This area agrees well with the actual crack.

The reconstructed image confirms that the diagonal wavenumbers represent waves that gather closely around the structural discontinuity, i.e. the crack. In another words, the diagonal wavenumbers are caused by abrupt changes of waves around the crack. The filter reconstruction imaging therefore provides a useful means of mapping the structural discontinuity, and yields the location and size of the discontinuity. From the imaging result in Figure 7.3 d, we can estimate the location (crack center at (132.6 mm, 56.1 mm) with relative errors (1.22%, 1.58%)) and length of the crack (28.1 mm with a relative error 9.35%).

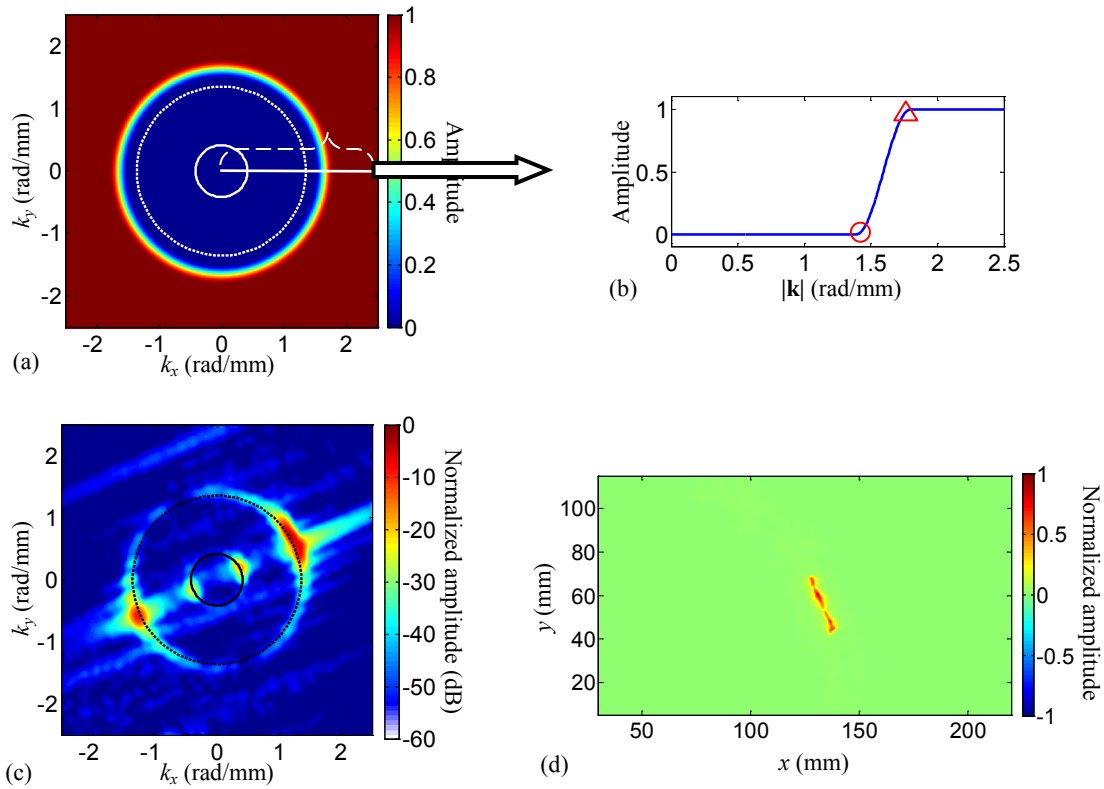


Figure 7.3 Filter reconstruction imaging with experimental data in an aluminum plate with a TT crack: (a) high-pass wavenumber filter, (b) illustration of the filter along the k_x axis, (c) the frequency-wavenumber spectrum at 360 kHz, and (d) the reconstructed imaging of the plate indicating the presence of the crack damage. Solid and broken lines in figures a and c are theoretical wavenumber curves of S_0 and A_0 modes.

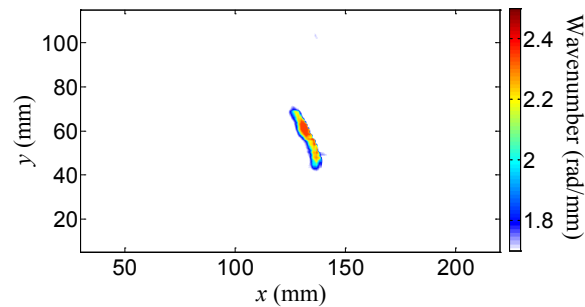


Figure 7.4 Spatial Wavenumber imaging with experimental data in an aluminum plate with a TT crack.

The spatial wavenumber imaging is also applied to the wavefield measured by the SLDV. Figure 7.4 gives the imaging result over the scan area at the excitation frequency 360 kHz. The crack damage is clearly indicated by a region with large wavenumbers. This means the wavenumber increases due to the influence of the structural discontinuity. From the imaging result in Figure 7.4, we can estimate the location (crack center at (131.9 mm, 56.8 mm) with relative errors (0.69%, 0.35%)) and length of the crack (29.2 mm with a relative error 5.81%). Thus, the spatial wavenumber imaging provides another method to detect crack damage and quantify the crack location and size.

7.3.2. Crack detection and quantification with simulation data

Modeling can serve as an efficient and cost effective way to assist the development of diagnostic algorithms [1, 8, 36, 37]. In this study, the EFIT modeling technique is used to simulate the cases of (i) a plate with a through-thickness (TT) crack, (ii) a plate with the same crack as in case (i), except with three times the crack width (3X), and (iii) a plate with the same crack as in case (i) except with the crack extending only half-way through the plate thickness (hTT). Then the simulation data generated from EFIT is used to demonstrate the quantifications of crack length, depth and width using the filter reconstruction imaging and spatial wavenumber imaging. The layout of the simulation is given in Figure 7.1 b, which is the same as the layout of the experiment. The plate in simulation is the same as the plate in experiment. A round shaped PZT (7 mm in diameter and 0.2 mm thick) is used for generating Lamb waves and its location is set as the origin of the x - y coordinate system. In order to closely approximate the PZT actuation, the EFIT source excitation is implemented as in-plane displacements occurring at edges of the PZT actuator (assuming a ring-type excitation source) [47]. The excitation signal is a 3 count

toneburst with a frequency of 360 kHz. Three cases (TT, 3X and hTT cracks) are simulated using EFIT method. The centers of cracks are at the coordinates (131mm, 57mm), with the same distance from the crack center to the actuator in all three cases (143 mm). More details of simulations can be found in reference [183]. The time-space wavefields generated from simulations are then processed by using the two imaging methods for crack quantification.

The results of filter reconstruction imaging at 360 kHz are given in Figure 7.5. The reconstructed images show locations and lengths of cracks. It is also noted that amplitudes in the reconstructed images are different among the three cracks. For direct comparison, the amplitudes along these cracks are plotted in Figure 7.6. It shows that the 3X crack has the largest amplitude, the TT crack has the medium amplitude, and the hTT crack has the smallest amplitude. The comparison in Figure 7.6 indicates that the more significant discontinuity leads to the higher amplitude in the imaging results. Hence, the filter reconstruction imaging method can detect crack damage, quantify the crack size, and show the crack severity.

The results of spatial wavenumber imaging at 360 kHz are given in Figure 7.7. Cracks are represented as larger wavenumbers in contrast to wavenumbers at all other locations. It is observed that the spatial wavenumber images are different for the three cracks. For comparison, the wavenumber values along the three cracks are plotted in Figure 7.8. The 3X crack has the largest wavenumber value, the TT crack has the medium value, and the hTT crack has the smallest value. As the filter reconstruction imaging, the spatial wavenumber imaging can also detect crack damage, quantify the crack size, and show the crack severity.

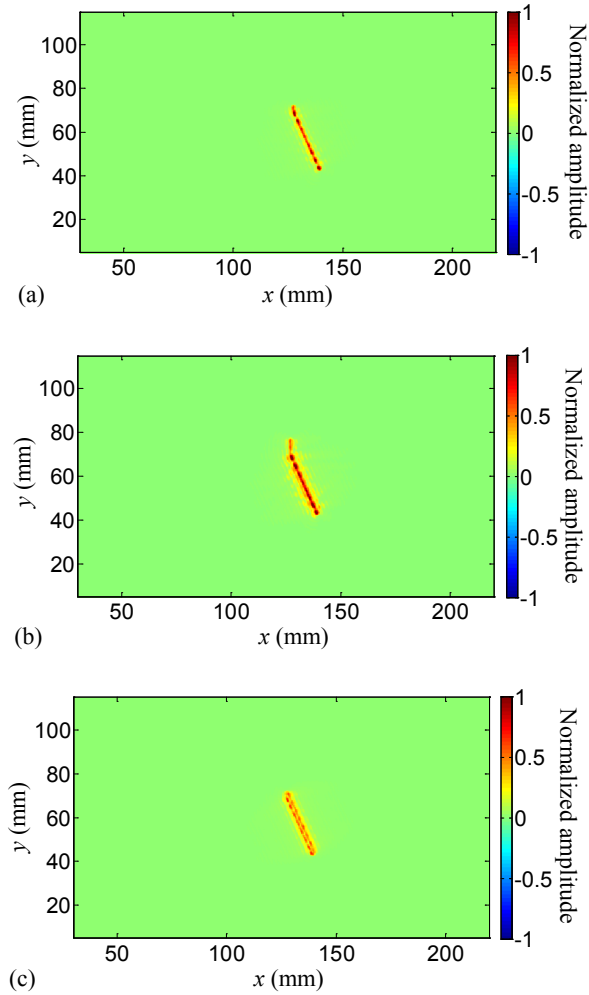


Figure 7.5 The filter reconstruction imaging results at 360 kHz: (a) for the TT crack plate, (b) for the 3X crack plate, and (c) for the hTT crack plate.

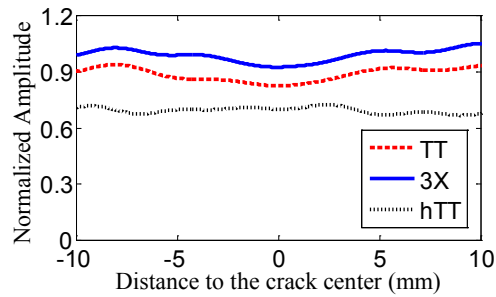


Figure 7.6 Amplitudes along the cracks extracted from the filter reconstruction imaging results. Broken, solid and dotted lines are for TT, 3X and hTT cracks, respectively.

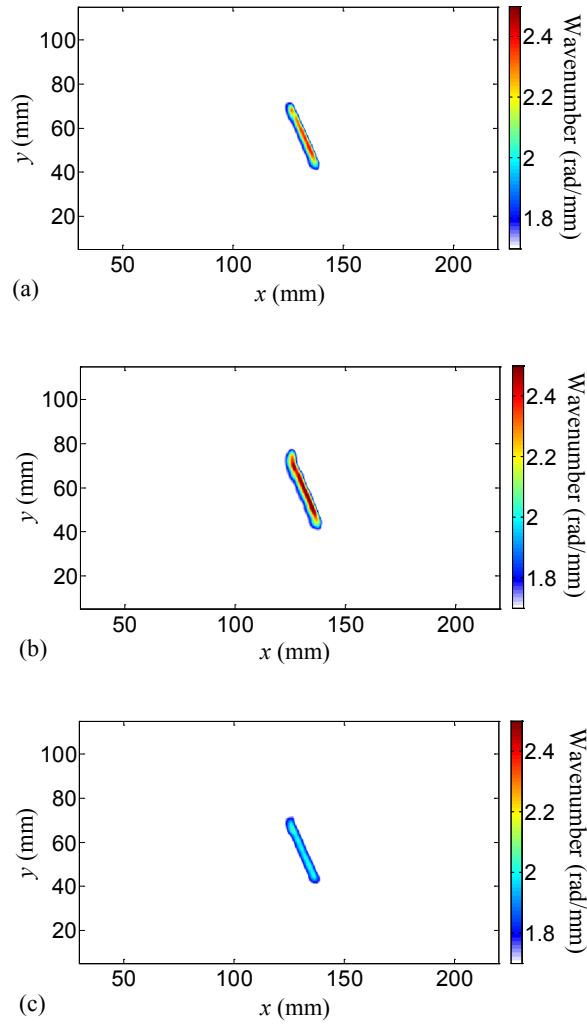


Figure 7.7 Spatial wavenumber imaging results at 360kHz: (a) for the TT crack plate; (b) for the 3X crack plate; (c) for the hTT crack plate.

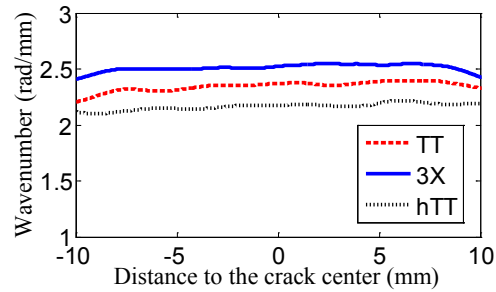


Figure 7.8 Wavenumber distributions along the crack. Broken, solid and dotted lines are for TT, 3X and hTT cracks, respectively.

CHAPTER 8

THICKNESS LOSS EVALUATION IN ISOTROPIC PLATES

8.1. MOTIVATION AND INTRODUCTION

Intensive studies have been presented in the literature about using Lamb waves to determine the presence of damage in plates as well as quantify the damage location and size [29-32, 103, 104, 106, 107, 109, 110, 113, 114, 140, 142, 143, 148, 149, 161, 184-193]. However, applications of Lamb waves for quantifications of material thickness and damage depth are much less discussed. The work presented in this chapter focuses on material thickness and damage depth quantifications by using Lamb waves.

Recently, wavefield analysis methods have been used for the quantification of delamination depth by using correlations with dispersion curves [32, 149, 194, 195]. In this study, in order to quantify the material thickness as well as the damage depth in isotropic plates, a dispersion curve regression method is developed and verified through experiments. It is shown that the dispersion curve regression method can quantify the material thickness and damage depth in isotropic plates. Moreover, this technique can be potentially used for detection and quantification of corrosion damage.

8.2. WAVE INTERACTION WITH MATERIAL LOSS DAMAGE

The test specimen is a 610×610×3.2 (unit: mm) aluminum 6061-T6 plate with material loss damage. The damage is created by removing a portion of the plate material using a milling machine. By removing different portions of the material in the same area, damage with different depths can be created. Figure 8.1 a gives a photo of damage with a

diameter of 25.4 mm and a depth of 0.5 mm. Four different cases are studied, when the damage depths are 0.25 mm, 0.50 mm, 0.75 mm and 1.00 mm. Figure 8.1 a gives the overall experimental setup. Figure 8.1 c is a schematic of the PZT-SLDV sensing layout. A PZT (APC 851 type with diameter 7 mm diameter and 0.2 mm thickness) is installed on the plate surface to excite Lamb waves. The center of the PZT is set as the coordinate origin. The center of damage is at (0, 60) mm. A SLDV is used to acquire the time-space wavefields $v(t, \mathbf{x})$ in the scanning area. Once the wavefield is acquired, it is transformed to the spectral field $V(f, \mathbf{x})$ through FT.

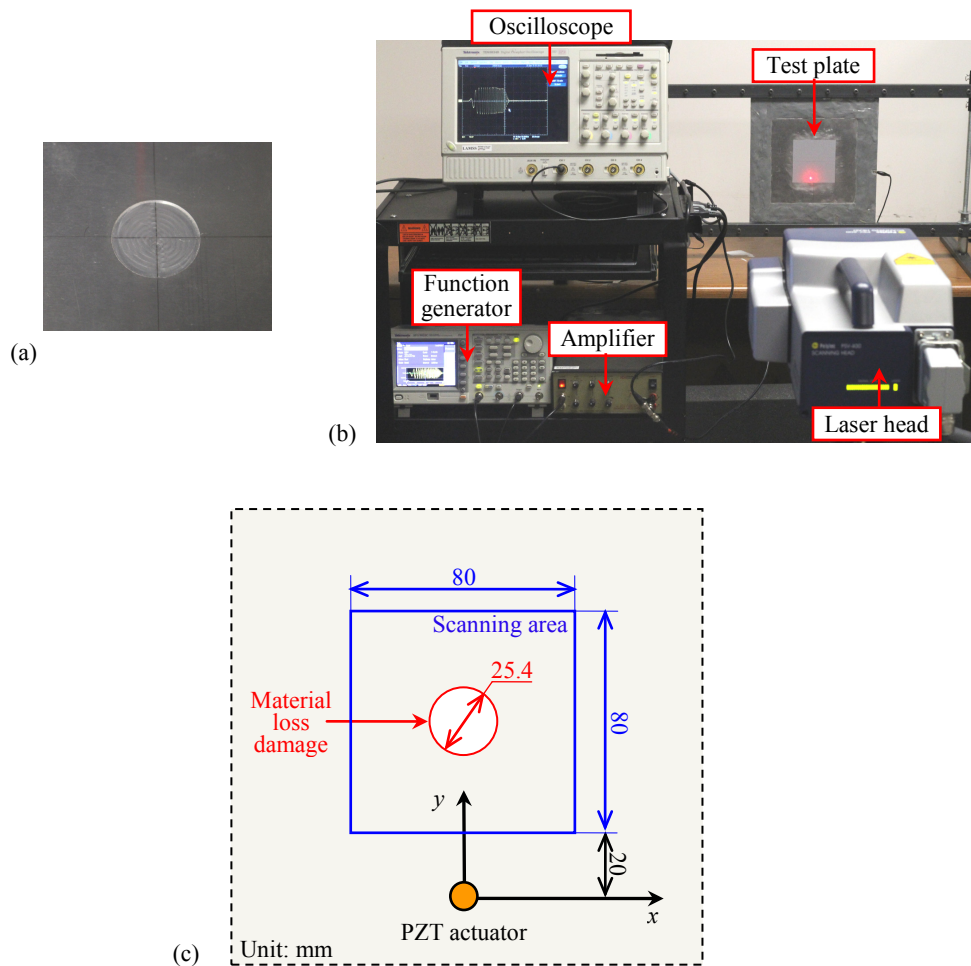


Figure 8.1. Experimental setup: (a) material loss damage with a diameter of 25.4 mm and a depth of 0.5 mm on the front side of the test specimen, (b) photo of the setup, and (c) schematic of the sensing layout.

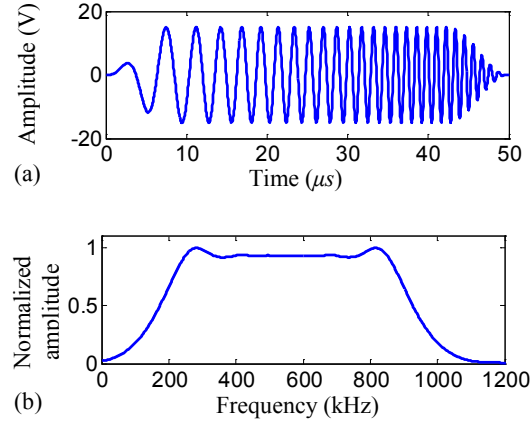


Figure 8.2. Chirp excitation: (a) the waveform, and (b) the frequency spectrum

The PZT excitation is a chirp signal with wide band frequency components. Figure 8.2 a and b plot the waveform and the frequency spectrum of the chirp excitation. In the frequency range 300~800 kHz, the chirp signal has stable dominant magnitudes. According to Lamb wave dispersion curves, for the chirp excitation over 300 to 800 kHz, both the fundamental A_0 and S_0 Lamb modes can be generated. Since the A_0 mode has smaller wavelengths and is more sensitive to thickness variations than the S_0 mode, the study focuses will be on the application of A_0 mode for the quantification of material thickness and damage depth.

The A_0 mode is extracted from the spectra field $V(f, \mathbf{x})$ through the frequency-wavenumber filtering technique. Figure 8.3 a and b plot real parts of the A_0 mode spectral fields at 300 kHz and 500 kHz when the damage depth is 0.75 mm. The spectral fields show complex wave propagation and interaction. At the location of the damage, discontinues of wave fronts can be observed. For further characterization, the spatial wavenumber analysis is applied, with the results given in Figure 8.4 a and b. The spatial wavenumber images show an area with larger wavenumber values. The larger

wavenumber values are induced by the thickness reduction at the material loss damage, for the reason that the wavenumber increases with the decrease of material thickness (as indicated in Figure 8.5). In addition, the location and size of the area with larger wavenumbers agree well with those of the actual material loss damage. Although the damage location and size can be determined from the spatial wavenumber images in Figure 8.4 a and b, the damage depth is still unknown.

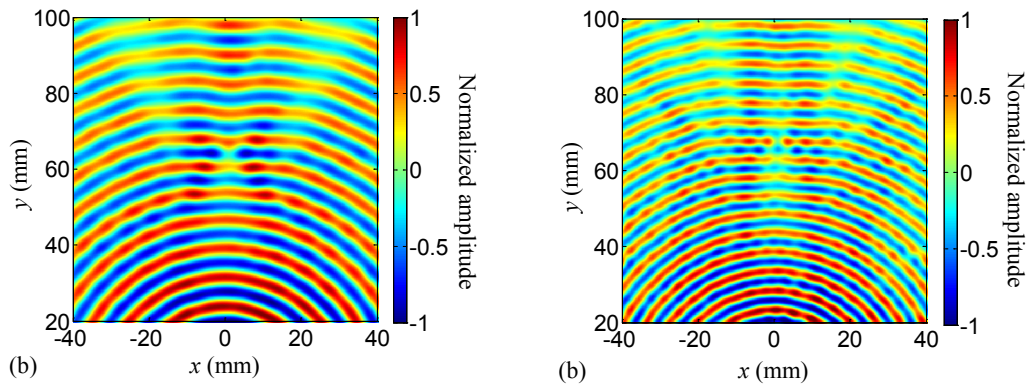


Figure 8.3 Spectral fields (real parts) for the plate with 0.75 mm depth material loss damage: (a) at 300 kHz, and (b) at 500 kHz.

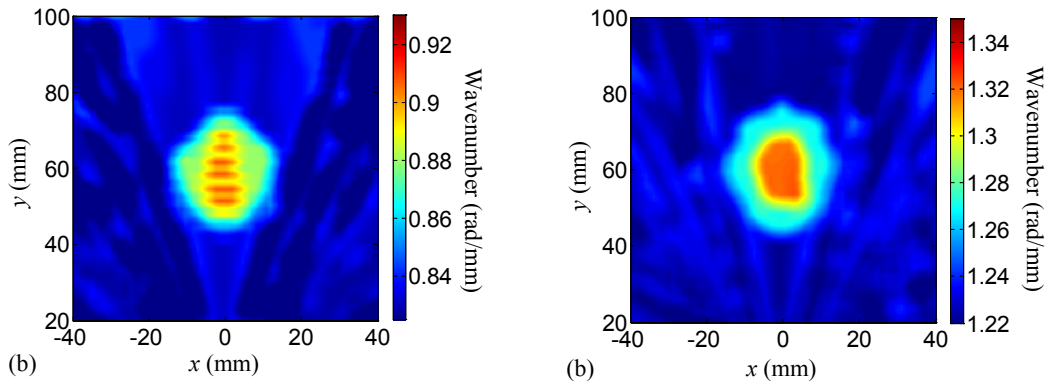


Figure 8.4 Spatial wavenumber images for the plate with 0.75 mm depth material loss damage: (a) at 300 kHz, and (b) at 500 kHz.

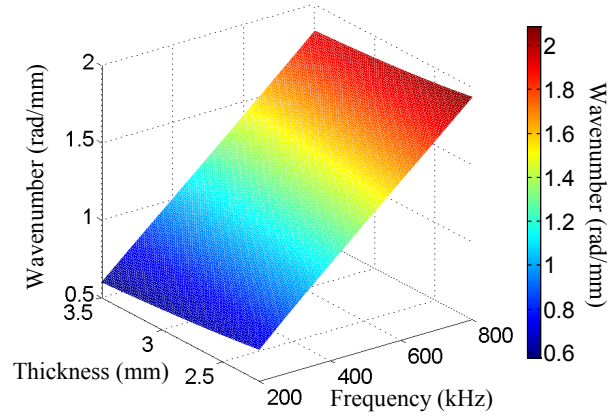


Figure 8.5 A_0 mode wavenumber versus plate thickness and wave frequency.

8.3. DISPERSION CURVE REGRESSION FOR MATERIAL THICKNESS QUANTIFICATION

The spatial wavenumber result $k_{sw}(\bar{\mathbf{x}}, f)$ can be used for damage imaging and quantification. In addition, the wavenumber information can be used for evaluating the material thickness, since the wavenumber is correlated to the plate thickness. Thus, the plate thickness can be quantified by comparing the spatial wavenumber $k_{sw}(\bar{\mathbf{x}}, f)$ to the theoretical dispersion curve $k(d, f)$, as

$$d(\bar{\mathbf{x}}) = \arg \min_d \sum_{i=1}^N [k_{sw}(\bar{\mathbf{x}}, f_i) - k(d, f_i)]^2 \quad (6.45)$$

where f_i ($i=1,2,3\dots N$) represents a series of frequency samples over a frequency bandwidth Δf , and $d(\bar{\mathbf{x}})$ is the material thickness determined through a least square regression process. To evaluate the performance of the regression in Eq. (6.45), the standard wavenumber deviation is calculated, as

$$\sigma_k(\bar{\mathbf{x}}) = \sqrt{\frac{1}{N} \sum_{i=1}^N [k_{sw}(\bar{\mathbf{x}}, f_i) - k(d(\bar{\mathbf{x}}), f_i)]^2} \quad (6.46)$$

Moreover, the standard deviation for thickness evaluation can be expressed as

$$\sigma_d(\bar{x}) = \frac{\sigma_k(\bar{x})}{N} \sum_{i=1}^N \frac{2\delta d}{|k(d(\bar{x}) + \delta d, f_i) - k(d(\bar{x}) - \delta d, f_i)|} \quad (6.47)$$

where δd is a small thickness perturbation.

Figure 8.6 gives a dispersion curve regression result at the location (0, 60) mm, when the damage depth is 0.75 mm. In Figure 8.6, the experimental data is from the spatial wavenumber $k_{sw}(\bar{x}, f)$. Through the regression, the dispersion curve of A_0 mode that fits the experimental data can be found, and the material thickness can be determined. The solid line in Figure 8.6 is the dispersion curve obtained from the regression. The dotted and broken lines represent the upper and lower boundaries of the 95% confident region.

With the dispersion curve regression method, the material thickness can be quantified. In addition, the thickness loss at the damage can also be found. Figure 8.7 a, b, c and d plot the thickness loss images for the four cases when the depths of defects are 0.25 mm, 0.50 mm, 0.75 mm and 1.00 mm, respectively. These four images clearly show the locations, sizes and depths of the four defects.

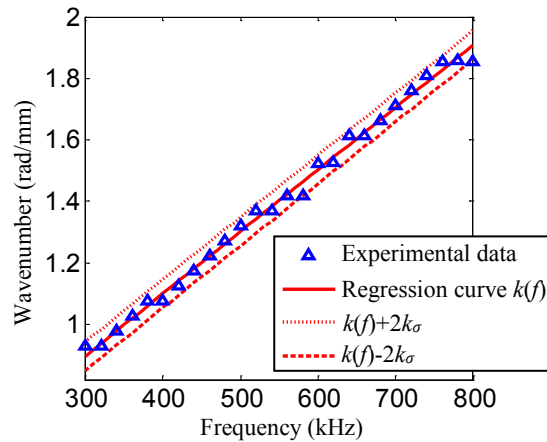


Figure 8.6 Dispersion curve regression result at the location (0, 60) mm, when the damage depth is 0.75 mm. The experimental data is from the spatial wavenumber $k_{sw}(\bar{x}, f)$. The solid line is the dispersion curve obtained from the least square regression. The dotted and broken lines represent the upper and lower boundaries of the 95% confident region.

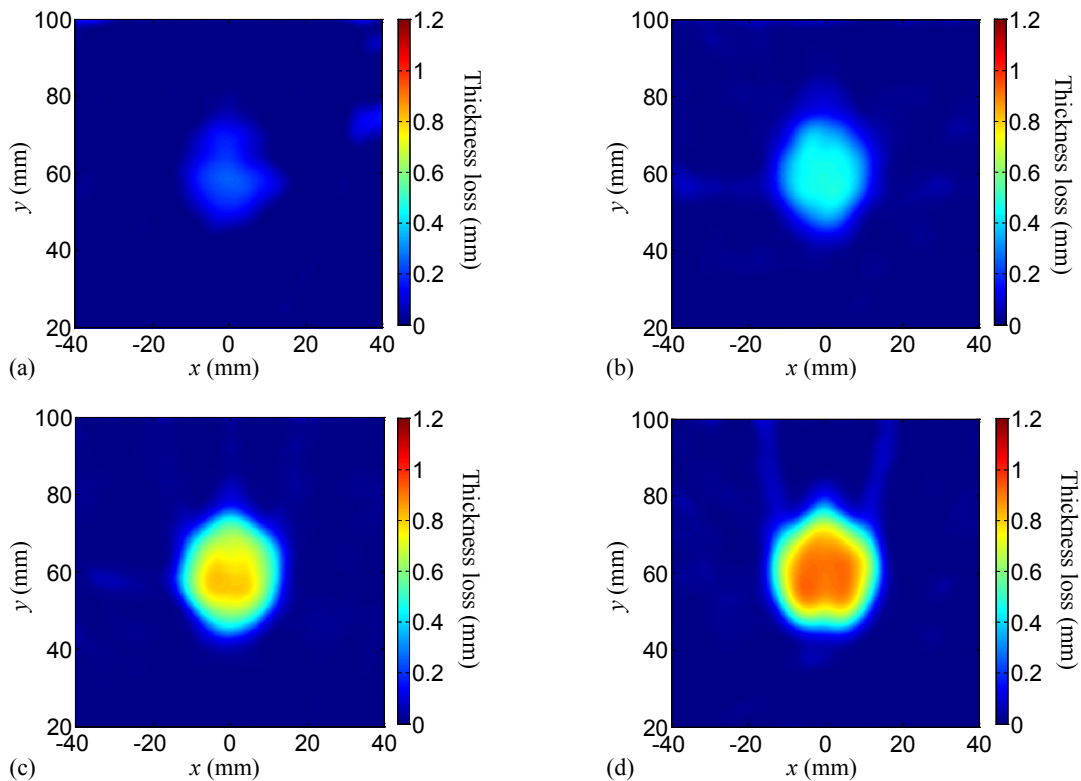


Figure 8.7 The thickness loss quantification results: (a), (b), (c) and (d) are for the plates with 0.25 mm, 0.50 mm, 0.75 mm and 1.00 mm depth damage, respectively.

8.4. EVALUATION OF SIMULATED PITTING CORROSION DAMAGE

In this subsection, the developed material loss evaluation method is used to detect and quantity pitting corrosion damage. Figure 8.8 a plots the sensing layout. The pitting corrosion damage is simulated by a nine-hole cluster on a 3×3 grid with the center at (0, 60) mm. Figure 8.8 b gives a photo of the simulated pitting corrosion. The holes are half ball shaped with the diameter of 2 mm, which are created by a ball-end end mill. The spatial intervals in x and y directions are both 4 mm.

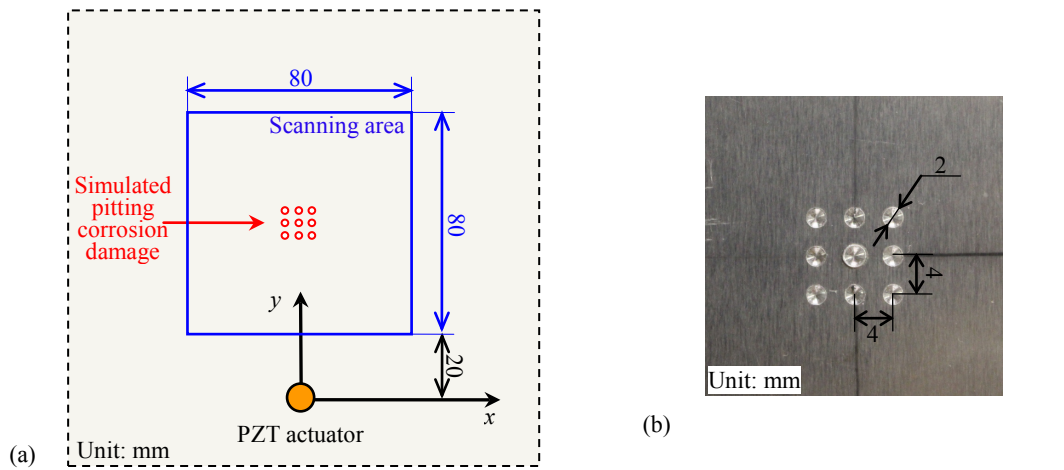


Figure 8.8. Experimental setup: (a) schematic of the sensing layout, and (b) photo of pitting corrosion damage simulated by a nine-hole cluster.

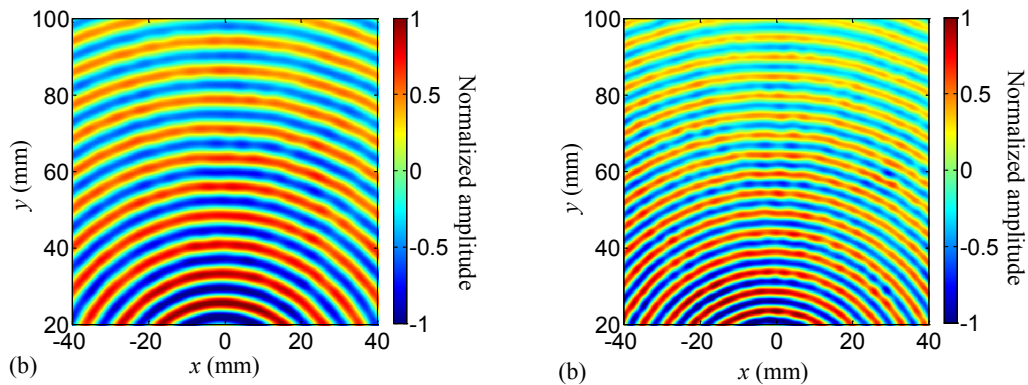


Figure 8.9 Spectral fields (real parts) for the plate with simulated pitting corrosion damage: (a) at 300 kHz, and (b) at 500 kHz.

Figure 8.9 a and b plot real parts of spectral fields measured at 300 kHz and 500 kHz. It is hard to see any spectral field discontinuity induced by the damage, since the influence of the damage is so weak. The dispersion curve regression method is applied to the spectral field $V(f, \mathbf{x})$ with the result plotted in Figure 8.10. The imaging result clearly shows an area with larger thickness loss than the rest. The location and size of this area agree well with those of the simulated pitting corrosion damage (the nine-hole cluster). Therefore, the presented method has the capability of detecting pitting corrosion damage and quantifying its size. Note that although the imaging result in Figure 8.10 shows the nine-hole cluster, the 2 mm diameter small holes are not distinguished in space. One possible reason of this effect is that the wavelengths of incident waves are too large to distinguish the holes with such small intervals in the nine-hole cluster.

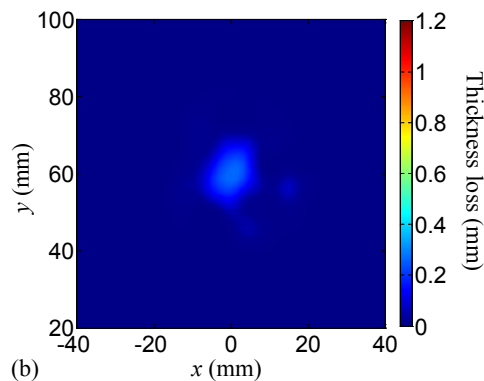


Figure 8.10. Imaging result of the plate with simulated pitting corrosion damage.

CHAPTER 9

DELAMINATION DETECTION AND QUANTIFICATION IN COMPOSITE LAMINATES

9.1. MOTIVATION AND INTRODUCTION

Unexpected damage can occur in aerospace composites due to impact events or material stress during off-nominal loading events. In particular, laminated composites are susceptible to delamination damage due to weak transverse tensile and interlaminar shear strengths [191]. Developments of reliable and quantitative techniques to detect delamination damage in laminated composites are imperative for safe and functional optimally-designed next-generation composite structures. Delamination damage can occur largely internally in composites, while damage indications are barely visible on composite surfaces to the naked eye [196]. Such hidden delamination damage must be detected and evaluated before it becomes critical. The problem of how best to detect such damage in laminated composites is still being solved, and a solution to this problem will be imperative for safety-critical composites. Current composite “safety margin” design comes with a weight penalty and could be mitigated by efficient and reliable NDE/SHM methods to rapidly and accurately locate and quantify the damage in composite materials.

Among various NDE/SHM methods, ultrasonic guided waves have proven effective for damage detection in plate-like metallic and composite structures due to their ability to inspect large areas while maintaining sensitivities to small defects in the structures [1, 8, 36, 197-199]. Advances in guided wave based NDE/SHM technologies over the last decade have demonstrated feasibilities of detecting and locating damage in

composite structures [29, 32, 74, 136, 184, 193, 200-208]. Despite these advances, the state-of-the-art is still insufficient in regards to a quantitative understanding of the mechanism of wave interaction with delamination damage in composites. In addition, the state-of-the-art is insufficient for evaluating delamination damage details that are necessary to feed into damage progression models. Last but not least, most delamination detection methods focus on locating the delamination in plane, without quantifying the delamination depth.

This chapter presents studies of guided wave interaction with delamination damage in laminated composites, and delamination detection and quantification. EFIT simulations and PZT-SLDV experiments are performed to investigate guided wave interaction with delamination damage. In order to understand complex wave interactions that occur when incident waves encounter delamination damage, guided wavefields and wavenumber spectra are analyzed. These analyses are applied to a composite laminate plate containing a simulated (Teflon insert) single delamination and to a plate with impact-induced delamination damage (multiple ply layer delamination damage).

To detect and quantify impact-induced delamination damage, this chapter presents a combined phased array and wavefield based imaging methodology. First, the phased array imaging is used to generate an intensity image of the composite being inspected to visualize and locate delamination damage in the composite. Once the delamination damage is detected, wavefield based imaging methods such as filter reconstruction imaging and spatial wavenumber imaging are performed to further quantify the damage. The systemic combination of phased array imaging and wavefield based imaging

provides a hierarchical damage diagnosis, which can efficiently and effectively locate the damage, and quantify the damage size and depth.

9.2. WAVE INTERACTION WITH DELAMINATION DAMAGE

Compared to guided waves in isotropic materials, guided waves in composite materials present additional complexities, especially when guided waves interact with delamination damage [192]. When guided waves propagate in delaminated composites, multiple reflections induced by delamination damage can occur, as shown in references [103, 141, 143, 209, 210]. Hence, a considerable amount of wave energy can be “trapped” above, below, and between delaminated regions until eventually the energy dissipates. Ramadas et al. studied the interaction of the anti-symmetric A_0 mode with symmetric delamination damage [210]. They identified multiple reflections in the delamination region. The trapped energy phenomenon of guided waves in delaminated composites has also been studied experimentally through the use of wavefield images obtained from laser vibrometry tests [103, 141]. It has been found that upon entering the delaminated region, the incident waves will be split above and below the delamination, propagating independently through upper and lower laminates (for a single delamination scenario). As waves propagate towards the edge of delamination damage (exit region), a portion of wave energy is reflected backwards from the far edge of the delamination. The reflected waves in the damage region then pass back above (or below) the delaminated area and experience reflections at the original entrance to the delamination region. The process is repeated until the energy is dissipated, as found in the simulation work reported by Hayashi and Kawashima [209]. Some portion of the wave energy exits the delaminated region into the pristine region, re-forming the guided wave modes that exist in the

pristine plate [74]. Glushkov et al. also observed similar wave energy trapping and localization in a strip delamination from wavefields measured by laser vibrometry [143]. Guided wave energy trapping in delamination damage has recently been quantitatively studied [149]. As expected from the guided wave theory, the trapped waves have different wavenumbers compared to those traveling in the undamaged area. Therefore, it is expected that by analyzing the trapped waves, the delamination dimensions can be quantified. Rogge and Leckey demonstrated that wavenumber analysis can be used to determine the approximate depth and size of near-surface delamination damage through a localized wavenumber field imaging method [32]. In this work, both EFIT simulations and PZT-SLDV experiments are performed to investigate the wave interaction with delamination damage.

9.2.1. Simulations of guided waves in composites

The EFIT simulations are implemented to investigate the guided wave interaction with delamination damage. The guided wave interaction with delamination damage in a $[0_2/90_2]_s$ layup CFRP composite plate is simulated. Moreover, interactions of A_0 and S_0 modes with delamination damage are simulated and analyzed. The simulation results show that when incident waves interact with the delamination damage, mode conversion, reflection and transmission waves appear. Moreover, waves in the delamination area show different wave lengths and wave speeds compared to those in the rest area. The details of the EFIT model setup and simulation results can be found in Chapter 3.

9.2.2. Experimental characterizations using the PZT-SLDV sensing

Experiments are performed using the PZT-SLDV sensing. Two 380 mm×380 mm 8-ply IM7/8552 composite laminate plates (material properties in Table 9.9.1) with the same

layup $[0_2/90_2]_S$ are provided by NASA Langley Research Center (LaRC). One plate is the pristine, while the other contains delamination damage created by inserting a 20 mm \times 20 mm Teflon film under the second ply during manufacturing, as shown in Figure 9.1.

The overall experimental setup is shown in Figure 9.1 c. Guided waves are actuated with a surface bonded 0.2 mm thick and 7 mm round PZT patch. The PZT excitation signal is a 3-cycle toneburst with 300 kHz frequency and 40 V amplitude. The out-of-plane wavefield data are acquired using the SLDV. The spatial resolution of the SLDV scan grid is set at 0.2 mm.

Figure 9.2 plots time-space wavefields of guided waves propagating along the y -axis (1-D wave propagation). For the pristine case in Figure 9.2 a, a faster S_0 mode and a slower A_0 mode can clearly be observed. For the delaminated case in Figure 9.2 b, guided waves propagating back and forth between the top ($y=20$ mm) and bottom ($y=40$ mm) boundaries of the delamination can be distinctively seen, exhibiting the “trapped wave” phenomenon [141-143].

Figure 9.3 a and b plot snapshots of wavefields at the time 15 μ s in the scan area (2-D wave propagation) in the pristine and delaminated plates. In the snapshot of the pristine plate, two wave modes, a faster S_0 mode and a slower A_0 mode, are observed. In the snapshot of the delaminated plate, interactions at the delamination region are observed as waves propagating between delamination boundaries (denoted by the dotted box), after the incident S_0 mode has passed the delamination region.

Table 9.1 Material properties of the IM7/8552 lamina.

ρ (kg/m ³)	E_1 (GPa)	E_2 (GPa)	E_3 (GPa)	G_{12} (GPa)	G_{13} (GPa)	G_{23} (GPa)	ν_{12}	ν_{13}	ν_{23}	Thickness (mm)
1570	171.4	9.08	9.08	5.29	5.29	2.80	0.32	0.32	0.34	0.1068

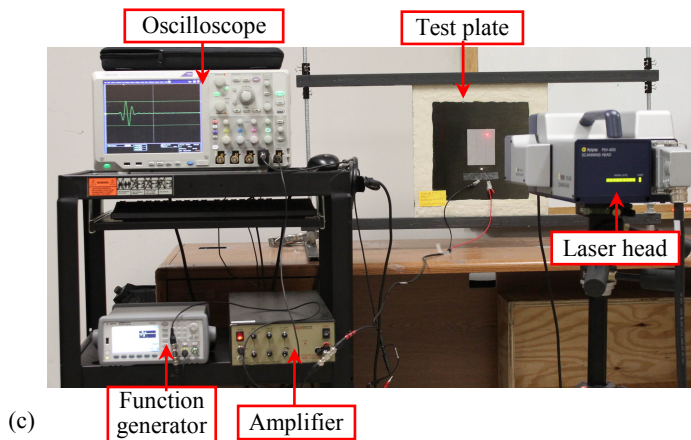
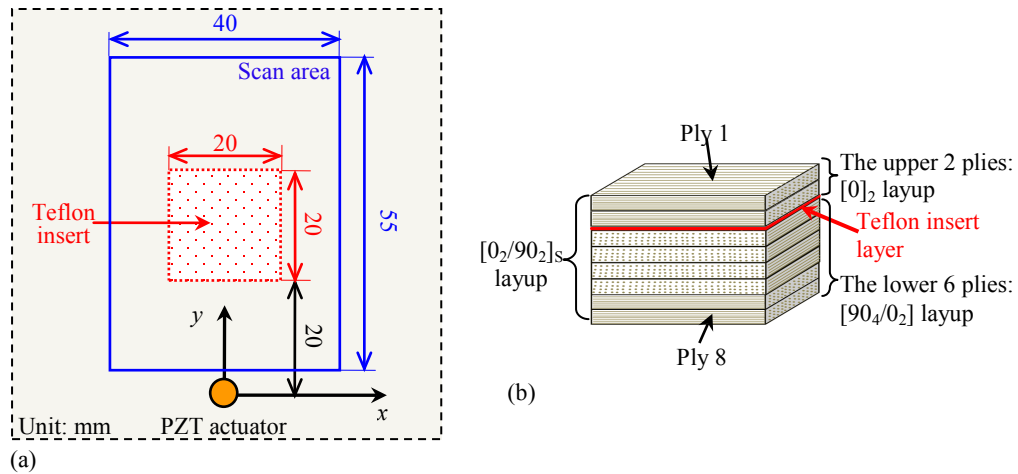


Figure 9.1 The scanning laser vibrometry test: (a) the sensing layout, (b) the side view of the $[0_2/90_2]_s$ composite plate with a Teflon insert, and (c) the experimental setup.

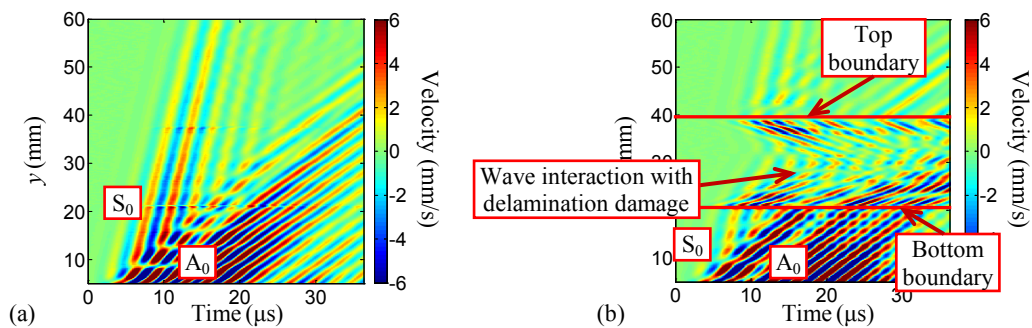


Figure 9.2 Time-space wavefields of waves propagating along the y axis: (a) for the pristine plate, and (b) for the plate with a Teflon insert. The two solid black lines at 20 mm and 40 mm are bottom and top boundaries of the delamination area.

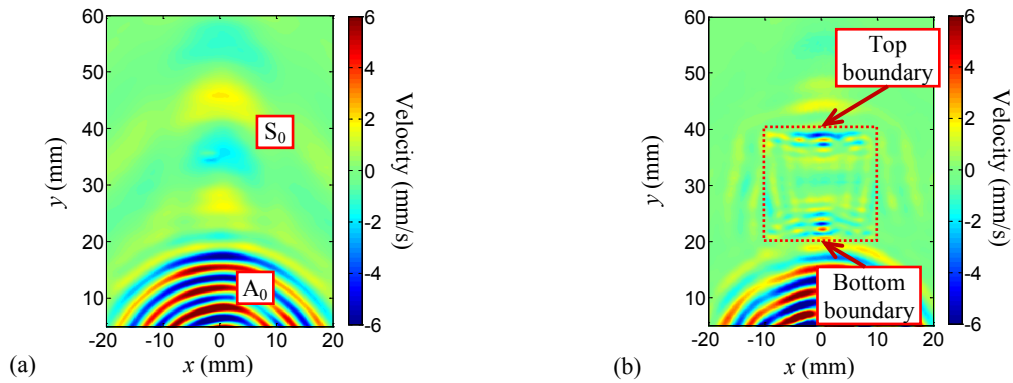


Figure 9.3 SLDV wavefield snapshots at 15 μ s: (a) for the pristine plate, and (b) for the plate with a Teflon insert. The red dotted box indicates the actual Teflon insert.

9.2.3. Frequency-wavenumber analysis

Complicated localized wave interactions at the Teflon delamination region are observed in the raw wavefield snapshot. To better understand the wave interactions occurring at the delamination region, time-space wavefields are converted to frequency-wavenumber representations by the 3-D FT. Figure 9.4 a and b plot the wavenumber spectra at 300 kHz achieved by the 3-D FT for the pristine and delaminated cases, respectively. To identify wave mode information, wavenumber spectra are compared to theoretical wavenumber curves which are plotted as dotted (A_0) and solid (S_0) lines. The pristine plate wavenumber spectrum (Figure 9.4 a) shows components, which match well with the theoretical wavenumber curves of A_0 and S_0 modes in the $[0_2/90_2]_S$ composite.

In the Teflon delaminated plate, the delamination damage splits the originally well bonded full laminate into two parts (above and below the delamination). Since the two separated material portions have different layups and thicknesses, compared to the original pristine laminate, the guided waves in the delaminated region will have modified propagation characteristics (such as modified dispersion and wavenumbers).

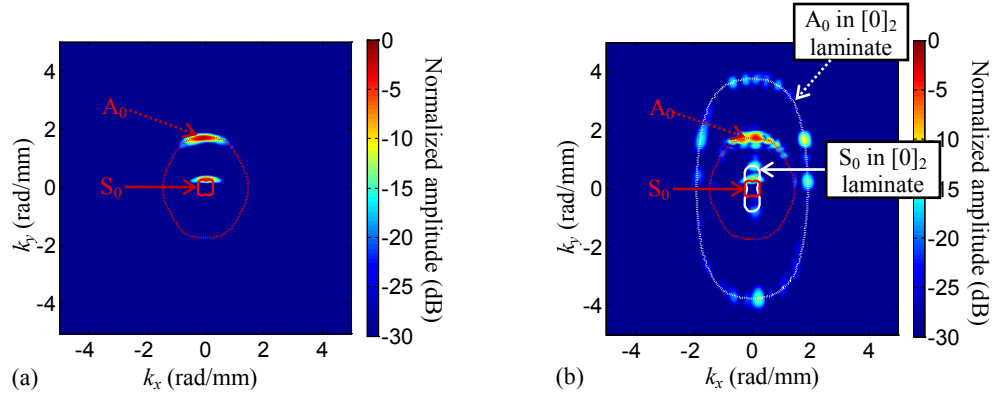


Figure 9.4 Wavenumber spectra at 300 kHz excitation frequency: (a) for the pristine plate, and (b) for the plate with a Teflon insert. The dotted and solid lines are theoretical wavenumber curves for A_0 and S_0 modes.

As expected, the spectrum of the delaminated case (Figure 9.4 b) shows wavenumber components in addition to the original A_0 and S_0 modes. The additional wavenumber components include both positive and negative counterparts, which correspond to forward and backward propagating waves, respectively. The additional wavenumber components are compared to wavenumber curves of the material above the delamination, equivalent to a two ply $[0]_2$ laminate, since only the waves in the top plate surface were measured in the experiment. The comparison in Figure 9.4b shows the additional wavenumber values match well with the theoretical curves of A_0 and S_0 modes in the two ply $[0]_2$ laminate.

9.3. DETECTION AND QUANTIFICATION OF SIMULATED DELAMINATION DAMAGE

9.3.1. Filter reconstruction imaging

From the frequency-wavenumber representation, additional wavenumber components are identified and believed to be related to the trapped waves in the delamination region. To confirm the correlation between the additional wavenumbers and the trapped waves, a filtering technique is applied to acquire and study only the additional wavenumbers in the

spectrum given in Figure 9.4 b, and then to reconstruct them back to the time-space domain.

To retain the additional wavenumbers that are believed to be correlated with the delamination (as indicated in Figure 9.4 b), a “band-pass” wavenumber filter is designed, as shown in Figure 9.5 a. The filter is then implemented by multiplying the band-pass filter with the spectrum $V(f, \mathbf{k})$. The resulted filtered spectrum in Figure 9.5 b only contains the delamination induced additional wavenumbers.

To understand what waves the filtered spectrum $V_F(f, \mathbf{k})$ represents, the corresponding time-space representation $v_F(t, \mathbf{x})$ is reconstructed by transforming the filtered spectrum $V_F(f, \mathbf{k})$ back to the time-space domain. Figure 9.6 a, b and c are filtered wavefields at 5 μs , 15 μs and 25 μs , respectively. It is seen that the additional wavenumbers correspond to waves that are well confined in the delaminated area.

With the filtered wavefield $v_F(t, \mathbf{x})$, we can therefore generate an intensity map or image of the cumulative wave energy that is trapped in the delamination area. The resulting energy map of the delaminated plate is given in Figure 9.6 d showing high energy concentrations at the delaminated region due to the wave trapping phenomenon. The energy map achieved from the filter reconstruction imaging can locate and roughly image the size and shape of the delamination damage in the laminated composite.

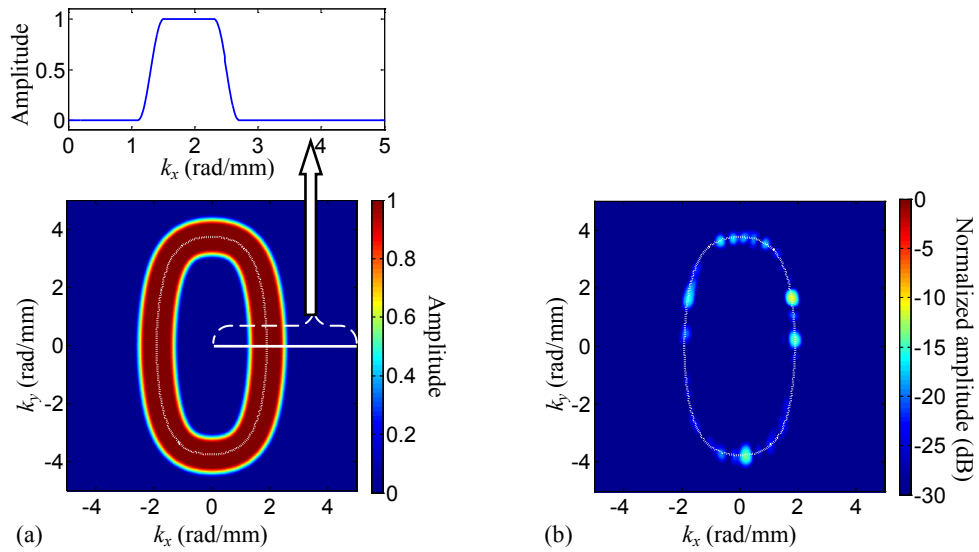


Figure 9.5 The filtering process in wavenumber domain: (a) band-pass wavenumber filter; (b) filtered spectrum for the plate with a Teflon insert. The dotted line is the theoretical wavenumber curve of the A_0 mode in the $[0]_2$ laminate above the delamination.

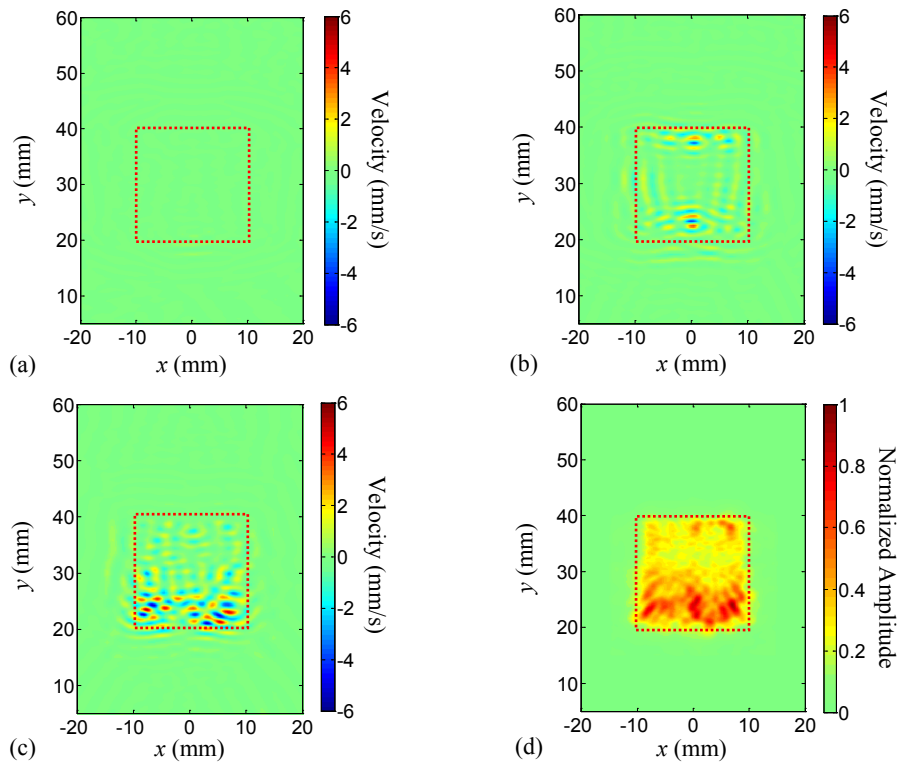


Figure 9.6 The filter reconstruction imaging results: (a) at $5 \mu\text{s}$, (b) at $15 \mu\text{s}$, (c) at $25 \mu\text{s}$, and (d) energy map. The red dotted box indicates the actual Teflon insert.

9.3.2. Spatial wavenumber imaging

The spatial wavenumber analysis is also applied for delamination detection and quantification. Figure 9.7 gives the spatial wavenumber image calculated from the wavefield data of the delaminated plate at the excitation frequency 300 kHz. The spatial wavenumber image indicates an area approximately $20 \text{ mm} \times 20 \text{ mm}$ in size which has significantly larger wavenumber values than the rest of the plate. This region matches well with the Teflon insert delamination location, shape, and size (indicated by the red dotted box in Figure 9.7). Clearly, the delamination affects wavenumbers of waves that interacts in the delamination region. The spatial wavenumber imaging shows its potential for detecting and quantifying the delamination damage.

Compared to the filter reconstruction imaging, the spatial wavenumber imaging is more robust. For the filter reconstruction imaging, wavenumber components need to be identified and selected from the wavenumber spectrum for the filtering process. However, if the excitation frequency and/or plate thickness increases, more wave modes are present and propagate in the plate. It can become difficult to identify and isolate specific wavenumber values in the spectrum of the damaged plate for the filter reconstruction imaging. In contrast, the spatial wavenumber imaging can directly generate a spatial map of wavenumber variations, and the delamination damage is directly observable as a region with altered wavenumbers.

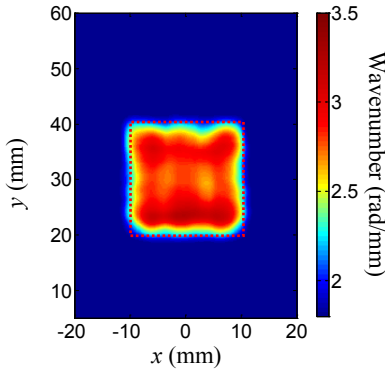


Figure 9.7 Spatial wavenumber image of the Teflon delaminated plate. The red dotted box indicates the actual Teflon insert.

9.3.3. Delamination depth quantification

It has been shown that the simple delamination (such as the Teflon insert in the experimental specimen) that splits the originally bonded laminate into two parts will result in waves propagating above and below the delamination. Since the materials above and below the delamination have different layups and thicknesses compared to the original pristine laminate, waves measured at an outer plate surface region above (or below) the delamination will have modified propagation characteristics and wavenumbers (which will depend on the number of plies in the split parts). Hence, the delamination depth can be estimated by relating the wavenumbers to the number of plies above (or below) the delamination.

In this study, the plies from the surface where waves are measured are numbered as ply 1, 2... etc., as shown in Figure 9.1 b. A set of theoretical dispersion curves is generated for laminates with different plies. Figure 9.8 a plots dispersion curves of A_0 modes in laminates of 1 to 8 plies. For example, a 5 ply laminate would consist of the uppermost 5 plies, [0/0/90/90/0]. Figure 9.8 b plots a theoretical wavenumber curve at 300 kHz for laminates of 1 to 8 plies. The theoretical wavenumber curve shows a relation

of wavenumber versus the number of plies. Therefore, if we know the wavenumber at the delamination damage, by fitting the delamination induced wavenumber to the theoretical wavenumber curve, the number of plies above the delamination (delamination depth) can be determined. For the spatial wavenumber image in Figure 9.7, the wavenumber is around 3.5 rad/mm in the delamination area. By comparing the wavenumber 3.5 rad/mm to the theoretical wavenumber curve in Figure 9.8 b, we can find the delamination damage is under the second ply.

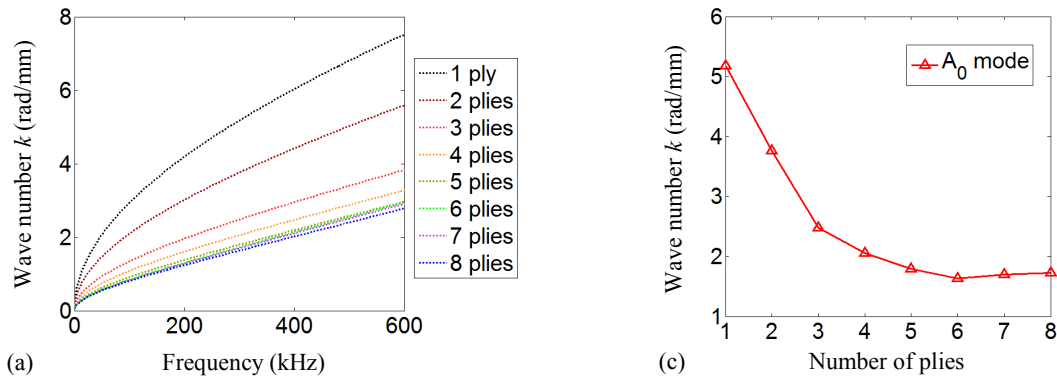


Figure 9.8 Dispersion curves of A_0 modes propagating towards the 90° direction: (a) dispersion curves for laminates of 1 to 8 plies; (b) wavenumbers at 300 kHz vs. the number of plies. (Note: the number of plies is counted from the top lamina).

9.4. DETECTION AND QUANTIFICATION OF IMPACT-INDUCED DELAMINATION DAMAGE

Although wavefield based imaging methods can give promising delamination detection and quantification results, these methods are based on full wavefields that usually take a long time to acquire since the SLDV needs to measure guided waves at a large number of points in the scanning area. Moreover, the wavefield based imaging methods only detect and quantify damage in the scanning area.

In contrast, the SLDV phased array imaging is a more efficient way to quickly inspect the specimen. The phased array imaging only needs to acquire guided waves in a

small scanning area. Moreover, the phased array imaging can detect damage outside the scanning area. Therefore, the SLDV phased array imaging is first used as a quick means to inspect the composite plate and to locate the delamination damage. Once the delamination damage is detected, wavefield based imaging methods are performed to further quantify the damage. The systemic combination of phased array imaging and wavefield based imaging provides a hierarchical damage diagnosis, which can efficiently and effectively locate the damage, and further quantify the damage. In this section, the combined phased array and wavefield based imaging methodology is used to detect and quantify impact-induced delamination damage in a composite plate.

9.4.1. Impact-induced delamination damage

The test specimen is a 26 ply IM7/8552 composite laminate (material properties listed in Table 9.9.1) with a quasi-isotropic layup of $[(0_2/45_2/-45_2)_2/90]_S$ and dimensions 381 mm \times 381 mm provided by LaRC. The delamination damage is created by a quasi-static indentation, which has been shown by other researchers to be an ideal method for controlled growth of impact-induced damage in composite laminates [32, 211]. Figure 9.9 a gives the quasi-static indentation setup. The composite plate is loaded in a mechanical testing system using a 50.8 mm diameter indenter at a constant displacement rate of 1.27 mm/min. The displacement and load are monitored during the indentation test and the composite is unloaded when the data shows a sudden drop in the load (due to damage growth), as shown in Figure 9.9 b. A photo of the composite plate after the indentation test is shown in Figure 9.10 a. In the zoomed in view, Figure 9.10 b, a very slight indentation can be observed on the surface with no other damage.

Following the quasi-static indentation test, an ultrasound C-scan is conducted at LaRC to quantify the delamination damage in the composite plate. The ultrasound data are collected in an immersion tank using a 10 MHz transducer and a scan step size of 0.25 mm. The resulting C-scan image in Figure 9.10 c shows multiple delaminations within a 32.3 mm × 22.6 mm damage zone, occurring at various depths (ply layers) through the plate thickness. The figure notes the ply depths at which the delaminations occur, determined through time of flight measurements from the ultrasound data.

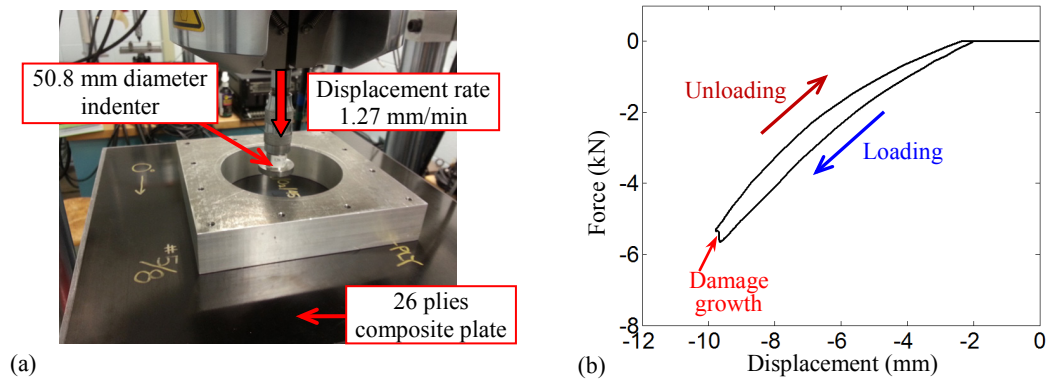


Figure 9.9 Quasi-static indentation for delamination damage growth: (a) the indentation setup, and (b) the curve of indentation force versus displacement.

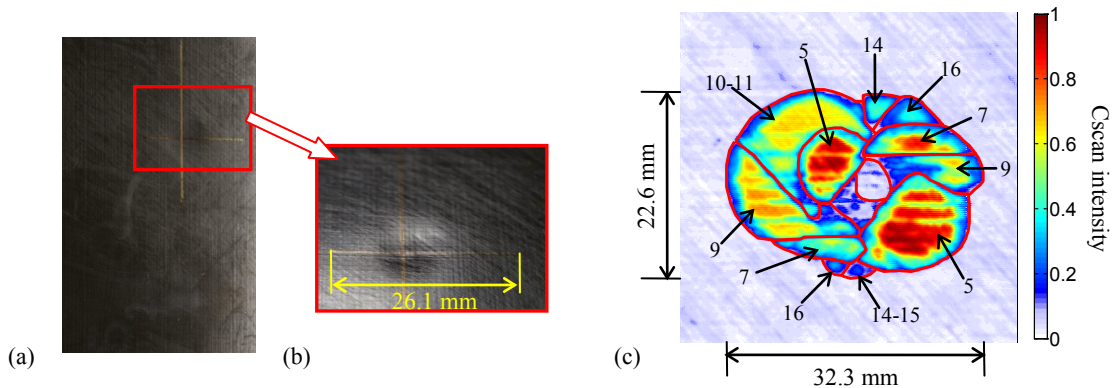


Figure 9.10 The 26 ply laminate after the quasi-static indentation test: (a) a photo of the specimen, (b) a zoomed in view of the indentation, and (c) an ultrasonic C-scan image showing internal delamination damage generated by the indentation test. The red solid lines in figure (c) represent boundaries of delaminations. The numbers in figure (c) represent delamination depths. For example, the number 5 represents the delamination is under the fifth ply.

9.4.2. Delamination detection using SLDV phased arrays

9.4.2.1. Experimental setup

Figure 9.11 plots a schematic of the SLDV phased array sensing layout for the impact induced delamination detection. A PZT wafer (7 mm diameter, 0.2 mm thickness) is bonded on the plate to generate guided waves. The center of the PZT is set as the coordinate origin. The center of the delamination is at the location (0 mm, 100 mm). A 3-cycle toneburst with the frequency 150 kHz and amplitude 30V is applied to the PZT wafer for excitation. The time-space wavefield in the scanning area, a 45 mm \times 45 mm square with the center at the coordinate origin, is measured by the SLDV. The horizontal and vertical spatial resolutions of the scanning are 0.1 mm. At 30 μ s, the measured wavefield in Figure 9.12 a shows incident waves generated from the PZT wafer. At 140 μ s, the wavefield in Figure 9.12 b shows guided waves reflected by the delamination damage. The wavenumber spectra in Figure 9.12 c and d reveal wavenumber components on the wavenumber curve of A_0 mode, indicating that the incident and reflected waves are A_0 mode.

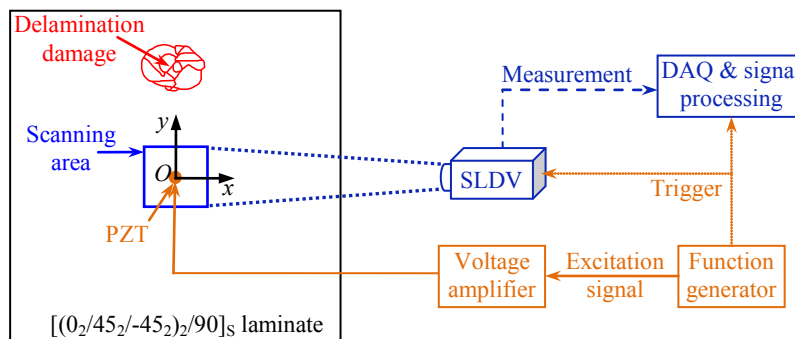


Figure 9.11 The SLDV phased array sensing layout for detecting and imaging the impact-induced delamination damage.

9.4.2.2. Array imaging results

31×31 points with the intervals $d_x=d_y=2$ mm, and the center at the origin are chosen from the SLDV scanning area to generate a grid array. Applying array imaging algorithms presented in Chapter 5, a beamformed wavefield $z(t, \mathbf{x})$ is obtained. The wavefield images at $t=80 \mu\text{s}$, $40 \mu\text{s}$ and $0 \mu\text{s}$ (Figure 9.13 a, b and c) show beamformed waves propagate in the 90° direction. At the time $t = 80 \mu\text{s}$, waves propagate from the phase array to the delamination damage. At the time $t = 0 \mu\text{s}$, waves arrive at the delamination damage. The imaging result in Figure 9.13 d reveals a damage area round the location $(-1.1, 103.5)$ mm with the error $(-1.1, 3.5)$ mm.

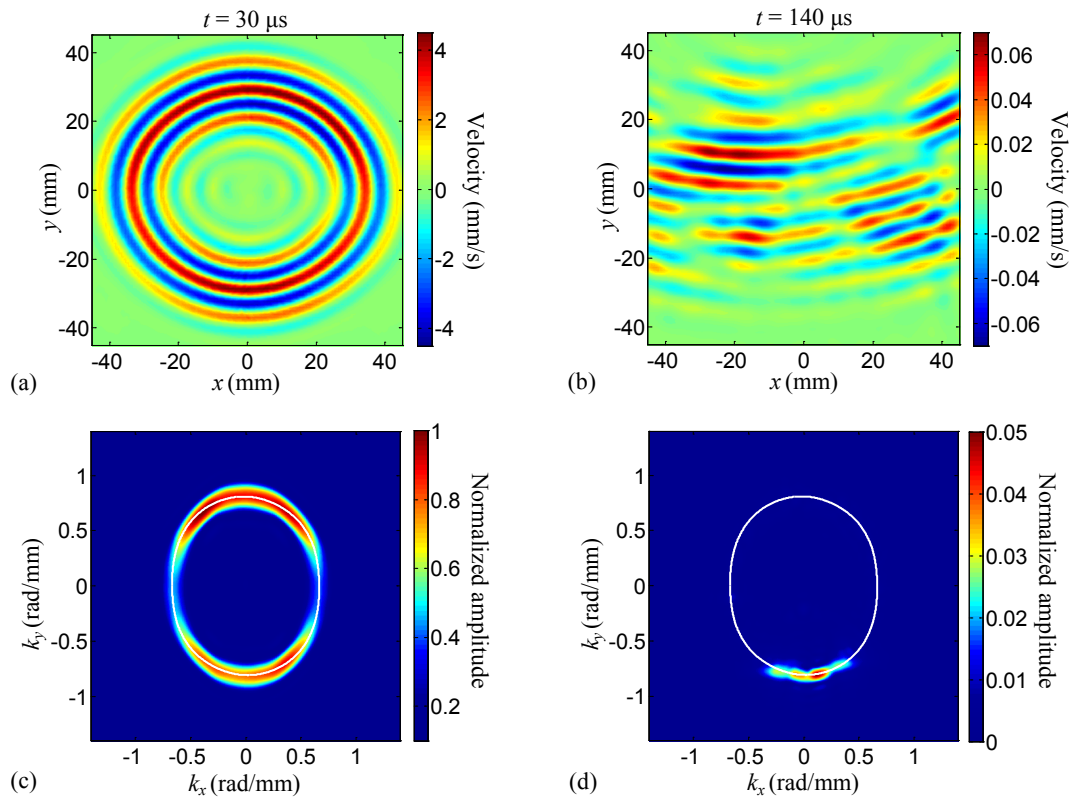


Figure 9.12. SLDV measurements: (a) and (b) are wavefields at $30\mu\text{s}$ and $140 \mu\text{s}$, showing the incident and reflected waves; (c) and (d) are wavenumber spectra of incident and reflected waves. The solid white lines in (c) and (d) are dispersion curves of the A_0 mode in the full layup laminate.

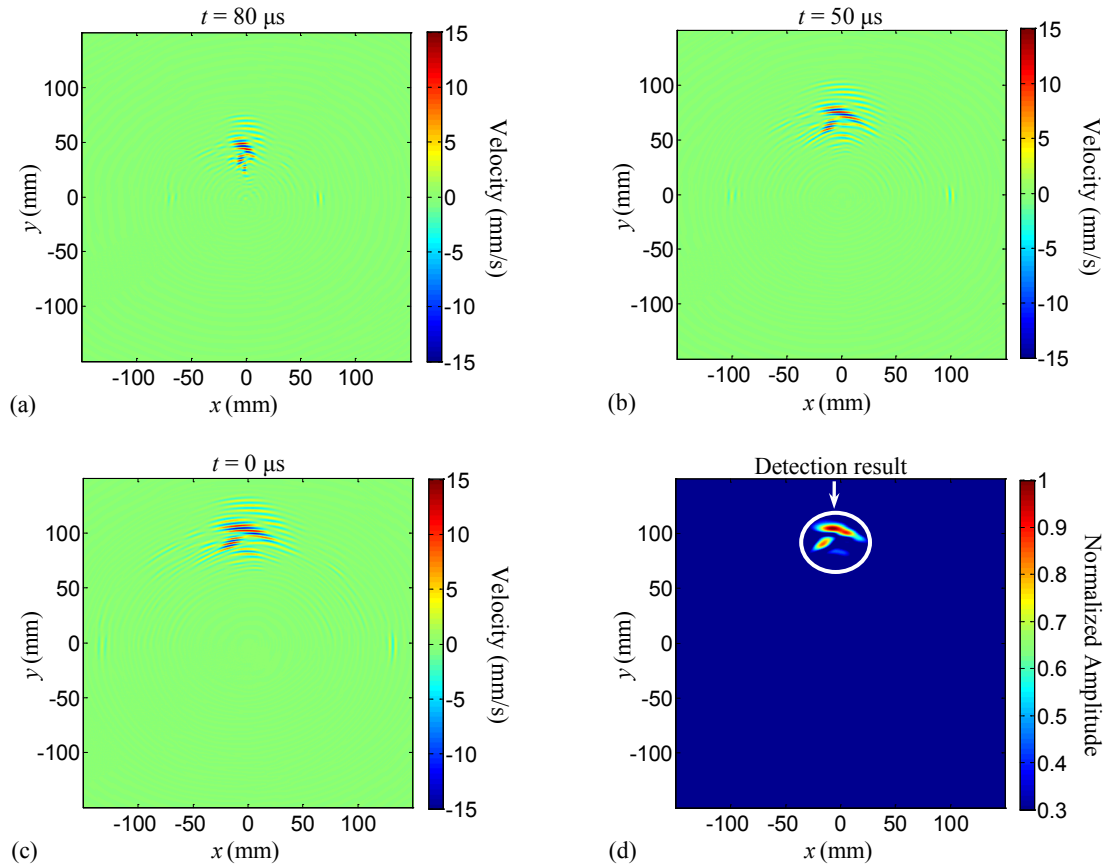


Figure 9.13 Phased array imaging results for detecting and imaging the impact-induced delamination damage: (a), (b), (c) are beamformed wavefields at 80, 40 and 0 μs , and (d) is the delamination detection result.

9.4.3. Delamination quantification using wavefield based imaging

Once the delamination damage is detected by the efficient SLDV phased array imaging, a refined scan will be performed in the damage region in order to perform the wavefield based imaging for damage quantification.

9.4.3.1. Experimental setup

Figure 9.14 plot a schematic of the experimental setup for the quantification of the impact-induced delamination damage. A 0.2 mm thick 7 mm round PZT is installed on the plate surface to actuate the guided waves. The center of the PZT is set as the origin.

The wavefields at two different excitation frequencies (low frequency 100 kHz and high frequency 500 kHz) are measured using the SLDV. Figure 9.15 a and b plot wavefields measured at the 100 kHz excitation frequency for the pristine and damaged plates. The pristine wavefield shows a single incident wave mode with a wavelength of 11.5 mm. The damaged wavefield shows strong wave interactions at the damage, compared to the pristine case. Figure 9.16 a and b plot wavefields at the 500 kHz excitation frequency for the pristine and damaged plates. Compared to the low frequency wavefield at 100 kHz in Figure 9.15 a, the pristine wavefield at 500 kHz in Figure 9.16 a is much more complex. For example, Figure 9.16 a shows various wave modes with different wavelengths, while the wavefield at 100 kHz only has one incident wave mode. Figure 9.16 b plots the 500 kHz wavefield for the damaged case. The wavefield shows strong wave interactions at the damage region. Moreover, the interaction pattern at 500 kHz in Figure 9.16 b is more complex than that at 100 kHz in Figure 9.15 b.

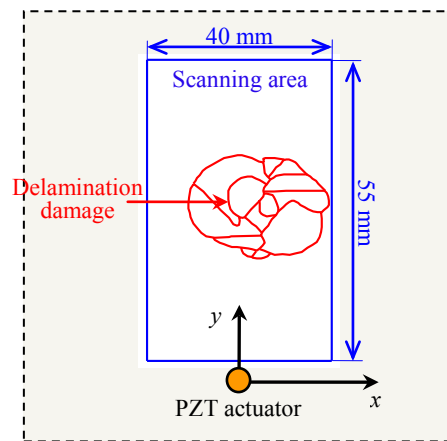


Figure 9.14 Experimental setup for quantifying the impact-induced delamination.

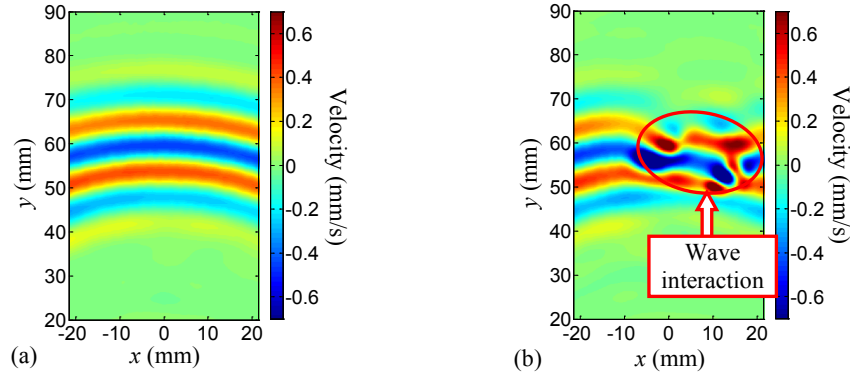


Figure 9.15 SLDV wavefield images at 45 μ s for 100 kHz excitation: (a) for the pristine plate, and (b) for the plate with damage.

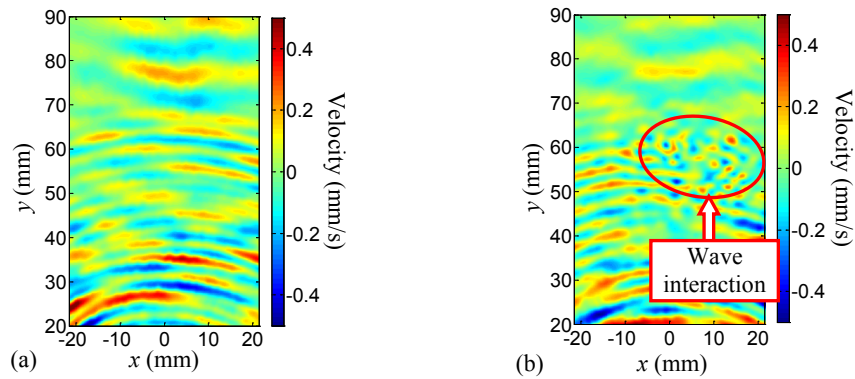


Figure 9.16 SLDV wavefield images at 40 μ s for 500 kHz excitation: (a) for the pristine plate, and (b) for the plate with damage.

9.4.3.2. Filter reconstruction imaging

To quantify the impact-induced delamination damage, the filter reconstruction imaging method is applied to wavefields measured from experiments. Figure 9.17 shows the filter reconstruction imaging process and result at the low frequency 100 kHz. In the pristine wavenumber spectrum Figure 9.17 a, there is only the incident A_0 wave mode, while additional wavenumber components present in the damaged plate spectrum Figure 9.17 b. The wavenumbers corresponding to the A_0 mode is removed using a band-stop filter. The resulted filtered spectrum is plotted in Figure 9.17 c. The energy map of the filtered components is given in Figure 9.17 d. The delamination damage shows up as an area with high energy which matches well with the C-scan result (contour plot).

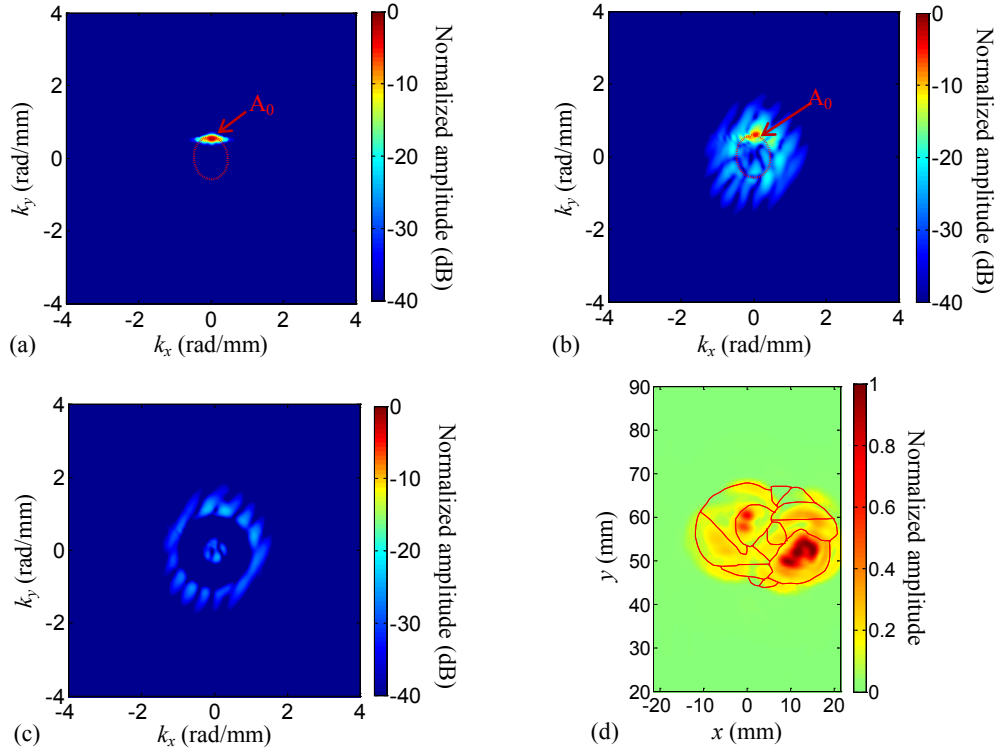


Figure 9.17 Filter reconstruction imaging at the low frequency 100 kHz: (a) wavenumber spectrum for the pristine plate, (b) wavenumber spectrum for the damaged plate, (c) filtered wavenumber spectrum, and (d) energy map. The red solid lines in figure (d) represent boundaries extracted from the C-scan image.

Figure 9.18 shows the filter reconstruction imaging process and result at the high frequency 500 kHz. Compared to the pristine spectrum at the low frequency 100 kHz, the pristine spectrum at 500 kHz in Figure 9.18 a contains more wave modes, including the A_0 , A_1 , S_0 , S_1 and S_2 modes. Moreover, the identification and isolation of additional wavenumbers in the spectrum of the damaged plate become more difficult than the low frequency case. A high-pass filter is applied to extract the additional wavenumbers that are larger than the A_0 mode. The filtering result in wavenumber domain is shown in Figure 9.18 c. The energy map of the filtered components is constructed and plotted in Figure 9.18 d. Compared to the low frequency 100 kHz, the energy map at 500 kHz

matches with a smaller portion of the C-scan result. It is expected that the portion of damage that does not show up in Figure 9.18 d may coincide with the delamination induced additional wavenumbers appearing in Figure 9.18 b that are cut out by the chosen filter.

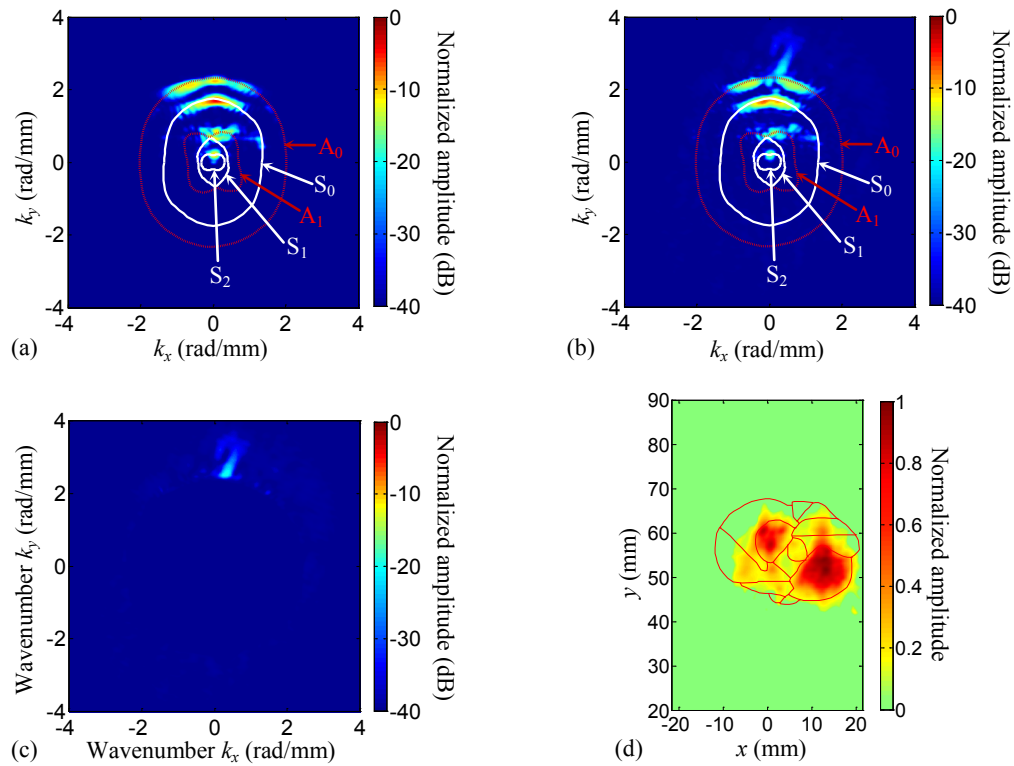


Figure 9.18 Filter reconstruction imaging at the high frequency 500 kHz: (a) wavenumber spectrum for the pristine plate, (b) wavenumber spectrum for the damaged plate, (c) filtered wavenumber spectrum, and (d) energy map. The red solid lines in figure (d) represent the boundaries extracted from the C-scan image.

9.4.3.3. Spatial wavenumber imaging

At the high frequency 500 kHz, the spatial wavenumber imaging method is applied to quantify the impact-induced delamination damage. Figure 9.19 plots the spatial wavenumber imaging result in the frequency band 480~520 kHz. The imaging result shows a region with increased wavenumbers, indicating the delamination damage. The

increased wavenumber region is observed to fall within the boundaries of the ultrasonic C-scan result (plotted as red solid lines in Figure 9.19).

In Figure 9.19, the detected delamination size in the wavenumber field is approximately $30 \text{ mm} \times 20 \text{ mm}$, which agrees well with the C-scan result ($32.3 \text{ mm} \times 22.6 \text{ mm}$). The delamination shape in the spatial wavenumber image matches closely with the uppermost portion of the delamination damage in the C-scan image. It is expected, as reported by other researchers, that the deeper delamination damage is more difficult to detect using wavefield based imaging methods [32]. The spatial wavenumber result shows that the delaminations closer to the SLDV scanned composite surface are easier to detect and result in relatively higher wavenumber modes in the damage region. For example, in the close surface delamination region under the fifth ply, the spatial wavenumber image gives large wavenumbers of nearly 3.4 rad/mm .

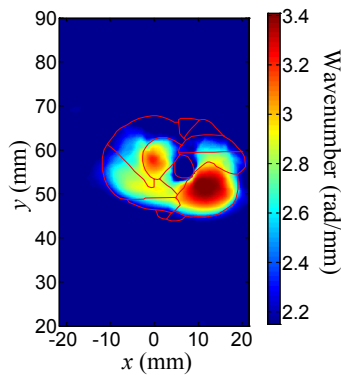


Figure 9.19 Spatial wavenumber imaging result in the frequency band 480~520 kHz.

CHAPTER 10

DEBONDING DETECTION AND QUANTIFICATION IN HONEYCOMB SANDWICH STRUCTURES

10.1. MOTIVATION AND INTRODUCTION

Honeycomb sandwich structures have been increasingly used for aerospace, marine and automotive applications, since they have attractive features such as high strength/stiffness-to-weight ratio, effective acoustic insulation, noise control and vibration damping [212-215]. However, due to the weak shear strength of the bonding layer, honeycomb sandwich structures are susceptible to debonding damage along the skin-core interface, especially under an intensive or repeating loading on the honeycomb core [72, 203, 216-218]. Since the debonding damage occurs internally between the skin panel and the honeycomb core, it is not visible to the naked eye [196]. The hidden debonding damage must be detected and evaluated, since it affects the integrity and safety of the whole structure.

In recent years, researchers investigated debonding detection in honeycomb sandwich structures by using guided waves [72, 188, 203, 216-221]. However, there are still many difficulties and challenges. Honeycomb sandwich structures have more complicated guided waves, compared to those in the traditional simple structures like metallic plates. In addition, honeycomb sandwich structures can have debonding damage between the skin panel and the complex geometry honeycomb core. Effects of debonding damage on guided waves are less studied in the literature.

This chapter presents the fundamental studies of guided waves in honeycomb sandwich structures, and the debonding detection and quantification using wavefield based imaging methods. Both finite element simulations as well as laser vibrometry experiments are performed to investigate guided waves in honeycomb sandwich structures. Guided wavefields at different frequencies are acquired and compared. To further understand the guided wave propagation fundamentals, the guided wavefields are transformed to wavenumber spectra. In the wavenumber domain, the wavenumber components of guided waves in honeycomb sandwich structures are investigated. Moreover, the guided wave interaction with debonding damage is investigated by using guided wavefields and wavenumber spectra. Last, wavefield based imaging methods are adopted to detect and quantify the debonding damage.

10.2. GUIDED WAVES IN HONEYCOMB SANDWICH STRUCTURES

10.2.1. Simulations of guided waves by using FEM

To understand how guided waves propagate in honeycomb sandwich structures, the commercial FEM software, ANSYS/Multiphysics 11.0, is used to simulate the guided waves. A finite element model of a honeycomb sandwich panel is built. The model setup is presented in Chapter 3. Guided waves in the sandwich at different frequencies, 15 kHz, 50 kHz, and 100 kHz, are simulated and compared. The simulation results show that at the low frequency 15 kHz, there are global guided waves in the entire sandwich plate, which have large wavelengths and elliptical wave fronts. At the higher 50 kHz, although global guided waves can still be observed, their wave fronts become closer to circular shapes other than elliptical shapes. At the highest frequency 100 kHz, global guided waves disappear, while guided waves in the skin plates with circular wave fronts are

observed. Moreover, the 100 kHz simulation result shows complex wave interactions with the honeycomb core. The details of simulation results can be found in Chapter 3.

10.2.2. Experimental characterizations by using the PZT-SLDV sensing

Laser vibrometry tests are performed to investigate guided waves in honeycomb sandwich structures. Figure 10.1 gives a schematic of the experimental setup. The honeycomb sandwich (dimensions: 305 mm \times 305 mm \times 15 mm) is composed of top and bottom aluminum alloy skins (T3003 aluminum alloy plates) and one hexagonal-celled $\frac{1}{4}$ inch aluminum core. The geometry parameters are listed in Table 10.10.1. Guided waves are excited by a surface bonded PZT actuator (APC 851: 7 mm diameter, 0.2 mm thickness) located at the coordinate origin. The SLDV is used to acquire the time-space wavefield over the scanning area. The scanning is performed in a 135 mm \times 135 mm scanning area with a spatial resolution of 0.2 mm. At each point, the measurement is averaged 30 times to improve the signal to noise ratio. Besides the guided waves in honeycomb sandwich, the guided waves in a single free top skin plate are measured for comparison purpose. Hence, the influence of the aluminum core on the wave propagation can be studied.

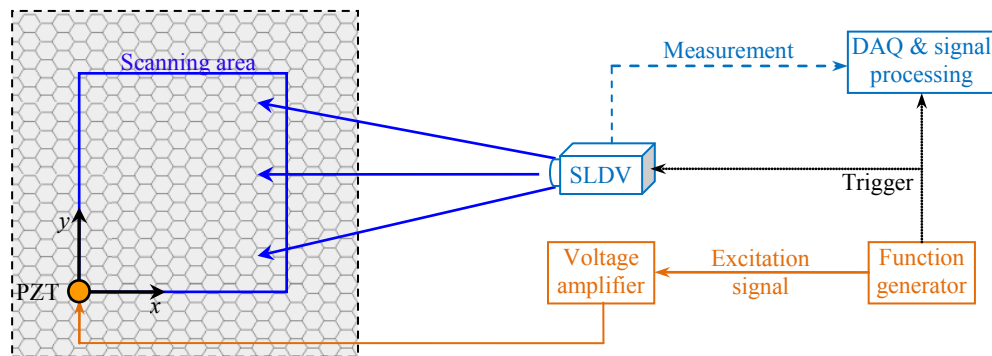


Figure 10.1 A schematic of the PZT-SLDV sensing setup.

Table 10.1 Geometry parameters of the honeycomb sandwich structure (units: mm).

Skin panels			Honeycomb core		
Length	Width	Thickness	Cell size	Wall thickness	Height
135	135	1	6.35	0.055	12.7

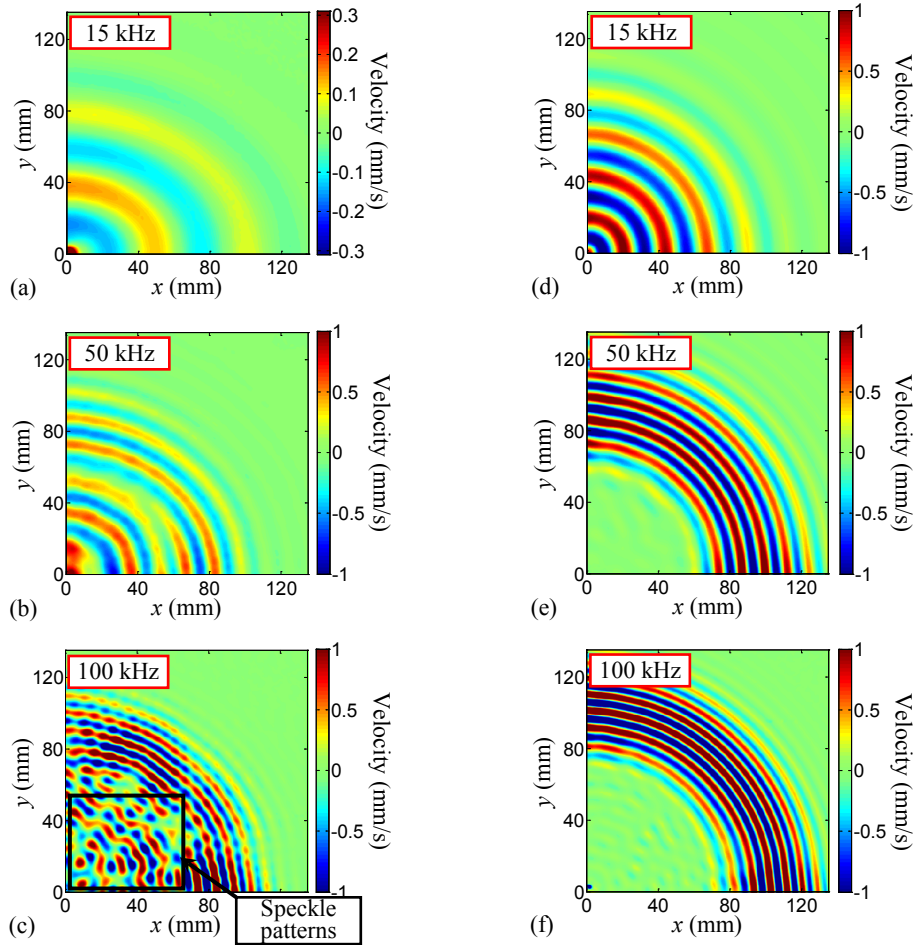


Figure 10.2 Wavefields measured from the experiment: (a), (b) and (c) are wavefields in the honeycomb sandwich at 15 kHz, 50 kHz and 100 kHz; (d), (e) and (f) are wavefields in the single skin plate at 15 kHz, 50 kHz and 100 kHz.

Figure 10.2 a, b and c are experimental results of the honeycomb sandwich at three different excitation frequencies 15 kHz, 50 kHz and 100 kHz, respectively; and

Figure 10.2 d, e and f are the results of the single skin plate. At the low frequency 15 kHz, guided waves in the honeycomb sandwich have elliptical wave fronts and larger wavelengths, compared to those in the single skin plate. When the frequency goes higher from 15 kHz to 100 kHz, the wave fronts in the honeycomb sandwich are gradually changing from elliptical fronts to circular fronts, as the wavelengths in the honeycomb sandwich are getting closer to the wavelengths in the single skin plate. At the highest frequency 100 kHz, the wave fronts in the honeycomb sandwich become circular, and the wavelength in the honeycomb sandwich is nearly the same as the wavelength in a single plate. Moreover, at 100 kHz, the wavefield in Figure 10.2 c shows speckle patterns which might be induced by the wave interaction with the inside honeycomb core.

10.2.3. Frequency-wavenumber analysis

The frequency-wavenumber analysis is applied to the experimental guided wavefields in order to investigate the wavenumber information. For the single skin plate, wavenumber spectra in Figure 10.3 d, e and f show circular ring-shaped wavenumber bands which agree well with theoretical wavenumber curves of the plate A_0 mode. Compared to the single skin plate, the honeycomb sandwich gives different wavenumber spectra, as shown in Figure 10.3 a, b and c. The spectrum at 15 kHz shows an elliptical ring-shaped wavenumber band, which has smaller wavenumbers than the plate A_0 mode (represented by the solid line). With the increase of frequency from 15 kHz to 100 kHz, the wavenumber band expands and the wavenumber values increase. Moreover, the elliptical-shaped wavenumber band is gradually getting closer to the wavenumber curve of the plate A_0 mode. The comparisons show that guided waves in the honeycomb sandwich have different wavenumbers compared to the single skin plate, and with the

increase of wave frequency, the wavenumber in the honeycomb sandwich is gradually asymptotic to that in the single skin plate.

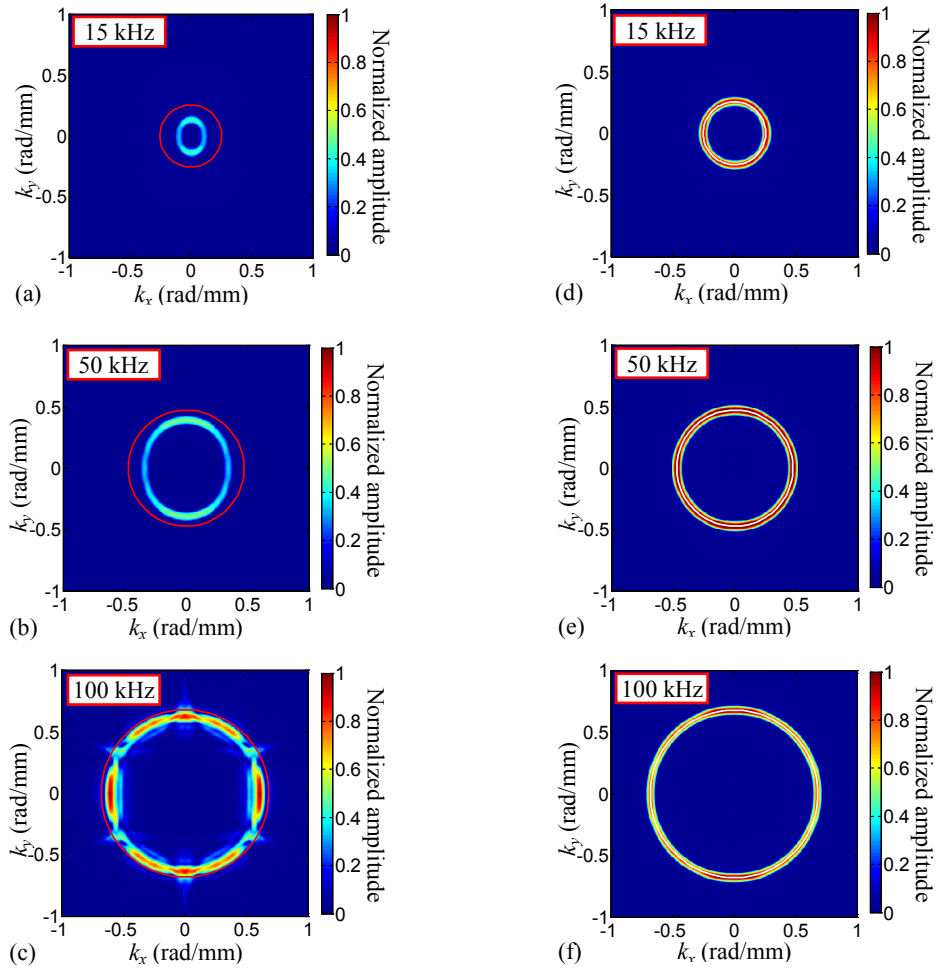


Figure 10.3 Wavenumber spectra: (a), (b) and (c) are spectra at 15 kHz, 50 kHz and 100 kHz for the honeycomb sandwich; (d), (e), and (f) are spectra at 15 kHz, 50 kHz and 100 kHz for the single skin plate. The solid line represents the theoretical wavenumber curves of the A_0 mode in the single skin plate.

10.3. WAVE INTERACTION WITH DEBONDING DAMAGE

10.3.1. Experimental setup

The influences of debonding damage on guided waves in honeycomb sandwich structures are investigated. Two sandwiches with the same dimensions $305 \text{ mm} \times 305 \text{ mm} \times 15 \text{ mm}$ are used. One is the pristine, while the other contains debonding damage with the size of $58 \text{ mm} \times 58 \text{ mm}$, which is created by removing the adhesive during the manufacturing process. Figure 10.4 gives the experimental sensing layout. The scanning is performed in a $150 \text{ mm} \times 150 \text{ mm}$ scanning area with a spatial resolution of 0.2 mm . Two frequencies, the high frequency 100 kHz and the low frequency 40 kHz , are tested.

10.3.2. Wave interaction with debonding damage at 100 kHz

Figure 10.5 plots the SLDV measurements at the high frequency 100 kHz for the pristine and damaged sandwiches. The results of both the pristine and damaged sandwiches show waves generated from the PZT propagating forward. Moreover, there are speckle patterns left behind the wave fronts, which are induced by wave interactions with the honeycomb core. Compared to the pristine sandwich, the damaged sandwich has less wave interactions with the honeycomb core: (i) the wave fronts are smoother and (ii) the speckle patterns have lower amplitudes in the damage sandwich.

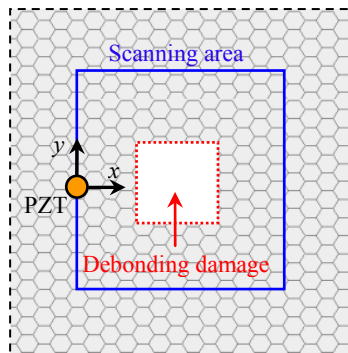


Figure 10.4 The sensing layout of the PZT-SLDV experiment on a honeycomb sandwich with debonding damage in the center of the sandwich.

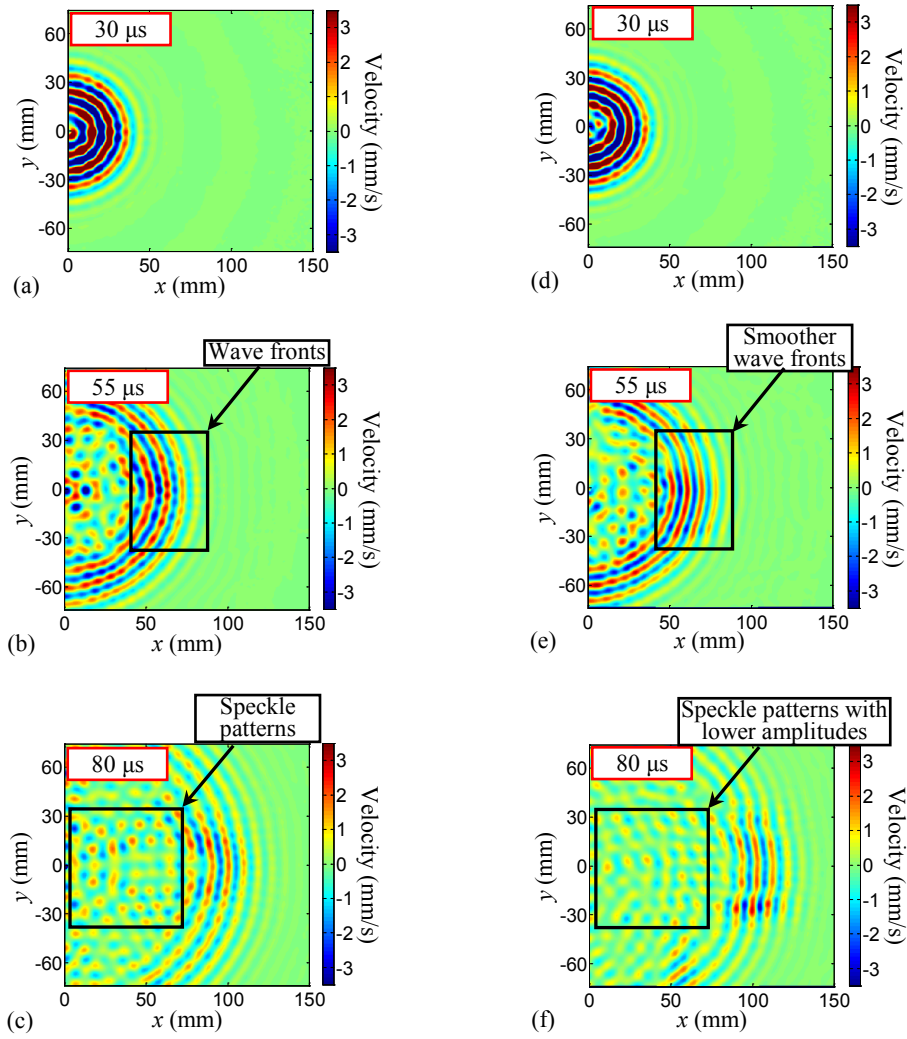


Figure 10.5 Experimental results at the high frequency 100 kHz for the pristine (left column) and damaged (right column) sandwich structures: (a) and (d) at 30 μs ; (b) and (e) at 55 μs ; (c) and (f) at 80 μs .

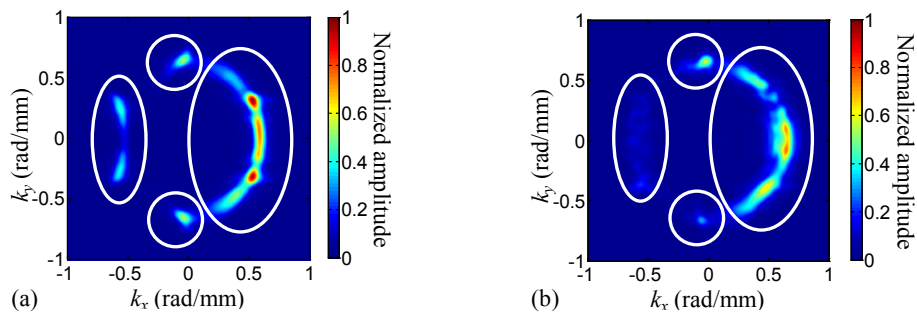


Figure 10.6 Wavenumber spectra at 100 kHz: (a) for the pristine sandwich and (b) for the sandwich with debonding damage.

For further analysis, the wavefields are transformed to the frequency-wavenumber spectra. For the pristine sandwich, the spectrum is plotted in Figure 10.6 a, which shows four distinct wavenumber components, the right, left, top and bottom components. In order to know why these components appear and what waves do they represent, the wavenumber spectrum in Figure 10.6 a is decomposed into individual components, as plotted in Figure 10.7 a, b, c and d. By using the inverse Fourier transform, the wavefields that correspond to the decomposed spectra in Figure 10.7 a, b, c and d are constructed, as plotted in Figure 10.7 e, f, g and h, respectively. The constructed wavefields show waves propagate forward, backward, upward and downward. The forward waves in Figure 10.7 e are generated from the PZT actuator and gradually propagate away from the actuator. The backward waves in Figure 10.7 f are the reflection waves induced by the honeycomb core. Moreover, the upward and downward waves in Figure 10.7 g and h are the scattering waves induced by the honeycomb core.

Figure 10.6 b plots the wavenumber spectrum for the honeycomb sandwich with debonding damage. Figure 10.8 a, b, c and d are the decomposed wavenumber spectra. Figure 10.8 e, f, g and h are the decomposed wavefields. These decomposed wavefields are compared to the wavefields for the pristine sandwich in Figure 10.7 e, f, g and h. It can be found that the amplitudes of backward waves (in Figure 10.8 f) are lower in the sandwich with debonding damage. The possible reason is that in the ideal debonding region the honeycomb core is fully detached from the skin plate and cannot induce any reflection wave.

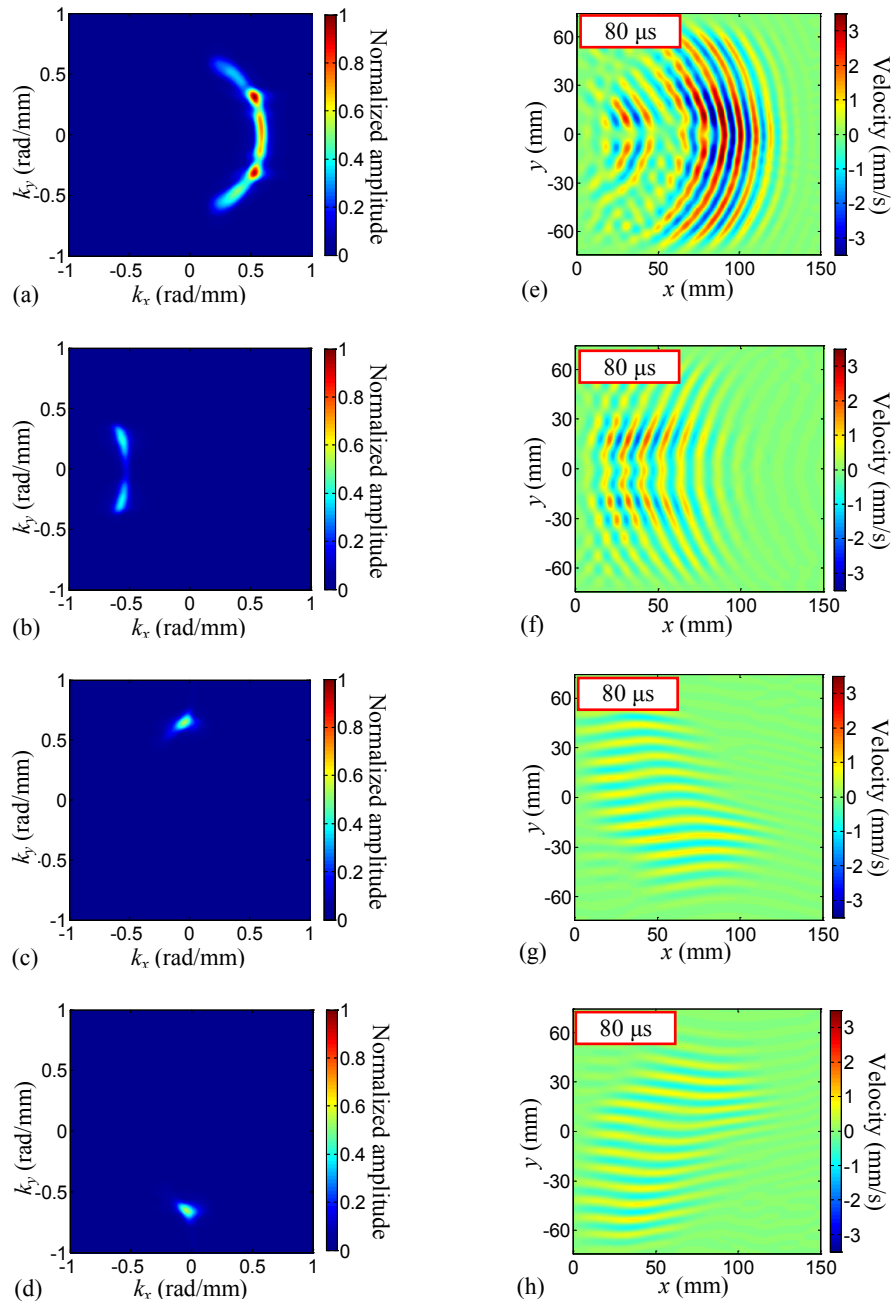


Figure 10.7 Wave decomposition for the pristine sandwich: (a), (b), (c) and (d) are decomposed right, left, top and bottom parts of the wavenumber spectrum at 100 kHz, respectively; (e), (f), (g) and (h) are decomposed wavefields at $80 \mu\text{s}$, which correspond to the spectra in (a), (b), (c) and (d), respectively.

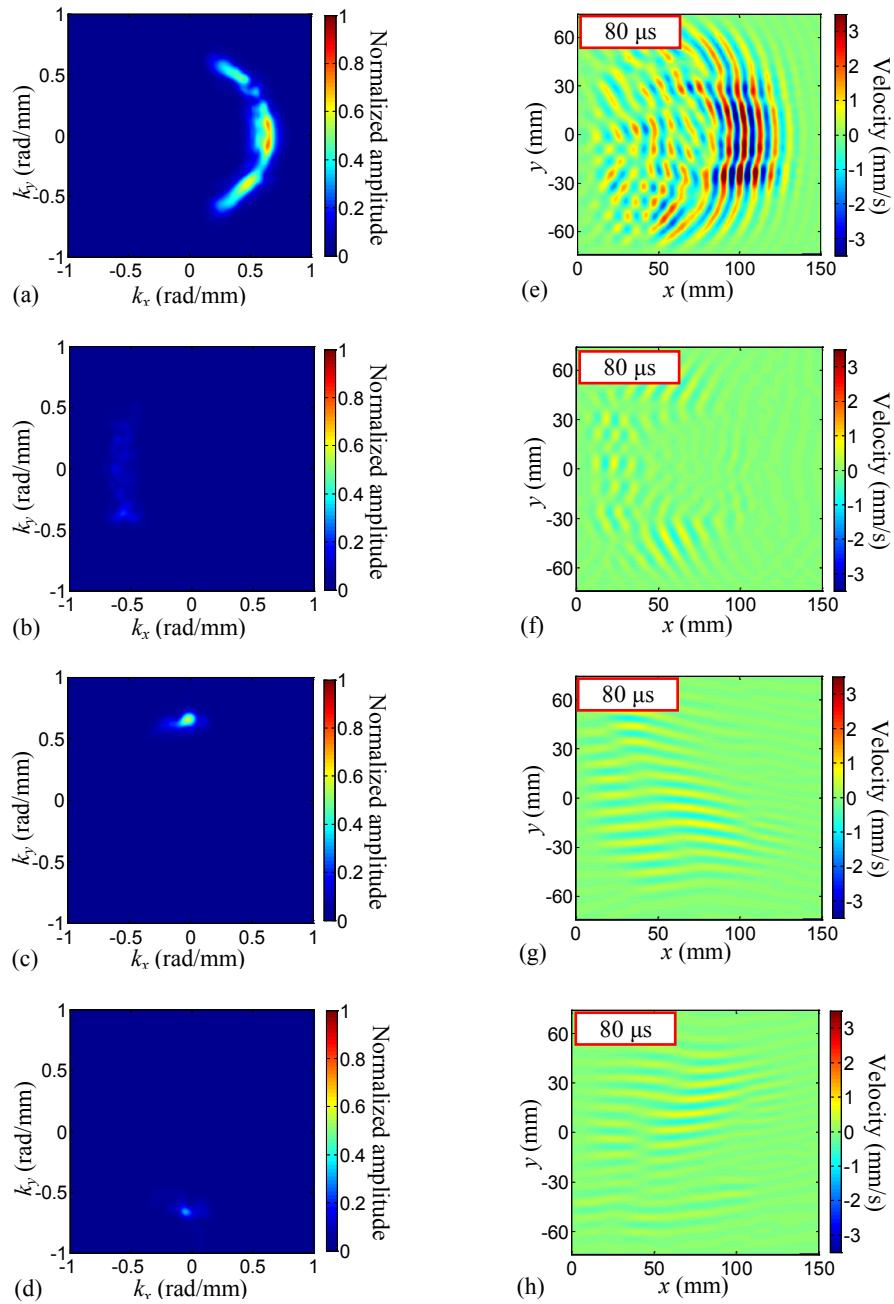


Figure 10.8 Wave decomposition of the waves in the sandwich with debonding damage: (a), (b), (c) and (d) are decomposed right, left, top and bottom parts of the wavenumber spectrum at 100 kHz, respectively; (e), (f), (g) and (h) are decomposed wavefields at 80 μ s which corresponds to the spectra in (a), (b), (c) and (d), respectively.

10.3.3. Wave interaction with debonding damage at 40 kHz

Figure 10.9 plots the experimental measurements at the low frequency 40 kHz for the pristine and damaged sandwich structures. Compared to the waves in the pristine sandwich, the waves in the damaged sandwich show strong interactions with the debonding damage. Moreover, at 160 μs after passed the damage area, the waves in the damaged sandwich (Figure 10.9 f) show higher amplitudes than the waves in the pristine sandwich (Figure 10.9 c).

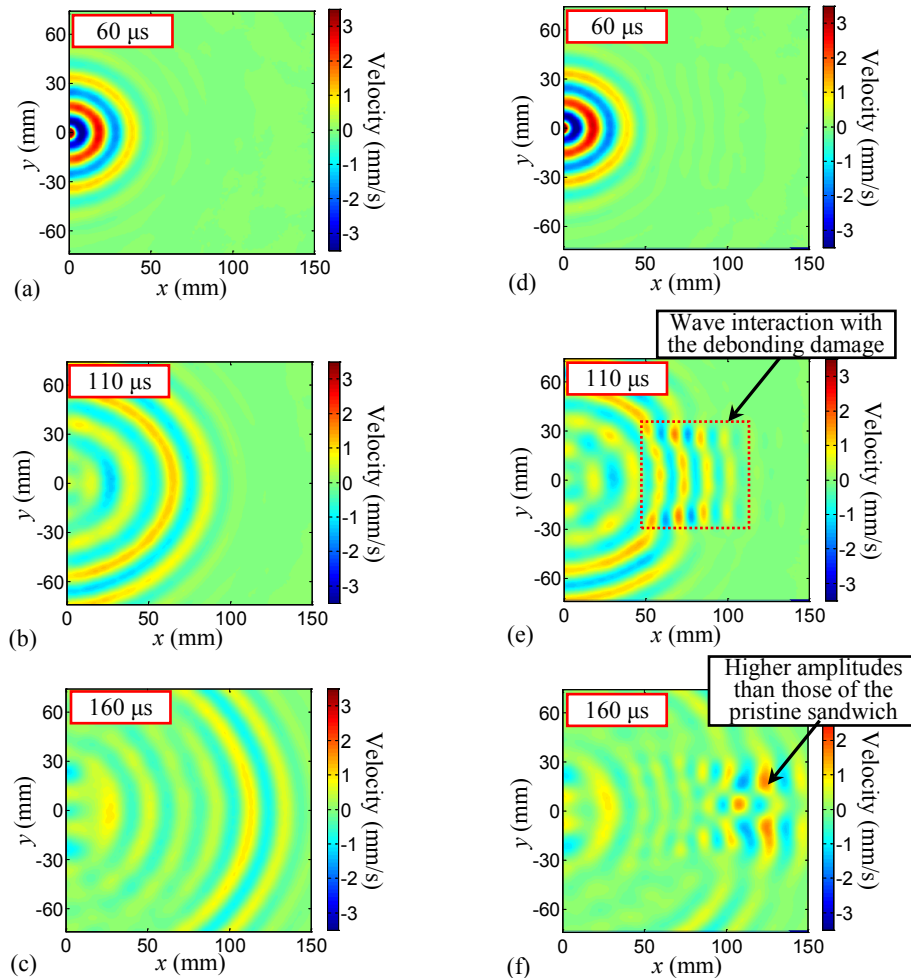


Figure 10.9 Experimental results at the low frequency 40 kHz for the pristine (left column) and damaged (right column) sandwich structures: (a) and (d) at 60 μs ; (b) and (e) at 110 μs ; (c) and (f) at 160 μs .

Figure 10.10 a and b are wavenumber spectra for the pristine and damaged honeycomb sandwiches. The wavenumber spectrum of the damaged sandwich in Figure 10.10 b shows an additional wavenumber component, compared to the spectrum of the pristine sandwich. To identify the waves of the additional wavenumber component, this additional component is extracted by using the frequency-wavenumber filtering (in Figure 10.10 c), and then reconstructed to the wavefield (in Figure 10.10 d). The reconstructed wavefield shows waves inside the debonding area. This means the additional wavenumber component is related to the waves inside the debonding area. Therefore, the additional wavenumber component can be used for debonding detection.

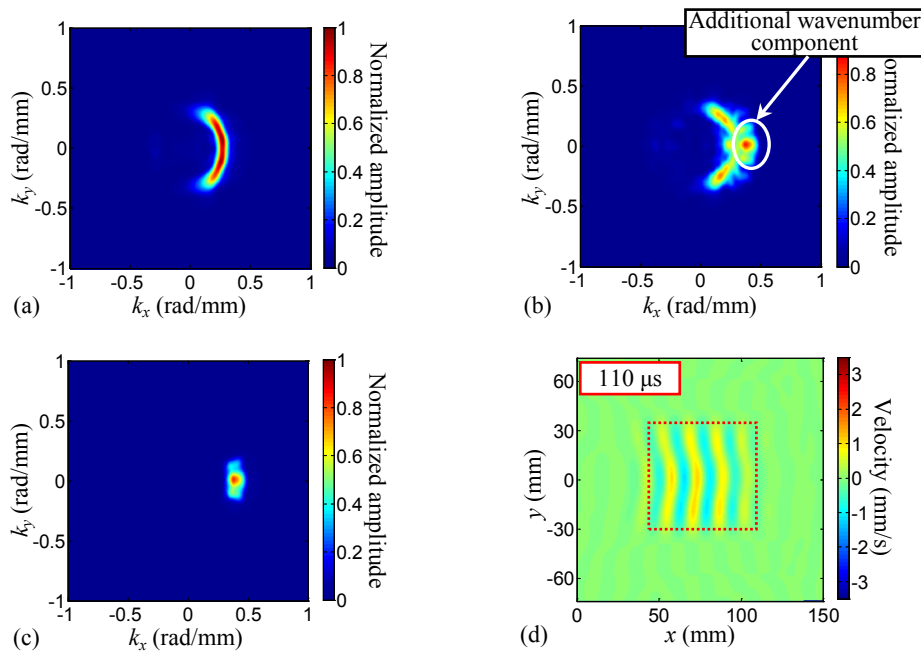


Figure 10.10 Wavenumber analysis results at 40 kHz: (a) wavenumber spectrum for the pristine sandwich, (b) wavenumber spectrum for the sandwich with debonding damage, (c) filtered wavenumber spectrum, and (d) reconstructed wavefield at 110 μ s that corresponds to the spectrum in (c). The dotted box represents the area of actual debonding damage.

10.4. DEBONDING DETECTION AND QUANTIFICATION

The analysis of wave interaction with debonding damage at 40 kHz show that additional wavenumber component which relates to the waves in the debonding area appears in the wavenumber spectrum. To detect and quantify the debonding damage, the filter reconstruction imaging method is applied. The energy map of the filtered waves is shown in Figure 10.11 a. The energy map shows a high energy area which matches well with the debonding damage (the dotted box in Figure 10.11 a).

Besides the filter reconstruction imaging, the spatial wavenumber imaging is applied. Figure 10.11 b plots the result of spatial wavenumber imaging in the frequency band 35~45 kHz. The imaging result shows an area with increased wavenumber values, indicating the debonding damage. The increased wavenumber area agrees well with the debonding damage (the dotted box in Figure 10.11 b).

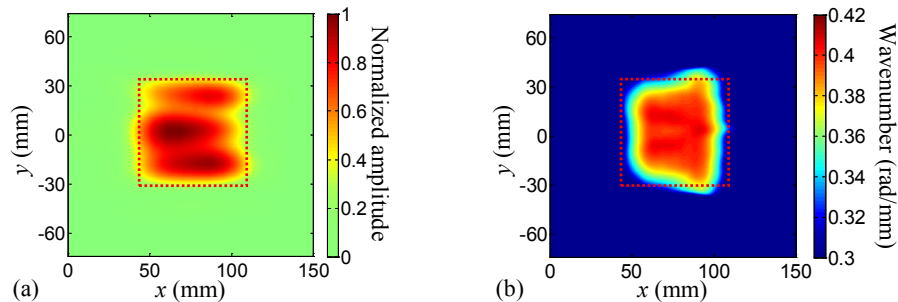


Figure 10.11 Debonding detection and quantification: (a) the result of filtering reconstruction imaging, and (b) the result of spatial wavenumber imaging. The dotted box represents the area of actual debonding damage.

CHAPTER 11

CONCLUDING REMARKS AND FUTURE WORK

This dissertation research develops guided wave based integrated SHM/NDE methodologies for damage detection and quantification in complex structures. The integrated SHM/NDE methodologies provide non-contact guided wave sensing for wave visualization and high spatial resolution wavefield acquisition, intrinsic wavefield analysis and characterization methods for the interpretation of complex wave propagation and interaction phenomenon, and hierarchical damage diagnosis for quantitative and visualized damage detection.

Part I focuses on the development of integrated SHM/NDE methodologies. First, a non-contact laser vibrometry sensing system is optimized to visualize the guided wave propagation and interaction and to acquire high spatial resolution wavefields of guided waves. Second, to extract informative wave signatures from the wavefields and characterize complex wave propagation and interaction phenomenon, guided wavefield analysis methods, including frequency-wavenumber analysis, wavefield decomposition and space-frequency-wavenumber analysis are investigated. Using these analysis methods, multi-modal and dispersive guided waves can be resolved and complex wave propagation and interaction can be interpreted and analyzed in time, space, frequency and wavenumber multi-domains. Third, a hierarchical damage diagnosis methodology is developed for quantitative and visualized damage detection. The hierarchical

methodology systematically combines phased array imaging and wavefield based imaging to achieve efficient and precise damage detection and quantification.

In Part II, the developed methodologies are applied to five different SHM/NDE applications: (1) gas accumulation detection and quantification in water loaded structures, (2) crack damage detection and quantification in isotropic plates, (3) thickness loss evaluation in isotropic plates, (4) delamination damage detection and quantification in composite laminates, (5) debonding detection and quantification in honeycomb sandwich structures.

This dissertation research will initiate sensing and diagnosis methodologies that provide rapid non-contact inspection of damage and diagnosis of structural health. Moreover, this research provides intrinsic guided wave analysis methods which can be used to analyze multi-modal wave propagation and interaction in complex structures. These analysis methods will benefit researchers in understanding complex wave propagation and interaction phenomenon and acquiring intrinsic wave signatures. Last but not least, this dissertation research provides efficient and precise integrated SHM/NDE methodologies for quantitative and visualized damage detection in complex structures. In the long run, this research will contribute to the development of advanced sensor and sensing technologies based on guided waves, and to providing on-demand health information at component or subsystem level for the safety and reliability of structures.

11.1. RESEARCH CONCLUSIONS

11.1.1. Analytical and numerical studies of guided waves

In Chapter 3, both analytical and numerical studies of guided waves are performed to provide preliminary understanding of guided waves in complex structures, theoretical data for assisting experimental work, and abundant information for parametric studies. Both analytical and numerical methods are used to investigate guided waves in different complex structures and wave interactions with defects or changes of boundary conditions.

Guided waves in a plate with one side in water are investigated. By using the GMM, dispersion curves and mode shapes of guided waves in the plate with one side in water are derived. Compared to dispersion curves of a free plate, those of the plate in water have an additional wave mode, the quasi-Scholte mode, which is dispersive at low frequencies and asymptotes to the non-dispersive Scholte mode at high frequencies. Moreover, EFIT simulations are performed to simulate guided waves in the plate with one side in water. The simulation results confirm the appearance of the quasi-Scholte mode. The simulation results also show leak guided waves in water induced by the energy leakage of guided waves in the plate.

Guided waves in composite laminates are investigated. By using the SAFE method, dispersion curves and mode shapes of guided waves in a composite laminate are derived. From dispersion plots, it is found that both wavenumber and group velocity depend on wave propagation direction. Moreover, EFIT simulations are performed to investigate guided wave interaction with delamination damage. Simulation results show that once arrived to the delamination damage, incident guided waves separate to different waves propagating in the materials above and below the delamination damage. These

waves above and below the delamination have different wavenumbers and wave speeds compared to the incident waves in the full laminate.

Guided waves in honeycomb sandwich structures are simulated by using FEM. The finite element model is constructed of a hexagonal aluminum core and two aluminum skins. FEM results show that at low frequency 15 kHz, the entire sandwich serves as a waveguide, in which global guided waves propagate with large wavelengths and elliptical wave fronts. With the increase of wave frequency from 15 kHz to 100 kHz, wavelengths gradually decrease and wave fronts gradually change from elliptical wave fronts to circular wave fronts. Moreover, global guided waves gradually disappear which means it becomes difficult for the global guided waves to propagate in the entire sandwich. At high frequency 100 kHz, the global guided waves completely disappear, and most of wave energy propagates in the skin plate in the form of Lamb waves. These Lamb waves strongly interact with the honeycomb core, generating complex wave interactions.

11.1.2. Wavefield acquisition and intrinsic characterization

In Chapter 4, a laser vibrometry sensing system is optimized to achieve rapid, high spatial resolution and non-contact sensing for guided wave visualization and wavefield measurements. The optimized laser vibrometry sensing system can be used to visualize guided wave propagation and interaction. Moreover, the sensing system provides an immediate means of damage evaluation. Experiments have been performed to demonstrate the sensing system for crack detection in an aluminum plate and delamination detection a composite plate. For the crack detection, the experimental measurement visualizes incident waves, crack reflection waves and transmission waves.

The crack location can be qualitatively identified from the measurement. For delamination detection, the experimental measurement visualizes complex wave interactions at the delamination damage. Guided waves propagating back and forth between the delamination boundaries are observed, exhibiting the “trapped wave” phenomenon. The location of delamination damage can also be qualitatively seen from the experimental measurement.

Guided wavefields in terms of time and space dimensions contain a wealth of information regarding guided wave propagations in structures and wave interactions with structural discontinuities. To extract informative wave signatures from the time-space wavefields and characterize the complex wave propagation and interaction phenomenon, guided wavefield analysis methods, including frequency-wavenumber analysis, wavefield decomposition and space-frequency-wavenumber analysis, are investigated. Using these analysis methods, multi-modal and dispersive guided waves can be resolved, and complex wave propagation and interaction can be interpreted and analyzed in time, space, frequency and wavenumber multi-domains.

11.1.3. Quantitative and visualized damage diagnosis

In Chapter 5, a hierarchical damage diagnosis methodology is developed for quantitative and visualized damage detection. The hierarchical methodology systematically combines phased array imaging and wavefield based imaging to achieve efficient and precise damage detection and quantification. Using the phased array imaging, an intensity scanning image of the structure is generated to efficiently visualize and locate the damage zone. Then the wavefield based imaging is applied to precisely quantify the damage size, shape and depth.

The generic phased array imaging is developed based on the classic delay-and-sum principal, in which directional dependent guided wave parameters are considered. This formulation is valid not only for the case that phase and group velocities have the same orientation, but also for the general case that the two velocities are in different directions. Therefore, this generic phased array imaging works for both isotropic and anisotropic materials. For the proof of concept, an experimental test is performed using the generic phased array imaging to detect multiple defects in an anisotropic composite laminate. In the test, the phased array is constructed with scanning points of a non-contact SLDV. Experimental results show that multiple defects in different directions *w.r.t.* the array center can be successfully detected.

Two wavefield based imaging methods, the filter reconstruction imaging and the spatial wavenumber imaging, are investigated to precisely quantify the damage size, shape and depth. The filter reconstruction imaging is based on the frequency-wavenumber filtering process by extracting damage induced frequency-wavenumber components and reconstructing them to a time-space wavefield which only contains damage induced waves. The filter reconstruction imaging provides a rapid technique to locate the damage by showing the damage induced waves.

The spatial wavenumber imaging calculates the wavenumber value at each spatial location and generates a spatial wavenumber image of the structure, in which the damage is indicated by different wavenumbers compared to the area without damage. Moreover, the wavenumber information can be used to quantify the damage depth, since the damage depth or material thickness affects the wavenumber value. Last but not least, compared to the filter reconstruction imaging, the spatial wavenumber imaging is more robust, since

it works for the cases when multiple wave modes exist and when damage induced waves are difficult to be extracted using the filter reconstruction imaging.

11.1.4. Guided waves in water loaded structures and water level detection

In Chapter 6, guided waves in water loaded structures are investigated through simulations, laser vibrometry experiments, and wavefield analyses. Moreover, water level detection and gas accumulation quantification methodologies are developed.

Water effects on guided wave propagation are investigated. Results of both simulations and experiments confirm energy leakage through the solid water interface and the existence of quasi-Scholte waves, when a plate is loaded by water. Due to energy leakage, wave energy in the plate decreases when the plate is immersed in water. Moreover, at low frequencies guided waves travel in the water loaded plate as quasi-Scholte waves, while guided waves travel in the free plate as Lamb waves.

The influence of water level on wave propagation is investigated through a pitch-catch sensing test on a plate with a portion in water. The test result shows that wave traveling time in the pitch-catch path is determined by lengths of water path (the portion of plate in water) and dry path (the portion of plate out of water). Moreover, the wave traveling time increases with the increase of water path. A linear relationship between the change of traveling time and the length of water path is confirmed. Thus, by measuring the traveling time of guided waves, the water level (length of water path) can be estimated. This sensing methodology can potentially be applied for water level detection and gas accumulation detection.

11.1.5. Crack detection and quantification in isotropic plates

In Chapter 7, guided wave interaction with crack damage is investigated through laser vibrometry experiments and wavefield analyses. Moreover, the work presented in this chapter demonstrates contactless wavefield measurements using laser vibrometry sensing and crack quantification using both filter reconstruction imaging and spatial wavenumber imaging. These two methods are able to detect crack location, quantify crack length, and provide information about crack severity.

The cases investigated in this chapter involve scenarios where two Lamb wave modes are generated. It is expected that the presented methods are also applicable to scenarios with more than two Lamb wave modes, particularly the filter reconstructed imaging method. It is also expected that the presented methods could be applied to the scenario of multiple cracks in various orientations with respect to incident waves.

11.1.6. Thickness loss evaluation in isotropic plates

In Chapter 8, guided wave interaction with thickness loss damage is investigated through laser vibrometry experiments. Moreover, a dispersion curve regression method is developed to quantify material thickness and damage depth in isotropic plates.

In this work, a wide band chirp signal is used to generate guided waves with various wavelengths in a wide frequency band. Interactions of these guided waves with damage include information at various wavelengths which can benefit the precision of damage quantification. The guided wavefield is measured by using the non-contact laser vibrometry sensing. Once the wavefield is acquired, it is transformed to the spectral field, which is a function of frequency and space.

For wave characterization, damage detection and quantification, the spatial wavenumber imaging is applied first. The imaging result shows that the wavenumber becomes larger at the material loss damage. In order to quantify material thickness as well as damage depth, the dispersion curve regression is applied. These methods have been applied to detect and quantify material loss damage in an aluminum plate. The location, size and depth of the damage are successfully detected and quantified. Overall the method outlined in this chapter provides an effective means for detection and quantification of material loss damage. This method can potentially be used for detection and quantification of corrosion damage.

11.1.7. Delamination detection and quantification in composite laminates

Chapter 9 presents studies on guided wave interaction with delamination damage and delamination detection and quantification techniques for laminated composite plates. The wavefield data analysis confirms the wave trapping phenomenon. Quantitative interpretation of wave behaviors in the delamination region is demonstrated. Among the wavenumber analysis methods studied, the frequency-wavenumber analysis shows that the frequency-wavenumber spectrum can indicate the presence of additional wavenumbers created by the damage. The reconstructed wavefield images created by inverting only these additional wavenumber components demonstrate that the additional wavenumbers correlate to trapped waves in the delamination region.

The phased array imaging and wavefield based imaging methods are applied to detect and quantify impact-induced delamination damage in a CFRP composite plate. The delamination damage is created by a quasi-static indentation test, and is barely visible even with careful visual inspection. By using the phased array imaging, the delamination

damage is detected. To further quantify the delamination damage, the wavefield based imaging methods are applied. The quantification result provides the location, size and shape of the delamination damage.

11.1.8. Debonding detection and quantification in honeycomb sandwich structures

In Chapter 10, guided wave propagation in a honeycomb sandwich structure and wave interaction with skin-core debonding damage are investigated. Moreover, the non-contact laser vibrometry sensing and wavefield based imaging are performed for detection and quantification of debonding damage.

The honeycomb sandwich used in this study is composed of two aluminum skin plates and a hexagonal aluminum core. To investigate the guided wave propagation in the honeycomb sandwich, FEM is used to simulate the wave propagation. Moreover, laser vibrometry experiments are performed. The simulation results agree well with the experimental results.

From results of simulations and experiments, it is found that global guided waves with elliptical wave fronts propagate in the entire sandwich at low frequency 15 kHz. It means that, the entire sandwich can be considered as a waveguide which supports global guided waves at this low frequency. With the increase of wave frequency from 15 kHz to 100 kHz, wave fronts gradually change from elliptical wave fronts to circular wave fronts. Moreover, global guided waves gradually disappear which means it becomes difficult for the global guided waves to propagate in the entire sandwich. At the high frequency 100 kHz, global guided waves completely disappear, and most of the wave energy propagates in the skin plate in the form of Lamb waves. These Lamb waves strongly interact with the honeycomb core generating complex wave interactions.

For further interpretation, guided wavefields acquired from experiments are transferred to wavenumber spectra. At 15 kHz, the wavenumber spectrum of the honeycomb sandwich shows an elliptical ring-shaped wavenumber band which has smaller wavenumbers than the plate A_0 mode. With the increase of frequency from 15 kHz to 100 kHz, the wavenumber value in the honeycomb sandwich becomes larger, and the elliptical-shaped wavenumber band gradually gets closer to the plate A_0 mode. The wavenumber comparison shows that guided waves in the honeycomb sandwich have different wavenumbers compared to those in the single plate, and the wavenumber is gradually asymptotic to that of the plate wave mode with the increase of wave frequency.

Interactions of global guided waves with debonding damage are investigated by using non-contact laser vibrometry test and wavefield analysis. Wavefield measurements show strong interactions with debonding damage. In wavenumber domain, additional wavenumbers induced by the debonding damage are observed. The reconstructed wavefield images created by inverting only these additional wavenumber components demonstrate that the additional wavenumbers correlate to the waves in the debonding area. Moreover, the result of spatial wavenumber imaging shows an area with increased wavenumber values, indicating the debonding damage.

11.2. MAJOR CONTRIBUTIONS

This dissertation research provides the following contributions to the state of the art:

- (1) A non-contact laser vibrometry sensing system is optimized to acquire a high spatial resolution guided wavefield. It also enables non-contact inspection of damage and diagnosis of structural health.

- (2) Multi-modal and dispersive guided waves are able to be decomposed into separated wave components through guided wave decomposition. Moreover, all separated wave components can provide abundant information of wave interaction with damage and the contributions of these components will lead to robust damage detection and quantification.
- (3) Complex wave propagation and interaction can be characterized and their signatures can be achieved through wavefield analysis methods. Moreover, these analysis methods unveil information of guided waves in time, space, frequency and wavenumber multi-domains.
- (4) The guided wave decomposition and wavefield analysis methods enable the use of wideband guided wave signals for damage diagnosis. Compared to the guided waves generated from the traditional narrowband tone burst excitation, those generated from the wideband short-duration pulse or wideband chirp excitation can contain waves of various modes and wavelengths. The use these multi-modal and multi-wavelength guided waves will lead to robust and multi-scale damage detection and quantification.
- (5) A hierarchical damage diagnosis methodology is developed for quantitative and visualized damage detection. This hierarchical methodology systematically combines phased array imaging and wavefield based imaging, which achieves efficient and precise damage detection and quantification.
- (6) The generic phased array beamforming is developed, in which directional dependent guided wave parameters are considered. This generic beamforming method is valid not only for the case that phase and group velocities have the

same orientation, but also for the general case that the two velocities are in different directions. Moreover, this generic method works for both isotropic and anisotropic materials. Last but not least, it has been shown that this method can detect multiple defects in different directions *w.r.t.* the array center in an anisotropic composite plate.

- (7) The wavefield based imaging method that integrates both the filter reconstruction imaging and spatial wavenumber imaging are developed. It takes advantages of both methods and lead to a more efficient and robust imaging method for damage visualization and quantification.
- (8) Water effects on guided wave propagation are investigated. This study confirms the energy leakage through solid water interface and the existence of quasi-Scholte waves when a plate has one side in water. Moreover, a linear relationship between the change of traveling time and the length of water path is confirmed. By measuring the traveling time of guided waves, the length of water path can be determined. This sensing methodology can potentially be applied for water level detection and gas accumulation detection in closed containers.
- (9) Guided wave interaction with crack damage is studied. This study identifies additional wavenumber components in wavenumber domain, which correlate to the crack induced wavefield discontinuities. Moreover, this study shows that wavefield based imaging methods are able to detect the crack location, quantify the crack length, and provide information about the crack severity.
- (10) A dispersion curve regression method is developed to quantify material thickness and damage depth in isotropic plates. The location, size and depth of material loss

damage can be detected and quantified. This method can potentially be used for detection and quantification of corrosion damage.

(11) Guided wave interaction with delamination damage is investigated. This study not only confirms the wave trapping at delamination damage, but also quantitatively interprets the trapped waves via various wavenumber analysis methods. In wavenumber domain, additional wavenumbers are observed, which correlate to trapped waves in the delamination region. Moreover, the developed phased array imaging successfully detects impact-induced delamination damage. Last but not least, the wavefield based imaging detects and quantifies the location, size and shape of the delamination damage.

(12) The guided wave propagation in a complex geometry honeycomb sandwich is investigated. The study confirms global guided waves in the full sandwich at low frequencies and strong wave interaction with the inside core at high frequencies. Moreover, the wavenumber distribution of guided waves is determined through experiments, which is an elliptical wavenumber band.

The guided wave interaction with debonding damage is investigated. The study shows mode conversion at debonding damage. Moreover, in wavenumber domain, additional wavenumbers are observed which correlate to waves in the debonding area. Last but not least, the study shows that wavefield based imaging methods successfully detect and quantify the location and size of hidden debonding damage.

11.3. RECOMMENDATION FOR FUTURE WORK

This dissertation research focuses on guided wave based integrated SHM/NDE. Non-contact sensing, intrinsic wave analysis and advanced damage diagnosis methods are used to analyze complex wave propagation and interaction, and to detect and quantify structural damage. The following tasks are recommended to be undertaken for further studies:

- (1) In Chapter 3, guided waves are generated by surface bonded PZT transducers. The non-contact guided wave excitation by using non-contact transducers, such as air-coupled transducers and pulse-laser transducers, should be investigated. Moreover, an integration of these wave excitation methods and laser vibrometry sensing will lead to a fully non-contact guided wave excitation and sensing system.
- (2) In Chapter 4, wavefield analysis methods are presented to analyze waves propagating along a 1-D straight line and waves propagating in a 2-D surface. Wavefield analysis methods that can be used to analyze waves propagating along curves such as spiral curves and elliptical curves should be investigated. Moreover, analysis methods for analyzing waves in a 3-D space should be investigated. It is expected that by using these analysis methods, the wave propagation and interaction at various structural depths can be characterized and interpreted.
- (3) In Chapter 5, the generic beamforming considers directional dependent guided wave parameters and works for both isotropic and anisotropic materials. However, the roles of weighting factors are not investigated. In the future, selections of

- weighting factors should be investigated to further improve the beamforming results. Moreover, the wavefield based imaging methods in Chapter 5 are based on the interpretation of wavenumber information. Other methods such as machine learning and statistical based methods can also be investigated to achieve robust damage detection and quantification.
- (4) In Chapter 6, the water level detection and gas accumulation detection methods only use one pitch-catch sensing path to determine the location of water surface in the path. It is recommended that sensor arrays should be designed to fully quantify the shape of water surface. Moreover, it is also interesting to investigate sensing methods that can be used to detect both water surface and structural damage.
 - (5) In Chapter 7, the wavefield based imaging methods are used to detect and quantify cracks of different widths and depths. It is also interesting to investigate cases of multiple cracks, cracks with different lengths, and cracks in different orientations.
 - (6) In Chapter 8, the material loss defects created by using a milling machine only have simple geometries. The detection and quantification of material loss defects such as realistic corrosion damage and erosion damage should be studied.
 - (7) In Chapter 9, a single impact induced defect is detected and quantified. Future research can be performed to detect and quantified multiple defects of different types.
 - (8) In Chapter 10, wave propagation and interaction in honeycomb sandwich structures are investigated by using FEM simulations and laser vibrometry

experiments. Theoretical work should be performed to achieve wave dispersion curves and modes shapes, and to improve the understanding of waves in honeycomb sandwich structures. Moreover, the effects of core size, core geometry and core material on guided wave propagation can also be investigated.

REFERENCES

- [1] Giurgiutiu, V., *Structural Health Monitoring with Piezoelectric Wafer Active Sensors*. Boston, MA, USA: Academic Press, 2008.
- [2] Worden, K., Farrar, C. R., Manson, G., and Park, G., "The Fundamental Axioms of Structural Health Monitoring," *Proceedings of the Royal Society a-Mathematical Physical and Engineering Sciences*, vol. 463, pp. 1639-1664, 2007.
- [3] Rose, J. L., "The Upcoming Revolution in Ultrasonic Guided Waves," *Proceedings of SPIE*, vol. 7983, p. 798302, March 06, 2011.
- [4] Speckmann, H. and Henrich, R., "Structural Health Monitoring (Shm)-Overview on Technologies under Development," in *16th world conference on NDT*, Montreal, Canada, 2004, p. 563.
- [5] Rytter, A., "Vibration Based Inspection of Civil Engineering Structures," Ph. D., Department of Building Technology and Structural Engineering, Aalborg University, Aalborg University, Denmark, 1993.
- [6] Rose, J. L., "The Upcoming Revolution in Ultrasonic Guided Waves," presented at the Nondestructive Characterization for Composite Materials, Aerospace Engineering, Civil Infrastructure, and Homeland Security 2011, San Diego, CA, 2011.
- [7] Miklowitz, J., *Theory of Elastic Waves and Waveguides*. North Holland, 1978.
- [8] Rose, J. L., *Ultrasonic Waves in Solid Media*. Cambridge: Cambridge University Press, 1999.
- [9] Viktorov, I. A., *Rayleigh and Lamb Waves*: Plenum Press, 1967.
- [10] Graff, K. F., *Wave Motions in Solids*. Mineola, NY, USA: Dover Publications, Inc., 1975.
- [11] Nayfeh, A. H., *Wave Propagation in Layered Anisotropic Media*. Amsterdam, The Netherlands: Elsevier, 1995.
- [12] Giurgiutiu, V. and Bao, J., "Embedded-Ultrasonics Structural Radar for in Situ Structural Health Monitoring of Thin-Wall Structures," *Structural Health Monitoring-an International Journal*, vol. 3, pp. 121-140, Jun 2004.
- [13] Kim, D. and Philen, M., "Guided Wave Beamsteering Using Mfc Phased Arrays for Structural Health Monitoring: Analysis and Experiment," *Journal of Intelligent Material Systems and Structures*, vol. 21, pp. 1011-1024, Jul 2010.

- [14] Purekar, A. S. and Pines, D. J., "Damage Detection in Thin Composite Laminates Using Piezoelectric Phased Sensor Arrays and Guided Lamb Wave Interrogation," *Journal of Intelligent Material Systems and Structures*, vol. 21, pp. 995-1010, 2010.
- [15] Ruzzene, M., Xu, B., Lee, S. J., Michaels, T. E., and Michaels, J. E., "Damage Visualization Via Beamforming of Frequency-Wavenumber Filtered Wavefield Data," in *Health Monitoring of Structural and Biological Systems 2010*, 2010, p. 76500L.
- [16] Wilcox, P. D., "Omni-Directional Guided Wave Transducer Arrays for the Rapid Inspection of Large Areas of Plate Structures," *Ieee Transactions on Ultrasonics Ferroelectrics and Frequency Control*, vol. 50, pp. 699-709, Jun 2003.
- [17] Yu, L. and Giurgiutiu, V., "In Situ 2-D Piezoelectric Wafer Active Sensors Arrays for Guided Wave Damage Detection," *Ultrasonics*, vol. 48, pp. 117-134, Apr 2008.
- [18] Romanoni, M., Gonella, S., Apetre, N., and Ruzzene, M., "Two-Dimensional Periodic Actuators for Frequency-Based Beam Steering," *Smart Materials & Structures*, vol. 18, p. 125023, Dec 2009.
- [19] Yoo, B., Purekar, A. S., Zhang, Y., and Pines, D. J., "Piezoelectric-Paint-Based Two-Dimensional Phased Sensor Arrays for Structural Health Monitoring of Thin Panels," *Smart Materials & Structures*, vol. 19, p. 075017, 2010.
- [20] Senesi, M., Xu, B., and Ruzzene, M., "Experimental Characterization of Periodic Frequency-Steerable Arrays for Structural Health Monitoring," *Smart Materials & Structures*, vol. 19, p. 055026, 2010.
- [21] Lee, S. J., Gandhi, N., Hall, J. S., Michaels, J. E., Xu, B., Michaels, J. E., and Ruzzene, M., "Baseline-Free Guided Wave Imaging Via Adaptive Source Removal," *Structural Health Monitoring*, vol. 11, pp. 472-481, 2012.
- [22] Michaels, J. E., "Detection, Localization and Characterization of Damage in Plates with an in Situ Array of Spatially Distributed Ultrasonic Sensors," *Smart Materials & Structures*, vol. 17, p. 035035, Jun 2008.
- [23] Clarke, T., Cawley, P., Wilcox, P. D., and Croxford, A. J., "Evaluation of the Damage Detection Capability of a Sparse-Array Guided-Wave Shm System Applied to a Complex Structure under Varying Thermal Conditions," *Ieee Transactions on Ultrasonics Ferroelectrics and Frequency Control*, vol. 56, pp. 2666-2678, Dec 2009.
- [24] Zhu, R., Huang, G. L., and Yuan, F. G., "Fast Damage Imaging Using the Time-Reversal Technique in the Frequency-Wavenumber Domain," *Smart Materials and Structures*, vol. 22, p. 075028, Jul 2013.
- [25] Park, H. W., Kim, S. B., and Sohn, H., "Understanding a Time Reversal Process in Lamb Wave Propagation," *Wave Motion*, vol. 46, pp. 451-467, Nov 2009.

- [26] Sohn, H., park, H. W., Law, K. H., and Farrar, C. R., "Damage Detection in Composite Plates by Using an Enhanced Time Reversal Method," *Journal of Aerospace Engineering*, vol. 20, pp. 141-151, 2007.
- [27] Hay, T. R., Royer, R. L., Gao, H. D., Zhao, X., and Rose, J. L., "A Comparison of Embedded Sensor Lamb Wave Ultrasonic Tomography Approaches for Material Loss Detection," *Smart Materials & Structures*, vol. 15, pp. 946-951, Aug 2006.
- [28] Leonard, K. R. and Hinders, M. K., "Lamb Wave Tomography of Pipe-Like Structures," *Ultrasonics*, vol. 43, pp. 574-583, Jun 2005.
- [29] Michaels, T. E., Michaels, J. E., and Ruzzene, M., "Frequency-Wavenumber Domain Analysis of Guided Wavefields," *Ultrasonics*, vol. 51, pp. 452-466, 2011.
- [30] Ruzzene, M., "Frequency-Wavenumber Domain Filtering for Improved Damage Visualization," *Smart Materials and Structures*, vol. 16, pp. 2116-2129, 2007.
- [31] Flynn, E. B., Chong, S. Y., Jarmer, G. J., and Lee, J. R., "Structural Imaging through Local Wavenumber Estimation of Guided Waves," *Ndt & E International*, vol. 59, pp. 1-10, 2013.
- [32] Rogge, M. D. and Leckey, C. A. C., "Characterization of Impact Damage in Composite Laminates Using Guided Wavefield Imaging and Local Wavenumber Domain Analysis," *Ultrasonics*, vol. 53, pp. 1217-1226, 2013.
- [33] Lowe, M. J. S., "Matrix Techniques for Modeling Ultrasonic Waves in Multilayered Media," *Ieee Transactions on Ultrasonics Ferroelectrics and Frequency Control*, vol. 42, pp. 525-542, 1995.
- [34] Rogge, M. D. and Johnston, P. H., "Wavenumber Imaging for Damage Detection and Measurement," *Review of Progress in Quantitative Nondestructive Evaluation*, vol. 31, pp. 761-768, 2012.
- [35] Roberge, P. R., *Corrosion Inspection and Monitoring*. Hoboken, New Jersey: John Wiley & Sons, Inc., 2007.
- [36] Staszewski, W. J., Boller, C., and Tomlinson, G. R., *Health Monitoring of Aerospace Structures*. Chichester: John Wiley & Sons, 2004.
- [37] Boller, C., Chang, F. K., and Fujino, Y., *Encyclopedia of Structural Health Monitoring*. new york: wiley, 2009.
- [38] Bartoli, I., Marzani, A., di Scalea, F. L., and Viola, E., "Modeling Wave Propagation in Damped Waveguides of Arbitrary Cross-Section," *Journal of Sound and Vibration*, vol. 295, pp. 685-707, Aug 22 2006.
- [39] Maess, M., Herrmann, J., and Gaul, L., "Finite Element Analysis of Guided Waves in Fluid-Filled Corrugated Pipes," *Journal of the Acoustical Society of America*, vol. 121, pp. 1313-1323, Mar 2007.

- [40] Fan, Z., "Applications of Guided Wave Propagation on Waveguides with Irregular Cross-Section," Doctor of Philosophy, Department of Mechanical Engineering, Imperial College London, London, 2010.
- [41] Predoi, M. V., Castaings, M., Hosten, B., and Bacon, C., "Wave Propagation Along Transversely Periodic Structures," *Journal of the Acoustical Society of America*, vol. 121, pp. 1935-1944, Apr 2007.
- [42] Ruzzene, M., Scarpa, F., and Soranna, F., "Wave Beaming Effects in Two-Dimensional Cellular Structures," *Smart Materials & Structures*, vol. 12, pp. 363-372, 2003.
- [43] di Scalea, F. L., Rizzo, P., and Marzani, A., "Propagation of Ultrasonic Guided Waves in Lap-Shear Adhesive Joints: Case of Incident $a(0)$ Lamb Wave," *Journal of the Acoustical Society of America*, vol. 115, pp. 146-156, Jan 2004.
- [44] Barshinger, J. N. and Rose, J. L., "Guided Wave Propagation in an Elastic Hollow Cylinder Coated with a Viscoelastic Material," *Ieee Transactions on Ultrasonics Ferroelectrics and Frequency Control*, vol. 51, pp. 1547-1556, 2004.
- [45] Fan, Z. and Lowe, M. J. S., "Elastic Waves Guided by a Welded Joint in a Plate," *Proceedings of the Royal Society A*, vol. 465, pp. 2053-2067, 2009.
- [46] Gopalakrishnan, S., Ruzzene, M., and Hanagud, S., *Computational Techniques for Structural Health Monitoring*. London: Springer, 2011.
- [47] Raghavan, A. and Cesnik, C. E. S., "Finite-Dimensional Piezoelectric Transducer Modeling for Guided Wave Based Structural Health Monitoring," *Smart Materials & Structures*, vol. 14, pp. 1448-1461, Dec 2005.
- [48] Shen, Y. and Giurgiutiu, V., "Predictive Modeling of Nonlinear Wave Propagation for Structural Health Monitoring with Piezoelectric Wafer Active Sensors," *Journal of Intelligent Material Systems and Structures*, vol. 25, pp. 506-520, 2014.
- [49] Reddy, J. N., *An Introduction to the Finite Element Method (Third Edition)*. New York: McGraw-Hill, 1985.
- [50] Cook, R. D., Malkus, D. S., Plesha, M. E., and Witt, R. J., *Concepts and Applications of Finite Element Analysis (4th Edition)*. New York: Wiley, 2001.
- [51] Bathe, K. J., *Finite Element Procedures*. Englewood Cliffs: Printice Hall, 1997.
- [52] Fellinger, P. and Langenberg, K. J., "Numerical Techniques for Elastic Wave Propagation and Scattering," *Proceedings of IUTAM Symposium*, pp. 81-86, 1990.
- [53] Leckey, C., Rogge, M. D., Miller, C., and Hinders, M., "Multiple-Mode Lamb Wave Scattering Simulations Using 3d Elastodynamic Finite Integration Technique," *Ultrasonics*, vol. 52, pp. 193-207, 2012.
- [54] Leckey, C. A. C., Rogge, M. D., and Parker, F. R., "Microcracking in Composite Laminates: Simulation of Crack-Induced Ultrasound Attenuation," in *39th Annual*

- Review of Progress in Quantitative Nondestructive Evaluation Conference*, Denver, CO, 2012, pp. 947-954.
- [55] Lui, Q., Schoen, E., Daube, F., Randall, C., Liu, H., and Lee, P., "Large-Scale 3d Finite-Difference Simulation of Elastic Wave Propagation in Borehole Environments," *Journal of Acoustic Society of America*, vol. 96, pp. 3337-3337, 1994.
- [56] Leutenegger, T. and Dual, J., "Detection of Defects in Cylindrical Structures Using a Time Reverse Method and a Finite-Difference Approach," *Ultrasonics*, vol. 40, pp. 721-725, 2002.
- [57] Kelly, K., "Numerical Study of Love Wave Propagation," *Geophysics*, vol. 48, pp. 833-853, 1983.
- [58] Virieux, J., "Wave Propagation in Heterogeneous Media : Velocity-Stress Finite-Difference Method," *Geophysics*, vol. 49, pp. 1933-1957, 1984.
- [59] Peng, H. K., Ye, L., Meng, G. A., Mustapha, S., and Li, F. C., "Concise Analysis of Wave Propagation Using the Spectral Element Method and Identification of Delamination in Cf/Ep Composite Beams," *Smart Materials & Structures*, vol. 19, p. 085018, Aug 2010.
- [60] Kim, Y., Ha, S., and Chang, F. K., "Time-Domain Spectral Element Method for Built-in Piezoelectric-Actuator-Induced Lamb Wave Propagation Analysis," *Aiaa Journal*, vol. 46, pp. 591-600, Mar 2008.
- [61] Sundararaman, S. and Adams, D. E., "Modeling Guided Waves for Damage Identification in Isotropic and Orthotropic Plates Using a Local Interaction Simulation Approach," *Journal of Vibration and Acoustics-Transactions of the Asme*, vol. 130, pp. -, Aug 2008.
- [62] Lee, B. C. and Staszewski, W. J., "Lamb Wave Propagation Modelling for Damage Detection: Ii. Damage Monitoring Strategy," *Smart Materials & Structures*, vol. 16, pp. 260-274, Apr 2007.
- [63] Banerjee, S. and Kundu, T., "Ultrasonic Field Modeling in Plates Immersed in Fluid," *International Journal of Solids and Structures*, vol. 44, pp. 6013-6029, Sep 2007.
- [64] Gresil, M. and Giurgiutiu, V., "Time-Domain Hybrid Global-Local Concept for Guided-Wave Propagation with Piezoelectric Wafer Active Sensor," *Journal of Intelligent Material Systems and Structures*, vol. 24, pp. 1897-1911, 2013.
- [65] Mal, A. and Zensheu, C., "A Semi-Numerical Method for Elastic Wave Scattering Calculations," *Geophysical Journal International*, vol. 143, pp. 328-34, 11/ 2000.
- [66] Srivastava, A. and di Scalea, F. L., "Quantitative Structural Health Monitoring by Ultrasonic Guided Waves," *Journal of Engineering Mechanics-Asce*, vol. 136, pp. 937-944, Aug 2010.

- [67] Mansur, W. J. and Brebbia, C. A., "Numerical Implementation of the Boundary Element Method for Two Dimensional Transient Scalar Wave Propagation Problems," *Applied Mathematical Modeling*, vol. 6, pp. 299-306, 1982.
- [68] Zhu, W. and Rose, J. L., "Lamb Wave Generation and Reception with Time-Delay Periodic Linear Arrays: A Bem Simulation and Experimental Study," *Ieee Transactions on Ultrasonics Ferroelectrics and Frequency Control*, vol. 46, pp. 654-663, 1999.
- [69] Aimi, A., Gazzola, S., and Guardasoni, C., "Energetic Boundary Element Method Analysis of Wave Propagation in 2d Multilayered Media," *Mathematical Methods in the Applied Sciences*, vol. 35, pp. 1140-1160, 2011.
- [70] Soni, S., Das, S., and Chattopadhyay, A., "Simulation of Damage-Features in a Lug Joint Using Guided Waves," *Journal of Intelligent Material Systems and Structures*, vol. 20, pp. 1451-1464, Aug 2009.
- [71] Pistone, E., Li, K., and Pizzo, P., "Noncontact Monitoring of Immersed Plates by Means of Laser-Induced Ultrasounds," *Structural Health Monitoring*, vol. 12, pp. 549-565, 2013.
- [72] Song, F., Huang, G. L., and Hudson, K., "Guided Wave Propagation in Honeycomb Sandwich Structures Using a Piezoelectric Actuator/Sensor System," *Smart Materials & Structures*, vol. 18, pp. -, Dec 2009.
- [73] Liu, Y., Lissenden, C. J., and Rose, J. L., "Cumulative Second Harmonics in Weakly Nonlinear Plates and Shells," in *Health Monitoring of Structural and Biological Systems 2013*, 2013.
- [74] Leckey, C. A. C., Rogge, M. D., and Parker, R., "Guided Waves in Anisotropic and Quasi-Isotropic Aerospace Composites: Three-Dimensional Simulation and Experiment," *Ultrasonics*, vol. 54, pp. 385-394, 2014.
- [75] Schubert, F., Peiffer, A., and Kohler, B., "The Elastodynamic Finite Integration Technique for Waves in Cylindrical Geometries," *Journal of the Acoustical Society of America*, vol. 104, pp. 2604-2614, 1998.
- [76] Bingham, J. and Hinders, M., "3d Elastodynamic Finite Integration Technique Simulation of Guided Waves in Extended Built-up Structures Containing Flaws," *Journal of Computational Acoustics*, vol. 18, pp. 1-28, 2010.
- [77] Rudd, K. E., Leonard, K. R., Bingham, J. P., and Hinders, M. K., "Simulation of Guided Waves in Complex Piping Geometries Using the Elastodynamic Finite Integration Technique," *Journal of the Acoustical Society of America*, vol. 121, pp. 1449-1458, Mar 2007.
- [78] Halkjaer, S., "Elastic Wave Propagation in Anisotropic Inhomogeneous Materials," Ph.D. Thesis, Institute of Mathematical Modelling, Technical University of Denmark, Denmark, 2000.

- [79] Schubert, F., "Numerical Time-Domain Modeling of Linear and Nonlinear Ultrasonic Wave Propagation Using Finite Integration Techniques - Theory and Applications," *Ultrasonics*, vol. 42, pp. 221-229, Apr 2004.
- [80] Wilcox, P. D., Lowe, M., and Cawley, P., "Omnidirectional Guided Wave Inspection of Large Metallic Plate Structures Using an Emat Array," *Ieee Transactions on Ultrasonics Ferroelectrics and Frequency Control*, vol. 52, pp. 653-665, Apr 2005.
- [81] Murayama, R. and Mizutani, K., "Conventional Electromagnetic Acoustic Transducers Development for Optimum Lamb Wave Modes," *Ultrasonics*, vol. 40, pp. 491-495, 2002.
- [82] Ann, A. K., Kim, H. M., Jhang, K. Y., Park, I. K., Kwag, N. G., and Lee, C. M., "Detection of Laser Excited Lamb Wave Using Air Coupled Transducer and Wave Mode Identification Using Wavelet Transform," *Review of Progress in Quantitative Nondestructive Evaluation*, vol. 760, pp. 1018-1025, 2004.
- [83] Garcia-Hernandez, M. J., Chavez, J. A., Yanez, Y., Kichou, H. B., Prego-Borges, J. L., Salazar, J., Turo, A., and de Espinosa, F. M., "Ultrasonic Lamb Wave Nde System Using an Air Coupled Concave Array Transducer," *IEEE Ultrasonics Symposium, 2004 IEEE International Ultrasonics, Ferroelectrics, and Frequency Control Joint 50th Anniversary Conference*, vol. 2, pp. 1282-1285, 2004.
- [84] Rose, J. L., "A Comb Transducer for Mode Control in Guided Wave Nde," *Ultrasonics*, vol. 36, pp. 163-169, 1998.
- [85] Wevers, M., Fransens, F., and Leuven, K. U., "Ultrasonic Lamb Wave Inspection of Aircraft Components Using Integrated Optical Fibre Sensing Technology," *ECNDT 2006*, vol. Mo.2.7.1, 2006.
- [86] Li, F. C., Murayama, H., Kageyama, K., and Shirai, T., "Guided Wave and Damage Detection in Composite Laminates Using Different Fiber Optic Sensors," *Sensors*, vol. 9, pp. 4005-4021, May 2009.
- [87] Dupont, M., Osmont, R., Gouyon, R., and Balageas, D. L., "Permanent Monitoring of Damage Impacts by a Piezoelectric Sensor Based Integrated System," *Structural Health Monitoring*, pp. 561-570, 2000.
- [88] Yu, L. and Giurgiutiu, V., "Piezoelectric Wafer Active Sensors," in *Encyclopedia of Structural Health Monitoring* vol. 3, C. Boller, F. K. Chang, and Y. Fujino, Eds., ed: John Wiley & Sons, Ltd., 2009, pp. 1013-1027.
- [89] Williams, R. B., Park, G., Inman, D. J., and Wilkie, W. K., "An Overview of Composite Actuators with Piezoceramic Fibers," presented at the 20th International Modal Analysis Conference, Los Angeles, CA, USA, 2002.
- [90] Raghavan, A. and Cesnik, C. E. S., "Review of Guided-Wave Structural Health Monitoring," *The Shock and Vibration Digest*, vol. 39, pp. 91-114, 2007.

- [91] di Scalea, F. L., Matt, H., Bartoli, I., Coccia, S., Park, G., and Farrar, C., "Health Monitoring of Uav Wing Skin-to-Spar Joints Using Guided Waves and Macro Fiber Composite Transducers," *Journal of Intelligent Material Systems and Structures*, vol. 18, pp. 373-388, Apr 2007.
- [92] Rose, J. L., "A Baseline and Vision of Ultrasonic Guided Wave Inspection Potential," *Journal of Pressure Vessel Technology*, vol. 124, pp. 273-282, 2002.
- [93] Culshaw, B., Pierce, S. G., and Staszewski, W. J., "Condition Monitoring in Composite Materials: An Integrated Systems Approach," *Proceedings of the Institution of Mechanical Engineers, Journal of Systems and Control Engineering, Part I*, vol. 212, pp. 189-202, 1998.
- [94] Sohn, H., "Noncontact Laser Sensing Technology for Structural Health Monitoring and Nondestructive Testing," in *Bioinspiration, Biomimetics, and Bioreplication 2014*, San Diego, California, USA, 2014, p. 90550W.
- [95] Rajic, N., Davis, C., and Thomson, A., "Acoustic-Wave-Mode Separation Using a Distributed Bragg Grating Sensor," *Smart Materials & Structures*, vol. 18, pp. -, Dec 2009.
- [96] Ke, W., Castaings, M., and Bacon, C., "3d Finite Element Simulations of an Air-Coupled Ultrasonic Ndt System," *Ndt & E International*, vol. 42, pp. 524-533, 2009.
- [97] Lee, H. and Sohn, H., "Damage Detection in Nuclear Power Plant Pipes Using Laser-Based Mechanical Impedance," *Review of Progress in Quantitative Nondestructive Evaluation*, 2014.
- [98] Giurgiutiu, V., Zagrai, A., and Bao, J. J., "Damage Identification in Aging Aircraft Structures with Piezoelectric Wafer Active Sensors," *Journal of Intelligent Material Systems and Structures*, vol. 15, pp. 673-687, Sep-Oct 2004.
- [99] Giurgiutiu, V., Xu, B. L., and Liu, W. P., "Development and Testing of High-Temperature Piezoelectric Wafer Active Sensors for Extreme Environments," *Structural Health Monitoring-an International Journal*, vol. 9, pp. 513-525, Nov 2010.
- [100] Santoni, G. B., Yu, L., Xu, B., and Giurgiutiu, V., "Lamb Wave-Mode Tuning of Piezoelectric Wafer Active Sensors for Structural Health Monitoring," *Journal of Vibration and Acoustics-Transactions of the Asme*, vol. 129, pp. 752-762, Dec 2007.
- [101] Giurgiutiu, V., "Tuned Lamb Wave Excitation and Detection with Piezoelectric Wafer Active Sensors for Structural Health Monitoring," *Journal of Intelligent Material Systems and Structures*, vol. 16, pp. 291-305, Apr 2005.
- [102] Drain, L. E., *The Laser Doppler Concepts*. New York, NY: John Wiley Sons, 1980.
- [103] Sohn, H., Dutta, D., Yang, J. Y., DeSimio, M., Olson, S., and Swenson, E., "Automated Detection of Delamination and Disbond from Wavefield Images

- Obtained Using a Scanning Laser Vibrometer," *Smart Materials & Structures*, vol. 20, p. 045017, 2011.
- [104] Staszewski, W. J., Lee, B. C., and Traynor, R., "Fatigue Crack Detection in Metallic Structures with Lamb Waves and 3d Laser Vibrometry," *Measurement Science & Technology*, vol. 18, pp. 727-739, Mar 2007.
- [105] Michaels, T. E., Ruzzene, M., and Michaels, J. E., "Incident Wave Removal through Frequency-Wavenumber Filtering of Full Wavefield Data," *Review of Progress in Quantitative Nondestructive Evaluation*, vol. 1096, pp. 604-611, 2009.
- [106] Swenson, E. D., Sohn, H., Olson, S. E., and DeSimio, M. P., "A Comparison of 1d and 3d Laser Vibrometry Measurements of Lamb Waves," *Proceedings of SPIE*, vol. 7650, p. 765003, 2010.
- [107] Olson, S. E., DeSimio, M. P., Matthew, J. D., Swenson, E. D., and Sohn, H., "Computational Lamb Wave Model Validation Using 1d and 3d Laser Vibrometer Measurement," *Proc. SPIE 7650, Health Monitoring of Structural and Biological Systems 2010*, vol. 7650, p. 76500M, 2010.
- [108] Ostachowicz, W., Wanddowski, T., and Malinowski, P., "Damage Detection Using Laser Vibrometry," in *2nd International Symposium on NDT in Aerospace 2010*, 2010.
- [109] Kudela, P., Radzienski, M., and Ostachowicz, W., "Identification of Cracks in Thin-Walled Structures by Means of Wavenumber Filtering," *Mechanical Systems and Signal Processing*, vol. 50-51, pp. 456-466, Jan 2015.
- [110] Ostachowicz, W., Radzienski, M., and Kudela, P., "50th Anniversary Article: Comparison Studies of Full Wavefield Signal Processing for Crack Detection," *Strain*, vol. 50, pp. 275-291, 2014.
- [111] Yu, L., Leckey, C., and Tian, Z., "Study on Crack Scattering in Aluminum Plates with Lamb Wave Frequency-Wavenumber Analysis," *Smart Materials & Structures*, vol. 22, pp. 1-12, 2013.
- [112] Staszewski, W. J., Mahzan, S., and Traynor, R., "Health Monitoring of Aerospace Composite Structures - Active and Passive Approach," *Composites Science and Technology*, vol. 69, pp. 1678-1685, Sep 2009.
- [113] Alleyne, D. N. and Cawley, P., "A Two Dimensional Fourier Transform Method for the Measurement of Propagating Multimode Signals," *Journal of Acoustic Society of America*, vol. 89, pp. 1159-1168, 1991.
- [114] Hayashi, T. and Kawashima, K., "Single Mode Extraction from Multiple Modes of Lamb Wave and Its Application to Defect Detection," *JSME International Journal Series A, Solid Mechanics and Material Engineering*, vol. 46, pp. 620-626, 2003.
- [115] Michaels, J. E., "Detection, Localization and Characterization of Damage in Plates with an in Situ Array of Spatially Distributed Ultrasonic Sensors," *Smart Materials & Structures*, vol. 17, pp. -, Jun 2008.

- [116] Hall, J. S. and Michaels, J. E., "Minimum Variance Ultrasonic Imaging Applied to an in Situ Sparse Guided Wave Array," *Ieee Transactions on Ultrasonics Ferroelectrics and Frequency Control*, vol. 57, pp. 2311-2323, Oct 2010.
- [117] Wang, C. H., Rose, J. T., and Chang, F. K., "A Synthetic Time-Reversal Imaging Method for Structural Health Monitoring," *Smart Materials & Structures*, vol. 13, pp. 415-423, Apr 2004.
- [118] Michaels, J. E. and Michaels, T. E., "Guided Wave Signal Processing and Image Fusion for in Situ Damage Localization in Plates," *Wave Motion*, vol. 44, pp. 482-492, Jun 2007.
- [119] Yu, L. and Leckey, C., "Lamb Wave-Based Quantitative Crack Detection Using a Focusing Array Algorithm," *Journal of Intelligent Material Systems and Structures*, vol. 29, pp. 1138-1152, 2013.
- [120] Su, Z. Q., Cheng, L., Wang, X. M., Yu, L., and Zhou, C., "Predicting Delamination of Composite Laminates Using an Imaging Approach," *Smart Materials & Structures*, vol. 18, pp. -, Jul 2009.
- [121] Cho, H. J. and Lissenden, C. J., "Structural Health Monitoring of Fatigue Crack Growth in Plate Structures with Ultrasonic Guided Waves," *Structural Health Monitoring-an International Journal*, vol. 11, pp. 393-404, Jul 2012.
- [122] Chen, X., Michaels, J. E., Lee, S. J., and Michaels, T. E., "Load-Differential Imaging for Detection and Localization of Fatigue Cracks Using Lamb Waves," *Ndt & E International*, vol. 51, pp. 142-149, Oct 2012.
- [123] Wilcox, P. D., "Guided-Wave Array Methods," in *Encyclopedia of Structural Health Monitoring* vol. 1, C. Boller, F. K. Chang, and Y. Fujino, Eds., ed: John Wiley & Sons, Ltd., 2009, pp. 333-352.
- [124] Purekar, A. S., Pines, D. J., Sundararaman, S., and Adams, D. E., "Directional Piezoelectric Phased Array Filters for Detecting Damage in Isotropic Plates," *Smart Materials & Structures*, vol. 13, pp. 838-850, Aug 2004.
- [125] Ambrozinski, L., Stepinski, T., and Uhl, T., "2d Aperture Synthesis for Lamb Wave Imaging Using Co-Arrays," presented at the Health Monitoring of Structural and Biological Systems 2014, San Diego, CA, 2014.
- [126] de Marchi, L., Moll, J., and Marzani, A., "A Sparsity Promoting Algorithm for Time of Flight Estimation in Guided Waves-Based Shm," in *EWSHM-7th European Workshop on Structural Health Monitoring*, Nantes, France, 2014, pp. 583-590.
- [127] Engholm, M. and Stepinski, T., "Direction of Arrival Estimation of Lamb Waves Using Circular Arrays," *Structural Health Monitoring-an International Journal*, vol. 10, pp. 467-480, Sep 2011.
- [128] Fromme, P., Wilcox, P. D., Lowe, M. J. S., and Canvley, P., "On the Development and Testing of a Guided Ultrasonic Wave Array for Structural

- Integrity Monitoring," *Ieee Transactions on Ultrasonics Ferroelectrics and Frequency Control*, vol. 53, pp. 777-785, Apr 2006.
- [129] Leleux, A., Micheau, P., and Castaings, M., "Long Range Detection of Defects in Composite Plates Using Lamb Waves Generated and Detected by Ultrasonic Phased Array Probes," *Journal of Nondestructive Evaluation*, vol. 32, pp. 200-214, Jun 2013.
- [130] Malinowski, P., Wandowski, T., Trendafilova, I., and Ostachowicz, W., "A Phased Array-Based Method for Damage Detection and Localization in Thin Plates," *Structural Health Monitoring-an International Journal*, vol. 8, pp. 5-15, Jan 2009.
- [131] Ambrozinski, L., Stepinski, T., and Uhl, T., "Efficient Tool for Designing 2d Phased Arrays in Lamb Waves Imaging of Isotropic Structures," *Journal of Intelligent Material Systems and Structures*, p. online, 2014.
- [132] Koduru, J. P., Momeni, S., and Rose, J. L., "Phased Annular Array Transducers for Omnidirectional Guided Wave Mode Control in Isotropic Plate Like Structures," *Smart Materials and Structures*, vol. 22, p. 8, Dec 2013.
- [133] Yan, F. and Rose, J. L., "Guided Wave Phased Array Beam Steering in Composite Plates - Art. No. 65320g," *Health Monitoring of Structural and Biological Systems 2007*, vol. 6532, pp. G5320-G5320, 2007.
- [134] Rajagopalan, J., Multila, K. H. M. O. A., Balasubramaniam, K., and Krishnamurthy, C. V., "A Phase Reconstruction Algorithm for Lamb Wave Based Structural Health Monitoring of Anisotropic Multilayered Composite Plates," *Journal of the Acoustical Society of America*, vol. 119, pp. 872-878, Feb 2006.
- [135] Osterc, P., Kim, D., and Yoo, B., "Phased Array Beamsteering in Composite Laminates for Guided Wave Structural Health Monitoring," presented at the ASME 2013 Conference on Smart Materials, Adaptive Structures and Intelligent Systems, Snowbird, Utah, USA, 2013.
- [136] Wang, L. and Yuan, F. G., "Group Velocity and Characteristic Wave Curves of Lamb Waves in Composites: Modeling and Experiments," *Composites Science and Technology*, vol. 67, pp. 1370-1384, Jun 2007.
- [137] Glushkov, E., Glushkova, N., and Eremin, A., "Group Velocity of Cylindrical Guided Waves in Anisotropic Laminate Composites," *Journal of Acoustic Society of America*, vol. 135, pp. 148-154, 2014.
- [138] Lamb, H., "On Waves in an Elastic Plate," *Proceedings of Royal Society, A: Mathematical, Physical and Engineering Sciences*, vol. 93, pp. 114-128, 1917.
- [139] Cegla, F. B., Cawley, P., and Lowe, M. J. S., "Material Property Measurement Using the Quasi-Scholte Mode - a Waveguide Sensor," *Journal of the Acoustical Society of America*, vol. 117, pp. 1098-1107, Mar 2005.

- [140] Yu, L. and Tian, Z., "Lamb Wave Structural Health Monitoring Using a Hybrid Pzt-Laser Vibrometer Approach," *Structural Health Monitoring*, vol. 12, pp. 469-483, 2013.
- [141] Sohn, H., Dutta, D., Yang, J. Y., Park, H. J., DeSimio, M. P., Olson, S. E., and Swenson, E. D., "Delamination Detection in Composites through Guided Wave Field Image Processing," *Composites Science and Technology*, vol. 71, pp. 1250-1256, 2011.
- [142] Tian, Z. and Yu, L., "Lamb Wave Frequency-Wavenumber Analysis and Decomposition," *Journal of Intelligent Material Systems and Structures*, vol. 25, pp. 1107-1123, 2014.
- [143] Glushkov, E., Glushakova, N., Golub, M. V., Moll, J., and Fritzen, C. P., "Wave Energy Trapping and Localization in a Plate with a Delamination," *Smart Materials & Structures*, vol. 21, p. 125001, 2012.
- [144] Johnson, D. H. and Dudgeon, D. E., *Array Signal Processing: Concepts and Techniques*. Upper Saddle River, New Jersey, USA: Prentice-Hall Inc., 1993.
- [145] Oppenheim, A. V., Willsky, A. S., and Hamid, S., *Signals and Systems (2nd Edition)*. New Jersey, USA: Prentice Hall, 1997.
- [146] Cohen, L., *Time Frequency Analysis: Theory and Applications*. Upper Saddle River, New Jersey, USA: Prentice-Hall Inc., 1994.
- [147] Leckey, C. A. C. and Seebo, J. P., "Guided Wave Energy Trapping to Detect Hidden Multilayer Delamination Damage," *AIP Conference Proceedings*, vol. 1650, pp. 1162-1169, 2015.
- [148] Tian, Z., Leckey, C. A. C., Seebo, J. P., and Yu, L., "Guided Wave Delamination Detection and Quantification with Wavefield Data Analysis," presented at the ASME 2014 Conference on Smart Material, Adaptive Structures and Intelligent Systems, Newport, Rhode Island, 2014.
- [149] Tian, Z., Yu, L., and Leckey, C. A. C., "Delamination Detection and Quantification on Laminated Composite Structures with Lamb Waves and Wavenumber Analysis," *Journal of Intelligent Material Systems and Structures*, 2014.
- [150] Na, W. B. and Kundu, T., "Underwater Pipeline Inspection Using Guided Waves," *Journal of Pressure Vessel Technology*, vol. 124, pp. 196-200, 2002.
- [151] Bingham, J., Hinders, M., and Friedman, A., "Lamb Wave Detection of Limpet Mines on Ship Hulls," *Ultrasonics*, vol. 49, pp. 706-722, Dec 2009.
- [152] Chen, J. G., Su, Z. Q., and Cheng, L., "Identification of Corrosion Damage in Submerged Structures Using Fundamental Anti-Symmetric Lamb Waves," *Smart Materials & Structures*, vol. 19, p. 015004, Jan 2010.

- [153] Rizzo, P., Han, J. G., and Ni, X. L., "Structural Health Monitoring of Immersed Structures by Means of Guided Ultrasonic Waves," *Journal of Intelligent Material Systems and Structures*, vol. 21, pp. 1397-1407, Sep 2010.
- [154] Pistone, E., Li, K. Y., and Rizzo, P., "Noncontact Monitoring of Immersed Plates by Means of Laser-Induced Ultrasounds," *Structural Health Monitoring-an International Journal*, vol. 12, pp. 549-565, Sep 2013.
- [155] Koduru, J. P. and Rose, J. L., "Mode Controlled Guided Wave Tomography Using Annular Array Transducers for Shm of Water Loaded Plate Like Structures," *Smart Materials and Structures*, vol. 22, p. 10, Dec 2013.
- [156] Chimenti, D. E. and Nayfeh, A. H., "Leaky Lamb Waves in Fibrous Composite Laminates," *Journal of Applied Physics*, vol. 58, pp. 4531-4538, 1985.
- [157] Wu, J. and Zhu, Z., "The Propagation of Lamb Waves in a Plate Bordered with Layers of a Liquid," *Journal of Acoustic Society of America*, vol. 91, pp. 861-867, 1992.
- [158] Shuvalov, A. L., Poncelet, O., and Deschamps, M., "Analysis of the Dispersion Spectrum of Fluid-Loaded Anisotropic Plates: Leaky-Wave Branches," *Journal of Sound and Vibration*, vol. 296, pp. 494-517, 2006.
- [159] Cegla, F. B., Cawley, P., and Lowe, M. J. S., "Fluid Bulk Velocity and Attenuation Measurements in Non-Newtonian Liquids Using a Dipstick Sensor," *Measurement Science & Technology*, vol. 17, pp. 264-274, Feb 2006.
- [160] "Managing Gas Accumulation in Emergency Core Cooling, Decay Heat Removal, and Containment Spray Systems," *NRC Generic Letter 2008-01*, p. ML072910759, January 11 2008.
- [161] Michaels, J. E., Dawson, A. J., Michaels, J. E., and Ruzzene, M., "Approaches to Hybrid Shm and Nde of Composite Aerospace Structures," in *Health Monitoring of Structural and Biological Systems 2014*, San Diego, CA, USA, 2014.
- [162] Su, Z. Q., Wang, X. M., Chen, Z. P., and Ye, L., "A Hierarchical Data Fusion Scheme for Identifying Multi-Damage in Composite Structures with a Built-in Sensor Network," *Smart Materials & Structures*, vol. 16, pp. 2067-2079, Dec 2007.
- [163] Kim, S. B. and Sohn, H., "Instantaneous Reference-Free Crack Detection Based on Polarization Characteristics of Piezoelectric Materials," *Smart Materials & Structures*, vol. 16, pp. 2375-2387, Dec 2007.
- [164] Ihn, J. B. and Chang, F. K., "Pitch-Catch Active Sensing Methods in Structural Health Monitoring for Aircraft Structures," *Structural Health Monitoring-an International Journal*, vol. 7, pp. 5-19, Mar 2008.
- [165] Yu, L. and Leckey, C., "Lamb Wave-Based Quantitative Crack Detection Using a Focusing Array Algorithm," vol. 29, pp. 1138-1152, 2013.
- [166] Kundu, T., "Acoustic Source Localization," *Ultrasonics*, vol. 54, pp. 24-38, 2014.

- [167] Tua, P. S., Quek, S. T., and Wang, Q., "Detection of Cracks in Plates Using Piezo-Actuated Lamb Waves," *Smart Materials & Structures*, vol. 13, pp. 643-660, Aug 2004.
- [168] Bagheri, A., Li, K. Y., and Rizzo, P., "Reference-Free Damage Detection by Means of Wavelet Transform and Empirical Mode Decomposition Applied to Lamb Waves," *Journal of Intelligent Material Systems and Structures*, vol. 24, pp. 194-208, Jan 2013.
- [169] Hall, J. S., McKeon, P., Satyanarayan, L., Michaels, J. E., Declercq, N. F., and Berthelot, Y. H., "Minimum Variance Guided Wave Imaging in a Quasi-Isotropic Composite Plate," *Smart Materials and Structures*, vol. 20, p. 8, Feb 2011.
- [170] Zhao, X. L., Gao, H. D., Zhang, G. F., Ayhan, B., Yan, F., Kwan, C., and Rose, J. L., "Active Health Monitoring of an Aircraft Wing with Embedded Piezoelectric Sensor/Actuator Network: I. Defect Detection, Localization and Growth Monitoring," *Smart Materials & Structures*, vol. 16, pp. 1208-1217, Aug 2007.
- [171] Levine, R. M. and Michaels, J. E., "Model-Based Imaging of Damage with Lamb Waves Via Sparse Reconstruction," *Journal of Acoustic Society of America*, vol. 133, pp. 1525-1534, 2013.
- [172] Castaings, M., Le Clezio, E., and Hosten, B., "Modal Decomposition Method for Modeling the Interaction of Lamb Waves with Cracks," *Journal of the Acoustical Society of America*, vol. 112, pp. 2567-2582, Dec 2002.
- [173] An, Y.-K., Kwon, Y., and Sohn, H., "Noncontact Laser Ultrasonic Crack Detection for Plates with Additional Structural Complexities," *Structural Health Monitoring*, vol. 12, pp. 522-538, 2013.
- [174] Cammarata, M., Rizzo, P., Dutta, D., and Sohn, H., "Application of Principal Component Analysis and Wavelet Transform to Fatigue Crack Detection in Waveguides," *Smart Structures and Systems*, vol. 6, pp. 349-362, May 2010.
- [175] Betz, D. C., Staszewski, W. J., Thursby, G., and Culshaw, B., "Multi-Functional Fibre Bragg Grating Sensors for Fatigue Crack Detection in Metallic Structures," *Proceedings of the Institution of Mechanical Engineers Part G-Journal of Aerospace Engineering*, vol. 220, pp. 453-461, Oct 2006.
- [176] Lu, Y., Ye, L., and Su, Z. Q., "Crack Identification in Aluminium Plates Using Lamb Wave Signals of a Pzt Sensor Network," *Smart Materials & Structures*, vol. 15, pp. 839-849, Jun 2006.
- [177] Renshaw, J., Holland, S. D., and Thompson, R. B., "Measurement of Crack Opening Stresses and Crack Closure Stress Profiles from Heat Generation in Vibrating Cracks," *Applied Physics Letters*, vol. 93, pp. -, Aug 25 2008.
- [178] Rizzo, P., Cammarata, M., Dutta, D., Sohn, H., and Harries, K., "An Unsupervised Learning Algorithm for Fatigue Crack Detection in Waveguides," *Smart Materials & Structures*, vol. 18, pp. -, Feb 2009.

- [179] Ihn, J. B. and Chang, F. K., "Detection and Monitoring of Hidden Fatigue Crack Growth Using a Built-in Piezoelectric Sensor/Actuator Network: I. Diagnostics," *Smart Materials & Structures*, vol. 13, pp. 609-620, Jun 2004.
- [180] Lu, Y., Ye, L., Su, Z. Q., and Yang, C. H., "Quantitative Assessment of through-Thickness Crack Size Based on Lamb Wave Scattering in Aluminium Plates," *Ndt & E International*, vol. 41, pp. 59-68, Jan 2008.
- [181] An, Y. K., Kim, J. M., and Sohn, H., "Laser Lock-in Thermography for Detection of Surface-Breaking Fatigue Cracks on Uncoated Steel Structures," *Ndt & E International*, vol. 65, pp. 54-63, Jul 2014.
- [182] An, Y.-K., Park, B., and Sohn, H., "Complete Noncontact Laser Ultrasonic Imaging for Automated Crack Visualization in a Plate," *Smart Materials & Structures*, vol. 22, p. 025022, 2013.
- [183] Yu, L., Tian, Z., and Leckey, C. A. C., "Crack Imaging and Quantification in Aluminum Plates with Guided Wave Wavenumber Analysis Methods," *Ultrasonics*, 2015.
- [184] Castaings, M. and Hosten, B., "Ultrasonic Guided Waves for Health Monitoring of High-Pressure Composite Tanks," *Ndt & E International*, vol. 41, pp. 648-655, Dec 2008.
- [185] Tian, Z., Yu, L., and Leckey, C. A. C., "Guided Wave Propagation Study on Laminated Composites by Frequency-Wavenumber Technique," in *Nondestructive Characterization for Composite Materials, Aerospace Engineering, Civil Infrastructure, and Homeland Security 2014*, San Diego, California, USA, 2014, p. 906310.
- [186] Yu, L., Cara, L., and Tian, Z., "Study on Crack Scattering in Aluminum Plates with Lamb Wave Frequency-Wavenumber Analysis," *Smart Materials & Structures*, vol. 22, p. 065019, 2013.
- [187] Tian, Z., Leckey, C., Rogge, M. D., and Yu, L., "Crack Detection with Lamb Wave Wavenumber Analysis," presented at the Health Monitoring of Structural and Biological Systems 2013, San Diego, CA, 2013.
- [188] Tian, Z., Huang, G. L., and Yu, L., "Study of Guided Wave Propagation in Honeycomb Sandwich Structures," presented at the ASME 2014 Conference on Smart Materials, Adaptive Structures and Intelligent Systems, Newport, Rhode Island, USA, 2014.
- [189] Tian, Z. and Yu, L., "Lamb Wave Propagation Study Using Frequency-Wavenumber Analysis," *ASME 2012 Conference on Smart Material, Adaptive Structures and Intelligent Systems*, vol. SMASIS2012-8013, 2012.
- [190] An, Y. K., Park, B., and Sohn, H., "Complete Noncontact Laser Ultrasonic Imaging for Automated Crack Visualization in a Plate," *Smart Materials and Structures*, vol. 22, Feb 2013.

- [191] Ip, K. H. and Mai, Y. W., "Delamination Detection in Smart Composite Beams Using Lamb Waves," *Smart Materials & Structures*, vol. 13, pp. 544-551, Jun 2004.
- [192] Ricci, F., Mal, A. K., Monaco, E., Maio, L., Boffa, N. D., Di Palma, M., and Lecce, L., "Guided Waves in Layered Plate with Delaminations," presented at the Proceedings of 7th European Workshop on Structural Health Monitoring, La Cite, Nantes, France, 2014.
- [193] Salamone, S., Bartoli, I., di Scalea, F. L., and Coccia, S., "Guided-Wave Health Monitoring of Aircraft Composite Panels under Changing Temperature," *Journal of Intelligent Material Systems and Structures*, vol. 20, pp. 1079-1090, Jun 2009.
- [194] Mesnil, O., Leckey, C. A. C., and Ruzzene, M., "Instantaneous and Local Wavenumber Estimations for Damage Quantification in Composites," *Structural Health Monitoring*, vol. 14, pp. 193-204, 2014.
- [195] Juarez, P. D. and Leckey, C. A. C., "Multi-Frequency Local Wavenumber Analysis and Ply Correlation of Delamination Damage," *Ultrasonics*, vol. 62, pp. 56-65, 2015.
- [196] Staszewski, W. J., Mahzan, S., and Traynor, R., "Health Monitoring of Aerospace Composite Structures-Active and Passive Approach," *Composites Science and Technology*, vol. 69, pp. 1678-1685, 2009.
- [197] Alleyne, D. N. and Cawley, P., "The Interaction of Lamb Waves with Defects," *Ieee Transactions on Ultrasonics Ferroelectrics and Frequency Control*, vol. 39, pp. 381-397, 1992.
- [198] Boller, C., "Next Generation Structural Health Monitoring and Its Integration into Aircraft Design," *International Journal of Systems Science*, vol. 31, pp. 1333-1349, 2000.
- [199] Ong, W. H. and Chiu, W. K., "Redirection of Lamb Waves for Structural Health Monitoring," *Smart Materials Research*, vol. 2012, p. 718686, 2012.
- [200] Kundu, T., Das, S., Martin, S. A., and Jata, K. V., "Locating Point of Impact in Anisotropic Fiber Reinforced Composite Plates," *Ultrasonics*, vol. 48, pp. 193-201, Jul 2008.
- [201] Su, Z. Q., Cheng, L., Wang, X. M., Yu, L., and Zhou, C., "Predicting Delamination of Composite Laminates Using an Imaging Approach," *Smart Materials & Structures*, vol. 18, p. 074002, Jul 2009.
- [202] Salas, K. I. and Cesnik, C. E. S., "Guided Wave Structural Health Monitoring Using Clover Transducers in Composite Materials," *Smart Materials & Structures*, vol. 19, p. 015014, Jan 2010.
- [203] Song, F., Huang, G. L., and Hu, G. K., "Online Guided Wave-Based Debonding Detection in Honeycomb Sandwich Structures," *Aiaa Journal*, vol. 50, pp. 284-293, 2012.

- [204] Giurgiutiu, V. and Soutis, C., "Enhanced Composites Integrity through Structural Health Monitoring," *Applied Composite Materials*, vol. 19, pp. 813-829, 2012.
- [205] Guo, N. and Cawley, P., "The Interaction of Lamb Waves with Delaminations in Composite Laminates," *Journal of Acoustic Society of America*, vol. 94, pp. 2240-2246, 1993.
- [206] Petculescu, G., Krishnaswamy, S., and Achenbach, J. D., "Group Delay Measurements Using Modally Selective Lamb Wave Transducers for Detection and Sizing of Delaminations in Composites," *Smart Materials & Structures*, vol. 17, p. 015007, Feb 2008.
- [207] Purekar, A. S. and Pines, D. J., "Damage Detection in Thin Composite Laminates Using Piezoelectric Phased Sensor Arrays and Guided Lamb Wave Interrogation," *Journal of Intelligent Material Systems and Structures*, vol. 21, pp. 995-1010, Jul 2010.
- [208] Yeum, C. M., Sohn, H., Ihn, J. B., and Lim, H. J., "Instantaneous Delamination Detection in a Composite Plate Using a Dual Piezoelectric Transducer Network," *Composite Structures*, vol. 94, pp. 3490-3499, 2012.
- [209] Hayashi, T. and Kawashima, K., "Multiple Reflections of Lamb Waves at a Delamination," *Ultrasonics*, vol. 40, pp. 193-197, 2002.
- [210] Ramadas, C., Balasubramaniam, K., Joshi, M., and Krishnamurthy, C. V., "Interaction of the Primary Anti-Symmetric Lamb Mode (A0) with Symmetric Delaminations: Numerical and Experimental Studies," *Smart Materials & Structures*, vol. 18, p. 085011, Aug 2009.
- [211] Williams, G., Trask, R., and Bond, I., "A Self-Healing Carbon Fibre Reinforced Polymer for Aerospace Applications," *Composites Part a-Applied Science and Manufacturing*, vol. 38, pp. 1525-1632, 2007.
- [212] Fatemi, J. and Lemmen, M., "Effective Thermal/Mechanical Properties of Honeycomb Core Panels for Hot Structure Applications," *Journal of Spacecraft and Rockets*, vol. 46, pp. 514-525, 2009.
- [213] T., B., *Honeycomb Technology: Materials, Design, Manufacturing, Applications and Testing*: Springer, 1997.
- [214] Zenkert, D., *The Handbook of Sandwich Construction*. London: EMAS Publishing, 1997.
- [215] Vinson, J. R., *The Behavior of Sandwich Structures of Isotropic and Composite Materials*. Lancaster: Technomic Publishing Company, 1999.
- [216] Minakuchi, S., Okabe, Y., and Takeda, N., "Real-Time Detection of Debonding between Honeycomb Core and Facesheet Using a Small-Diameter Fbg Sensor Embedded in Adhesive Layer," *Journal of Sandwich Structures & Materials*, vol. 9, pp. 9-33, 2007.

- [217] Takeda, N., Minakuchi, S., and Okabe, Y., "Smart Composite Sandwich Structures for Future Aerospace Application -Damage Detection and Suppression: A Review," *Journal of Solid Mechanics and Materials Engineering*, vol. 1, pp. 3-17, 2007.
- [218] Goswami, S. and Becker, W., "Analysis of Debonding Fracture in a Sandwich Plate with Hexagonal Core," *Composite Structures*, vol. 49, pp. 385-392, 8// 2000.
- [219] Hosseini, S. M., Willberg, C., Kharaghani, A., and Gabbert, U., "Characterization of the Guided Wave Propagation in Simplified Foam Honeycomb and Hollow Sphere Structures," *Composite: Part B*, vol. 56, pp. 553-566, 2014.
- [220] Chakraborty, N., Rathod, V. T., Mahapatra, D. R., and Gopalakrishnan, S., "Guided Wave Based Detection of Damage in Honeycomb Core Sandwich Structures," *Ndt & E International*, vol. 49, pp. 27-33, Jul 2012.
- [221] Hou, Y., Neville, R., Scarpa, F., Remillat, C., Gu, B., and Ruzzene, M., "Graded Conventional-Auxetic Kirigami Sandwich Structures: Flatwise Compression and Edgewise Loading," *Composites Part B: Engineering*, vol. 59, pp. 33-42, 2014.